INAUGURAL-DISSERTATION
zur Erlangung der Doktorwürde der
Naturwissenschaftlich-Mathematischen Gesamtfakultät der
Ruprecht-Karls-Universität Heidelberg

vorgelegt von
Dipl.-Phys. Martin Matthias Härtig
aus Münsingen

Tag der mündlichen Prüfung:
20. November 2019

MOTION MANAGEMENT FOR CARBON ION THERAPY AT THE HEIDELBERG ION-BEAM THERAPY CENTER

MARTIN MATTHIAS HÄRTIG

Gutachter: Prof. Dr. Oliver Jäkel
Prof. Dr. João Seco

Martin Matthias Härtig
Motion Management for Carbon Ion Therapy
at the Heidelberg Ion-Beam Therapy Center

ZUSAMMENFASSUNG

Anfang 2011 wurde am Heidelberger Ionenstrahl-Therapiezentrum HIT die extrakranielle Stereotaxie zur Behandlung des Hepatozellulären Karzinoms eingeführt. Zunächst wurden dreizehn Patienten behandelt, einschließlich des ersten Patienten mit atemgesteuerter Bestrahlung (Gating). In dieser Arbeit werden der neu eingeführte Behandlungsablauf und die Datenerfassung für die Behandlung bewegter Organe vorgestellt. Aufgrund der Patientendatensätze sind simulierte und rekonstruierte zeitabhängige 4D-Dosisverteilungen der Bestrahlungen verfügbar.

Simulationen von 4D-Dosisverteilungen erfordern genaue Kenntnis der Organbewegung und korrekte Vorhersagen des Zeitverhaltens des Beschleunigers. Um die Vorhersage zu verbessern, wurden die Eigenschaften des HIT-Synchrotron-Zyklus untersucht; bei dieser Untersuchung wurden energieabhängige und stochastische Aspekte sowie tägliche Schwankungen der Strahlintensität festgestellt. Eine Simulation-Software wurde implementiert, die auf einem realistischen Modell des Beschleunigers beruht. Die Genauigkeit der errechneten Bestrahlungsabläufe wurde mit Bestrahlungsaufzeichnungen überprüft. Eine experimentelle Überprüfung des Algorithmus wurde anhand eines Patienten-Behandlungsplans in einem bewegten Wasserphantom durchgeführt. Hierbei wurde eine Dosisabweichung von $(1.0 \pm 7.3)\%$ ermittelt.

Seit Ende 2012 eröffnet die HIT-Schwerionen-Gantry neue Bestrahlungsmöglichkeiten. In einer Planungsstudie wurden die optimalen Plangeometrien für die Behandlung von Ösophagus-Karzinomen ermittelt. Grundlage der Studie waren vier Patientendatensätze und dreizehn vorgeschlagene Plangeometrien. Über eine quasi-statische Dosisberechnung wurden die Effekte von intrafraktioneller Organbewegung berücksichtigt. Die berechneten Dosisverteilungen können als Grundlage für die Definition von Sicherheitssäumen und Gatingfenstergrößen dienen.

ABSTRACT

In 2011, stereotactic body radiotherapy was introduced for the treatment of hepatocellular carcinoma at the Heidelberg Ion-Beam Therapy Center (HIT). Initially, thirteen patients were treated, including the first patient treated using respiratory beam gating. This thesis presents the work flow and data acquisition for the treatment of moving organs. Based on the acquired patient data, simulated and reconstructed 4D dose distributions are now available.

Simulations of 4D dose distributions require precise knowledge of the organ motion and accelerator timing. To improve the prediction, the properties of the HIT synchrotron cycle were investigated, revealing energy-dependent and stochastic aspects and day-to-day beam intensity fluctuations. A simulation was implemented based on a realistic model of the accelerator. The accuracy of calculated irradiation sequences was verified using treatment records. Experimental verification using a patient treatment plan was performed in a moving water phantom, where a total dose deviation of $(1.0 \pm 7.3)\%$ was determined.

Since 2012, the HIT heavy-ion gantry offers new treatment options. In a treatment planning study, optimal plan geometries for the treatment of esophageal carcinoma were determined. Effects of intrafractional organ motion were accounted for in a quasi-static dose calculation. Results can potentially be used for margin and gating window definition.

PUBLICATIONS RELATED TO THIS WORK

Peer-Reviewed Articles

Habermehl D., Debus J., Ganten T., Ganten M.-K., Julia Bauer J., Brecht I. C., Brons S., Haberer T., **Härtig M.**, Jäkel O., Parodi K., Welzel T., and Combs S. E.: "Hypofractionated Carbon Ion Therapy Delivered with Scanned Ion Beams for Patients with Hepatocellular Carcinoma – Feasibility and Clinical Response" *Radiation Oncology,* 2013, 8:59.

Richter D., Saito N., Chaudhri N., **Härtig M.**, Ellerbrock M., Jäkel O., Combs S. E., Habermehl D., Herfarth K., Durante M., Bert C.: "Four-Dimensional Patient Dose Reconstruction for Scanned Ion Beam Therapy of Moving Liver Tumors" *International Journal of Radiation Oncology, Biology, Physics,* 2014, 89(1):175–181

Häfner M.F., Sterzing F., Krug D., Körber S.A., Jäkel O., Debus J. and **Härtig M.M.**: "Intrafractional Dose Variation and Beam Configuration in Carbon Ion Radiotherapy for Esophageal Cancer" *Radiation Oncology,* 2016, 11:150

Scientific Reports

Richter D., Steidl P., Saito N., **Härtig M.**, Jäkel O., Durante M. and Bert C.: "Simulation of Uncompensated and Gated Treatments of a Liver Cancer Patient with Scanned Carbon Ions" *GSI Scientific Report 2011*, 548.

Conference Contributions

Chaudhri N., Richter D., **Härtig M.**, Ecker S., Ackermann B., Naumann J., Haberer T., Bert C., Habermehl D., Herfarth K., Ellerbrock M., Jäkel O.: "Clinical Implementation of Gating and Dose Verification with Scanned Ion Beams at HIT" *Medical Physics,* 06/2012, 39(6):3780-3781.

Richter D., Saito N., Chaudhri N., **Härtig M.**, Combs S. E., Habermehl D., Herfarth K., Jäkel O., Durante M., Bert C.: "4D Treatment Dose Reconstruction for Scanned Ion Beam Therapy" *International Journal of Radiation Oncology, Biology, Physics,* 2013, 87(2), Supplement, S183.

CONTENTS

ACS Accelerator Control System

BAMS Beam Application and Monitoring System

BDS Beam Delivery Sequence

CT Computed Tomography

CTV Clinical Target Volume

DCU Device Control Unit

DFG Deutsche Forschungsgemeinschaft (German Research Foundation)

DKFZ Deutsches Krebsforschungszentrum (German Center for Cancer Research), Heidelberg, Germany

DIC Dynamic Intensity Control

DICOM Digital Imaging and Communications in Medicine

DTL Drift Tube Linac

DVH Dose Volume Histogram

Ex Exhale

ECR Electron Cyclotron Resonance

GSI GSI Helmholtz Centre for Heavy Ion Research, Darmstadt, Germany

GTV Gross Tumor Volume

HCC Hepatocellular Carcinoma

HEBT High Energy Beam Transport

HICAT Heavy Ion Cancer Therapy (Accelerator)

HIT Heidelberger Ionenstrahl-Therapiezentrum (Heidelberg Ion-Beam Therapy Center), Heidelberg, Germany

HLUT Hounsfield Look-Up Table

HU Hounsfield Unit

IC Ionization Chamber

IGRT Image Guided Radiotherapy

IMPT Intensity (Fluence-) Modulated Particle Therapy

IMRT Intensity (Fluence-) Modulated Radiotherapy

ITV Internal Target Volume

KS Kolmogorov-Smirnov (Statistical Test)

LEBT Low Energy Beam Transport

LEM Local Effect Model

LET Linear Energy Transfer

MEBT Medium Energy Beam Transport

MRI Magnetic Resonance Imaging

MWPC Multi-Wire Proportional Counter

NCT Nationales Centrum für Tumorerkrankungen (National Center for Tumor Diseases), Heidelberg, Germany

NIRS National Institute of Radiological Sciences, Chiba, Japan

PACS Picture Archiving and Communication System

PET Positron Emission Tomography

PTV Planning Target Volume

QA Quality Assurance

RF Radio Frequency

RFQ Radio Frequency Quadrupole

RBE Relative Biological Effectiveness

SBRT Stereotactic Body Radiotherapy

TCS Treatment Control System

TPS Treatment Planning System

TRiP Treatment Planning for Particles

WEPL Water-Equivalent Path Length

1 INTRODUCTION

Tumor diseases are the second most common cause of death in the developed countries, surpassed only by diseases of the cardio-vascular system. In 2015, 39% of all deaths in Germany were attributed to cardio-vascular diseases, 25% to tumor diseases[1]. Furthermore, 44% of women and 50% of men can be expected to develop cancer in their lifetime[2].

In this thesis, the focus is on two tumor localizations: Cancer of the liver, which is responsible for 2% of cancer related deaths in women and 4% in men, and cancer of the esophagus, responsible for 1% of cancer related deaths in women and 3% in men. In 2014, 13,000 patients died from cancer of the liver and esophagus in Germany, with increasing numbers expected in the upcoming years. Viable treatment options for liver and esophageal cancer are limited, which is reflected by low five-year-survival rates. Only 11% of women and 14% of men diagnosed with liver cancer, and 21% of patients diagnosed with esophageal cancer survive five years after the diagnosis.

Studies at the National Institute of Radiological Sciences, Chiba, Japan (NIRS) suggest carbon ion therapy may be a viable treatment option for hepatocellular carcinoma, with five-year-survival rates increased to 33% (Kamada et al. (2015)). Studies on the efficacy of treating esophageal carcinoma with carbon ions have not been published yet, but carbon ion therapy has been shown to be beneficial in treating adenoid cystic carcinoma (Jensen et al. (2015)) and highly conformal irradiations have been shown to be beneficial in esophageal carcinoma (Carrington et al. (2016)). Hence, highly conformal carbon ion boosts could increase local control and survival rates.

Particle therapy has been pioneered in the Lawrence Berkeley National Laboratory, USA. Here, the first patients were treated with proton beams in 1954. In 1974, the first patients received treatment with heavy ions. To offer particle therapy to an increasing number of patients, the first dedicated proton therapy facility started operation in 1990 at the Loma Linda University Medical Center, USA. The first dedicated carbon ion therapy facility followed in 1994, when the Heavy-Ion Medical Accelerator Complex in Chiba, Japan, started its operation. In Germany, carbon ion therapy has been pioneered at the GSI Helmholtz Centre for Heavy Ion Research in Darmstadt, where patients were treated in a dedicated clinical treatment room. From 1997 to 2008, over 440 patients were irradiated using carbon ions with an active raster scanning technique. After the success of this pilot project, the Heidelberg Ion-Beam Therapy Center (HIT) was built as a dedicated clinical ion beam facility, which began patient operation in November 2009. In October 2012, the first patients were irradiated using the heavy ion gantry.

Organ motion is an issue when treating tumors of the thorax and abdomen, where daily variations of the patient anatomy may require plan adaptations. Additionally, the liver moves by 1 to 2 centimeters due to breathing motion and

1 See: Statistisches Bundesamt (Destatis) (2017)

2 See: Robert Koch-Institut (Hrsg.) und die Gesellschaft der epidemiologischen Krebsregister in Deutschland e.V. (Hrsg.) (2017)

heart palpitation (Langen and Jones (2001); Liang et al. (2018)). In combination with fluence-modulated radiotherapy (IMRT or IMPT), the interference between the fluence pattern and the organ motion can negatively impact the resulting dose distribution (Phillips et al. (1992); Bert and Durante (2011)). This can have a detrimental effect on the treatment outcome. Several mitigation strategies are available, including passive techniques like motion reduction, rescanning, and margin concepts; and active techniques like beam gating and beam tracking. Further, 4D treatment planning systems are being developed which include organ motion in the dose calculation and can be used to simulate or reconstruct doses delivered to patients (Richter et al. (2013a,b)).

Most research relevant to this thesis has been performed in close collaboration with the GSI biophysics research group. Because of the similarities between the techniques used in the pilot project and the HIT facility, results and new developments from GSI can be directly integrated into clinical research at HIT. The cooperation between Heidelberg University Hospital, German Cancer Research Center (DKFZ), National Center for Tumor Diseases (NCT) and GSI has led to the creation of a German Research Foundation (DFG) founded clinical research group, which started in 2009. Research topics include the therapy of gastrointestinal tumors including beam gating (Richter et al. (2014)), adaptive planning for prostate and pancreatic cancer (Ruciński (2013); Batista (2016); Batista et al. (2018)), and 4D treatment plan optimization (Richter et al. (2013b)). This work was funded by the German Research Foundation as part of the clinical research group KFO 214 *Heavy Ion Therapy*.

SCOPE OF THIS THESIS

The integration of new therapy concepts, developed in collaboration with the GSI biophysics research group, into the clinical routine of patient therapy at HIT is the main focus of the work done in this thesis. It is presented in three main parts:

- Adaptation of the treatment work flow for the treatment of patients suffering from hepatocellular carcinoma. From May 2011 to July 2013, thirteen patients were treated using this work flow, including the first beam gating patient at HIT. Here, the data acquisition necessary to simulate and reconstruct dose distributions is presented.
- Development and introduction of an improved simulation of the HIT accelerator timing structure, necessary for accurate predictions of dose distributions and variability. The model is verified using irradiation records and measurements in a moving water phantom.
- Presentation of a treatment planning study for esophageal cancer, using the newly available heavy ion gantry at HIT. Organ motion is taken into account using a simplified quasi-static dose calculation approach.

Chapter 2 is dedicated to the research fundamentals relevant to this thesis. Chapter 3 describes the improved treatment work flow introduced for the treatment of hepatocellular carcinoma. Chapter 4 covers the improved accelerator timing simulation necessary for 4D dose calculation. Chapter 5 presents an esophagus treatment planning study which aims to find the optimal treatment geometry for the new heavy ion gantry.

2 MATERIALS AND METHODS

In this chapter, the fundamentals of ion beam therapy will be described. This encompasses the physical and radiobiological properties of ion beams, an outline of the Heidelberg Ion Therapy Center (HIT), the properties of the treatment planning software used in this thesis and the basic principles of treating moving organs.

2.1 FUNDAMENTALS OF ION BEAM THERAPY

Megavoltage photon beams from linear accelerators or radioactive sources are widely used in radiotherapy. In comparison, beams of high-energy ions such as protons or heavier elements offer advantages beneficial to the treatment of tumors: While the entrance dose in tissue is low, the depth-dose distribution exhibits a distinct maximum and steep fall-off (Bragg peak) with a well-defined range. Ion beams have a small lateral spread and especially heavier particles have an increased biological effectiveness in the Bragg peak region due to higher density ionization. These properties make ion beams well suited for the treatment of radio-resistant tumors located near organs at risk.

2.1.1 *Physical Properties of Ion Beams*

ABSORBED DOSE One of the fundamental quantities of radiation therapy is the *absorbed dose* D. All biological effects of radiotherapy (like cell death and tumor control) are linked to the energy dose deposited in tissue. It is defined in the ICRU report 90 (Seltzer et al. (2014)) as the mean energy imparted by ionizing radiation $d\bar{\varepsilon}$ in a given volume to a mass element dm:

$$D = \frac{d\bar{\varepsilon}}{dm} \quad [1\,\mathrm{Gy} = 1\,\mathrm{J/kg}] \tag{1}$$

The imparted energy ε is defined as the sum of all energy deposits ε_i in the volume:

$$\varepsilon = \sum_i \varepsilon_i, \text{ with } \varepsilon_i = \varepsilon_{in} - \varepsilon_{out} + Q \tag{2}$$

Each energy deposit ε_i is the result of a single interaction of an incoming particle. ε_{in} is the energy of the incident particle and ε_{out} is the sum of the energies of all particles leaving the interaction. Q is the change in rest energies of all involved particles.

MASS STOPPING POWER The mean energy loss dE of a particle traversing a distance dl in a material of density ρ is described by the *mass stopping power* S/ρ:

$$\frac{S}{\rho} = \frac{1}{\rho}\frac{dE}{dl}, \text{ with } S = \frac{dE}{dl} \tag{3}$$

as the *linear stopping power*.

In general, the mass stopping power is described by three components:

$$\frac{S}{\rho} = \frac{1}{\rho}\left(\frac{dE}{dl}\right)_{el} + \frac{1}{\rho}\left(\frac{dE}{dl}\right)_{rad} + \frac{1}{\rho}\left(\frac{dE}{dl}\right)_{nuc}, \tag{4}$$

where the first term is the *mass electronic stopping power* due to ionization or excitation of atomic electrons, the second term is the *mass radiative stopping power* due to emission of bremsstrahlung and the third term is the *mass nuclear stopping power* due to elastic Coulomb interactions with the nucleus of an atom.

The typical range requirement for radiotherapy using charged particles is 30 cm, which translates to particle energies of 220 MeV for protons and 430 MeV/u for carbon ions. At this energy, the energy loss is dominated by inelastic collisions with target electrons, described by the electronic stopping power term. Radiative stopping power is relevant for interactions of electron or positron beams, but is reduced by a factor of $(m_e/M)^2$ for ions, where m_e is the rest mass of the electron and M is the rest mass of the incident ion. Nuclear stopping power is only relevant for ions of low kinetic energy.

A calculation of the electronic stopping power for charged particles has been performed by Bethe, using the first Born approximation (Bethe (1930); Fano (1963)). For the interaction of heavy ion beams with electrons, the assumption $m_e << M$ can be used to arrive at the *modified Bethe-Bloch formula*:

$$\frac{1}{\rho}S_{el} = \frac{1}{\rho}\left(\frac{dE}{dl}\right)_{el} = \frac{4\pi r_e^2 m_e c^2}{\beta^2}\frac{Z}{uA}z^2 \cdot B(\beta), \tag{5}$$

where $B(\beta)$ is the stopping number per electron:

$$B(\beta) = \ln\left(\frac{2m_e c^2\beta^2}{(1-\beta^2)I}\right) - \beta^2 - \frac{\delta}{2} - \frac{C}{Z} + zB_1 + z^2B_2. \tag{6}$$

Here, r_e is the classical electron radius, c is the speed of light in vacuum, β is the velocity of the particle v divided by c, Z is the charge of the target nucleus, z is the charge of the projectile, u is the atomic mass constant and A is the relative atomic weight. I is the mean excitation energy of the medium. This formula contains the Barkas correction zB_1, Bloch correction z^2B_2, shell correction C/Z and density-effect correction δ (Bloch (1933a,b); Seltzer et al. (2014)).

PARTICLE RANGE Assuming a continuous loss of energy for a particle traversing through matter, its path length can be calculated from the initial energy using the mass stopping power. The approach is called *continuous-slowing-down approximation (CSDA)* and the mass CSDA range is defined as:

$$\rho\, r_0(E_0 \to E_{fin}) = \rho\int_{E_{fin}}^{E_0}\frac{1}{S(E')}dE', \tag{7}$$

with the initial particle energy E_0 and a final particle energy E_{fin}, which is usually the lowest ionization potential of the medium (Seltzer et al. (2014)). Note that, due to angular deflections in the medium, the CSDA range is not the same as the penetration depth.

ENERGY LOSS AND RANGE STRAGGLING The Bethe-Bloch formula only describes the mean energy loss of a charged particle. Taking only the Bethe formula

into account, the energy loss of an ion beam would result in an extremely sharp dose peak towards the end of its path. In reality, the energy loss is a stochastic process and the energy loss and range is different for each individual ion, an effect known as *energy loss straggling*. This leads to a broadening of the peak.

For particles traversing a thin layer, these fluctuations are described by the Vavilov distribution (Vavilov (1957)). For practical reasons, the energy loss can be approximated as a Gaussian distribution (Bohr (1940); Ahlen (1980)). The ratio of the *straggling width* σ_R and *mean range* R can be expressed as

$$\frac{\sigma_R}{R} = \frac{1}{\sqrt{M}} \, f\left(E/Mc^2\right), \tag{8}$$

where E is the energy and M is the mass of the ion. f is a slowly varying function of particle energy and mass. For light ions stopping in water, σ_R/R is approximately $1:1000$. Due to the difference in mass, range straggling of protons is approximately 3.5 times larger than of carbon ions of similar range.

In practice, range straggling is also introduced by inhomogeneities in the target tissue. For practical reasons, a broadened peak is desired in spot- and raster-scanning techniques and may be enhanced using a ripple filter. This reduces the number of planes to be irradiated and increases the speed of irradiation.

LATERAL BEAM SPREAD In general, ion beams show a small lateral deflection in comparison with electron or positron beams. While the stopping of an ion beam is mainly due to electronic interactions, the lateral spread of an ion beam is the result of elastic Coulomb interactions with the target nuclei. Physically, this effect is well described by Molière scatter theory (Molière (1948)) and has been confirmed by high energy proton beam experiments (Gottschalk et al. (1993)).

One result of the theory, relevant for particle therapy, is that lighter particles are deflected more at similar ranges. A proton beam at a mean range of $R = 15.6$ cm shows an angular beam spread more than three times larger than a carbon ion beam of the same range (Schardt and Elsässer (2010)).

NUCLEAR FRAGMENTATION While nuclear interactions have almost no effect on the energy loss of an ion beam, they have other effects which are significant at larger penetration depths. At high beam energies, collisions between projectile and target nuclei lead to the beam particles losing one or more nucleons. This is described in the abrasion-ablation model (Serber (1947)). In this model, parts of the nuclei are sheared off, creating lighter (low-Z) fragments of the projectile and target nucleus.

In carbon ion therapy, this means a loss of primary beam particles and build-up of lighter fragments. At higher beam energies, lighter fragments can comprise a significant fraction of the particles in the peak region. Usually, the lighter fragments have a longer range, creating a dose tail behind the Bragg peak.

One advantage of this effect is the creation of PET-active ^{10}C, ^{11}C, and ^{15}O fragments. This is useful in PET imaging for in-vivo range verification (Parodi (2004); Parodi et al. (2007, 2008); Bauer et al. (2013b)).

BRAGG PEAK A prominent reason to use charged particles for radiotherapy is its *inverted dose profile* with the *Bragg peak*, named after Sir William Henry Bragg, who discovered the effect when he investigated the stopping of alpha particles in air (Bragg and Kleeman (1905)). Robert Wilson proposed the use of protons and

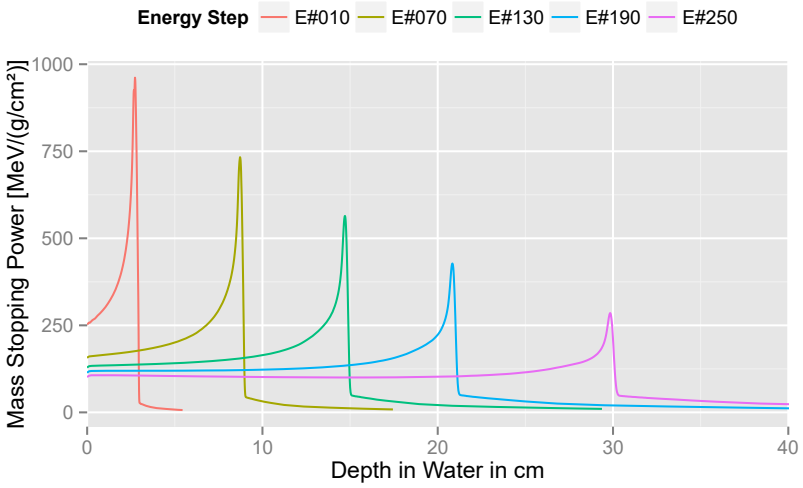

Figure 1: Mass Stopping Power S/ρ of a carbon ion beam used at HIT as a function of depth in water. Five beam energies have been selected: 109 MeV/u, 204 MeV/u, 276 MeV/u, 340 MeV/u and 423 MeV/u. With increasing beam energy, the range increases. At the same time, range straggling increases, increasing peak width and the plateau-to-peak ratio. Beam data taken from TRiP depth-dose tables.

heavy ions for precision radiotherapy (Wilson (1946)) due to the distinct narrow peak of the dose distribution. This specific form of the Bragg peak is explained by the $1/\beta^2$ dependence in the Bethe formula: With decreasing particle velocity, the energy loss increases.

In Fig. 1, examples of the dose profile are shown for carbon ions used for therapy at the HIT Heidelberg Ion-Beam Therapy Center. As can be seen from the figure, the range of the beam can be precisely adjusted by changing the kinetic energy of the ion beam. Also, the effects of range straggling and fragmentation, which increase with the mean range R, can be observed.

2.1.2 *Radiobiology*

In addition to the advantageous depth-dose profile, beams of heavy ions offer radiobiological benefits (Suit et al. (2010)). The increased stopping power of heavy ions compared to photon beams results in a larger energy deposition and more severe cell damage. This effect is larger in the peak region than in the entrance channel, leading to an increased biological effect inside the target volume (Kraft (2000)).

RELATIVE BIOLOGICAL EFFECTIVENESS To account for the biological effects, the *relative biological effectiveness* (RBE) has been introduced. It is defined as the ratio of the dose of X-ray irradiation D_γ^{Ref} divided by the dose of ion irradiation D_{Ion} resulting in the same biological effect (Schardt and Elsässer (2010)):

$$RBE = \left.\frac{D_\gamma^{Ref}}{D_{Ion}}\right|_{Isoeffect} \tag{9}$$

The value of the RBE depends on several factors, including the desired effect level (usually 1% or 10% cell survival), tissue properties and beam quality. For proton beams, the RBE is usually assumed to be a fixed value (RBE = 1.1), except

for the distal 1-2 mm of the Bragg peak, where an increased *linear energy transfer* (LET) may cause an increased RBE (Paganetti et al. (2002)). For beams of heavy ions, the RBE depends on the dose level (Weyrather et al. (1999); Furusawa et al. (2000)), linear energy transfer (Belli et al. (1998); Furusawa et al. (2000)), particle type and tissue type (Weyrather et al. (1999); Suzuki et al. (2000)).

For patient treatment, the RBE is calculated from biophysical models integrated into the treatment planning software. In this study, the *local effect model* (LEM), developed at GSI and integrated into the treatment planning software TRiP, was used for all dose calculations (Scholz and Kraft (1996); Krämer and Scholz (2000)).

PHOTON-EQUIVALENT DOSE In order to facilitate the transfer of knowledge from conventional radiotherapy, the absorbed (physical) dose D is weighted with the RBE factor:

$$D_{\text{Biol.}}(\vec{x}) = \text{RBE}(\vec{x}) \cdot D_{\text{Phys.}}(\vec{x}) \tag{10}$$

To distinguish this *photon-equivalent dose* from the absorbed dose, the weighted dose is usually indicated as *Gray-equivalent dose*, abbreviated Gy (RBE).

Based on the photon-equivalent dose, results can be compared to data from conventional radiotherapy, like *tumor control probability* (TCP) and *normal tissue complication probability* (NTCP).

CELL SURVIVAL Survival probabilities of cells subject to irradiation are an important property in the characterization of tissues and irradiation qualities. Usually, cell survival is measured following the procedure proposed by Puck (Puck and Marcus (1956)): One to two weeks after an irradiation with dose D, the proliferation of cells is analyzed. Colonies with at least 50 cells are considered as *surviving* and are counted. The fraction of surviving cells S is then usually parametrized by the linear-quadratic (LQ) model (Hall (2000)):

$$S(D) = \exp\left(-\alpha D - \beta D^2\right) \tag{11}$$

The parameters α and β are experimentally determined. The property α/β is an important quantity in conventional radiotherapy and is also used as a basis in the local effect model.

2.2 ION BEAM THERAPY AT HIT

The *Heidelberg Ion-Beam Therapy Center* (HIT) is a dedicated facility for proton and heavy ion beam therapy. Patients at HIT were initially mainly treated for chordoma, chondrosarcoma and adenoidcystic carcinoma using active raster scanning of carbon ion and proton beams. This section describes the history and technical properties of HIT and its accelerator facility.

2.2.1 *The Heidelberg Ion-Beam Therapy Center*

Based on the experience gained from the experimental cancer treatment program at GSI, the creation of a dedicated ion beam therapy facility was proposed as early as 1998 (Debus et al. (1998); Eickhoff et al. (2000)). Initial proposals included the installation of two heavy ion gantries, which was later changed to two treatment rooms with fixed beam lines and one heavy ion gantry.

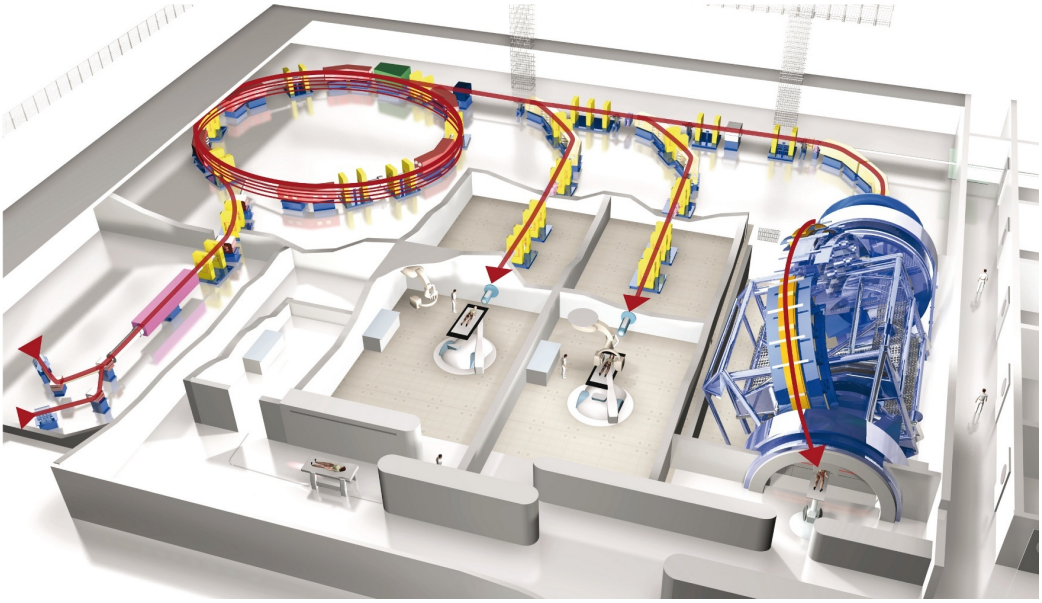

Figure 2: Illustrated Overview of the HIT Facility: Starting on the lower left, low-energy ion beams are created in ECR ion sources, accelerated by a linear accelerator and injected into the synchrotron (upper left). After acceleration and extraction, the beam is transferred to one of two horizontal fixed beam patient treatment rooms (center) or to the heavy ion gantry treatment room (right).
Image: Courtesy of Universitätsklinikum Heidelberg.

Apart from this major change, most properties have been implemented as in the early proposals (Haberer et al. (2004); Heeg et al. (2004); Eickhoff et al. (2004)): Patients are treated using an intensity controlled raster scan method, and both low LET ion species (protons, helium ions) and high LET ions (carbon and oxygen) are available. Three patient treatment rooms are available, two with a horizontal fixed beam line and one heavy ion gantry. Fig. 2 presents an overview of the HIT facility, showing the two horizontal fixed beam treatment rooms in the center and the heavy ion gantry on the right.

Construction of HIT started in November 2003; in June 2006, construction of the HIT building and accelerator were completed. Beam commissioning was finished in April 2008 (Ondreka and Weinrich (2008)) and the first patient was treated in November 2009. In October 2012, the first patient was treated using the heavy ion gantry (Galonska et al. (2013)). By the end of 2016, more than 3,900 patients had been treated at HIT (PTCOG and Jermann (2017)); by July 2019, a total of 5,725 patients[1].

The HIT accelerator offers a large variation of beam parameters. Both proton and carbon ion beams have a maximum penetration depth of up to 30 cms and variable beam diameters and intensities. Part of the specifications was a beam range between 20 and 300 mm in water and a dose rate of 2 Gy/min. The energy can be varied in 255 discrete steps, each step amounting to a range difference of approximately one millimeter. Table 1 gives an overview over the available parameter space.

For the irradiation, a *slow knock-out* (KO) extraction with an extraction time of five seconds is used. The extraction can be interrupted up to five times and stored for up to 30 seconds for complex irradiation fields or for gated irradia-

1 Prof. Dr. Oliver Jäkel, private communication

Parameter	Steps	Proton Beam	Carbon Ion Beam
Energy	255	$48 - 221$ MeV/u	$88 - 430$ MeV/u
Penetration Depth	255	$20 - 300$ mm	$20 - 300$ mm
Beam Size (FWHM)	4	$8 - 20$ mm	$4 - 12$ mm
Intensity	10	$8 \cdot 10^7 - 2 \cdot 10^9$ 1/s	$2 \cdot 10^6 - 8 \cdot 10^7$ 1/s
Ions per Spill	10	$4 \cdot 10^8 - 1 \cdot 10^{10}$	$1 \cdot 10^7 - 4 \cdot 10^8$

Table 1: HIT Beam Parameters (taken from Ondreka and Weinrich (2008))

tions. Further, the system has been designed to allow for fast switching of beam properties and treatment rooms.

2.2.2 *Composition of the HICAT Accelerator Facility*

At the heart of HIT, the *Heavy Ion Cancer Therapy* (HICAT) accelerator facility generates the ion beams necessary for patient treatment. It has been specifically designed for clinical use, offering proton and carbon ion beams for clinical operation. Because the properties and working principles of the accelerator are crucial in understanding the work done in Chapter 4, they are presented more detailed in the next section.

2.2.2.1 *Overview*

The HICAT accelerator was designed as a therapy accelerator for proton and carbon ion beams. To be usable in a clinical setting, a compact design, highly reliable beam operation, and a low number of critical components were part of the design criteria (Dolinskii et al. (2000)). Further, the accelerator should be capable of quickly switching ion species and treatment rooms, making a combined treatment with protons and carbon ions possible.

Each step of the acceleration is shown in Fig. 2. An ion beam is generated in one of three *ECR ion sources*. This low-energy beam is transferred to the *linear accelerator*, where it is accelerated to 7 MeV/u for injection into the *synchrotron*. In the synchrotron, the beam is accelerated to the desired energy. Using *slow knock-out extraction*, the beam is removed from the synchrotron over the period of five seconds. The extracted beam is transfered to one of the *treatment rooms*, including the *heavy ion gantry*. In the treatment room, the *beam delivery system* uses active beam scanning to irradiate the correct position inside the patient.

2.2.2.2 *ECR Ion Sources*

At HIT, all ion beams are generated in one of three *electron cyclotron resonance ECR ion sources*. Proton beams are generated from hydrogen gas; carbon and oxygen ions from carbon dioxide gas and helium ions from helium gas (Winkelmann et al. (2014)). ECR ion sources offer stable ion beams, reliable long term operation and are easily maintained (Tinschert et al. (2008)).

Inside an ECR ion source, a plasma of the source gas is confined in a magnetic bottle. This plasma is further ionized using microwaves in a process called *electron cyclotron resonance heating* (Xie (1998)). Electrons are heated in a thin layer in

which the microwave frequency ω_f matches the electron cyclotron frequency ω_c

$$\omega_f = \omega_c = \frac{e\,B}{m_e}, \tag{12}$$

where e and m_e are the charge and mass of the electron and B is the local magnetic field. The heated electrons collide with gas molecules, ionizing them in the process and creating more plasma.

Using an electric field created by a set of extraction electrodes, a constant stream of generated ions is extracted out of the source. At HIT, the extracted ions have a kinetic energy of 8 keV/u.

The ion beam enters the *low energy beam transport (LEBT)* via an analyzing 90° dipole magnet. In the case of the combined carbon-oxygen source, the correct ion species is selected here. Also, contamination of ions with different charge-to-mass ratio are removed.

In the LEBT, the desired intensity of the ion beam is selected using an aperture and a focusing magnet. To decrease the intensity, the beam is defocused and more particles are stopped by the aperture. If more intensity is required, the beam is focused and more particles enter the linear accelerator.

2.2.2.3 *Linear Accelerator*

Between the sources and the synchrotron, an injector linac accelerates the particles from 8 keV/u to 7 MeV/u. At this energy, ion beams can be injected into the synchrotron more efficiently, increasing beam intensity and stability (Schlitt et al. (2004); Maier et al. (2007)).

The linear accelerator operates at 216 MHz and consists of two stages, a *radio frequency quadrupole* (RFQ) and an *IH-type drift tube linac* (DTL). The RFQ accelerates the ion beam to 400 keV/u. It also focuses the beam into bunches of 200 µs length, necessary for operation of the DTL. In the DTL, the ion beam is accelerated to 7 MeV/u and enters the *medium energy beam transport* (MEBT).

In the MEBT, the remaining electrons are removed from the ions using a stripper foil, a thin layer of graphite. Here, the proton charge state changes from H_3^{1+} to $3H^{1+}$, the carbon ions from C^{4+} to C^{6+}. Again, an analyzing dipole magnet removes contaminating ions with differing charge-to-mass ratios. Finally, a chopper system cuts the ion beam to 30 µs pulses, containing enough particles for five seconds of extraction.

2.2.2.4 *Synchrotron*

The synchrotron is responsible for the main part of the acceleration. An injected 7 MeV/u beam is accelerated to energies of up to 430 MeV/u, which is then extracted and transferred to the treatment rooms. This energy is equivalent to a range of 30 cm in water (Dolinskii et al. (2000)).

It has a circumference of 65 m and consists of six dipole bending magnets with a bending angle of 60° each. At the highest beam energy, the dipole magnets operate at a flux density of 1.53 T, with ramping rates of 1.5 T/s, allowing for acceleration within one second.

In order to increase the ion beam intensity, a *multi-turn injection* is used, which uses 15 turns of the synchrotron to distribute the 30 µs pulse from the linear accelerator in the horizontal phase plane. This increases the beam intensity by a factor of 15 compared to the MEBT.

The ions are accelerated using two *radio frequency* (RF) acceleration cavities. In these cavities, a standing electromagnetic wave bunches and accelerates the ion beam with each pass. To keep up with the increasing magnetic rigidity $B \cdot \rho$ of the beam, the magnetic flux density of the dipole magnets is increased synchronously to keep the beam in orbit. Depending on the requested energy, acceleration takes 0.5 to 0.9 seconds.

2.2.2.5 *Beam Extraction*

When the beam reaches the requested particle energy, it can be stored for up to 30 seconds, or extracted. Due to the limited speed of the beam delivery system, a slow beam extraction is required. At HIT, a transverse RF knock-out extraction has been implemented (Tomizawa et al. (1993); Dolinskii et al. (2000)).

For the extraction, the ion beam is excited using a transverse electromagnetic field. As a consequence, excited fractions of the beam leave the stable orbits of the phase space and can be extracted from the synchrotron. By controlling the amplitude and frequency of the excitation field, the beam extraction can be halted and resumed later.

At HIT, the extraction lasts for up to five seconds, after which the synchrotron is reset and prepared for the next injection of ions. Extraction can be interrupted for up to five times, which is favourable when irradiating complex treatment plans or for gated irradiations.

Ideally, the extracted beam intensity is characterized by a fast increase up to the nominal intensity, which is maintained until the end of the extraction. Initially, this was not the case, leading to interlocks in the beam delivery system and a decision to reduce the beam intensity (Peters et al. (2008)). Improvements were made when the intensity feedback system was installed in 2013, which increased stability and intensity (Schömers et al. (2011); Schömers (2013)). Ongoing improvements are made to provide patient-specific intensity modulation (Schömers et al. (2013)).

2.2.2.6 *High Energy Beam Transport*

From the synchrotron, the extracted ion beam is transported to its destination via the *high energy beam transport* (HEBT). In addition to the three treatment rooms, a quality assurance room is available for beam diagnostics and research purposes. If the beam is not required in any room, it can be safely disposed of using a beam dump in the HEBT.

All treatment rooms are using the same synchrotron and treatment can only be performed in one room at a time. If one treatment room is currently using the beam, the other rooms have to wait until the treatment is finished.

2.2.2.7 *Treatment Rooms*

Patient treatments are performed in each of three available treatment rooms. Two treatment rooms are equipped with a fixed horizontal beam line, one is equipped with the isocentric heavy ion gantry. All beam lines, including the quality assurance room, are equipped for intensity controlled rasterscanning (Haberer et al. (1993)).

The beam position is controlled by horizontal and vertical dipole scanner magnets. In the fixed beam line, the scanner magnets are located in a backroom, five

meters from the isocenter; on the heavy ion gantry, the scanner magnets are positioned on the gantry in front of the final 90° dipole magnet.

During treatment, the ion beam is monitored at all times by the *beam application and monitoring system* (BAMS). It is positioned directly in front of the patient and uses ionization chambers (IC) to measure the beam intensity and *multi-wire proportional counters* (MWPC) to measure beam position and width. Since 2013, the measured intensity is used to control the extraction system using the intensity feedback system.

During therapy, the patient is positioned on a treatment couch which is supported by a six-axis robotic arm. It can be used to correct minor setup inaccuracies prior to treatment. For *image guided radiotherapy* (IGRT), a kilo-voltage imaging system is available. Additionally, a patient transport system is available to transport the patient between the treatment room and an offline PET-CT system while still immobilized.

2.2.2.8 *Treatment Control System - Beam Delivery*

Patients at HIT are treated using an intensity controlled raster scan method (Haberer et al. (1993)), which is characterized by a continuous scanning motion of the ion beam over the target volume. Active scanning techniques offer high flexibility and a reduced neutron yield compared to passive beam shaping. During patient treatment, the *treatment control system* (TCS) supervises and controls all aspects of the irradiation. It processes the treatment plan and generates the list of required beam energies, raster point locations and particle numbers. It controls the scanning system to irradiate each raster point and keeps track of the already irradiated raster points.

To perform the irradiation, the TCS requests the necessary combination of ion species, beam energy, focus size, and beam intensity from the accelerator via the *accelerator control system* (ACS). The accelerator provides this ion beam automatically and transports it to the treatment room via the HEBT.

During irradiation, the TCS constantly monitors the beam intensity, position and width based on the BAMS measurements. The beam position is controlled by the scanner magnets; any deviation from the desired beam position is corrected using a position feedback system. The dose for each raster point is controlled based on the beam intensity measured in the BAMS. When the charge measured in the ionization chambers reaches a pre-calculated amount, the raster point has received the planned number of particles and the next raster point is selected. Without interruption, the particle beam is moved there, resulting in a sweeping beam motion, slowing down for raster points with higher particle numbers. Fig. 3 shows an illustration of this method.

If a beam parameter is incorrect, due to an intensity spike or a change in beam width, the TCS issues an interlock and interrupts the treatment. The beam abort is handled directly by the TCS, which safely stops the beam from reaching the treatment room within 200 µs.

2.2.2.9 *Heavy Ion Gantry*

The heavy ion gantry offers the same intensity controlled raster scanning technique as the fixed beam line. Additionally, the beam line can be rotated freely around the patient, offering new treatment planning options (Fuchs et al. (2004)).

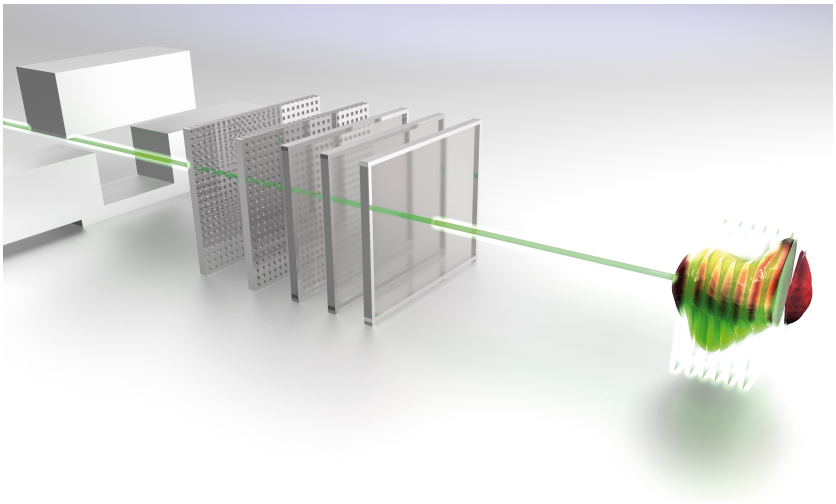

Figure 3: Intensity Controlled Raster Scan: A mono-energetic ion beam (green) is deflected by horizontal and vertical scanning magnets (left), while its position, width, and intensity is monitored by ionization chambers (center). The beam stops after a certain path length inside the target volume, releasing most of its energy in one iso-energy slice (right).
To irradiate a volume, the beam is scanned continuously over each raster point of an iso-energy slice of the target volume, after which the beam energy is changed. Then, the next slice is scanned, until all slices of the target volume are irradiated.
Image: Courtesy of Universitätsklinikum Heidelberg.

Commisioning of the gantry was finished in June 2007 (Fuchs et al. (2008)), the first patients were irradiated in October 2012 (Galonska et al. (2013)). It has a mass of 670 tons, of which 600 tons can be rotated, a diameter of thirteen meters and a length of 25 meters. It can be used for proton and carbon beams over the full energy range and offers a scanning field of 20x20 cm^2. The heavy ion gantry was designed by GSI and built by MT Mechatronics.

The treatment room is equipped with the same six-axis treatment couch as the fixed beam lines and offers kilo-voltage IGRT.

2.2.2.10 *Accelerator Control System*

The HICAT *accelerator control system* (ACS) is a software and hardware system which controls all aspects of accelerator operation (Bär et al. (2001); Mosthaf et al. (2008); Bär et al. (2012)). It is designed as a real-time accelerator control system. In order to fulfill the strict timing requirements, a real-time ethernet system (*real time bus*, RTB) has been implemented to synchronize *device control units* (DCUs). Each DCU controls an accelerator device like the linear accelerator, synchrotron magnets or accelerator RF cavities with microsecond precision.

During operation, the ACS synchronizes all accelerator components, which is crucial in several phases of the accelerator cycle (during injection, acceleration and extraction). The exact sequence is pre-programmed into the flash memory of the DCUs for each available combination of ion type, energy, focus size and intensity. This process and the accelerator cycle is described in more detail in chapter 4. During patient treatment, the ACS processes requests from the *treatment control system* (TCS).

2.3 TREATMENT PLANNING

For each patient, the treatment is prepared beforehand. Usually, specialized immobilization equipment is adapted to the patient to ensure high reproducibility of the patient position during treatment. Planning CTs and further diagnostic images are acquired of the patient in this position and used to create individual treatment plans. The treatment plans provide the therapy machine with the necessary instructions to create the desired dose distribution.

Treatment planning for tumors in the thorax and abdomen needs to account for organ motion. In this section, the influence of organ motion and the possible mitigation techniques are presented. Further, the treatment planning systems necessary for dose optimization and calculation are discussed.

2.3.1 *Treatment of Moving Tumors*

During treatment, patients are immobilized using masks, stereotactic frames or vacuum cushions. In the head and neck region as well as the extremities, this is sufficient to reliably position the patient and to irradiate the target volume correctly. However, in the thorax and abdomen, this is not sufficient to eliminate the organ motion due to breathing, heart pulsation and intestinal motion due to the filling of gut and bladder. Here, further mitigation strategies are necessary to achieve a reliable treatment.

2.3.1.1 *Characteristics and Impact of Organ Motion*

Patient motion can be subdivided into two categories, *inter-fractional* and *intra-fractional motion*. Inter-fractional motion is characterized as an irregular change of the patient anatomy due to intestinal motion or change in tumor size. This change is seen in between therapy fractions and can be countered by robust planning or adaptive planning strategies. Intra-fractional motion is characterized by a regular change in patient anatomy on a smaller time scale, due to breathing or heart beat. It can be anticipated, for example by using 4D imaging (Rietzel et al. (2005); Bert and Rietzel (2007); Schardt and Elsässer (2010)).

Of these sources of motion, respiratory motion and heart palpitation are the main contributors (Henkelman and Mah (1982); Langen and Jones (2001); Liang et al. (2018)). In this thesis, the main focus is on mitigation of respiratory motion effects.

Respiratory organ motion is mainly translational motion. When the target volume is close to a fixed structure, like the chest wall, the organ can also be subject to rotational motion. The consequence of this motion is usually a change in *radiological path length* or *water-equivalent path length* (WEPL), changing the range of the particle beam. This effect is more important for ion beams due to the re-positioning of the Bragg peak than for photon beam therapy.

In addition, scanning beam systems are susceptible to the *interplay effect*. Due to the superposition of the scanning motion and target motion, some parts of the target volume are irradiated more than intended, while others are irradiated less or not at all. This interference effect leads to severe under- and overdosage (cold/hot spots) and reduces the efficacy of the treatment (Phillips et al. (1992); Grözinger et al. (2006, 2008); Bert et al. (2008)).

2.3.1.2 *Motion Mitigation Techniques*

IMRT and particle therapy with scanned ion beams share similar characteristics and face similar challenges due to organ motion. Therefore, mitigation strategies used in particle therapy have been inspired by the experience made in photon therapy (Langen and Jones (2001); Keall et al. (2006); Rietzel and Bert (2010); Bert and Durante (2011); Korreman (2012)).

MOTION REDUCTION One passive approach is the reduction of the motion amplitude. For example, the breathing motion can be reduced via breath-hold commands or jet ventilation during the irradiation. For irradiation of the upper abdomen, belly compression plates can be used to reduce the organ motion. Finally, relaxation drugs can be administered to the patient to reduce motion amplitude.

MARGIN CONCEPTS The ICRU reports 50 and 62 describe a *margin concept*, in which the target volume is expanded to encompass setup errors and changes in target position (Landberg et al. (1993, 1999)). For the management of moving organs, the addition of an *internal margin* (IM) to the *clinical target volume* (CTV) is proposed to compensate for movement and size variation of the CTV. The sum of the CTV and the internal margin is the *internal target volume* (ITV). This ITV encompasses the CTV during the whole motion.

Using the internal margin is feasible in static field irradiations, although the dose to normal tissue and organs at risk is usually increased by this strategy. In ion beam therapy, the use of margins alone is not sufficient for the mitigation of interplay effects. It can however be used in combination with gating or rescanning techniques.

RESCANNING/REPAINTING In *rescanning,* a treatment plan is divided into multiple scans and irradiated repeatedly for a statistical dose-averaging effect. Assuming no correlation between the irradiation and the organ motion, the variance of the dose can be decreased a factor of $1/\sqrt{N}$ by irradiating N repetitions.

For this technique, the particle fluence has to be reduced for a precise dose application which leads to longer irradiation times. Further, with increasing motion amplitude, the steepness of the dose gradient is reduced.

BEAM GATING For *beam gating*, the respiration is monitored during treatment and the irradiation is only activated when the respiratory cycle is in between predefined limits. This way, the residual motion during the irradiation is reduced.

Some of the residual interplay effects can be mitigated by an increased overlap of beams, for example by increasing the beam focus size and decreasing the raster spacing (Bert et al. (2009)).

Due to the pauses introduced by the gating technique, treatment times are increased compared to irradiations with continuous beams.

BEAM TRACKING *Beam tracking* or *online motion compensation* performs a 3D compensation of the target motion in real time. The motion of the target volume is monitored during the irradiation and the position of the treatment beam is adjusted to match the current position. Ideally, this results in the same dose distribution in the target volume as in the static case, independent of motion amplitude, and treatment times are relatively unaffected.

Beam scanning techniques are a good starting point for beam tracking, as the treatment beam is already actively scanned by the scanner magnets and can be used to follow a moving target volume. Still, the approach is technically challenging, especially the energy change needed for range adaptation (Amaldi et al. (2004); Amaldi and Kraft (2007)).

In practice, combinations of different motion mitigation techniques are employed for the treatment of patients with moving target volumes. Further, ongoing improvements in image guided radiotherapy will likely improve the treatment quality (Mori et al. (2013)).

2.3.2 *Treatment Planning Systems*

Treatment plans are a set of instructions for a specific treatment machine, used to create a desired dose distribution. For example, a raster scanning treatment plan contains the gantry angle, ion species and energies, raster point positions and particle numbers for each irradiation field.

A treatment plan is created using a treatment planning system (TPS), which uses a volumetric image (usually a treatment planning CT image) and a physical beam model to calculate the resulting dose distribution. Most TPS may display additional images such as Magnetic Resonance Images (MRI), Positron Emission Tomography (PET) or time-resolved 4D-CT images for the delineation of target volumes and organs at risk.

For advanced treatment methods using fluence modulation (IMRT and IMPT), the treatment plan is created using inverse planning. An optimization algorithm uses a cost function which takes into account the dose to the target volume, the organs at risk and the normal tissue to determine the treatment plan quality. The particle fluence pattern is then adjusted to create the desired dose distribution. All treatment plans used in this thesis have been created using this technique.

Three different TPS have been used in this thesis: TRiP and TRiP-4D, developed at GSI Helmholtz Centre for Heavy Ion Research, and *syngo® RT Planning*, developed by *SIEMENS AG*. TRiP was originally created for the treatment of patients during the pilot project at GSI, it is now used for research purposes. TRiP-4D is a development version of TRiP and capable of 4D dose optimization and calculation. *syngo® RT Planning* is the commercial TPS used for patient treatment at HIT.

2.3.2.1 *GSI TRiP*

Treatment Planning for Particles, 1998 edition (TRiP), is a TPS for ion beams developed at GSI (Krämer et al. (2000)). It was used for treatment planning during the GSI pilot project (Jäkel et al. (2001b)), in which more than 400 patients were treated.

TRiP has been designed for the pencil beam active scanning system in use at GSI and HIT (Haberer et al. (1993)). It offers a double gaussian pencil beam model and a dose optimization algorithm, including biological dose calculation via the local effect model (LEM, Scholz and Kraft (1996); Krämer and Scholz (2000)). The conversion from the electron density represented in the Hounsfield units (HU) of the treatment planning CT to water-equivalent path length (WEPL)

necessary for dose calculation is performed using a Hounsfield Look-Up Table (HLUT, Jäkel et al. (2001a)).

Beam data and most other physical and biological properties are provided by external text files, which gives TRiP the flexibility to work with different particle types, accelerators and treatment rooms, such as the SIS at GSI, HICAT at HIT, the horizontal treatment rooms and the heavy ion Gantry at HIT. As a command line tool, dose calculations can be scripted and processed in a computation cluster.

In this thesis, TRiP was used to carry out the esophagus treatment planning study as well as calculating static dose distributions for the experiments.

2.3.2.2 *GSI TRiP-4D*

TRiP-4D is a 4D treatment planning system based on TRiP and has been developed further to offer 4D dose calculation and optimization. 4D dose calculation is necessary to quantify effects of motion and interplay.

4D treatment planning capabilities have initially been incorporated by Bert and Rietzel (Bert and Rietzel (2007)), including support for gating, rescanning, tracking and calculation of *internal target volumes* (ITV). Later developments by Gemmel (Gemmel et al. (2011)) allow the calculation of biological dose. TRiP-4D was further integrated for clinical use by Richter, who implemented interfaces for data input and contour models (Richter (2012); Richter et al. (2013b)).

4D treatment planning systems use time-resolved computed tomography (4D-CT) for dose calculation (Rietzel et al. (2005)). 4D-CT uses helical imaging spanning the whole motion cycle and allows the reconstruction of multiple motion phases, equivalent to a time series of conventional CTs. Deformable (non-rigid) image registration is used to calculate deformation vectors from one motion phase to another, usually using one phase as a reference. These vector fields are used for contour propagation and 4D dose calculation. Contours of target volumes and organs at risk are usually not available on each motion phase and manual delineation is time-consuming and impractical. Using vector fields, contours existing on one CT can be automatically transferred to another. Based on the 4D-CT and propagated contours, an internal target volume can be calculated. In the case of particle therapy, variations of the radiological path length need to be taken into account.

TRiP-4D calculates the time-resolved dose distribution by distributing the particle fluence of the treatment plan to several motion phases, based on the patient motion and irradiation time. For each motion phase, an independent dose calculation is performed. The final dose distribution is then calculated by deforming the dose grid using the deformation vector information and calculating the dose sum in one reference motion phase (Gemmel et al. (2011)).

Similar to TRiP, TRiP-4D is modular and uses a variety of data sources as input. Motion phases of 4D-CTs are converted from DICOM CTs. Deformation vector fields are calculated using *Plastimatch* (Sharp and Plastimatch Development Team (2011)) and converted to TRiP-4D format. Motion surrogate data can be imported from a wide range of sources. In this thesis, patient motion was recorded using the *ANZAI AZ-733V* system, which records the breathing motion of a patient using a piezo-electric load cell. Irradiation timing information can be imported from the therapy control system (TCS), which records each patient treatment, or simulated using an accelerator model.

In this thesis, TRiP-4D was used for the dose calculations performed for the stereotactic body radiotherapy of the hepatocellular carcinoma patients and to test the accelerator simulation.

2.3.2.3 *SIEMENS* syngo® RT Planning

syngo® RT Planning is the commercial treatment planning system used for treatment planning at HIT. It has been developed by *SIEMENS AG*. In contrast to TRiP and TRiP-4D, *syngo® RT Planning* is licensed as a medical product and can therefore be used as a TPS for the treatment of patients. It is part of the Record and Verify treatment system *syngo® PT Treatment*, which is responsible for DICOM communication with the picture archive (PACS) and the treatment control system, as well as integration of contouring and treatment verification. Similar to TRiP, it is capable of dose optimization and calculation for proton and carbon ion beams. However, in contrast to TRiP-4D, it is not a 4D TPS and incapable of 4D dose calculation.

In this thesis, *syngo® RT Planning* was used for the treatment planning of the hepatocellular carcinoma patients. In addition, the static dose calculations were used as a reference for the experimental verification.

3

INTRODUCTION OF A NEW WORK FLOW FOR LIVER IRRADIATIONS

In the time between May 2011 to July 2013, the first thirteen patients suffering from hepatocellular carcinoma were treated using stereotactic body radiotherapy (SBRT) at the Heidelberg Ion-Beam Therapy Center (HIT). These irradiations included the first patient treated using beam gating at HIT. To facilitate dose calculation accounting for intra-fractional organ motion, the 4D treatment planning system TRiP-4D was introduced. The necessary data acquisition and processing is presented in this section.

3.1 INTRODUCTION

Worldwide, tumors of the liver are the third most common cause of cancer-related death and the fifth most common type of tumor (Parkin et al. (2001)). In some parts of Asia, Hepatocellular Carcinoma (HCC) is the most common cause of cancer-related death. It is less common in Europe and the USA, albeit with an increase in incidence and mortality (Deuffic et al. (1998); El-Serag and Mason (1999); Robert Koch-Institut (Hrsg.) und die Gesellschaft der epidemiologischen Krebsregister in Deutschland e.V. (Hrsg.) (2017)), which is attributed to an increase in Hepatitis C infections, liver cirrhosis and alcohol consumption.

When diagnosed in an early stage, HCC may be treated curatively using surgical resection, liver transplantation, or local therapies (radio-frequency ablation, chemo-embolisation) (Llovet et al. (2003)). Unfortunately, only 30 to 40% of patients in the developed countries are diagnosed in the initial stages. In advanced stages, therapy options are limited to palliative treatment with poor prognosis, although liver transplantation may be a viable treatment even for unresectable hepatocellular carcinoma patients exceeding the Milan criteria (Mazzaferro et al. (1996, 2009)). Naturally, increasing patient numbers and limited availability of donor organs increase the waiting times.

External beam radiotherapy of HCC is limited by the low dose tolerance of the surrounding normal liver tissue. Doses of 30 to 35 Gy, delivered to the whole liver, are causing radiation induced liver disease (RILD) (Lawrence et al. (1992)), which can be avoided by reducing the high-dose volume in highly conformal radiotherapy (Robertson et al. (1993, 1997)). Tumor control can be further increased by the application of higher doses (Park et al. (2002)). Stereotactic body radiotherapy (SBRT) with photons has been successfully used for the treatment of HCC and liver metastases with high local control and low toxicities (Blomgren et al. (1995); Herfarth et al. (2000); Wulf et al. (2000); Timmerman et al. (2003); Combs et al. (2010); Petrelli et al. (2018)).

Offering high dose conformity and radiobiological benefits, therapy of HCC with carbon ion beams is a promising approach to increase local control and reduce toxicities. To evaluate the efficacy of carbon ion radiotherapy, a Phase-I study for the treatment of patients suffering from HCC was proposed for implementation at HIT (Combs et al. (2011)). This chapter will present the technical details of the treatment of these patients.

Focus of this Study

Most patients at HIT are treated for intracranial lesions and tumors of the head-and-neck region. For those patients, inter- and intra-fractional motion can usually be neglected or is already compensated by the usual *image guided radiotherapy* (IGRT). Depending on the tumor position, inter- and intra-fractional motion in the liver is 1 to 2 cm (Langen and Jones (2001); Liang et al. (2018)), which negatively impacts the dose distribution and treatment quality (Phillips et al. (1992); Bert and Durante (2011)). This study presents the additions to the work flow currently in use for patient treatment at HIT, introducing organ motion mitigation techniques as well as the steps necessary for calculating reconstructed dose distributions.

This includes further development and introduction of a 4D treatment planning system (4D TPS), initiated at the GSI Helmholtz Centre for Heavy Ion Research. This 4D TPS software, called TRiP-4D, is capable of dose calculation based on motion phases of 4D-CTs and calculation of dose distributions subject to organ motion (4D dose distributions). Additionally, it is able to calculate automatically propagated organ contours and internal target volume (ITV) margins based on non-rigid registration information.

In this study, the TRiP-4D software is utilized for the first time in a realistic clinical work flow with the goal of showing the feasibility of using the 4D TPS in this context. Based on this, more information should become available to the clinical staff for treatment planning and therapy decisions. In preparation for this work flow implementation, the compatibility of TRiP-4D with the different data sources at HIT was integrated by Daniel Richter (Richter et al. (2013b)). Reviewing this integration with all data sources and discovering useful alternative data sources is also researched in this study.

Finally, this study covers the necessary data acquisition to calculate the impact of organ motion on the dose distribution. Prior to the treatment, simulated dose distributions are of interest for the treatment planning and to ensure safe treatment of the patient. After treatment, reconstruction of the actual in-vivo dose distribution is of interest to assess the treatment outcome. To calculate this, 4D images, breathing motion curves and irradiation records must be acquired. From this information, deformation maps can be derived to calculate 4D dose distributions using TRiP-4D (von Siebenthal et al. (2007a,b); Richter et al. (2013a,b)). This complements the TPS in use at HIT, *syngo® RT Planning*, which is currently not capable of 4D dose calculation.

For the first time at HIT, beam gating is used during patient treatment. This includes more detailed data acquisition ahead of the treatment for the recording of breathing information as well as additional imaging and the acquisition of 4D-CTs to measure the extend of the target volume motion and to define an ITV.

In addition to the introduction of TRiP-4D and the necessary data acquisition, other additions are made to the patient work flow, introducing new immobilization equipment and pre-treatment imaging. Immobilization using thermoplastic mask systems is sufficient for high-precision radiotherapy in the head-and-neck region. For the extra-cranial SBRT, additional immobilization equipment is introduced to reduce the residual motion and intra-fractional variability, such as vacuum cushion and belly compression systems (Herfarth et al. (2000)). Position verification of the patient during the treatment is usually performed using conventional X-ray imaging, which is sufficient for high precision treatment of the

head-and-neck region but has low soft-tissue contrast. In this study, an offline PET/CT scanner is used for improved IGRT. For transportation of the patient between the CT scanner and the treatment room, a new patient transport system is introduced.

3.2 RESEARCH BACKGROUND

3.2.1 *4D Treatment Planning Development at GSI*

All advanced motion mitigation techniques introduced in this study are based on developments and research performed at the GSI Helmholtz Centre for Heavy Ion Research. This encompasses the use of the 4D treatment planning system TRiP-4D, which was developed by the GSI biophysics research group.

TRiP was initially conceived by Michael Krämer as a TPS for patient treatment planning during the GSI pilot project (Krämer et al. (2000); Krämer and Scholz (2000)). It was later expanded by Christoph Bert and Eike Rietzel to allow the calculation of motion effects (Bert and Rietzel (2007)). This 4D TPS was limited to the calculation of physical dose, which was later corrected by Alexander Gemmel (Gemmel et al. (2011)), who added the capability of biological 4D dose calculation.

As a part of the clinical research group KFO-214, Daniel Richter extended the functionality of TRiP-4D to allow the usage of different clinical sources of information (Richter (2012); Richter et al. (2013b)). This integration into a common framework facilitated the use of TRiP-4D and allowed the start of clinical integration.

Out of the features offered by TRiP-4D, several are of high interest in clinical routine and have been selected for integration into the current work flow:

- Integration of breathing-motion resolved 4D-CTs for 4D dose calculation and calculation of deformation vector fields
- Integration of an advanced contour model which allows the automatic propagation of patient contour information to all 4D-CT motion phases based on deformation vector fields and the automated calculation of ITVs
- Processing of breathing motion information for simulation and reconstruction of 4D dose distributions
- Reconstruction of 4D dose distributions of patient treatments, including gated irradiations

Integration of each feature requires data acquisition during a specific step of the patient treatment work flow. In this study, the necessary data acquisition and processing are described, as well as the new information available from the TRiP-4D calculations.

3.2.2 *The Clinical Work Flow at HIT*

For most patients treated at HIT, one common work flow is used. This work flow, designed with mainly head-and-neck patients in mind, is the basis for the liver irradiation work flow and is described here.

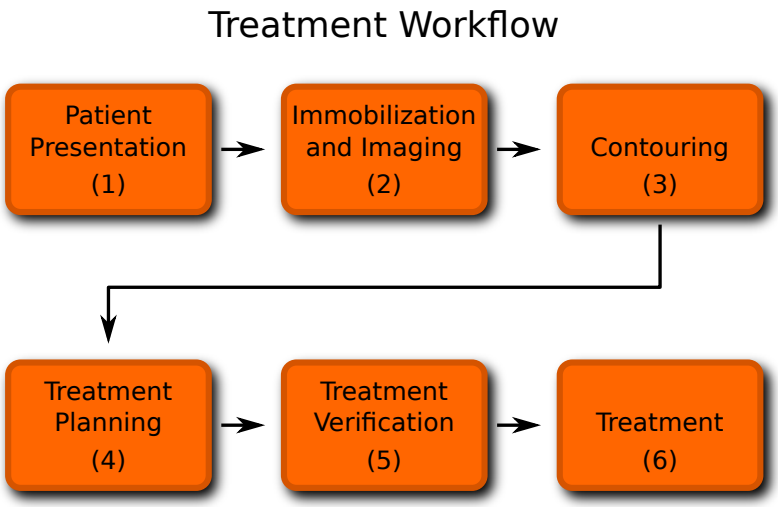

Figure 4: Overview of the clinical work flow common to all patient treatments performed at HIT.

At HIT, approximately 700 patients are treated per year (PTCOG and Jermann (2016, 2017)), equivalent to 14 new patients each week. For this reason, physicians, radiographers, technicians and physicists have to work coordinated to provide the best possible treatment decision, patient immobilization, treatment plan and irradiation. This is done in a work flow pattern shown in Fig. 4. It consists of six steps: Patient presentation, immobilization and imaging, contouring, treatment planning, treatment plan verification and patient treatment.

3.2.2.1 *Patient Presentation (1)*

At first, the patient and a physician discuss the treatment options, possible side effects and patient specific topics, like previous therapies and chronic conditions which could interfere with the treatment. The physician then decides if the radiotherapy is justified or not ("Rechtfertigende Indikation"), sets the aim of the treatment (curative or palliative) and prescribes the treatment dose.

3.2.2.2 *Immobilization and Imaging (2)*

In a next step, the patient is prepared for CT imaging using immobilization devices, for example thermoplastic masks, casts, vacuum cushions or leg rests. They are individually adjusted for each patient and ensure the same positioning for each treatment fraction, as well as increased comfort during the treatment.

When the immobilization equipment is adjusted, the patient is transferred to CT scanner, immobilized again and a treatment planning CT image is created. This CT image is used as the basis for contouring and treatment planning. In addition, more diagnostic imaging can be added, for example using contrast agents. If necessary, permanent markings are tattooed on the patient's body to reproduce the body position during therapy.

3.2.2.3 *Contouring (3)*

Using the treatment planning CT as well as overlayed diagnostic images (for example, PET, diagnostic CT or MRI images with or without contrast agents), physicians or technicians delineate target volumes and organs at risk. This yields

three-dimensional representations of the tumor volume, the patient's organs and other structures, for example markers or implants, which are the basis for treatment planning.

3.2.2.4 *Treatment Planning (4)*

In treatment planning, the treatment plan is created, which defines the patient positioning, couch and treatment beam angles, particle energies and fluence patterns which will be used during treatment to create the desired dose distribution. This complex task is performed using a treatment planning system (TPS), *syngo® RT Planning*, which takes into account the treatment planning CT and the contours created in step 3.

syngo® RT Planning is an inverse planning TPS, which optimizes the fluence based on a cost function using weighted dose constraints defined on the target volumes and the organs at risk. The TPS then calculates the biological dose resulting from this fluence. Once the resulting dose distribution is satisfactory, the resulting treatment plan and its corresponding dose distribution is checked and approved by medical physicists and physicians and ready for treatment.

Initially, *syngo® RT Planning* was not capable of calculating the resulting dose on a CT other than the treatment planning CT. Due to this limitation, a recalculation of the resulting dose on a multiphase CT or an optimization taking into account the motion of the target volume was not possible.

3.2.2.5 *Treatment Plan Verification (5)*

Before any treatment plan is used in patient treatment, it is first irradiated into a water phantom. Using a set of ionization chambers, the resulting dose is measured and compared to the dose distribution calculated in the TPS. This way, the calibration of the machine and the accuracy of the TPS can be monitored and the physicists can decide if the treatment plan is safe for the patient. Treatment plan verification is a standard approach for all advanced treatment techniques like IMRT (Intensity-Modulated RadioTherapy) or IMPT (Intensity-Modulated ParticleTherapy). In addition, if the treatment plan is yielding too many interlocks during irradiation, which can be the case for some combinations of energy, intensity or focus size settings, the treatment plan is re-planned to ensure a reliable treatment plan.

3.2.2.6 *Patient Treatment (6)*

Finally, the patient returns to the hospital for treatment. Inside the treatment room, he or she is positioned with the help of the immobilization equipment already used in step 2 to reproduce the same position in which the treatment planning CT was created. Based on the tattooed markings and X-ray radiography, the patient is positioned with sub-millimeter precision in front of the beam port and the irradiation is started.

The patient treatment is usually fractionated, hence the patient returns on weekdays for the course of up to two months. On each therapy day, this step is repeated, until all fractions of the series have been irradiated and the full dose has been applied. In hypofractionated or certain stereotactic treatments, the patient may only receive one to eight treatment fractions.

In addition to the treatment, the patient is examined regularly by a physician to ensure that the treatment is tolerated well. Sometimes, changes to the patient's

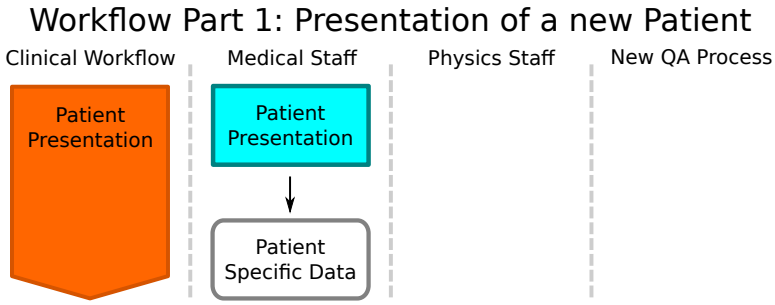

Figure 5: Patient Presentation: Physicians decide if the patient should receive particle therapy, gather relevant information and relay them to the physics staff.

anatomy require a re-planning on a new CT. In this case, the work flow is repeated from step 2. After the final treatment, follow-up appointments are scheduled, in which the well-being of the patient and the progress of the tumor growth is closely monitored.

3.3 RESULTS

This previously introduced usual work flow (Fig. 4) is well suited for most patients which are treated in the head or head-and-neck region, where organ motion can largely be neglected. For patients suffering from hepatocellular carcinoma, with larger inter- and intra-fractional motion of the target volume due to breathing and bowel motion, this work flow must be adjusted to ensure a high quality of treatment. In the following section, the measures taken to account for intra- and inter-fractional motion are presented as well as the resulting new information which is available due to this new work flow.

In the scope of this thesis, thirteen patients with hepatocellular carcinoma were treated in the time from May 2011 to July 2013. For each patient, the author and a small team of medical physicists accompanied the work flow steps to introduce new treatment techniques and to acquire patient data. The details of each step in this work flow as well as the differences to the common work flow and the additional information gained is presented in the following sections.

3.3.1 *Integration of TRiP-4D into the HIT Work Flow*

In collaboration with the physicists at GSI and HIT, as well as the physicians and technicians of the University Hospital of Heidelberg, several additions to the usual work flow were made. For each step of the work flow, a graph is used to illustrate the traditional tasks of the medical and physics staff (light blue boxes) and the new tasks performed by the research group (green boxes). In addition, the flow of information (white boxes) and newly gained information (yellow boxes) are shown, see Figs. 5, 6, 12, 14, 16 and 17.

3.3.1.1 *Step 1: Presentation of the Patient*

While the first step of the work flow is very similar to the usual work flow, physicians now also decide if the patient should receive a treatment with carbon ions or even a treatment using gated irradiation. If so, information relevant to

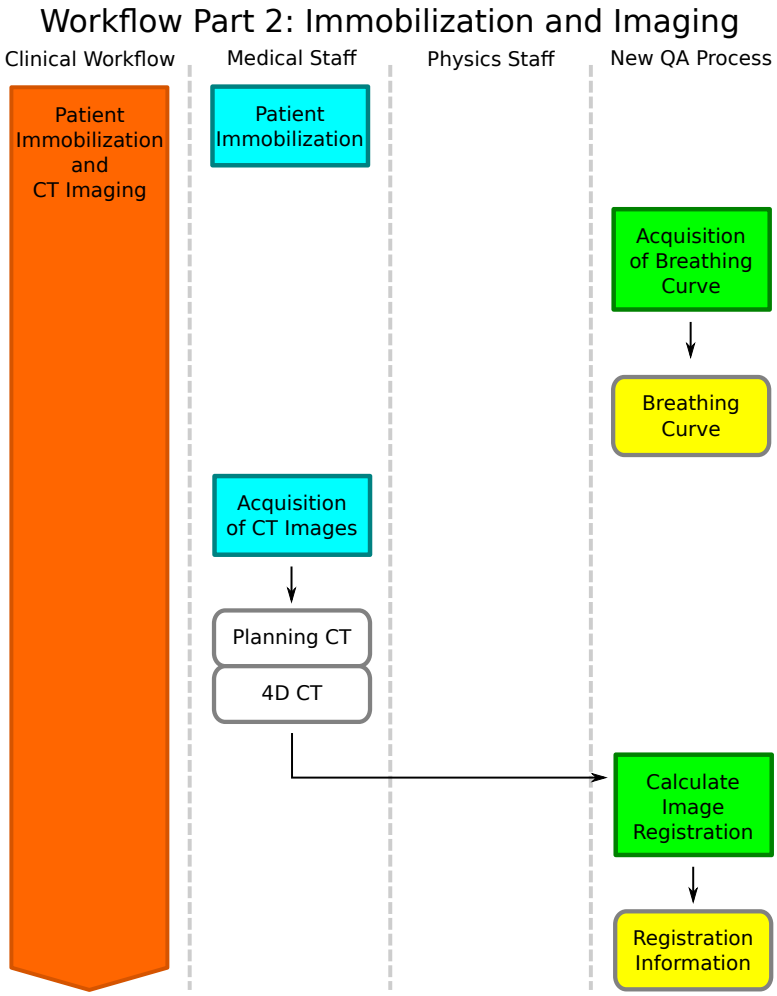

Figure 6: Immobilization and Image Acquisition: The acquisition of a breathing curve and the reconstruction of more motion phases with subsequent calculation of non-rigid image registration are introduced. Both are used for the calculation of dose distributions subject to organ motion.

the treatment, like general health problems, difficulty breathing or lying down as well as anxieties is gathered and used for treatment decisions.

If the physicians decide to use particle therapy, the medical physics staff is informed of this decision and can start the preparations for data acquisition. Fig. 5 shows a graphical representation of this step.

3.3.1.2 *Step 2: Immobilization and Image Acquisition*

In this step, several additions are made to the work flow: The patient is immobilized using vacuum cushions and a belly compression plate, a breathing curve is acquired using the *ANZAI AZ-733V* system and 4D-CT images are acquired. Furthermore, the breathing motion data and 4D-CTs are processed for use with TRiP-4D. This part of the work flow is represented in Fig. 6.

PATIENT IMMOBILIZATION: Most patients at HIT are treated using thermoplastic mask systems for immobilization. The patients suffering from hepatocellular carcinoma are immobilized in a supine position using various immobilization equipment from IT V (*Innovative Technologie Völp*, Austria). A vacuum cush-

(a) (b)

Figure 7: Patient Immobilization: (a) The vacuum cushion and arm rest which are used to stabilize the patient and reproduce the patient's position during treatment. (b) The belly compression which is used to reduce the breathing motion amplitude.

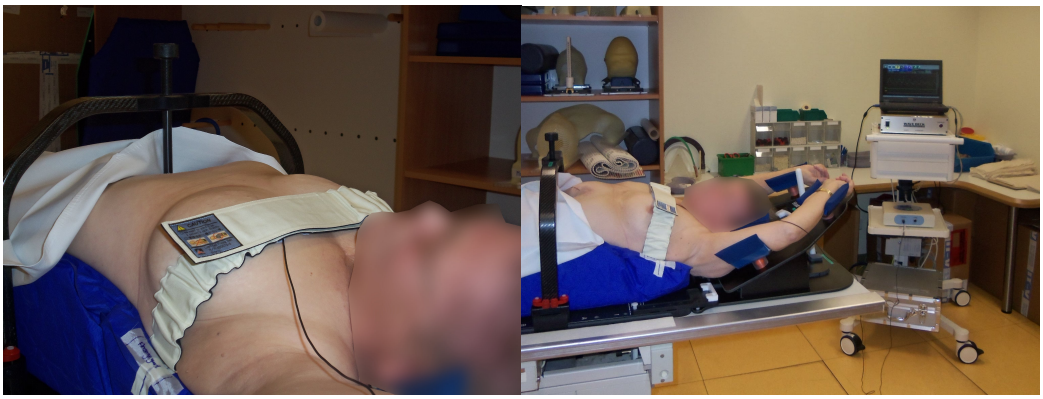

(a) (b)

Figure 8: Acquisition of breathing curves: (a) The *ANZAI AZ-733V* belt and pressure sensor used to record the breathing motion. (b) Recording the breathing motion using the *ANZAI AZ-733V* system.

ion (*BodyFIX BlueBAG TOTAL BODY*), ranging approximately from the shoulders to the knees, and an arm rest (*WingSTEP*) are used to ensure a reproducible body position and to keep the patient's arms outside of the irradiation field. Additionally, a belly compression (*BodyFIX Diaphragm Control*) is used. This plate, kept in place using a carbon frame and a screw, compresses the abdomen. Due to this compression, the patient cannot breathe in as deep as before and has to resort to a shallower breathing motion, hence reducing the motion in the upper abdomen. The vacuum cushion and belly compression equipment is presented in Fig. 7.

Some patients did not tolerate the belly compression. As a result, the motion of the target volume was considered and discussed by medical physicists and physician. If the motion was small enough, the patient was treated without compression. This immobilization strategy had already been introduced earlier for photon SBRT at Heidelberg University Clinic and was adapted for use at HIT (Herfarth et al. (2000)).

ACQUISITION OF BREATHING CURVES: When the patient is immobilized, a breathing motion curve is acquired for 10 to 20 minutes. This motion curve is the basis for later dose simulation calculations. In addition, the patient's tolerance to the immobilized state and the regularity of the breathing motion can be tested. Based on this information, physicians and physicists can decide if the patient can be subject to gated irradiation.

Acquisition of the breathing motion is performed using the *ANZAI AZ-733V* system, provided by *ANZAI MEDICAL CO., LTD*, Japan. It measures the motion of the chest wall using a pressure sensor (called a "Load Cell") inside a flexible belt around the thorax. When the patient breathes in, the pressure on the sensor increases, which is registered by the sensor port and wave deck electronics and relayed to a laptop computer which stores the motion data. Fig. 8 shows an overview of the setup. The same system is used for the acquisition of the 4D-CT and in the treatment room.

For the actual acquisition, the patient was told to breathe in a normal way, without speaking, for 10 to 20 minutes, simulating a regular irradiation time. When the patient became accustomed to the immobilization and had a regular breathing pattern, the motion amplitude was normalized and the acquisition started. In some cases, if the breathing was very regular and the patient cooperative, the belly compression was removed and another breathing curve was acquired, using the same amount of time.

Two examples of breathing motion curves are shown in Fig. 9, acquired over the time of ten minutes for two different patients. Breathing curve (a) was acquired from a patient who tolerated the belly compression. The patient exhibits a regular breathing pattern and almost no shift of the baseline and amplitude. If the patient breathes like this in a gated irradiation, one would expect an quick treatment without the need to adjust regularly.

Example (b) is from another, less compliant patient. The patient did not tolerate the belly compression, exhibited other motion (due to moving, coughing or talking) and a shift of the baseline. As the *ANZAI AZ-733V* system uses amplitude-based gating windows, such a patient could only be treated if the breathing curve was re-normalized during treatment, which would prolong the total treatment time.

Based on the acquired breathing motion curves, physicians and physicists can now decide more reliably if a patient should be treated using gating techniques or not. In addition, the breathing motion information is used in all dose calculations involving organ motion and can now be used in the simulations before the actual treatment.

ACQUISITION OF PLANNING AND 4D CT IMAGES: When the breathing motion has been recorded, patient and immobilization equipment are transferred to a *SIEMENS SOMATOM Sensation Open* CT scanner. The patient is immobilized again and three series of CT images are acquired: A treatment planning CT without contrast agent, a 4D-CT triggered by the breathing motion, and a diagnostic CT using contrast agent. While the acquisition of the planning CT and contrast agent CT are standard procedure, the acquisition of 4D-CTs was not done for patients treated at HIT before.

To acquire the 4D-CT, the patient's breathing motion is once again detected using the *ANZAI AZ-733V* system. Fig. 10 (b) shows the patient inside the CT, with the *ANZAI AZ-733V* system to the left. During a continuous CT scan, the

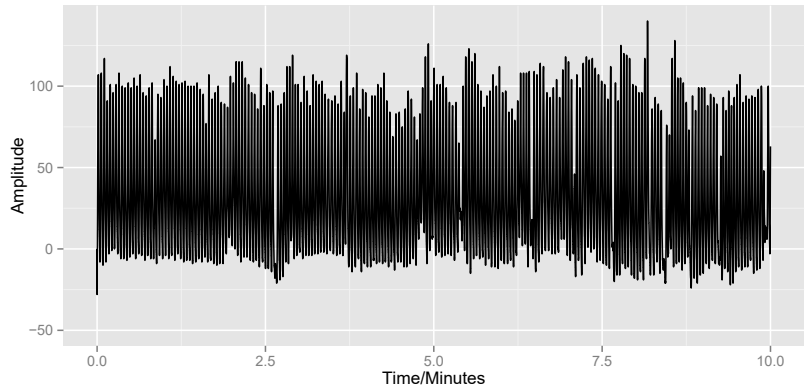

(a)

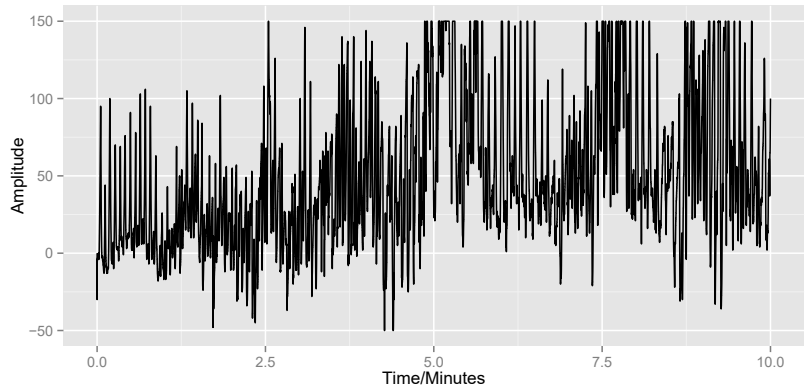

(b)

Figure 9: Breathing Curves of two different patients: (a) Compliant patient with belly compression, the patient exhibits a regular breathing pattern with constant amplitude, higher frequency and without baseline drift. (b) Non-compliant patient who did not tolerate the belly compression and exhibits a very irregular breathing pattern, in part due to moving, talking or coughing.

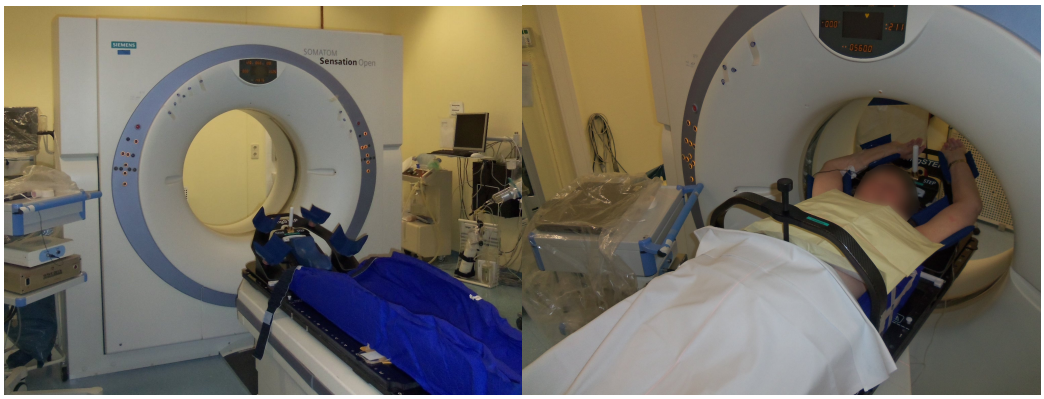

(a) (b)

Figure 10: CT Aquisition: (a) All immobilization equipment is transferred to the CT scanner. (b) The patient is immobilized again for treatment planning imaging. To the left, the *ANZAI AZ-733V* system is visible which is used for triggered acquisition of 4D-CT images.

patient's breathing motion is also recorded. The acquisition settings are chosen so that each patient region is scanned at least once in each motion phase (from full inhale to full exhale and to full inhale again). After acquisition, the CT sinograms are sorted according to the motion phase in which they were created and reconstructed. When reconstruction is finished, a set of CTs is available, each CT corresponding to one motion phase.

POST-PROCESSING OF THE ACQUIRED CT IMAGES: When all CT images have been acquired, some post-processing of the image data has to be performed: Some 4D-CT motion phases have to be reconstructed manually and sent to the central image storage system (DICOM PACS). Then, all images have to be exported for processing in external software.

By default, only eight 4D-CT phases are reconstructed by the CT software: Four phases of the inhale period (20%, 25%, 50% and 75% lung volume) and four of the exhale period (100%, 70%, 40%, 0% lung volume). For a more accurate dose calculation, missing phases are reconstructed in 10% increments ($In_{0\%}$, $In_{10\%}$, ..., $In_{100\%}$ (inhalation), $Ex_{100\%}$, $Ex_{90\%}$, ..., $Ex_{0\%}$ (exhalation)). This is done manually in the CT software following the image acquisition. The CT images are then transferred to the DICOM PACS of HIT for treatment planning.

Most of the data processing and dose calculation software for research purposes must not be installed on a computer which is also used for the treatment of a patient (a medical product). Likewise, some calculations were performed in a computing cluster without connection to the HIT DICOM network. To allow for this, the patient data was exported, anonymized and further processed on research computers using a set of DICOM tools specifically written for this task. For all further calculations, the images are sorted, cropped to a similar length and co-registered.

NON-RIGID IMAGE REGISTRATION: With the planning CT and the 4D-CT available, it is now possible to calculate a non-rigid registration between them and among individual motion phases. The displacement of organs due to breath-

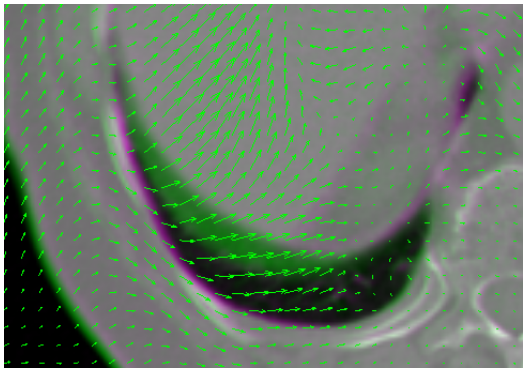

Figure 11: Image Registration: Two motion phases of a 4D-CT are shown in green and purple. The corresponding vector field, calculated using *Plastimatch*, is represented using green arrows.

ing motion is represented as a vector field and is the basis for 4D dose calculation.

Using the free open source software *Plastimatch* (Sharp and Plastimatch Development Team (2011)), the transformation vector fields of the patient's motion are calculated. The non-rigid registration is carried out using the built-in *B-spline* method of the *Plastimatch register* command. *Plastimatch* provides a vector field of the displacement, $\vec{u}_{r,i}$, between motion phases r and i. It is connecting the position of point $\vec{x}_r$ in reference motion phase r to its position $\vec{x}'_i$ in motion phase i:

$$\vec{x}'_i = \vec{x}_r + \vec{u}_{r,i}(\vec{x}_r). \tag{13}$$

Fig. 11 shows a result of this calculation. Two phases of a 4D-CT are overlaid in green and purple, the different positions of the diaphragm and liver are clearly visible. In addition, the green arrows show the projection of the calculated motion vectors in this plane.

Registration between the planning CT and the 4D-CTs is performed in two steps: First, the registration between the treatment planning CT and one reference phase of the 4D-CT is calculated, usually 0%Ex. Then, the registration between the reference phase of the 4D-CT and all other motion phases is calculated. This reduces the necessary number of registrations between motion phases.

The transformation vector field can now be used in TRiP-4D for further calculations. It is necessary for the calculation of 4D dose distributions (the dose is calculated in separate motion phases and must be summed up in the reference phase). It can also be used to automatically propagate contours created only on the treatment planning CT to the 4D-CT.

3.3.1.3 *Step 3: Contouring*

Based on the treatment planning CT and diagnostic imaging, contours of organs at risk and the target volume are created. TRiP-4D features a new contour model and offers the automated propagation of contours based on the deformation vector field. This encompasses an automated calculation of an ITV from propagated CTVs, taking into account the extend of the organ motion. In this section, the compatibility with the acquired data is tested. Fig. 12 gives an overview over this step.

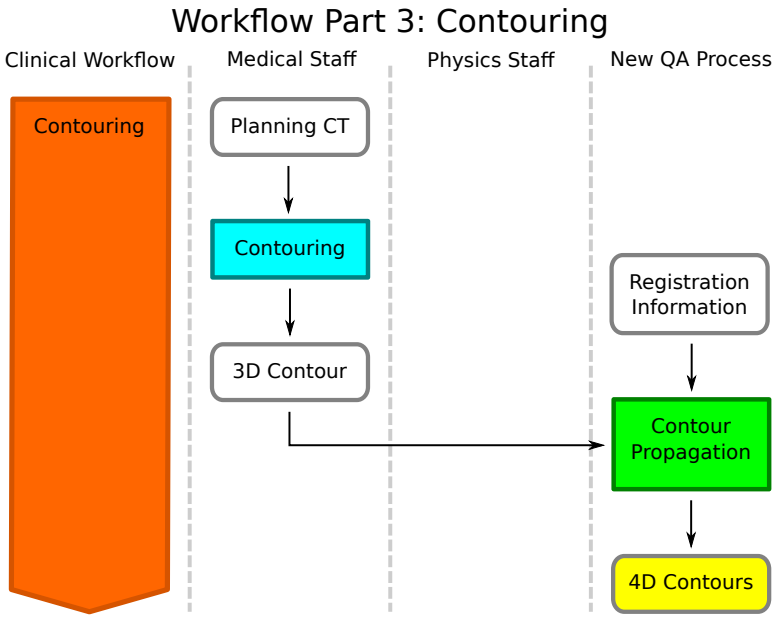

Figure 12: Contouring: Based on the planning CT, either a physician or technician creates a set of contours. These contours can be automatically propagated to the registered 4D-CT using vector fields.

CREATION OF CONTOURS ON THE PLANNING CT: Most of the contouring is done in the same way all patient contours are created at HIT. Using commercial contouring software provided by *SIEMENS*, specially trained technicians or physicians look at each slice of the planning CT image and draw the outlines of each organ at risk and of the visible tumor mass. If needed, other diagnostic images can be overlayed, such as contrast agent CTs, MRI and PET images. In this way, contours of the organs and the *Gross Tumor Volume* (GTV) are created. Based on clinical experience, physicians also delineate the areas in which microscopic tumor growth is expected, yielding the *Clinical Target Volume* (CTV).

To account for organ motion, a physician now estimates the motion of the target volume from the 4D-CTs. This is done by measuring the motion of the liver or visible lesions in or near the CTV. The maximum excursion in all three dimensions is added as an additional margin around the CTV to form the *Internal Target Volume* (ITV). An additional margin is added for known uncertainties due to patient setup, particle range and imaging uncertainties. This *Planning Target Volume* (PTV) is later used for treatment planning.

CALCULATION OF AUTOMATICALLY PROPAGATED CONTOURS: Contours are not only used for therapy planning, but also for evaluation of the treatment plan. To evaluate the quality of a treatment plan after dose calculation on the 4D-CT, the contours must be available on this CT as well. However, creation of contours by hand is a time-consuming and error-prone task, depending on the complexity of the treatment. Therefore, automated propagation of contours from the planning CT to the registered 4D-CT using the vector fields can help the process. Fortunately, TRiP-4D contains a newly added feature for automated contour transfer.

To propagate the contours, they are first exported from the HIT PACS as DICOM files and converted into TRiP format. Using the vector fields calculated

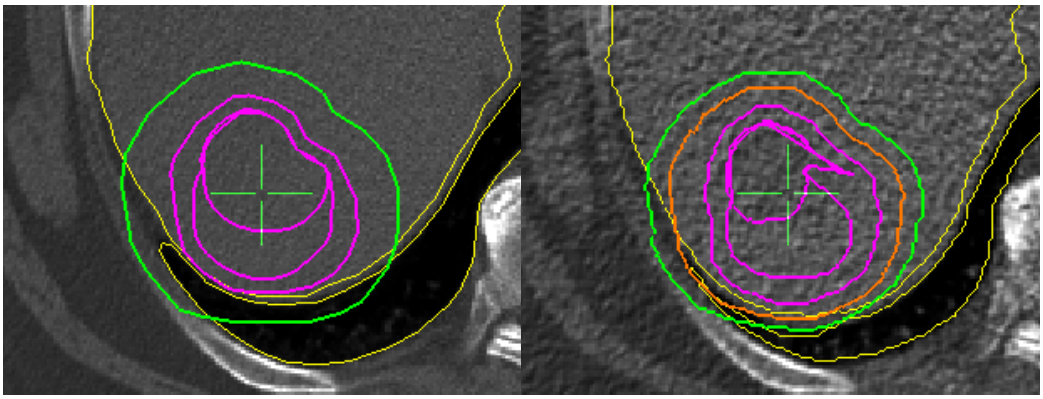

(a) Planning CT (b) 4D-CT, Motion Phase $Ex_{0\%}$

Figure 13: Automated Contour Propagation: Patient volumes are transferred from the planning CT to the reference phase of the 4D-CT. While the PTV (green), CTV (outer purple), liver and lung (both yellow) have been transferred well, the GTV and RF-ablated volume (innermost purple) show artifacts from a malformed vector field. In orange, an ITV has been created from all 4D-CTs.

in step 2, TRiP-4D is then used to propagate the contours to the reference phase of the 4D-CTs and further to all other motion phases.

Based on the transformed CTVs in all motion phases, TRiP-4D can then be used to calculate an ITV based on the transformation vector fields. This calculation can be an alternative to the usually used estimation of the motion of the target volume and adding this as a margin.

The resulting volumes are shown in Fig. 13. The contours, taken from the planning CT, have been transferred to the $Ex_{0\%}$ reference phase of the 4D-CT. In this case, the contours of the organs (liver and lung in yellow), PTV (in green) and CTV (outermost purple) have been transferred well and without artifacts. For the contours of the GTV and RF-ablated volume (medium and innermost purple), some artifacts are visible. Hence, when working with automated contour propagation, the user should at least check the quality of the transferred contours. In orange, the ITV created from all combined CTVs is shown. This volume is created automatically by TRiP-4D and can be used as a basis for robust 4D treatment planning.

3.3.1.4 *Step 4: Treatment Planning*

With the treatment planning CT and the patient contours available, medical physicists now create the treatment plan. As for all patients treated at HIT, treatment planning is done with the commercial treatment planning software *SIEMENS syngo® RT Planning*. This treatment plan is exported from the HIT PACS and converted to a TRiP-compatible format. Using the treatment plan and the information acquired in the previous steps, a simulated 4D dose can now be calculated using TRiP-4D, as shown in Fig. 14.

TREATMENT PLANNING: Patient treatment is based on the *PROMETHEUS-1* study design (Combs et al. (2011)), which proposes a hypo-fractionated dose escalation study starting at 4×10.0 Gy (RBE) and incrementing the fraction dose by 1.0 Gy (RBE) up to 4×14.0 Gy (RBE), depending on the toxicity. In this study, only carbon ions are used.

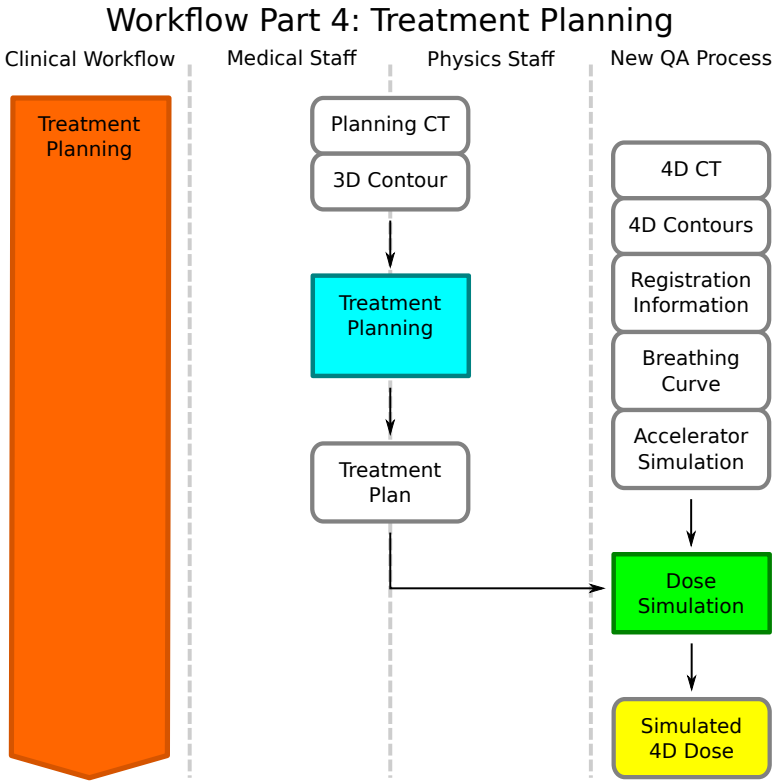

Figure 14: Treatment Planning: A treatment plan is created using the commercial TPS *SIEMENS syngo® RT Planning*. Based on the treatment plan and the information acquired in earlier steps, a 4D dose can now be simulated. This dose distribution can be helpful in decision making or defining a gating window.

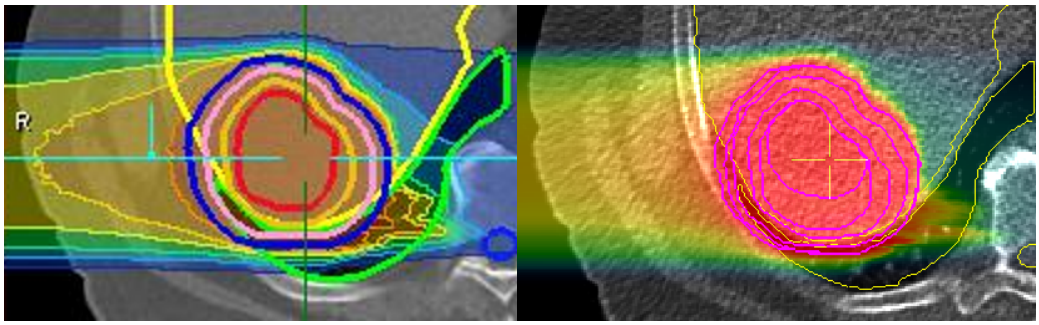

(a) Original Treatment Plan (b) Reconstructed on $Ex_{0\%}$ of the 4D-CT

Figure 15: Re-Calculation on a 4D-CT: Original treatment plan calculated on the treatment planning CT in the *SyngoPT* treatment planning system, re-calculated dose on the $Ex_{0\%}$ phase of the 4D-CT using TRiP. This calculation can determine if the dose coverage is sufficient in all motion phases or if there is an increased dose to organs at risk, in this example the spinal cord.

All treatment plans used a single treatment field with a gantry angle of 90° (horizontal), the treatment couch was positioned perpendicular to the beam (270°) so that the particles entered the patient from the right. If the belly compression bracket was in the way, the couch angle was altered. For target volumes on the cranial end of the liver, breathing in could result in an overshoot of dose into the spinal cord. In this case, the couch angle was also adjusted.

Treatment plans were created using the commercial *SIEMENS syngo® RT Planning* treatment planning system. At the time of this study, this TPS could not be used for dose calculation on motion phases of the 4D-CT. Hence, treatment planning with this TPS could not take the effects of organ motion into account.

4D DOSE SIMULATION USING TRIP-4D: As with the CT images and the contour data, the treatment plan is exported from the HIT PACS as a DICOM file and converted into a TRiP compatible treatment plan file. In combination with the 4D-CT, registration information and the patient's breathing curve, TRiP-4D is now used to calculate a 4D dose distribution.

In the simplest approach, instead of using the original treatment planning CT, TRiP is used to calculate a static dose using a single motion phase of the 4D-CT, ignoring all further motion and interplay effects. This simple reconstruction of dose can already reveal areas of over- or underdosage and can be used to determine the size of a gating window, for example if the PTV is not covered at full inhalation. Fig. 15 shows the result of such a calculation, and the esophagus treatment planning study in Chapter 5 uses the same approach.

In the example of Fig. 15, the liver moves downwards and partially out of the therapy beam when the patient inhales. In certain cases, this can lead to an increased dose in the spinal cord. Using this information, the decision to adjust the treatment plan or to use a gated treatment can be made.

Alternatively, it is also possible to do a more sophisticated 4D dose simulation using TRiP-4D. Using the known breathing motion curve from the immobilization step, 4D-CT images, non-rigid registration vector fields and the treatment plan, a 4D dose distribution is calculated which takes into account the effects of organ motion.

In the 4D calculation, TRiP-4D determines which part of the treatment plan is irradiated during each motion phase of the patient. In order to do this, the breathing motion curve is used to determine in which motion phase the patient is at a certain point in time of the irradiation. Additionally, an accelerator simulation is used to determine when each part of the treatment plan is irradiated. The treatment plan is then split up into several treatment plans with corresponding motion phases. TRiP-4D then calculates the dose irradiated in each of the 4D-CT motion phases. Using the vector fields, the dose is then transformed and summed up on the reference motion phase, usually $Ex_{0\%}$.

In comparison to the static dose calculation, this approach can be more accurate, taking into account interplay effects. On the other hand, the quality of the dose calculation depends on the quality of the input data and the reliability of the accelerator simulation.

Calculation of simulated dose distributions from data acquired based on the work in this thesis is discussed in more detail in Richter et al. (2011).

3.3.1.5 *Step 5: Treatment Plan Verification*

Like in the usual treatment work flow, verification measurements are carried out to guarantee that the treatment plan is irradiated correctly by the treatment machine and yields the correct dose distribution. Furthermore, the accelerator records from the irradiation are exported and used for improved dose calculations. Further, an advanced verification setup is introduced to assess the impact of motion on the dose distribution and can also be used to verify a gated irradiation.

IMPROVED DOSE SIMULATION: During verification, the treatment plan is irradiated into a water phantom with 24 pin-point ionization chambers. This measurement detects deviations from the computed dose distribution, errors in the dose prescription and determines if the accelerator provides the treatment in the necessary quality and without interlocks. In addition, the accelerator records of this irradiation give the most accurate information on the timing structure during treatment.

The accelerator records are now exported from the therapy control system (TCS) and converted into a TRiP-compatible format, a *Beam Delivery Sequence*, in the form of an *LMDOUT* file. Using TRiP-4D, this information is used to calculate a more accurate and reliable dose distribution. Fig. 16 gives an overview over this step.

This improved dose distribution, as well as the results of the verification, can be used to decide if a treatment plan can be administered to the patient or if it should be re-planned.

ADVANCED VERIFICATION TECHNIQUES: In addition to the water phantom normally used in treatment plan verification, a small water phantom, mounted on a *QUASAR(TM) Respiratory Motion Platform*, was introduced. This water phantom can be shifted horizontally based on a supplied motion trajectory. The setup is also used in Chapter 4 and shown in Fig. 46 on page 85.

When the recorded breathing motion of the patient is supplied to the motion platform, the water phantom moves in a similar pattern as the organs of the patient. By repeating the irradiation using this moving platform, more informa-

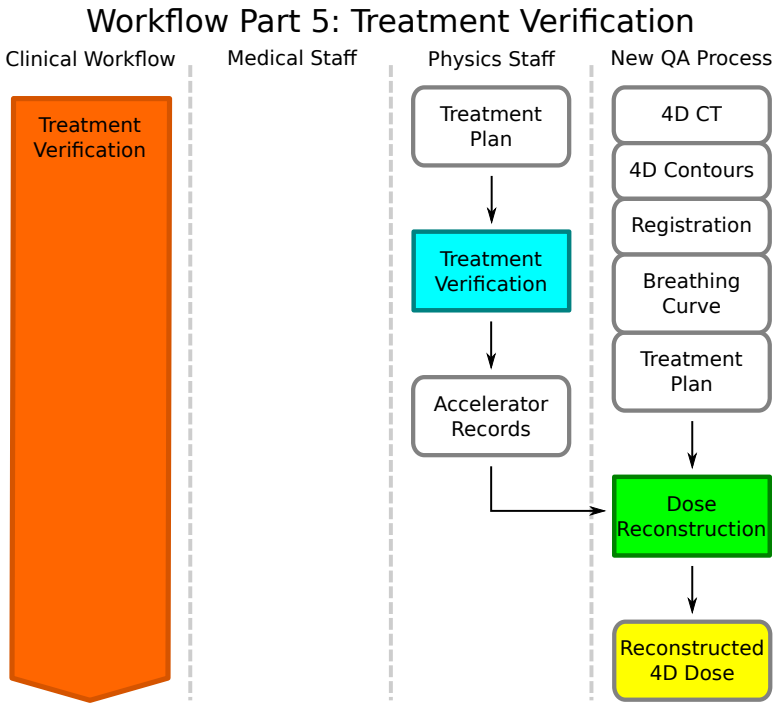

Figure 16: Treatment Plan Verification: Accelerator Records, created during the treatment plan verification, are used to calculate more reliable 4D dose distributions.

tion can be obtained from the verification which is important for the 4D dose calculation.

By irradiating the treatment plan into the moving water phantom, the resulting dose measurements can be compared to 4D dose calculations using TRiP-4D. This is an important check of the dose calculation software and can reveal problems in the data acquisition or dose calculation settings.

Further, the *ANZAI AZ-733V* respiratory gating system can be attached to the *QUASAR(TM) Respiratory Motion Platform* and the whole verification can be repeated in gated mode. In this mode, the gating system enables and disables the beam based on the motion amplitude. Based on this, the performance of the gating system can be checked as well as the approximate duration of the treatment using gated irradiation.

Also, as the accelerator simulation of TRiP-4D does not include gating as of this study, this is the only way of calculating simulated dose distributions for gated treatment.

3.3.1.6 *Step 6: Patient Treatment*

Several additions were made to the usual work flow for the actual patient treatment, both to improve treatment quality and to acquire data for the reconstruction of the actual dose distribution. In this step, the most intense changes to the work flow were introduced.

Prior to each treatment, a CT image is acquired to detect inter-fractional motion and setup inaccuracies. The patient is then transferred to the treatment room using a newly introduced patient shuttle system. During treatment, the breathing motion is recorded for later reconstruction of the applied dose to the

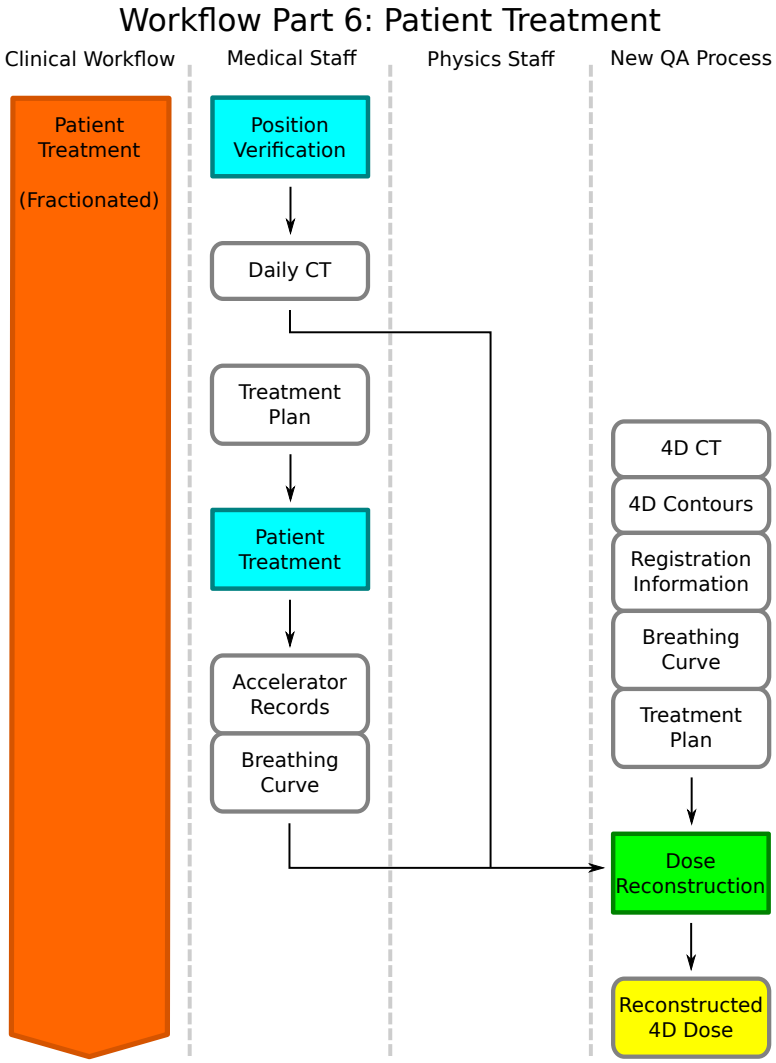

Figure 17: Patient Treatment: Prior to each treatment, a CT image is acquired in treatment planning quality for position verification. This image can be used for replanning or dose reconstruction. Additionally, the patient treatment yields accelerator records and a breathing motion curve, with which the irradiated 4D dose can be reconstructed.

patient using the *ANZAI AZ-733V* system. Based on this system, the first patient was treated using gated irradiation. After the treatment, the patient is transferred back to the HIT PET/CT scanner for acquisition of activity from ^{11}C decay. Finally, all data sets are exported from various sources, synchronized and converted to TRiP-compatible formats. Fig. 17 gives an overview of this step.

PRE-TREATMENT IMAGING: Each HIT treatment room is equipped with integrated radiography equipment used for image guided positioning of the patient prior to treatment. This system provides enough image information to accurately identify the position of the bony anatomy and is therefore sufficient for intra-cranial irradiation. Unfortunately, the contrast of the organs in the abdominal regions is not high enough and image guidance requires either a cone beam or in-room CT scanner. At HIT, pre-treatment imaging is provided by an additional PET/CT scanner next to the treatment rooms.

Due to the high dose per fraction, the acquisition of a CT image prior to each treatment is required to decide if the treatment can be administered safely. At the beginning of each treatment, the patient is immobilized inside HIT's PET/CT scanner room and inserted into the scanner. A CT image of treatment planning quality is aquired and compared to the original planning CT by a physician. If the image is similar enough for a safe treatment, it is continued, otherwise, the patient is irradiated on the following day. Reasons for anatomical deviations could be large abdominal motion a or a large buildup of gas compared to the original planning CT.

The patient is immobilized with the same vacuum cushion and belly compression already used when the treatment planning CT was acquired. Also, the *ANZAI AZ-733V* gating system used to measure the breathing motion is now attached to the patient and tested. Fig. 18 (a) shows the patient inside the HIT PET/CT scanner.

PATIENT TRANSPORT: Without interrupting the immobilization, the patient is transferred to the treatment room. This is done using the automated shuttle system *ONCOlog PatLog*, which picks up the CT couch top including immobilization equipment and patient, transfers it to the treatment room and places the couch top on top of the treatment couch.

Fig. 18 (b) shows the shuttle transporting the patient to treatment on the HIT corridor. In automatic mode, it is capable of moving from room to room without further interaction, following a black line on the floor. Fig. 18 (c) shows the shuttle in its final position inside the treatment room. The patient is then transferred on top of the treatment couch. The whole transport from the PET/CT scanner to the treatment room couch takes approximately five minutes, all patients tolerated the transport well.

TREATMENT: To start the treatment, the patient is positioned first using permanent markings on the patient's skin and the in-room laser system. Then, using orthogonal radiography, the patient is positioned using the bony anatomy. This final position is shown in Fig. 18 (d), with the beam nozzle coming in from the right and the patient positioned in front of it. Before treatment starts, the *ANZAI AZ-733V* gating system is connected to the therapy control system and to the pressure sensor already on the patient. The system is visible in the background, with the cable connected to the pressure sensor running along the patient's left side.

For improved control during treatment, the *ANZAI AZ-733V* control interface and breathing motion curve is relayed to the control room, shown in Fig. 18 (e) and (f). Here, the amplitude of the breathing motion curve is monitored during treatment and can be recorded. If the patient is treated using gating, it is enabled and disabled via this interface.

The resulting breathing motion curve is recorded by the *ANZAI AZ-733V* system, the irradiation information is logged by the therapy control system (TCS). The treatment information was extracted, converted to TRiP-readable formats and synchronized. It is later used for reconstruction of the resulting 4D dose distribution. As a backup measure, both informations were also recorded by the *Beckhoff EtherCAT* real time data logging system, which is part of the accelerator control system (ACS) and can store the data if the *ANZAI AZ-733V* system fails.

(a) (b)

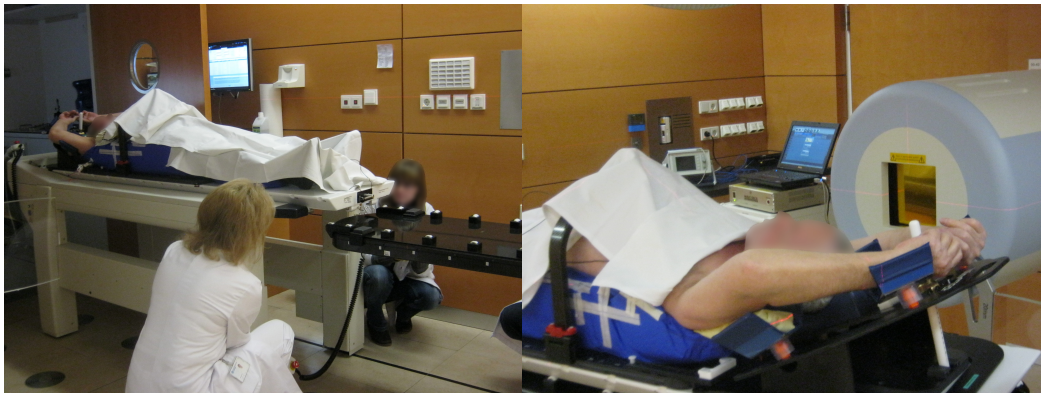

(c) (d)

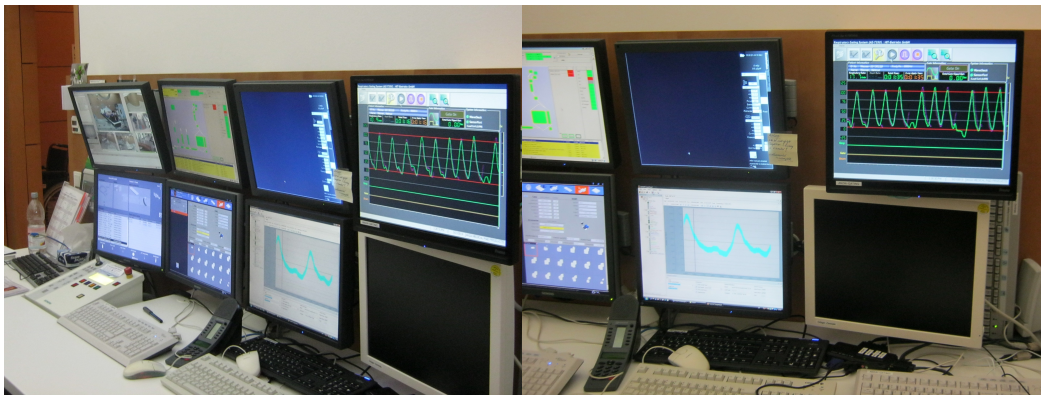

(e) (f)

Figure 18: Treatment: (a) Position Verification using the HIT PET/CT. (b), (c) Transfer to the treatment room using the patient shuttle. (d) Patient setup prior to treatment start. (e), (f) Data acquisition in the control room during treatment.

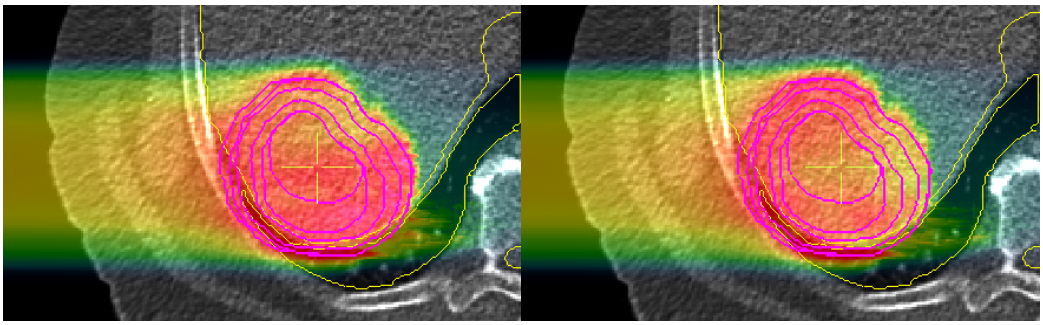

(a) Fraction 1 (b) Fraction 2

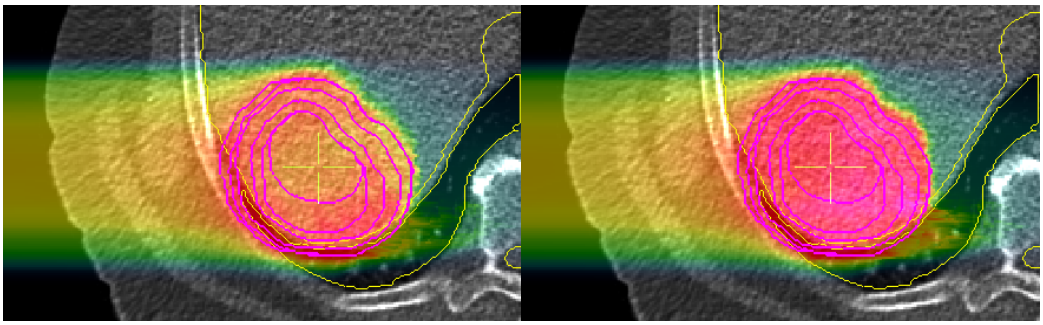

(c) Fraction 3 (d) Fraction 4

Figure 19: Reconstructed dose distributions of all four fractions of a patient treatment. Depending on the breathing motion and the accelerator timing pattern, the dose distribution changes.

Gating was introduced as a viable motion mitigation technique in one of the thirteen patients who were treated until July 2013. The data acquisition and preparation is the same as in the non-gated treatments, with the exception that the *ANZAI AZ-733V* system is used to enable the irradiation based on the breathing pattern.

POST-TREATMENT IMAGING: During the irradiation, ^{11}C and ^{15}O nuclei are created as fragments of carbon ions and atoms in the patient's tissue. Both nuclei are β^+ emitters and their activity can be captured using the PET/CT scanner. Some patients were transported back to the CT room using the *ONCOlog PatLog* shuttle system where the PET activity was measured for approximately 25 to 30 minutes.

Based on this data, the PET research group performed the first steps towards in vivo treatment verification in the clinical routine at HIT (Bauer et al. (2013a,b); Kurz et al. (2015); Gianoli et al. (2015)). This is done by comparing the measured activity distribution to model calculations and might at one point be able to detect range or setup errors.

DOSE RECONSTRUCTION: Using the data collected during treatment, it is now possible to reconstruct the actual 4D dose distribution applied in this fraction. The breathing motion curve and the accelerator records are exported and converted into TRiP-4D compatible formats. Using this information and the existing 4D-CT information, the dose is reconstructed using TRiP-4D.

Fig. 19 shows the dose distributions calculated for all four fractions of a patient treatment. All images use the same color-scale and all dose distributions are cuts

in the same height of the patient. The different dose distributions are a consequence of different breathing motion and accelerator timing patterns. Details of this dose reconstruction have been published as part of the clinical research group by Richter (2012) and by the author and Richter et al. (2013a, 2014).

In addition, the calculations can be improved by using the treatment planning CT which is acquired daily. For some patients, a new 4D-CT was also acquired, which could potentially also be used for improved reconstruction of the fraction dose. Based on the reconstructed dose distributions, a physician can now decide if the treatment should continue or if the patient treatment should be re-planned, for example if the target volumes do not receive enough dose or there is too much dose in an organ at risk.

3.4 SUMMARY

In the course of this study, thirteen patients suffering from hepatocellular carcinoma have been successfully treated using a new work flow, including the first patient irradiated using motion gating. The newly introduced data acquisition and data processing has been shown to be compatible with dose calculation using the TRiP-4D therapy planning system and was used for the reconstruction of individual therapy fraction dose distributions.

In the new work flow, time-resolved 4D-CTs are systematically acquired and additional motion phases are reconstructed. The 4D images were shown to be usable for 4D dose calculations and the calculation of deformation vector fields using the *Plastimatch* software. The deformation vector fields are necessary for 4D dose calculation in TRiP-4D and for automated contour propagation.

The integration of an advanced contour model in TRiP-4D allows automated contour propagation from the treatment planning CT to the motion phases of the 4D-CT and automated calculation of an ITV from propagated CTVs. The contours created at HIT could be imported into TRiP-4D and the contour propagation worked, albeit with some artifacts visible in the created contours. The automated creation of an ITV was usable, although the practical definition of the PTV used during treatment planning did not rely on the ITV.

Breathing motion information was acquired using the newly introduced *ANZAI AZ-733V* system. It was used during immobilization, during 4D-CT imaging and during treatment. During immobilization, a breathing motion curve was acquired to accustom the patient to regular breathing in the immobilization equipment. This information was also later used for verification and simulation purposes. The same equipment was used during 4D imaging to ensure the same motion surrogate is used as during treatment. During patient treatment, the *ANZAI AZ-733V* system was used for gated therapy and to acquire the actual breathing motion during the irradiation, both in gated and non-gated irradiations. The *ANZAI AZ-733V* data was found to be compatible with TRiP-4D and was used for dose calculations.

All data sources were used in combination for the calculation of 4D dose distributions using TRiP-4D. This encompasses the import of DICOM CT, contour and treatment plan information, treatment records from the therapy control system, deformation vector information and breathing motion information. All data sources were found to be compatible with the new TRiP-4D software.

Dose distributions can now be calculated in two different ways. Prior to the treatment, the available information can be used to calculate a simulated 4D

dose distribution, based on a simulated beam delivery sequence or on treatment records from the treatment plan verification. This results in a simulated 4D dose distribution.

During patient treatment, the breathing motion is acquired and can be used with the treatment records to reconstruct the actual fraction dose distribution. This results in a reconstructed 4D dose distribution. Examples of reconstructed 4D dose distributions can be found in Richter (2012); Richter et al. (2014).

In addition to the data acquisition necessary for motion-gated therapy and 4D dose calculation using TRiP-4D, passive motion mitigation measures were introduced as well. Based on the established practice at the Heidelberg University Clinic (Herfarth et al. (2000)), vacuum cushions and belly compression systems were successfully introduced for SBRT at HIT. To mitigate the lack of cone-beam CT image guided radiotherapy at HIT, the PET/CT was integrated into the work flow for pre-treatment imaging. To transfer the patient from the CT to the treatment room, a patient shuttle (*ONCOlog PatLog*) was introduced.

3.5 DISCUSSION

While the introduction of TRiP-4D and 4D dose calculations into the work flow for the treatment of hepatocellular carcinoma was a success, it is merely a starting point for further development. With the new work flow, more information is available for treatment decisions, but the data acquisition and processing required is both time-consuming and error-prone.

In its current implementation, the export of treatment data, synchronization of time-critical log files and conversion to TRiP-readable format is performed manually, taking approximately two weeks of intensive data processing and dose calculation to arrive at a usable 4D dose distribution. All of the data processing has to be done by researchers with intimate knowledge of the TRiP framework, which reduces usability for non-research clinical staff.

To facilitate the use of TRiP-4D, two strategies were pursued: Automation of the data processing and dose calculation, and integration of TRiP-4D into a visualization solution. This way, physicians and medical physicists would be able to get information fast and without the need to consult a research team.

Automation of the data processing has been achieved with the use of *Python* scripts for automatic processing of the DICOM files used in the calculations, including cropping of the CT images to a common length and conversion to a TRiP-compatible file format. The creation of command-files for the automatic calculation of registration vector fields using *Plastimatch* and for basic dose calculations using TRiP were also created. Unfortunately, the TRiP-4D version used in this thesis was only available at the AIX cluster at GSI; further steps for automation were postponed until a Linux version of TRiP-4D would become available on the HIT computing cluster.

Visualization options have been researched, with the *MeVisLab* framework as a promising basis. *MeVisLab* is already used by other research groups at HIT, allows the use of *Python* scripts for data processing and offers built-in visualization options for medical images. When combined with the automated data processing, this could offer the possibility to check plan quality and see the effects of a treatment decision almost instantaneously.

In addition to improved usability by means of automation and visualization, data acquisition could be further improved by using additional data sources.

Currently, data from different sources must be compiled and synchronized, for example the *ANZAI AZ-733V* breathing motion information and the therapy control system irradiation records. Both data set operate on different clocks and need manual synchronization. One solution could be the *EtherCat* system, which is part of the accelerator control system. This system already has real-time information on the irradiation and can accept external data input from the *ANZAI AZ-733V* system. By using log files created in the *EtherCat* system, the data acquisition could be further simplified and sources of error reduced.

When the automation is implemented, further research could be carried out to decide which information is most interesting for treatment decisions, for example, simulated dose distributions for during planning, reconstructed dose distribution after the verification measurements or reconstructed dose distributions after the patient treatment.

3.6 OUTLOOK

During the work on the treatment work flow, two interesting research topics were identified: For one, the simulation of the time structure of the therapy accelerator is not very detailed and ignores many properties of the actual accelerator. This leads to unreliable and imprecise dose calculations prior to treatment. Additionally, the complex data preparation necessary for a 4D dose calculation takes a lot of time and patient cooperation. Using a simplified approach for dose calculation might be sufficient in some cases and speed up the dose calculation process.

Therefore, in Chapter 4, the mode of operation of the HICAT accelerator installed at HIT is analyzed. Based on the the results of this analysis, an optimized simulation of the accelerator timing has been conceived, taking into account the energy-dependent and random properties of this accelerator. In an experimental verification, the efficacy of this approach for the calculation of simulated dose distributions is confirmed.

In Chapter 5, the complex 4D dose calculation approach is replaced by a simplified quasi static approach for the calculation of doses in a treatment planning study concerning esophageal carcinoma. While complex effects, like over- and underdosage due to interplay, are not taken into account, it can be used to gain initial insight into a treatment planning case and to decide between several plan variations or gating window definitions.

4

ANALYSIS AND MODELING OF THE HIT ACCELERATOR CYCLE

In this chapter, the properties of the HIT accelerator are analyzed to create a realistic energy-dependent model of the cycle timing. Based on the results, a simulation software is developed, which allows the prediction of realistic timing sequences for treatment plans, a key to the simulation of 4D dose distributions. To verify the accuracy of the predicted sequences, they are compared to treatment records and to experimental dose measurements using a moving phantom.

4.1 INTRODUCTION

When calculating a 4D dose distribution, two important pieces of information are necessary: The patient's motion sequence (usually supplied in the form of a breathing motion curve) and the accelerator's beam delivery sequence, which states the time in which each raster spot has been irradiated. Only when both are precisely known, the particle fluence of a treatment plan can be assigned to the right motion phase and the calculation of motion effects is reliable.

In the reconstruction of an already irradiated treatment plan, breathing motion curves and accelerator information is available and can be used for calculations. In simulations, either for analyzing a treatment plan for a single patient or as part of a treatment planning study, the beam delivery sequence is not known and must therefore be simulated using a sufficient accelerator model.

For the accelerator installed at HIT, the Heidelberg Ion-Beam Cancer Therapy (HICAT) accelerator, simulation software is available which translates a treatment plan into a beam delivery sequence. Unfortunately, this simulation only models the accelerator using a simplified approach. For example, the simulation assumes a fixed pause of 5 seconds between two acceleration cycles, when in reality this pause has both an energy-dependent and a random aspect. Also, the simulation assumes that the nominal beam intensity is available for treatment, when effectively an intensity of 50 to 95% of this value is realistically used. In this chapter, the existing simulation software is replaced by a more refined version, taking into account various effects which influence the timing of the beam delivery.

In the following sections, the timing properties of the HICAT accelerator are presented. Based on this information, the model base data to be used for the simulation is extracted from various sources. Furthermore, the fundamentals and implementation of the beam delivery sequence simulation software are described.

Finally, to check the validity of the simulation, the simulation results are compared to machine records of a treatment plan which is regularly used for quality assurance purposes. Additionally, verification measurements are carried out using dose measurements in a moving water phantom.

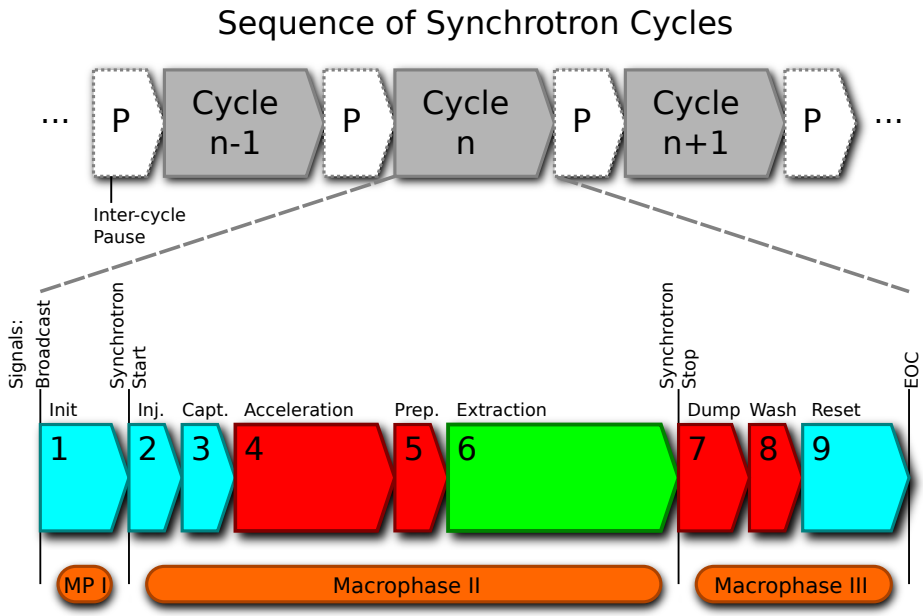

Figure 20: The accelerator cycle: Consisting of three Macrophases (initialization, acceleration and reset), it is repeated until the treatment plan has been fully irradiated. Phases with fixed duration are shown in cyan, energy dependent phases in red, the non-deterministic extraction phase in green.

4.2 CREATION OF THE ACCELERATOR SIMULATION

4.2.1 *Timing Characteristics of the HICAT Accelerator*

Patient treatments at HIT are performed using active raster scanning with fixed particle energy. To cover the full treatment volume, the energy of the particle beam is changed between each pass of the raster scan. Currently, the beam energy can not be changed during the extraction of a continuous beam; instead, the HICAT accelerator switches the energy between two extractions. With this pulsed mode, approximately five seconds of beam extraction time are available, with approximately five seconds between two extractions.

Irradiations are controlled by the therapy control system (TCS), which controls the beam position and dose monitoring during treatment. The TCS requests the required beam energy and intensity from the accelerator control system (ACS) which directs the accelerator, consisting of the sources, linear accelerator, synchrotron and other components, to provide the correct beam to the treatment room.

For each beam request from the TCS, the ACS follows a programmed sequence of events, called a synchrotron cycle, which is presented in Fig. 20. In each cycle, the synchrotron is prepared for ion beam injection, the particle beam is accelerated to the requested energy and extracted out of the synchrotron. Finally, any remaining particles are removed and the accelerator is reset to perform the next cycle. In a typical patient case, 50 to 100 cycles are necessary to irradiate the full volume.

Regardless of the requested particle type, energy or intensity, the accelerator cycle always consists of three distinct phases (called *macrophases*), which are followed by an inter-cycle pause. To understand the behavior and timing of the

HICAT accelerator, it is necessary to understand the timing properties of each of these phases and the pause.

Each macrophase is initiated by an event signal from the ACS to all devices of the accelerator. This signal both synchronizes all devices and selects the correct programmed sequence to accelerate the beam to the requested energy. Each macrophase is further divided into one or more *miniphases*, during which certain functional steps are performed. Miniphases are not initiated by event signals, their starting time is calculated via an offset from the event signal and they are mainly used for analysis and clarification.

MACROPHASE I (INITIALIZATION): This phase is initiated by the broadcast event signal (`evt_broadcast`) and prepares the synchrotron for injection of the particle beam, mainly by increasing the magnetic field of the synchrotron dipole magnets to the necessary field strength.

This macrophase consists only of one miniphase, *Initialisation* (`INIT`). Because the injection energy is the same for all requested particle energies and intensities, the duration of this macrophase is always the same. In Fig. 20, miniphases with a fixed duration are represented in cyan.

MACROPHASE II (BEAM ACCELERATION AND EXTRACTION): This phase is initiated via the synchrotron start event signal (`evt_RTBS_Start`). In this phase, the beam is injected into the synchrotron, bunched and prepared for acceleration, accelerated to the desired energy, prepared for extraction and finally extracted for treatment.

In terms of timing, the first two miniphases, *Injection* (`INJ`) and *Capture* (`CAPT`), are similar to the *Initialisation* miniphase. Because they are performed at the same injection energy regardless of the requested particle energy, these two miniphases are also of fixed duration. In Fig. 20, they are represented in cyan.

The *Acceleration* (`ACC`) miniphase is different in its timing behavior. During acceleration, the particle energy is increased gradually using a resonant radio-frequency cavity. Synchronously, the field strength of the dipole magnets in the synchrotron is increased to keep the particle beam from moving outwards. In order to reach higher energies, the radio-frequency cavities are accelerating the particle beam for a longer time.

At higher energies, the particle beam has a higher magnetic rigidity $R = B\rho$, that is, a higher magnetic field strength B is necessary to achieve the same bending radius ρ. This rigidity also affects the *Preparation* miniphase (`PREP`) in which the beam is prepared for extraction using sextupole magnets. A particle beam at higher particle energies takes longer to be prepared for extraction.

Hence, both the durations of the *Acceleration* and *Preparation* miniphase are energy-dependent. In Fig. 20, miniphases with an energy-dependent duration are represented in red.

Finally, during the *Extraction* miniphase (`EXTR`), the ion beam is slowly extracted out of the synchrotron. During extraction, accelerator control is handed over to the TCS, which determines the duration of this phase. Depending on the requirements of the treatment plan, the beam is extracted until either all raster points for the requested energy have been irradiated or until all particles have been extracted out of the synchrotron. The exact duration of this phase is dependent on the treatment plan, the raster points already irradiated in previous synchrotron cycles and the actual beam intensity, as well as possible interlocks,

gating commands or user interactions. Because of the special nature of this miniphase, it is covered in detail later, when the accelerator model is described. In Fig. 20, the *Extraction* miniphase is represented in green.

MACROPHASE III (ACCELERATOR RESET): This phase is initiated via the synchrotron stop event signal (`evt_RTBS_Stop`). During this phase, the remaining particles are removed from the synchrotron and the synchrotron is prepared for the next cycle.

When the TCS has finished irradiating all raster points of the current beam energy or once all particles have been extracted from the synchrotron, control of the synchrotron is returned to the ACS. Then, during the *Dump* microphase (`DUMP`), the remaining beam inside the synchrotron is deflected upwards until it hits a scraper target inside the synchrotron. As in the *Preparation* miniphase, a beam at higher energies is more rigid, therefore the *Dump* microphase takes longer for higher beam energies.

When the beam has been removed, the dipole and quadrupole magnets in the synchrotron are conditioned. During this, the magnetic field is increased up to a defined field strength, higher than the field strength necessary for the highest particle energies. This creates a defined magnetic remanence in the magnetic yokes, necessary for precise beam steering. Finally, the current through the dipole and quadropole magnets is reduced to zero and all accelerator parts are returned to their idle state.

Conditioning is performed during two miniphases, *Wash* (`WASH`) and *Reset* (`RESET`). During *Wash*, the magnetic field strength is increased to the maximum level. Depending on the field strength already reached during acceleration, this miniphase will have different durations and is therefore energy-dependent. During *Reset*, magnetic field strength is returned from the maximum level to zero, regardless of the beam energy. Therefore, the *Reset* phase has the same duration in every accelerator cycle.

Finally, the End-of-Cycle event signal `evt_EOC` is sent to all devices, which prompts them to return to the idle state. Most devices return status information to the ACS as a response.

INTER-CYCLE PAUSE: After each synchrotron cycle, consisting of the three macrophases, the TCS determines if there are parts of the treatment plan left to be irradiated. If so, the TCS sends a new beam request to the ACS, stating the type of particle, energy, focus size and intensity level required by the treatment plan, after which a new cycle is started by sending a broadcast event signal.

During the inter-cycle pause, both the ACS and TCS will report status information to a database, after which the next synchrotron cycle is started. There are no strict timing requirements for this operation and while the whole pause usually only takes 200 to 300 milliseconds, it can take take up to 3 seconds.

While the inter-cycle pause is not energy dependent, the actual duration of this phase is too uncertain to be considered in the fixed time category. Similar to the *Extraction* miniphase, the inter-cycle pause will be covered in detail later.

SUMMARY: The HICAT accelerator is operated in a sequence of synchrotron cycles. During the cycle, some phases are always taking the same time to complete (cyan in Fig. 20), some phases exhibit a deterministic energy dependence (red). The duration of particle extraction, controlled by the TCS, depends on

several factors such as the treatment plan and beam intensity. Finally, the duration of the inter-cycle pause depends on database operations and has therefore a random component.

In the following section, all necessary data to define the duration of each phase is presented. This model base data is later used in the simulation software.

4.2.2 *Determining the Model Base Data*

In order to compile the model base data for the simulation, several sources have been considered. The timing of the accelerator during operation is controlled by the ACS, and detailed information on the duration of each miniphase can be extracted from the control system. Additionally, to get information on the inter-cycle pause duration, the records of an internal ACS database were evaluated.

Furthermore, the two broadcast event signals in the beginning and the end of the synchrotron cycle, `evt_Broadcast` and `evt_E0C`, add a finite pause to each cycle. Not being part of the macrophases or the inter-cycle pause, the duration of this pause was measured using an oscilloscope during patient treatment.

To determine a realistic duration for the *Extraction* miniphase, the duration of each raster point irradiation will later be calculated using the required particle number and the real beam intensity. In this analysis, beam intensities were calculated from irradiation records created during patient therapy, extracted from the TCS database.

4.2.2.1 *Duration of the Synchrotron Cycle Macrophases*

Each device in the HICAT accelerator is controlled by a Device Control Unit (DCU) which, for example, controls the current profile of a dipole magnet or the amplitude and frequency of an accelerating radio-frequency cavity. In each DCU, the sequence of set-point values required for operation is stored in flash memory and is simply recalled when the *Broadcast* signal is received.

All this information can be obtained from the ACS in the form of a large XML file. At $\approx$ 500 MB, this *Flash Dump* contains the operation information for all DCUs of the HICAT accelerator, including the durations of the miniphases, from which the duration of the macrophases can be calculated.

For this analysis, only the data describing the operation of the synchrotron bending magnet power supply (S0MU1) was used. This magnet is relevant in all three macrophases, therefore the data derived from its DCU is reliable throughout the whole cycle.

For each of the 255 available carbon ion energies, there is a separate entry containing the polynomial functions for voltage, current and the duration of each miniphase in the flash dump. Using the self-written program `flashdump2csv.py`, the duration of all miniphases as well as the duration of the macrophases were extracted for each energy step.

Fig. 21a shows the duration of each Macrophase as a function of nominal energy. The solid black line is macrophase I (initialization), the dashed red line shows the energy-dependent duration of the macrophase II (acceleration), the dash-dotted blue line shows the duration of the macrophase III (reset). In this graph, the duration of the extraction miniphase (`EXTR`) is not yet taken into account.

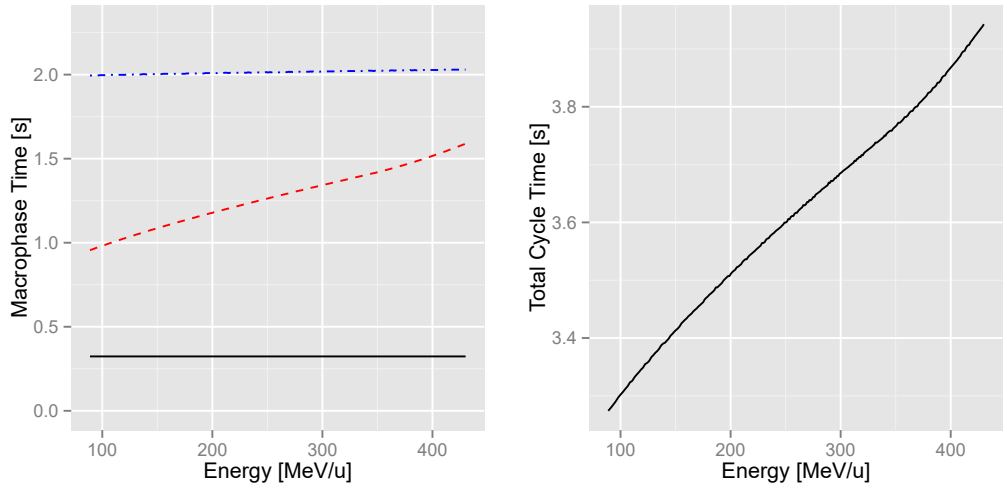

(a) Macrophases I to III

(b) Sum of all Macrophases

Figure 21: Energy-Dependent Duration of the Accelerator Macrophases: Left, from bottom to top: Initialization (black), acceleration without extraction (red) and reset (blue). On the right, the sum of all macrophases is shown.

To test the validity of this analysis, a set of macro phase durations was looked up using the official graphical user interface of the accelerator, *Modi(DVM)*, which matched the results of the analysis. Additionally, the analysis was repeated using old Flash Dump datasets. These were routinely created in the course of prior changes to the accelerator configuration. Based on this information, no deviation of the accelerator timing over the course of this analysis could be found.

In Fig. 21b, the sum of all macrophases is plotted, exhibiting an almost linear relation. Using linear regression, the following approximation was found:

$$T_{\text{Cycle - EXTR}} = \left(3.137 + 0.001828\,\frac{[E]}{\text{MeV/u}}\right)\text{s}. \tag{14}$$

Over the whole energy range, the uncertainty of this approximation is below 0.01 seconds. Therefore, this will be used later in the simulation software instead of a look-up table.

4.2.2.2 *Duration of the Inter-Cycle Pause*

Between two synchrotron cycles, the ACS and TCS performs post-processing and preparation tasks. Amongst other things, status information is saved into a control system database. Only when all tasks are finished, the next synchrotron cycle is initiated. Therefore, depending on the duration of these tasks, the duration of the inter-cycle pause varies.

In order to measure the duration of the pause, the status information saved into the ACS database was used. For each synchrotron cycle, the time stamps of the *Broadcast Start* (`evt_Broadcast`) and *Broadcast Stop* (`evt_EOC`) event signal are available. By calculating the time difference between *Broadcast Stop* and the subsequent *Broadcast Start*, the duration of the inter-cycle pause is easily determined.

From the database, the time stamps of all therapy mode irradiations of 39 weeks in 2012 were extracted from the accelerator. Based on this data, the du-

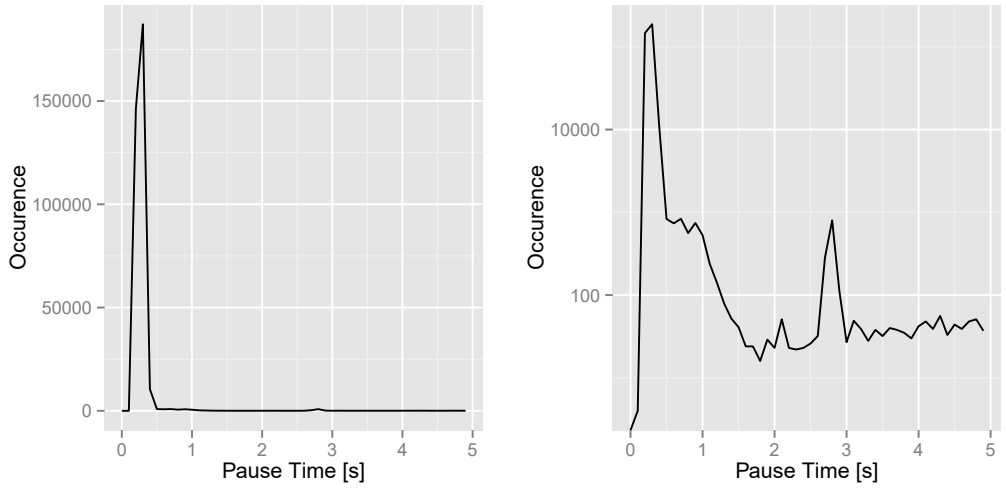

(a) Linear Scale

(b) Logarithmic Scale

Figure 22: Duration of Inter-Cycle Pauses: The majority (95%) of all inter-cycle pauses last 200 to 300 milliseconds. In logarithmic scale, a second peak at 2.7 to 2.8 seconds becomes apparent.

rations of the inter-cycle pause were calculated, using an upper cut-off of five seconds. From this dataset, a total of 350977 inter-cycle pause intervals were evaluated. A histogram of the resulting distribution is shown in Fig. 22.

Out of all inter-cycle pauses, 343911 (98%) lasted for less than 0.5 seconds, with 333434 (95%) attributed into the 0.2 and 0.3 second histogram bins. 2217 (0.6%) of all intervals were longer than two seconds, with an accumulation at 2.6 to 2.8 seconds.

The appearance of the second peak at 2.7 seconds can be explained when looking into the operation principles of the ACS. When the *Broadcast* event signal is sent to all DCUs of the accelerator to start a new synchrotron cycle, each DCU reports back with a status signal and if they need extra time for initialization. If any one of the DCUs does not respond to the *Broadcast* signal, the cycle does not start and a second *Broadcast* signal is sent after 2.5 seconds, precisely the interval seen in the data.

For approximately half of the weeks in the data set, an increased fraction of inter-cycle pause times between 0.5 and 1.0 seconds was found, while for the others, it was completely missing. From the available data, it was not possible to determine the reason for this behavior; the use of special treatment plans or accelerator settings during treatment was ruled out. Because of the minor impact of this effect, it was decided to treat the data of all weeks equally.

In the simulation, the duration of this inter-cycle pause could simply be implemented as a fixed pause of 250 milliseconds. While this is a viable approach, the duration of the simulated pauses is instead determined by calculating a random number which has the same probability density function as the histogram. This way, the random nature of this pause is preserved and included into the simulation, ensuring that all simulated irradiations are different.

4.2.2.3 *Duration of the Broadcast Delay*

During the first tests of the simulation software, the pause between two consecutive synchrotron cycles was found to be 400 milliseconds longer than expected. When no error could be found in the analysis of the synchrotron cycle and inter-cycle pause times, other sources of delay were investigated and found: The broadcast delay and the finite rise time of the beam intensity.

The main reason for the delay is the finite duration of the broadcast signals. When the ACS issues the *Broadcast Start* event signal, the first macrophase of the synchrotron cycle is not immediately started. Instead, it initiates communication between the DCUs and the ACS's *Timing Master* computer, after which the synchrotron cycle is started. Similarly, the *Broadcast Stop* event signal is also a result of communication after the third macrophase. Therefore, the inter-cycle pause also starts with a delay.

MEASURING THE BROADCAST DELAY TIME: To quantify the duration of the broadcast delay, direct measurements of the cycle times were carried out during patient treatment and compared to the model base data.

Each DCU has two output jacks which can be programmed to output a 5 Volt signal for 100 ms when it receives an event signal from the ACS. Using two DCUs and a digital oscilloscope for recording the wave forms, four different event signals were recorded for this analysis, in detail: *Broadcast* (`evt_Broadcast`), *Synchrotron Start* (`evt_RTBS_Start`), *Extraction* (`evt_phase_EXTR`) and *Synchrotron Stop* (`evt_RTBS_Stop`).

To determine the broadcast delay at the start of the synchrotron cycle ($T_{\text{Delay 1}}$), the time difference between the *Broadcast* and *Synchrotron Start* event signals is measured and compared to the expected duration of macrophase-I. The difference between the two is the broadcast delay:

$$T_{\text{MP-I}} + T_{\text{Delay 1}} = t_{\texttt{evt\_RTBS\_Start}} - t_{\texttt{evt\_Broadcast}} \tag{15}$$

To determine the broadcast delay at the end of the synchrotron cycle ($T_{\text{Delay 2}}$), the time difference between the *Synchrotron Stop* and *Broadcast* event signals is measured. This interval is as long as macrophase-III and the inter-cycle pause plus the broadcast delay:

$$T_{\text{MP-III + IC-Pause}} + T_{\text{Delay 2}} = t_{\texttt{evt\_Broadcast}} - t_{\texttt{evt\_RTBS\_Stop}} \tag{16}$$

To double-check the validity of the measurements, the duration of the second macrophase should not differ from the model calculations:

$$T_{\text{MP-II - Extr}} = t_{\texttt{evt\_EXTR}} - t_{\texttt{evt\_RTBS\_Start}} \tag{17}$$

And finally, the duration of the complete cycle and inter-cycle pause without the extraction phase should reflect both delays:

$$T_{\text{Cycle - Extr}} + T_{\text{Delay 1}} + T_{\text{Delay 2}} = t_{\texttt{evt\_EXTR}} - t_{\texttt{evt\_RTBS\_Stop}} \tag{18}$$

To acquire the data for this analysis, six data sets of approximately 30 seconds were recorded during regular patient therapy. In Fig. 23, one data set is portrayed, with the *Broadcast* signal in blue, *Synchrotron Start* in purple, start of the *Extraction* in green and *Synchrotron Stop* in yellow. In total, 24 full cycles were recorded at various carbon ion energies.

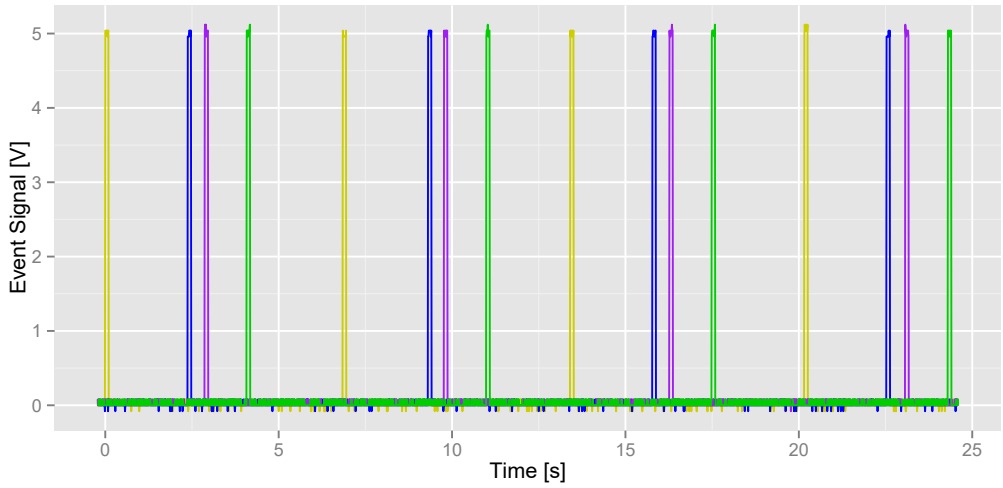

Figure 23: Broadcast Delay Investigation: Measurement of the accelerator timing during treatment, beginning with *Synchrotron Stop* (Yellow), then *Broadcast* (Blue), *Synchrotron Start* (Purple) and start of *Extraction* (Green). The measured times are compared to the model base data.

For each measured cycle, the energy-dependent duration of the macrophases was calculated using the data from the previous analysis, the inter-cycle pause was assumed to be 250 milliseconds long. It was then subtracted from the intervals measured with the oscilloscope. Table 2 shows the results of this analysis.

Interval	Difference/s
$T_{\text{MP-I}}$	$+0.19 \pm 0.03$
$T_{\text{MP-III + IC-Pause}}$	$+0.17 \pm 0.06$
$T_{\text{MP-II - Extr}}$	-0.01 ± 0.01
$T_{\text{Cycle - Extr}}$	$+0.35 \pm 0.07$

Table 2: Difference between simulated and measured synchrotron cycle times.

Based on this data, the duration of the broadcast delay in the beginning of the synchrotron cycle is $T_{\text{Delay 1}} = 190 \pm 30$ milliseconds, the duration of the broadcast delay at the end of the cycle is $T_{\text{Delay 2}} = 170 \pm 60$ milliseconds. This is compatible with the total cycle time ($T_{\text{Cycle - Extr}}$) being 350 ± 70 milliseconds longer than expected. In addition, macrophase-II is, within the measured uncertainty, as long as expected. In the simulation software, the broadcast delay duration of 350 ms is added to the pause time.

FINITE INTENSITY RISE TIME: Another delay has been identified when looking at the exact shape of the beam intensity profile. When the beam is extracted from the synchrotron using knock-out extraction, it does not immediately reach the full intensity (Hoffmann et al. (2008); Ondreka and Weinrich (2008)). Instead, it takes a certain amount of time for the first raster point to be irradiated. In this analysis, the remaining 50 ms are attributed to this effect.

The sum of both effects, the omission of the broadcast delay times and the finite rise time of the beam intensity, fully explain the 400 ms additional pause time. This extra pause time was implemented as a fixed pause time into the sim-

ulation. The effect of this correction is presented in the appendix, section A.2.1, page 132.

4.2.2.4 *Determination of the Beam Intensity using Irradiation Records*

The duration of the *Extraction* phase will be calculated based on the treatment plan using a procedure which will be described in detail later. In principle, the simulation calculates the time Δt_i which is needed to irradiate each raster point i by dividing the required number of particles N_i by the beam intensity I:

$$\Delta t_i = \frac{N_i}{I}. \tag{19}$$

For this calculation, the actual intensity of the therapy beam must be known. Unfortunatly, the nominal intensity and the actual intensity differ by as much as 50%, which must be accounted for in the simulation. In this analysis, the ratio between the actual beam intensity I and the nominal beam intensity $I_{Nominal}$ is described by the *Extraction Efficiency* η:

$$\eta = \frac{I}{I_{Nominal}}. \tag{20}$$

During each patient treatment, the TCS stores the irradiation records. The records contain the number of irradiated particles N_i and the time at which each raster point was irradiated, t_i, as well as the nominal beam intensity $I_{Nominal}$. From this information, the actual beam intensity I_i for each raster point can be calculated:

$$I_i = \frac{N_i}{\Delta t_i} = \frac{N_i}{t_{i+1} - t_i}, \tag{21}$$

with

$$\eta_i = \frac{N_i}{\Delta t_i \cdot I_{Nominal}}. \tag{22}$$

For each patient treatment plan, approximately 50,000 to 100,000 raster points are irradiated with various intensity and energy settings. Each month, over 1000 treatments are performed. This is sufficient data to derive reliable information on the actual intensity and the stability of the beam intensity over time.

DATA SETS USED FOR GENERATING THE SIMULATION MODEL BASE DATA: To create the model base data set to be used in the simulation, two sets of irradiation records were used:

- All patient irradiations using carbon ions from 2012-07-02 to 2012-07-31

and

- All patient irradiations using carbon ions from 2013-06-01 to 2012-07-14.

The two time periods were deliberately chosen because of a change in the particle extraction system. In early 2013, the HICAT accelerator's knock-out extraction system was improved by introducing a feed-back intensity control system as described by Schömers (2013); Schömers et al. (2013). This system provides a more stable extraction and higher beam intensities.

In the irradiation records from 2012, the old extraction system is still in use; in the record from 2013, all irradiations are already performed with the new extraction system. Using both data sets, the simulation capability in both the old and the new accelerator setup is explored.

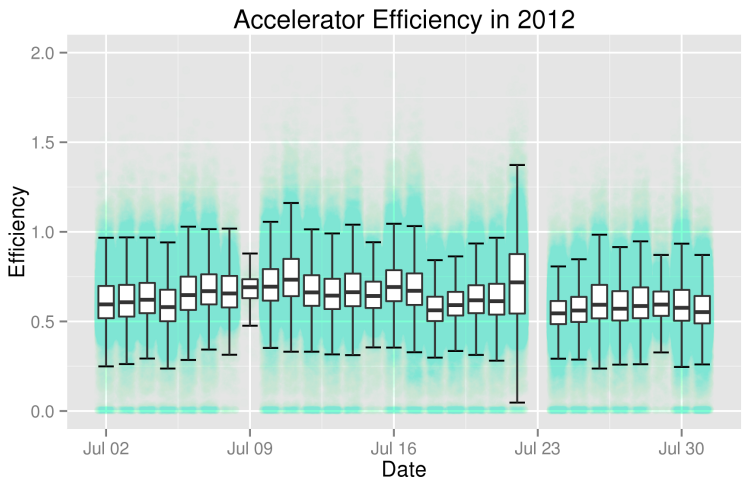

Figure 24: Deviation of Efficiencies in July 2012.

MEDIAN DAILY INTENSITY IN 2012: Using the data set from 2012, the extraction efficiency η was calculated for each irradiated raster point in patient therapy mode. In Fig. 24, the whole data set is shown, grouped by the irradiation date.

As a quick reference: The center line of the box plot marks the median value of the distribution. The edges of the box mark the first and third quantile, therefore, the box covers 50% of the data points. The whiskers are added at a distance of 1.5 inter-quartile ranges (IQR) from the box edges; in a gaussian distribution, this is equal to $2,7\sigma$ or approximately $99,3\%$ of all data. In addition, a transparent scatterplot in the background of the plot gives a graphical representation of the outlying points.

From the plot, the overall reduced intensity can be derived: During the period, the median extraction efficiency η is between 55% to 75%. In addition, the median extraction efficiency η can be seen to change from day to day.

The reduction of beam intensity is done mainly as a safety measure. During extraction, the beam intensity is not completely constant and sudden increases are expected. When the beam intensity increases during therapy, this is detected by the TCS, and if it exceeds a safety threshold, the treatment is aborted. To keep the rate of interlocks low, the total beam intensity was reduced accordingly.

The change in extraction efficiency can also be explained; in 2012, the HICAT accelerator still worked without active feedback knock-out extraction, where the beam intensity is directly proportional to the number of particles in the synchrotron and therefore directly dependent on the particle number extracted from the ion sources and injected into the synchrotron. The beam intensity from the ion sources fluctuates slowly and their extraction current was adjusted daily.

INTENSITY LEVEL DEPENDENCY IN 2012 DATA: To accurately describe the accelerator in the simulation, it is crucial to know if the variation in extraction efficiency η is uniform across all beam intensities and particle energies or not. If it is independent, a single value is sufficient to describe the actual beam intensity, else, a factor based on the nominal beam intensity or beam energy must be introduced.

In Fig. 25, the extraction efficiency is presented as a function of the nominal intensity step ($\eta(I_{Nominal})$) for three different therapy days. Already in the first

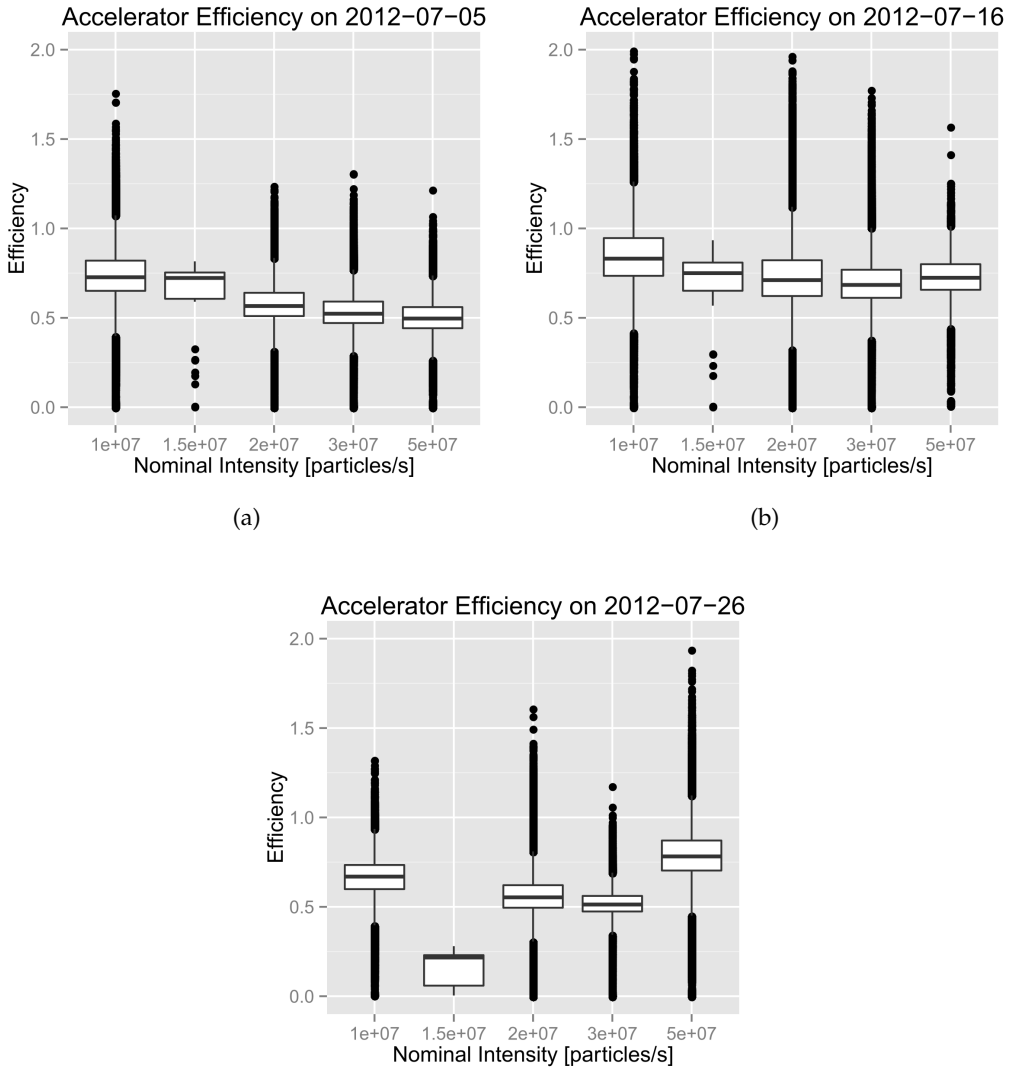

Figure 25: Extraction Efficiency $\eta(I_{Nominal})$ as a function of nominal beam intensity: For three days in July 2012, η is plotted as a function of nominal beam intensity, showing different and independent extraction efficiencies for each nominal beam intensity.

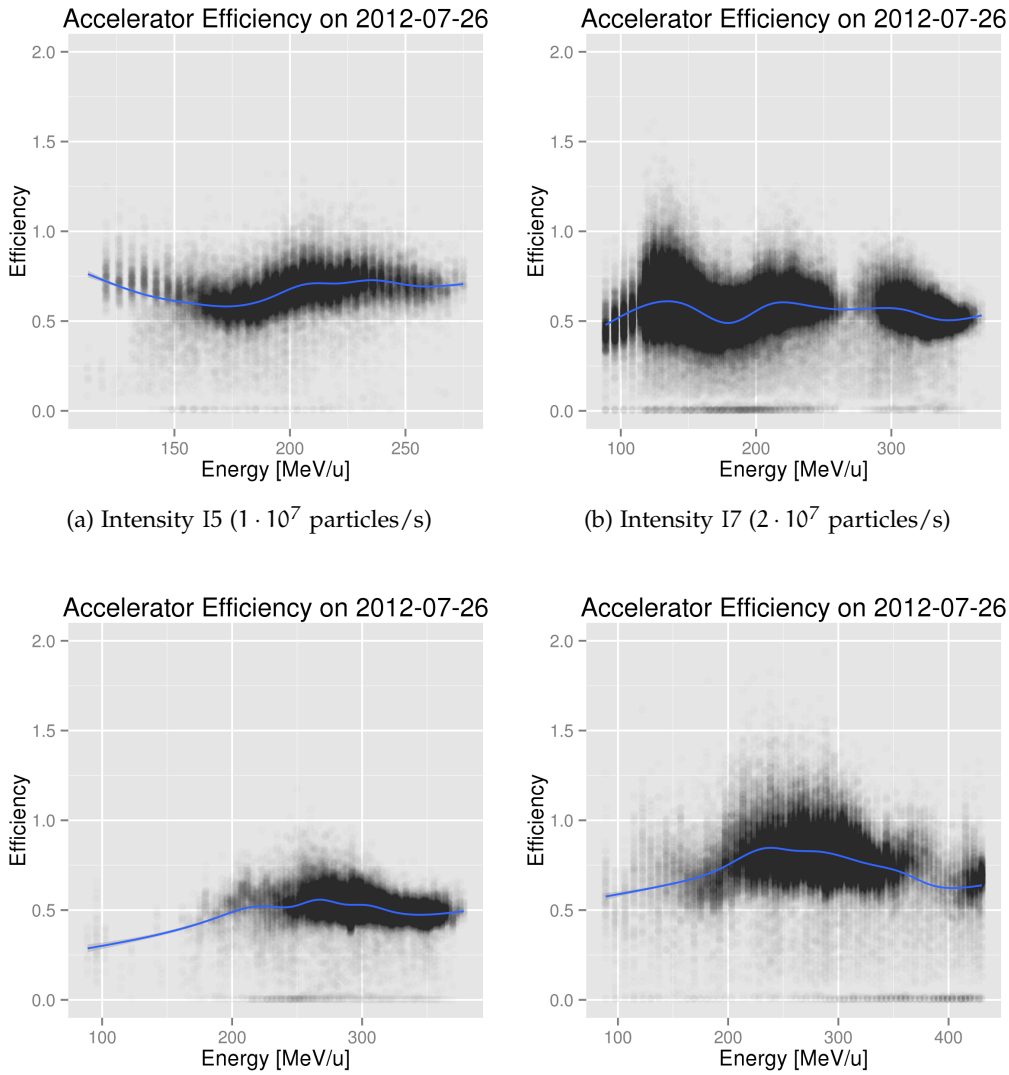

(a) Intensity I5 ($1 \cdot 10^7$ particles/s)

(b) Intensity I7 ($2 \cdot 10^7$ particles/s)

(c) Intensity I8 ($3 \cdot 10^7$ particles/s)

(d) Intensity I9 ($5 \cdot 10^7$ particles/s)

Figure 26: Extraction Efficiency $\eta(E)$ as a function of particle energy for individual intensity levels: The extracted beam intensity is mostly independent from particle energy.

plot, Fig. 25 (a), a significant difference between the η values between each intensity step can be found. Furthermore, the values change independently for each intensity step on different days.

PARTICLE ENERGY DEPENDENCY IN 2012 DATA: Having established a dependence on the nominal beam intensity, it is necessary to investigate a dependence on particle energy. In Fig. 26, extraction efficiency values of a single day have been separated by the nominal beam intensity and shown as a function of particle energy ($\eta(E)$). The trending line was added to the scatter plot to visualize the mean value. While there are fluctuations of η as a function of energy, no energy-dependent trend can be derived from the data.

In the accelerator model, the actual beam intensity will be accounted for by calculating an "intensity of the day" for each of the nominal intensity levels, but independent of the beam energy. This reflects the procedure of fine-tuning the

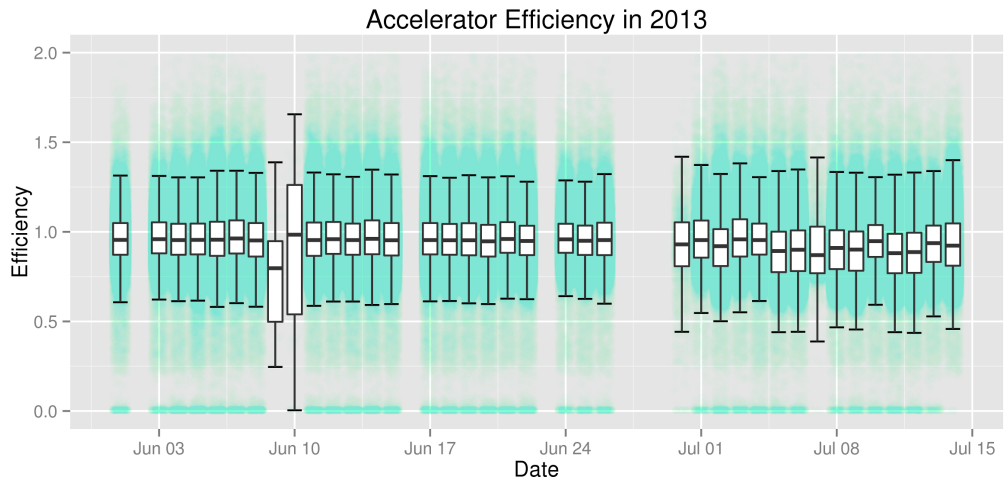

Figure 27: Deviation of Efficiencies in June and July 2013. Note the higher Efficiency η and smaller fluctuations due to the feed-back extraction. The gap end of June was due to a scheduled accelerator shutdown. On June 9 and 10, there were no regular patient treatments, only test-irradiations in patient mode.

beam intensity, which is performed daily by the accelerator staff. As the source output is slowly changing, it is necessary to adjust the injection intensity to keep the intensity at the right level, usually between 50 and 80%. As seen in the data set, this is done independently for each beam intensity, usually before patient treatment.

MEDIAN DAILY INTENSITY IN 2013: As for the 2012 data set, the extraction efficiency η was calculated for each raster point in the 2013 data set. In Fig. 27, the results are presented for the overall extraction efficiency.

In comparison to Fig. 24, it is apparent that the median beam intensity has increased, with η between 85% and 100%. The median daily value of η is still fluctuating, albeit with a reduced day-to-day variation.

This result is expected and a direct result of the introduction of the active intensity feedback system. This system controls the rate at which the particles are extracted, which reduces the fluctuation of the beam intensity. With less fluctuation, the intensity can be increased without the risk of causing interlocks during therapy.

INTENSITY LEVEL DEPENDENCY IN 2013 DATA: In Fig. 28, the extraction efficiency η is shown for two different dates as a function of the nominal beam intensity. On both dates, the values for η are almost the same for the same nominal intensity step. On both dates, the median extraction efficiency of the intensity steps I5, I7 and I8 (1.0, 2.0 and $3.0 \cdot 10^7$ particles/s nominal intensity) is close to 95%. For intensity step I9 ($5.0 \cdot 10^7$ particles/s), the median extraction efficiency is close to 75%

Note that there was a complete shutdown of the accelerator between the two dates, in which parts of the accelerator were revised and the sources completely cooled down and re-calibrated.

Reducing the beam intensity for the highest intensity level is deliberately done due to a limited number of particles in the accelerator. The synchrotron, when fully filled with particles, does not contain enough particles to sustain a beam

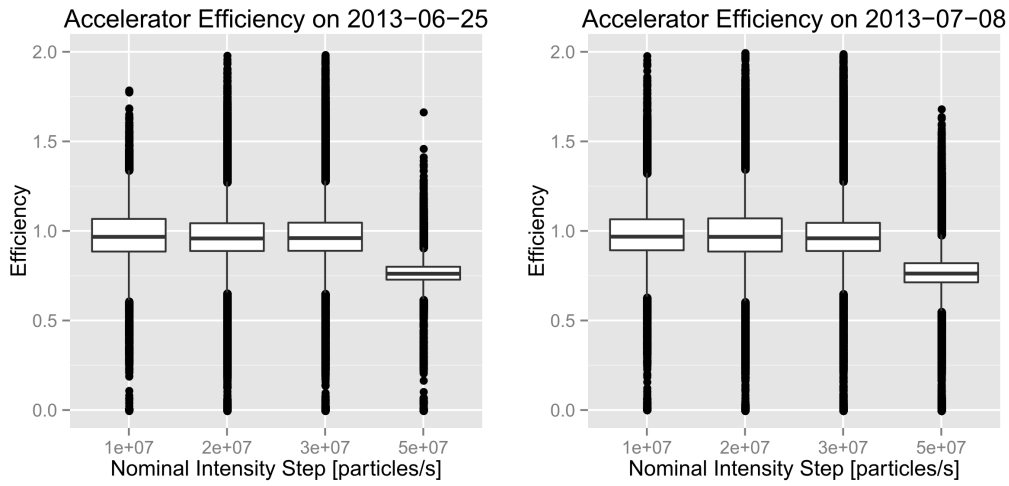

(a) (b)

Figure 28: Extraction Efficiencies ($\eta(I_{Nominal})$) as a Function of Nominal Intensity: After the installation of the intensity feedback system, the beam intensity is both higher and more stable. The highest intensity level is deliberately throttled to 80% of its nominal intensity.

extraction for five seconds at this intensity level. When the synchrotron runs out of particles this triggers an interlock in the TCS, delaying patient treatment. Hence, the intensity is reduced to approximately 80%.

PARTICLE ENERGY DEPENDENCY IN 2013 DATA: In Fig. 29, the extraction efficiency is shown as a function of particle energy, $\eta(E)$. Because all data sets for the lower intensity levels I5 to I8 (1.0 to $3.0 \cdot 10^7$ particles/s) are similar in this plot, they are shown in the same window (Fig. 29 (a)). The data for intensity level I9 ($5.0 \cdot 10^7$ particles/s) is shown seperately (Fig. 29 (b)). Again, a blue regression line indicates the mean η.

Apart from the low energy portion, the mean efficiency $\eta(E)$ is constant over the whole energy range in every beam intensity setting. In the lower energy range, a reduction of intensity is observed. This is due to overflow effects in the ionization chambers at very low energies. To prevent interlocks due to this, the intensity is lowered to 50% of the nominal value at energy step E1 (88.83 MeV/u) and linearly increased to 100% at E25 (136.92 MeV/u), at which the peak is in approximately 4 centimeters depth. Hence, this reduction is only noticeable in very shallow targets.

PROPERTIES OF THE EXTRACTION EFFICIENCY In both the 2012 and 2013 data sets, the extraction efficiency η is subject to fluctuation. Mainly random, the intensity varies from one raster point to the next. In addition, the median value of η varies with time and as a function of the nominal intensity. In addition, in the 2013 data, a reduction of η at lower particle energies is introduced.

In this analysis, a median "intensity of the day" is assumed. In this assumption, the random fluctuations in intensity between raster points cancel each other out, instead, all raster points are treated as if they are irradiated with the same median intensity. The median intensity is assumed to be independent for each intensity level, stable during one simulation run and changing for the next.

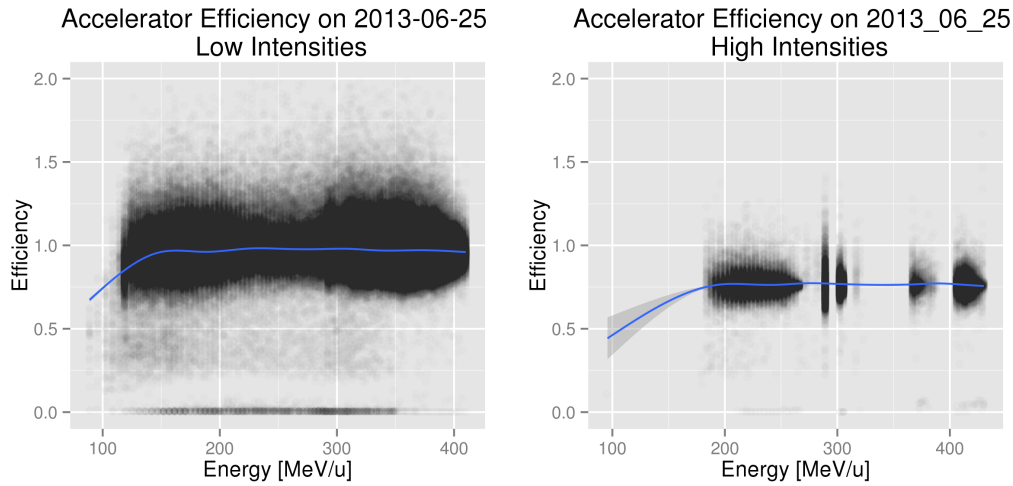

(a) Low Intensity $< 5 \cdot 10^7$ particles/s

(b) High Intensity $5 \cdot 10^7$ particles/s

Figure 29: Accelerator Efficiencies $\eta(E)$ as a function of energy for both low and high intensity levels. The fluctuations of the mean intensity are reduced. For low energies, the extraction efficiency is reduced to prevent an overflow in the ionization chamber.

The dependence on energy is not taken into account for this simulation. In the 2012 data set, the energy dependence is mostly random and is assumed to cancel out. In the 2013 data set, almost no energy-dependence is seen, apart from a deliberate throttling in the lowest energies. This is only relevant for a small fraction of patient plans and none of the test plans used in this thesis use relevant low energies.

4.2.2.5 *Subsampling of the Intensity Base Data*

The extracted beam intensity not only fluctuates from day to day; as can be seen from the scattered values in Fig. 29, the intensity even fluctuates when using the intensity feedback system to stabilize the beam. This fluctuation of the beam intensity on a much smaller time scale, most prominently due to a 150 Hz oscillation, alters the beam intensity from one raster point to the next.

To take this into account in the simulation, there are two possible approaches: Either, an individual extraction efficiency η_i is assigned to each irradiated raster point i. Or, the fluctuations are assumed to cancel each other out and a single median extraction efficiency η is assigned to all raster points. In this analysis, the latter option was chosen, with a single value for η for each intensity level.

For a typical patient treatment plan, the number of irradiated raster points is of the order of $\mathcal{O}\left(10^4\right)$. To calculate the median extraction efficiency, a similar number of raster points was sampled from the data set.

For the use in the simulation, all data was split up based on the irradiation day and nominal intensity. For each data set, the individual extraction efficiency values η_i were calculated for each raster point. Using this, $10,000$ η values were randomly selected from the ensemble and the median value $\langle\eta\rangle_{I_{\text{Nominal}},\text{Day}}$ of this sample was calculated. For each day and intensity step, 100 different samples were created.

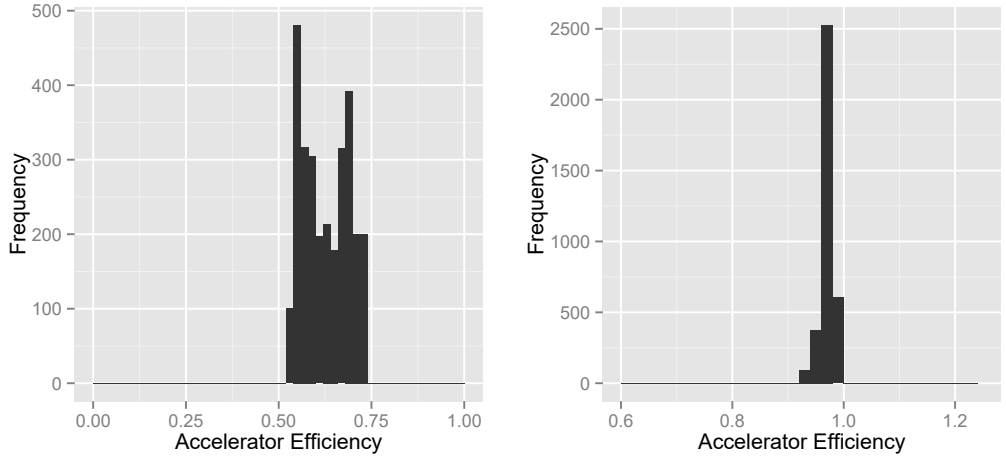

(a) I7 ($2.0 \cdot 10^7$ particles/s), 2012 data (b) I7 ($2.0 \cdot 10^7$ particles/s), 2013 data

Figure 30: Averaged Extraction Efficiencies: By randomly sampling 10,000 raster points, a median extraction efficiency was calculated. This was repeated 100 times for each day and nominal intensity level. The histograms are used to determine a median "intensity of the day" for the simulation.

In Fig. 30, the result of this averaging process is shown for intensity step I7 ($2.0 \cdot 10^7$ particles/s). Based on these histograms, the median intensity of the day is calculated for the simulations.

4.2.3 *Simulation Principles*

In order to calculate the irradiation time for each raster point of a treatment plan, the simulation software uses a simplified model of the accelerator which is described in this section.

Instead of simulating the whole accelerator, a simplified phenomenological model is used, which is summarized in Fig. 31. During operation, the accelerator can either emit a particle beam (*Beam Status "On"*) or not (*Beam Status "Off"*). While the beam status is "On", the raster points of a treatment plan are irradiated sequentially (the *Rasterpoint Index* i increases), at the same time, the number of particles remaining inside the synchrotron ring decreases (*Ring Fill Status*).

When the *Ring Fill Status* drops to 0%, no more particles can be extracted and the irradiation of raster points is halted (*Beam Status "Off"*). This also happens when the last raster point of a certain energy is irradiated and a different energy is requested. In both cases, a pause results, in which the synchrotron ring is "refilled" to 100% and the irradiation is resumed.

Using this model, the simulation software calculates a duration for each task of the accelerator. The time in between two extractions of the particle beam is designated T_{Pause} and depends on the particle energy and a random pause. The time needed to irradiate an individual raster point is designated $T_{Rasterpoint}$; it is dependent on the beam intensity and the number of particles prescribed to this raster point. By adding up the time needed to irradiate each individual raster point and the pauses in between irradiations, the irradiation time for each raster point is determined.

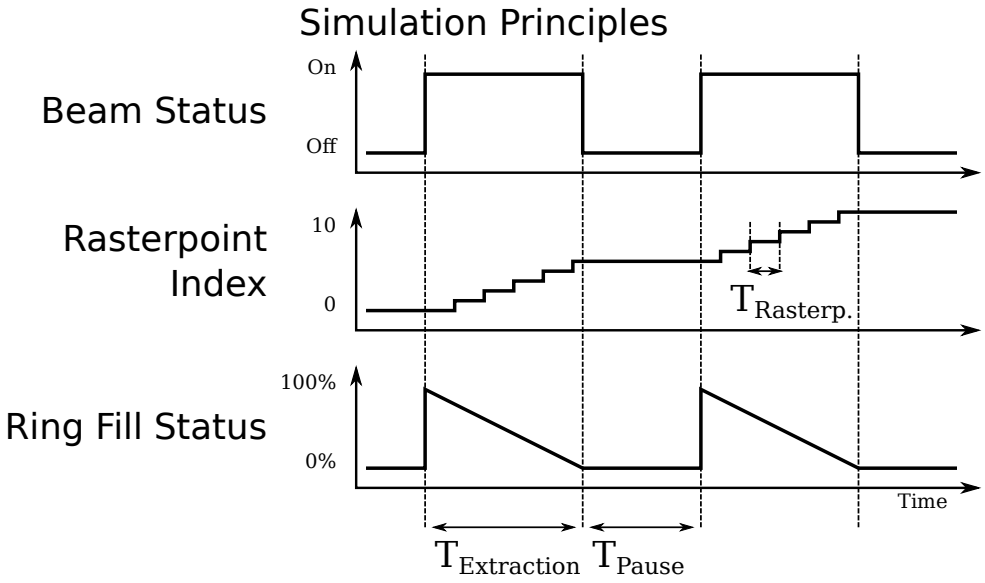

Figure 31: Simplified Accelerator Model: In the phenomenological model of the HICAT accelerator, the beam is in the "on" or "off" state. During "Beam on", raster points are irradiated while the number of particles in the synchrotron "Ring" decreases. Once all particles are extracted, the beam status switches to "off" until the synchrotron is refilled and the next irradiation can start.

4.2.3.1 *Calculation of the Inter-Cycle Pause*

Based on the duration of the synchrotron cycle, the inter-cycle pause and the broadcast delay, the pause time between two extractions can be calculated. In the previous section, the synchrotron cycle time was found to be energy dependent, the inter-cycle pause has a random component and the broadcast delay can be treated as fixed:

$$T_{\text{Pause}}\,(\text{Energy}) = T_{\text{Cycle}}\,(\text{Energy}) + T_{\text{Inter-Cycle}}\,(\text{Random}) + T_{\text{Broadcast}}, \qquad (23)$$

with $T_{\text{Broadcast}} = 400$ ms.

Calculating the deterministic synchrotron cycle time $T_{\text{Cycle}}\,(E)$ is achieved using equation 14 (page 50). The energy required in this formula is the nominal particle energy from the treatment plan.

The random duration of the inter-cycle pause $T_{\text{Inter-Cycle}}\,(\text{Random})$ is calculated using the *CERN ROOT* software package. Using *ROOT*'s `TH1` histogram class, random numbers can be created which follow the probability density function of the distribution entered into the histogram (Brun and Rademakers (1997)). To calculate the random duration of the inter-cycle pause, the contents of Fig. 22 were entered into a *ROOT* histogram. Using the `GetRandom()` function, a new random duration of the inter-cycle pause is calculated for each simulated pause.

4.2.3.2 *Calculation of the Raster Point Irradiation Time*

Calculating the irradiation time for each raster point is done by dividing the assigned number of particles N_i by the beam intensity I_i:

$$T_{\text{Rasterpoint},i} = \frac{N_i}{I_i}. \qquad (24)$$

While the number of particles is provided by the treatment plan, the beam intensity must be computed.

The HICAT accelerator provides several intensity levels which can be used for treatment. Selecting the appropriate beam intensity is part of the *process data generation* routine (*Prozessdatengenerierung*), which converts the treatment plan into a format which can be used by the TCS for irradiation.

During irradiation, the position of each raster point is measured by the TCS. If the position can not determined, an interlock stops the irradiation. To avoid the failure of a position measurement, the beam intensity is reduced until all raster points can be reliably measured. Due to the design of the accelerator, all raster points with the same particle energy have to be irradiated using the same beam intensity. Hence, the beam intensity for all raster points of a certain energy is determined by the raster point with the smallest number of particles, and the beam intensity is selected by the process data generation to ensure a certain irradiation time for each raster point.

SIEMENS provides the program code to calculate the process data generation via the software suite `XML-PT`. Using this software, the *nominal* beam intensities $I_{i,\mathrm{Nominal}}$ are calculated for the simulation.

To determine the actual beam intensity, the nominal intensities are then multiplied with the extraction efficiencies η. In the simulation, one value of η is calculated for each intensity level in the beginning of the calculation and used for the whole treatment plan.

Similar to the calculation of the random inter-cycle pause, the values for η are calculated using *CERN ROOT*'s `TH1` histograms, which are populated using the averaged extraction efficiency values (see Fig. 30). By choosing the 2012 or 2013 model base data, the same simulation software can be used to simulate to simulate the accelerator with or without the intensity feedback system.

By adding the irradiation times $T_{\mathrm{Rasterpoint},i}$ for each raster point, the time at which each raster point is irradiated can be calculated. In this model, all raster points of a certain energy are irradiated sequentially, after which the accelerator proceeds to the next energy with a delay of T_{Pause}.

4.2.3.3 *Limited Extraction Time*

Because of the limited number of particles in the accelerator, the extraction of particles is stopped after $T_{\mathrm{Extraction}}$, which is 5 seconds. After this time, a new beam has to be accelerated before the irradiation can be continued.

If the irradiation of all raster points of a certain particle energy takes less time than $T_{\mathrm{Extraction}}$, all raster points are irradiated with one fill of the accelerator. The accelerator then proceeds with the irradiation of the next energy, which starts after a delay of T_{Pause}. If the irradiation takes more time, raster points are irradiated until $T_{\mathrm{Extraction}}$ is reached. Then, the irradiation is halted, a new particle beam is accelerated to the same energy and the irradiation continues from the last irradiated raster point. This behavior is also shown in Fig. 31.

In the simulation, this is implemented by adding a pause of length T_{Pause} when the cumulative irradiation time exceeds $T_{\mathrm{Extraction}}$.

4.2.3.4 *Implementation of the Beam Delivery Sequence Generator*

Instead of creating the simulation software from scratch, the precursor software `makeLmdout`, created by Peter Steidl and Daniel Richter at GSI (Steidl (2011)), was taken as a basis. In its original form, `makeLmdout` was already able to import treatment plans and calculate a beam delivery sequence, although T_{Pause} was fixed

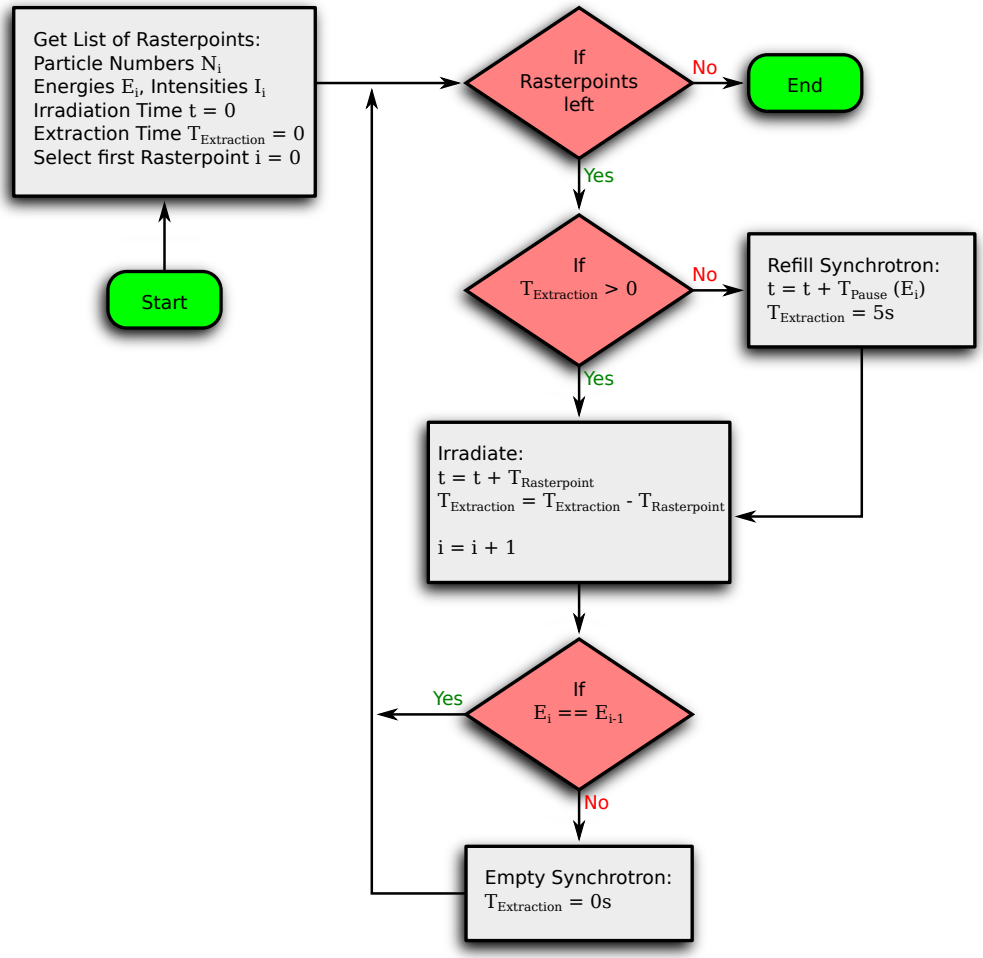

Figure 32: Simulation Flowchart

to 5 seconds and the beam intensity was fixed at 100% of the nominal intensity. For the final version of `makeLmdout`, realistic accelerator timing is factored into the calculations at several points of the simulation.

In Fig. 32, the implementation of the accelerator model into simulation software is presented as a flow chart. Beginning at "Start", the simulation is prepared, which includes retrieving a list of all raster points from the treatment plan and the calculation of energies and beam intensities. After this, a loop is started which calculates the irradiation times for each raster point. When the irradiation times have been calculated for each raster point, the loop ends and all information is written to the hard disk.

PRE-LOOP CALCULATIONS: These steps are only carried out once before the loop calculations start:

- At the start of the simulation, the treatment plan is imported from a DICOM file. From the file, a list of all raster points, the number of particles (N_i) and the beam energies (E_i) are extracted.
- Using the *SIEMENS* software suite `XML-PT`, the process data generation is emulated for the treatment plan. The result is a list of nominal intensities $I_{Nominal,i}$ for each raster point.

- Next, the actual beam intensities are calculated. This is done once for each intensity level to generate an "Intensity of the Day" and uses the random number generation of the averaged extraction efficiency histograms which was previously discussed. For each nominal intensity level, one extraction efficiency $\eta\left(I_{\text{Nominal}}\right)$ is calculated.

  For each raster point of the treatment plan, the actual beam intensity is then calculated by multiplying with the nominal beam intensity:

  $$I_i = I_{\text{Nominal},i} \cdot \eta\left(I_{\text{Nominal},i}\right). \tag{25}$$

  This way, intensities are varied each time the simulation is started, but fixed during one fraction of the treatment.

- Before the calculation loop is started, the variables describing the state of the accelerator are initialized. The clock is set to zero ($t = 0.0$) and the first raster point is selected ($i = 0$). Further, the synchrotron is assumed to be empty in the beginning, which is taken into account by setting the remaining extraction time to zero ($T_{\text{Extraction}} = 0.0$).

LOOP CALCULATIONS: During the loop, the duration of each raster point is calculated in sequential order, starting with the first one. It is then repeated until all raster points have been calculated. When no more raster points are left, the loop ends and the results are written to disk.

During the loop, several yes/no decisions are made, indicated by red diamonds in Fig. 32. Depending on the answer, different routes are taken through the flow chart.

- First, the loop checks if there are *raster points left* for irradiation. If *yes*, the loop is continued. If *no*, the loop is terminated.

- Next, the loop checks if there are particles left in the accelerator by checking if $T_{\text{Extraction}} > 0$. If *yes* (there are particles left), the loop is continued. If *no*, the synchrotron must be *refilled*.

- To *fill the synchrotron*, in the simulation, the time needed to refill the synchrotron is added to the total irradiation time t. This is done by calculating the pause time $T_{\text{Pause}}\left(E_i\right)$ corresponding to the current particle energy E_i. The time is then added to the clock:

  $$t \to t + T_{\text{Pause}}\left(E_i\right). \tag{26}$$

  After that, the extraction time is set to five seconds ($T_{\text{Extraction}} = 5$ s) and the loop is continued.

- To simulate the *irradiation*, the time needed for irradiation of the current raster point $T_{\text{Rasterpoint}}$ is calculated using the number of particles N_i and the beam intensity I_i for this raster point:

  $$T_{\text{Rasterpoint}} = \frac{N_i}{I_i}. \tag{27}$$

  This time is added to the clock t:

  $$t \to t + T_{\text{Rasterpoint}} \tag{28}$$

and also subtracted from the remaining extraction time $T_{Extraction}$:

$$T_{Extraction} \rightarrow T_{Extraction} - T_{Rasterpoint} \tag{29}$$

The clock time t and raster point index is saved and later saved to disk. After that, the next raster point is selected ($i \rightarrow i+1$).

- Finally, the loop checks if the beam energy for the next raster point is the same as for the current, $E_i == E_{i-1}$. If *yes*, the loop is restarted to calculate the next raster point. If *no*, the energy must be changed before the next raster point can be irradiated.

  In the simulation, this is done by setting the remaining extraction time to zero ($T_{Extraction} = 0$). In the next pass of the loop, this is recognized and the synchrotron is refilled. After that, the loop is restarted.

AFTER-LOOP CALCULATIONS When the duration of all raster points has been calculated, the simulation is finished by writing all necessary data to disk. The results are exported as a *LMDOUT* file, which can be used by TRiP-4D and contains the irradiation time for each raster point of the treatment plan. An example of the file format is presented in the appendix, section A.1 on page 131.

Concluding, the simulation now includes the calculation of an "intensity of the day" for each intensity level and calculates a realistic pause time. In the following sections, the performance of the simulation is compared to data and measurements created at the HICAT accelerator.

4.2.4 *Summary: System Analysis and Simulation Implementation*

In this first section, the timing of the HICAT accelerator cycle and beam intensity was analyzed. Each accelerator cycle consists of three energy-dependent macro phases and an inter-cycle pause of random duration. The beam intensity was found to vary from day to day, which has to be considered in a simulation.

Based on this knowledge, model data was determined for use in the simulation. Several phases of the accelerator cycle are deterministic and either have a fixed or energy-dependent duration. The duration of these phases were determined from the control data set used by the accelerator called the *Flash Dump*.

Data on the random inter-cycle pause time was extracted from the accelerator control system (ACS) data base, which automatically logs the beginning and end of each accelerator cycle. The duration of an additional broadcast delay time was measured using a direct measurement on an accelerator device control unit (DCU).

Information on the effective beam intensity was determined from irradiation records created by the therapy control system (TCS). For each irradiated raster point, nominal particle numbers and duration of the irradiation were used to calculate the effective beam intensity. Two data sets were used; the data set from 2012 indicates large variation of effective beam intensity due to intensity variations of the ECR ion-beam sources. In 2013, the introduction of the dynamic intensity control (DIC) system both increased and stabilized the effective beam intensity, reflected in the 2013 data set.

Based on this analysis, a simulation software to calculate realistic beam delivery sequences (BDS) from a treatment plan was implemented. The implementation uses realistic times between consecutive beam extractions based on the

model base data. The beam intensity is determined by sub-sampling the effective beam intensity from the model base data and selecting an *Intensity of the Day*, a set of fixed beam intensities used for the calculation of the entire treatment plan.

With the simulation software implemented, it is now necessary to analyzed the predictive power of the simulation. This is done in the following section.

4.3 VERIFICATION OF THE SIMULATION SOFTWARE

To assess the quality of the simulation software, simulated beam delivery sequences are compared to recorded sequences of a treatment plan. This test plan was irradiated regularly during 2012 and 2013 and the resulting data set is therefore used to evaluate simulations using both the 2012 and 2013 model base data.

Additionally, the predictive power of the simulation is verified experimentally by measuring a dose distribution in a moving water phantom. Using a test plan and a genuine patient treatment plan, the agreement between simulated and measured dose distributions is shown.

4.3.1 *Analysis of Beam Delivery Sequences*

To evaluate the predictive power of the simulation, the results of the simulation are compared retrospectively to irradiation records created in 2012 and 2013. During this time, the same treatment plan was irradiated regularly for quality assurance. By comparing the recorded beam delivery sequences with the simulated sequences, the simulation software and the model base data from the same time period is tested.

In this section, several approaches have been used to compare simulated and recorded data. Two analyses are based on comparing the irradiation times of simulated and recorded treatments. Furthermore, two analyses are based on dose calculations and directly reflect the impact of the sequences on dose distributions.

4.3.1.1 *VX-Vorbestrahlung as Test Treatment Plan*

Instead of creating a dedicated treatment plan for testing the simulation software and irradiating it repeatedly, a treatment plan was found which was already in use for regular quality assurance. The `VX-Vorbestrahlung` treatment plan was introduced to pre-irradiate the pin-point ionization chambers prior to verification measurements. It contains six energy levels and delivers a homogeneous physical dose of 1 Gy using a carbon ion beam. The treatment plan and the positions of the ionization chambers are shown in Fig. 33.

This treatment plan was irradiated repeatedly, typically on three days per week, and at similar times of the day, directly after the patient treatment. Each irradiation was performed by a medical physicist, usually two times in a row before the verification measurements were started. Because it is irradiated in verification mode, this data set is very close to patient treatment conditions, but not part of the training data set used in the creation of the model base data set.

For this analysis, only irradiation records from the same period as the training data set were used: During the 2012 period (July 2nd to July 31st 2012), the

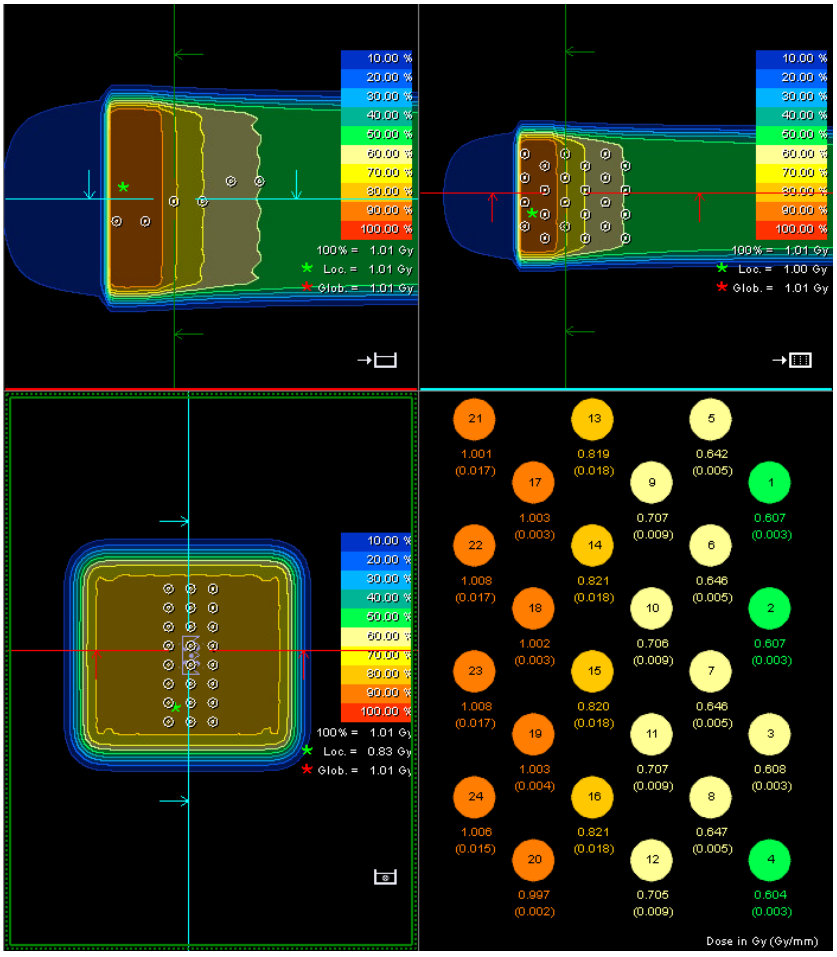

Figure 33: `VX-Vorbestrahlung` treatment plan as displayed in the HIT TPS *syngo® RT Planning*. The dose calculations are performed in a water phantom geometry, the positions of the ionization chambers are indicated by white circled dots. In the lower right, the dose values and gradients are reported. This treatment plan was used for ion chamber warm-up prior to verification measurements.

treatment plan was irradiated 31 times. During the 2013 period (June 1st to July 14th 2013), 26 irradiations were recorded.

In Fig. 34, four examples of recorded and simulated beam delivery sequences are presented for 2012 (top) and 2013 (bottom). On the y-axis, the raster point index indicates the progress of the treatment plan, the x-axis shows the total treatment time.

From these examples, the general ability of the simulation software to model the accelerator can be seen. The overall structure and duration of the irradiation is reflected in the simulated irradiation sequences. Further, the reduction of irradiation time due to the intensity feedback extraction (DIC) installed in 2013 is reflected, with fewer extractions needed to finish the irradiation, leading to a reduction of the total irradiation time of approximately 30 seconds.

4.3.1.2 *Finding a Similarity Measure*

One basic challenge in comparing beam delivery sequences is their random nature. Two irradiations of the same treatment plan under the same conditions will yield different sequences. And the simulation, by design, calculates varying sequences in much the same way. How can two sets of beam delivery sequences be compared to each other when they are intrinsically different?

While there are several standard methods of comparing dose distributions or treatment plan quality (like Γ-index, DVH parameters, dose conformity and dose homogeneity indices, see Chapter 5), there is no established method of comparing beam delivery sequences. Hence, the first step in comparing the sequences is to find a reasonable similarity measure.

One approach is to take the beam delivery sequences and perform a statistical analysis based on the individual raster point irradiation times. This approach has the benefit of not needing too many assumptions and being very universal; on the other hand, differences may be hard to interpret.

Another approach is to calculate a 4D dose distribution from the beam delivery sequences using a defined phantom setup and phantom motion. This approach requires a large set of assumptions, like phantom geometry, motion amplitude and speed, but it allows the evaluation of a dose distribution, and therefore the impact of the differences between simulation and recorded BDS.

Both approaches were evaluated in this analysis. The first two analyses are only taking the timing of raster points into account. Recorded and simulated beam delivery sequences are directly compared using statistical methods. In the latter two analyses, dose distributions are calculated from the recorded and simulated beam delivery sequences. Using two different statistical methods, the dose distributions are compared to each other.

ANALYSIS I: TIMING SPECTRA: In this analysis, the duration of each raster point irradiation, $T_{Rasterpoint}$, and inter-cycle pause, T_{Pause}, is calculated for a set of simulated and recorded beam delivery sequences. Histograms of the durations are evaluated and the spectra of real and simulated irradiations are compared to each other.

This method is sensitive enough to test the overall performance of the simulation and detect implementation errors. For example, the missing broadcast delay in the simulation of the inter-cycle pause was detected in this first analysis. Other analyses were performed to spot more subtle differences.

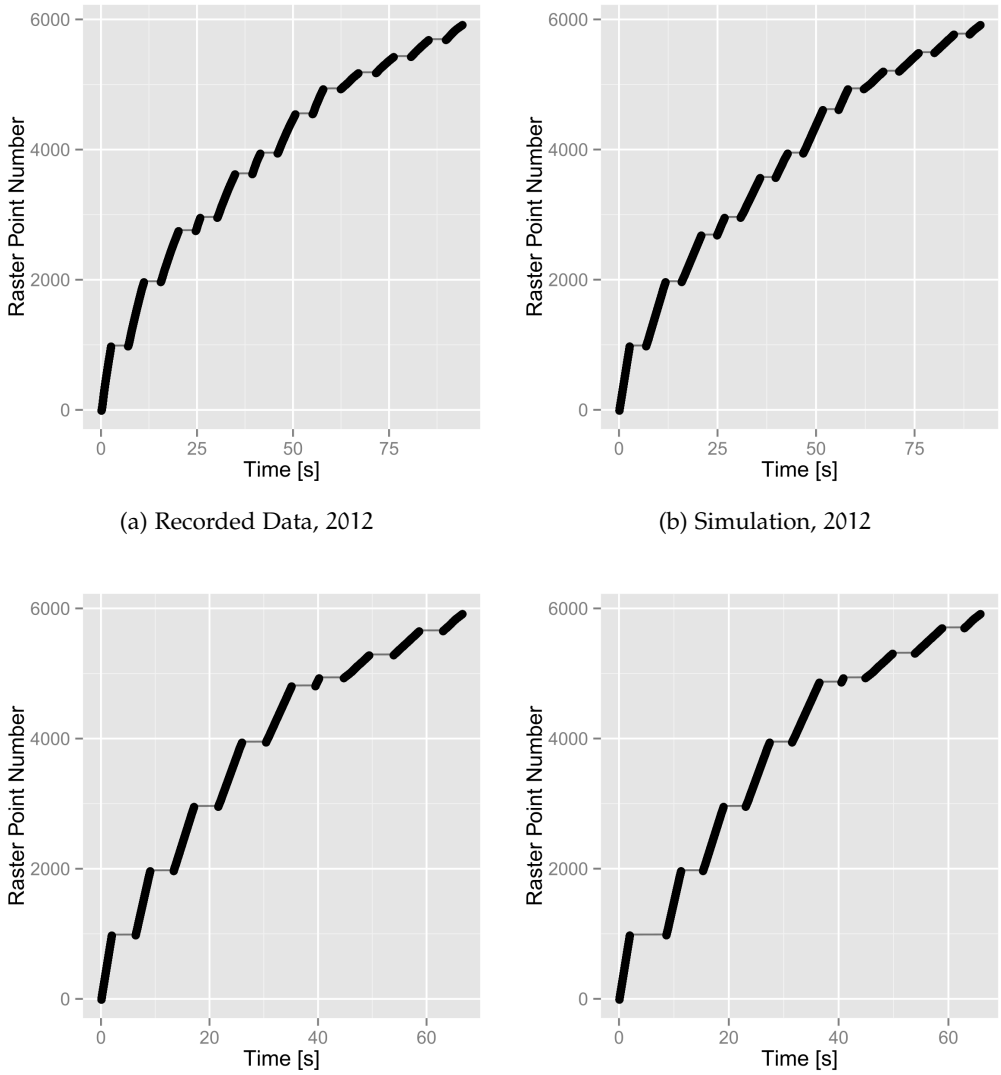

(a) Recorded Data, 2012

(b) Simulation, 2012

(c) Recorded Data, 2013

(d) Simulation, 2013

Figure 34: First Simulation Results: Recorded and simulated beam delivery sequences (BDS) for the `VX-Vorbestrahlung` treatment plan. The irradiations were performed in 2012 (a, b) and 2013 (c, d) and compared to simulations using model base data sets from the same time periods. Irradiated raster points are shown as circles, pauses between two raster points are indicated as horizontal lines.

Despite the random nature of the irradiation, similar irradiation sequences are found in the records and the simulation. Due to the intensity feedback extraction (DIC), the irradiation in 2013 is faster and exhibits less variation.

ANALYSIS II: ROOT-MEAN-SQUARE DEVIATION: In this analysis, the root-mean-square deviation of all raster points irradiation times t_i is calculated for a simulated and a recorded beam delivery sequence. Based on this property, the difference between the simulation and the irradiation is estimated which allows a first interpretation of the simulation quality.

ANALYSIS III: χ^2 CALCULATION: In this analysis, the simulated and recorded beam delivery sequences are used to calculate 4D dose distributions. For the calculations, a phantom geometry, motion amplitude and breathing curve must be assumed, ideally, they are close to the realistic motions of a patient.

Based on the calculated dose distributions, mean doses ($\mu_D(\vec{x})$) and standard deviations ($\sigma_D(\vec{x})$) are calculated for each voxel. From this, χ^2 values can be calculated for each 4D dose distribution. The χ^2 values are used to evaluate the similarity of the dose distribution and therefore the simulation quality.

ANALYSIS IV: VOLUMES OF INTEREST: In this analysis, the same 4D dose distributions are used as in the previous analysis, but instead of calculating the χ^2 values, dose values are evaluated in 24 volumes of interest, based on the detector positions used for treatment plan verification. The dose values calculated from the simulated and the recorded sequences are compared to each other using the Kolmogorov-Smirnov test.

As with the previous analysis, dose values calculated from a good simulation should be similar to the values of recorded beam delivery sequences. Further, this analysis is the basis for further experimental verification.

4.3.1.3 *Analysis I: Timing Spectra*

For this analysis, beam delivery sequences were simulated for the `VX-Vorbestrahlung` treatment plan. As for all following analyses, 200 simulation cycles were calculated using the 2012 model base data set, and 200 simulation cycles were calculated using the 2013 model base data set. All 31 (2012) and 26 (2013) recorded irradiations were evaluated.

From the simulated and the recorded beam delivery sequences, the time difference between two irradiated raster points was calculated:

$$\Delta t_i = t_{i+1} - t_i. \tag{30}$$

The calculated time differences Δt are shown in the histograms in Fig. 35 and Fig. 36. In the first histograms, the time scale is in milliseconds, which is the typical time for the irradiation of a single raster point and can be interpreted as the spectrum of $T_{Rasterpoint}$. In the second set of histograms, the time scale is from 2 to 8 s, which is typical for the the pause between two extractions and can be interpreted as T_{Pause}.

INTERPRETATION OF $T_{RASTERPOINT}$: In Fig. 35, the spectrum of $T_{Rasterpoint}$ is shown for the 2012 (top) and 2013 (bottom) data for the millisecond time scale. In general, there is a good agreement between the measured (left) and simulated (right) spectra. With the peak positions in the same position, this is the first hint that the beam intensity is correctly simulated. This is true for the 2012 data with the lower intensity (and longer irradiation time) and for the 2013 data with higher intensity (and shorter irradiation time).

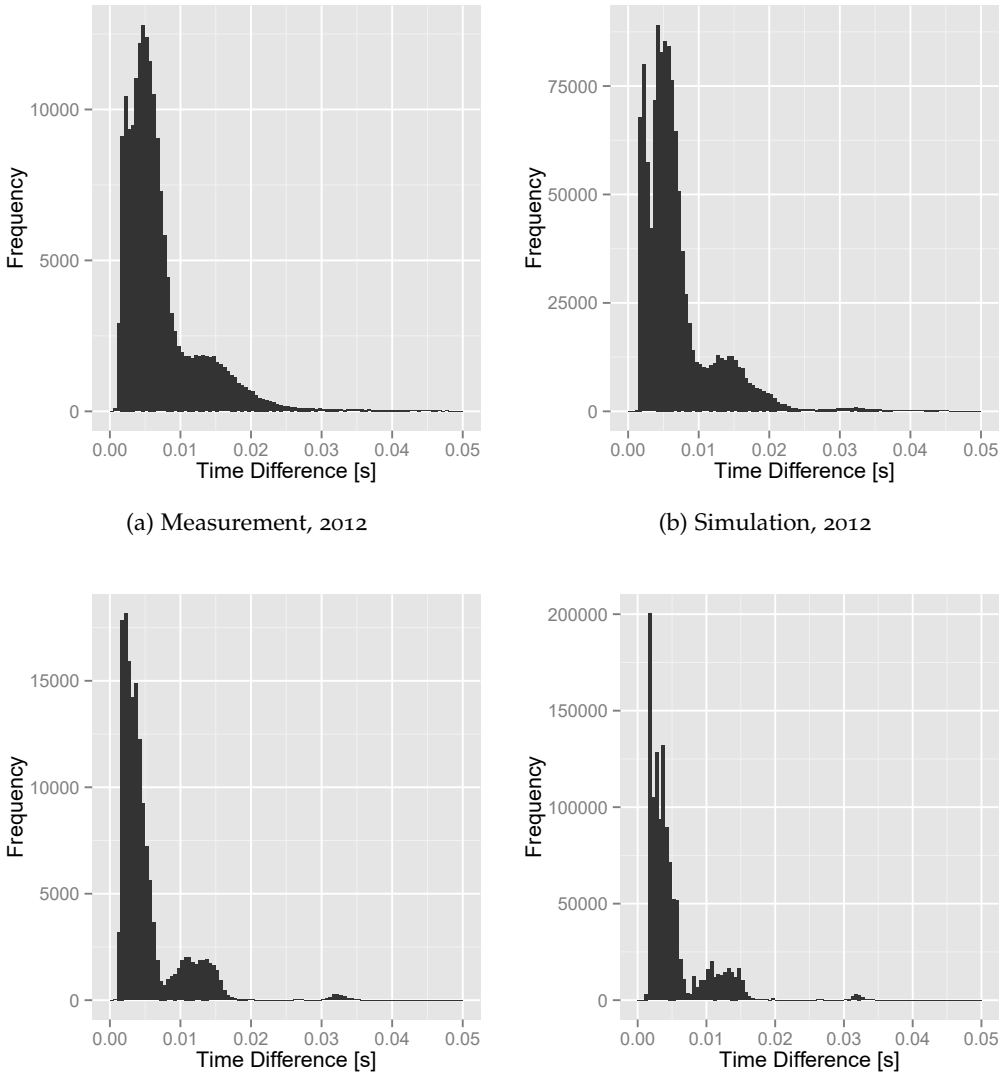

(a) Measurement, 2012

(b) Simulation, 2012

(c) Measurement, 2013

(d) Simulation, 2013

Figure 35: Spectrum of $T_{Rasterpoint}$ for measured and simulated beam delivery sequences: In both 2012 (top) and 2013 (bottom), the spectra of raster point irradiation times is similar to the simulation. In the simulated data, the distribution is less smooth due to one single intensity chosen for each simulation cycle, while the intensity is fluctuating more in the real irradiation.

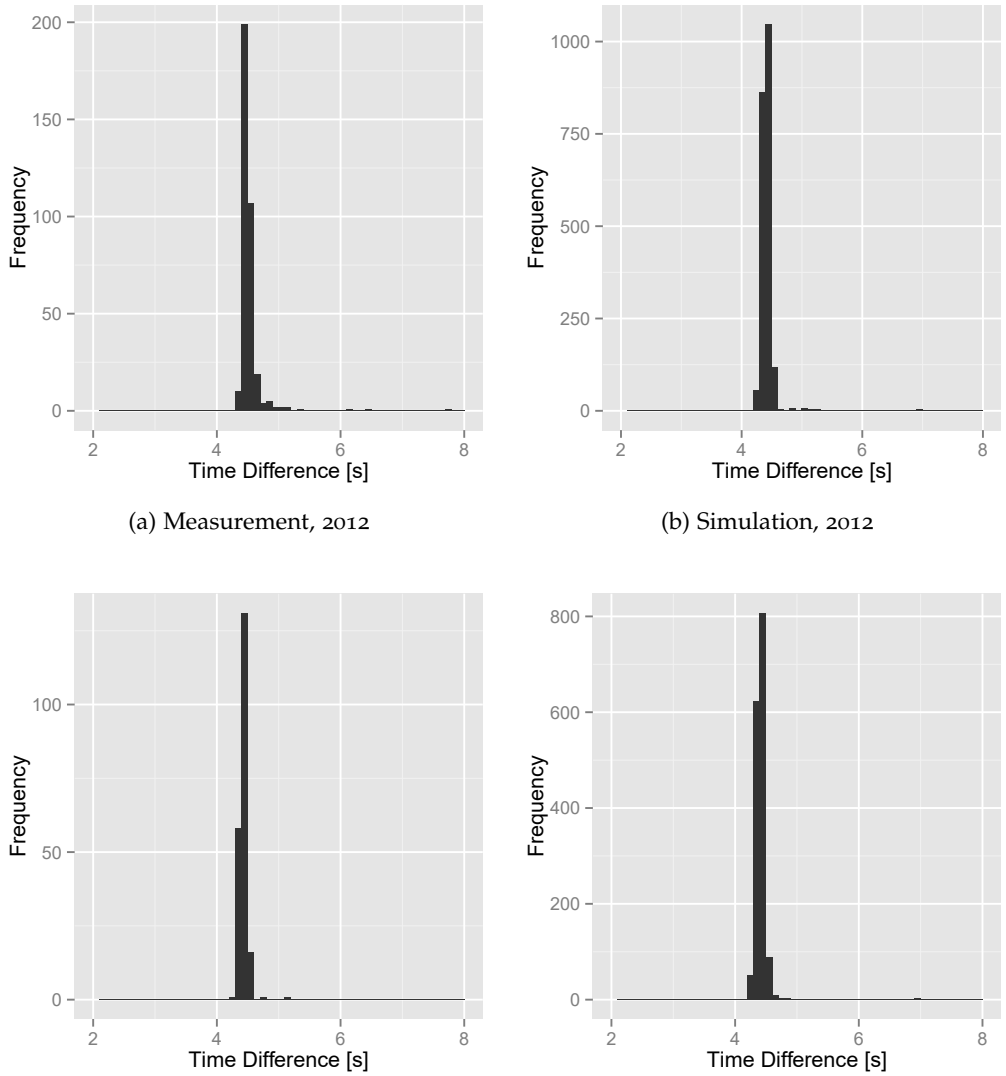

(a) Measurement, 2012

(b) Simulation, 2012

(c) Measurement, 2013

(d) Simulation, 2013

Figure 36: Spectrum of T_{Pause} for measured and simulated beam delivery sequences: The calculated pause times between two extractions are similar to the recorded differences, with similar median pause times and peak shapes in all data sets.

One difference is found in the width of the peaks, which are narrower in the simulation than in the recorded data. This is explained by examining the nature of the simulation: While the simulation assumes one constant extraction efficiency η for each simulation cycle, the beam intensity is fluctuating more in reality, leading to an extra broadening of the irradiation times. The impact of this difference on the simulation quality is further analyzed in the upcoming sections.

INTERPRETATION OF T_{PAUSE}: In Fig. 36, the timing spectrum for the pause time T_{Pause} is shown. Because the newly introduced intensity feedback system only affects the extraction and no changes have been made to the acceleration system, the base data for the pause time is the same for 2012 and 2013 and all four distributions should be essentially the same.

This is reflected in the data, the median duration of all pauses larger than 2 seconds in the 2012 irradiation records is 4.48 s, while the simulation has a median value of 4.41 s. Likewise, in the 2013 irradiation records, the median pause duration is 4.43 s, while the simulation yields a median value of 4.42 s. Also, the peak shape is the same in all data sets.

When this analysis was performed with the first version of the simulation, a discrepancy was found between the simulated and measured pause time. The difference of approximately 400 ms was mainly attributed to the omission of the broadcast delay time and corrected when the duration of the broadcast pause was confirmed. The data of this first analysis is found in the appendix in Section A.2.1 on page 132.

4.3.1.4 *Analysis II: Root Mean Square Deviation*

While the first analysis is sensitive enough to detect large deviations between the simulation and the real beam delivery sequences, undetected smaller deviations can add up over the course of a treatment plan, causing large deviations. In this analysis, the root mean square deviation (RMSD) of the absolute irradiation time of each raster point is calculated for simulated and recorded beam delivery sequences. As before, the analysis was performed using all irradiation records of the `VX-Vorbestrahlung` treatment plan and 200 simulation calculations using the 2012 and 2013 model base data.

Not all beam delivery sequences start at $t = 0$, in some recorded BDS, the first raster point is irradiated with an offset. For the first analysis, this offset did not matter, but to calculate a comparable RMSD for the whole data set, the offset between the simulated and recorded data is removed. This is done by calculating the mean offset $\langle \Delta t \rangle$ of all raster points:

$$\Delta t_i = t_{sim,i} - t_{exp,i} \qquad \langle \Delta t \rangle = \frac{1}{N} \sum_i \Delta t_i \tag{31}$$

The offset is subtracted from the irradiation times of each simulated raster point $t_{sim,i}$:

$$t_{sim,i} \to t'_{sim,i} = t_{sim,i} - \langle \Delta t \rangle \tag{32}$$

This time-shifted simulation data is used to calculate the root mean square deviation σ:

$$\sigma = \sqrt{\frac{1}{N} \sum_i \left(t'_{sim,i} - t_{exp,i} \right)^2} \tag{33}$$

The RMSD can be interpreted as the standard deviation of the predicted irradiation time.

In this analysis, the RMSD was calculated for each pair of simulated and recorded beam delivery sequences of the 2012 and 2013 data set. The resulting histograms are shown in Fig. 37. Additionally, to give an estimation of the simulation quality, the RMSD was calculated between pairs of recorded beam delivery sequences, comparable to an auto-correlation. Assuming that a recorded irradiation sequence is the optimal simulation result, the calculated RMSD values can be used as a reference for the analysis. The results are shown in Fig. 38.

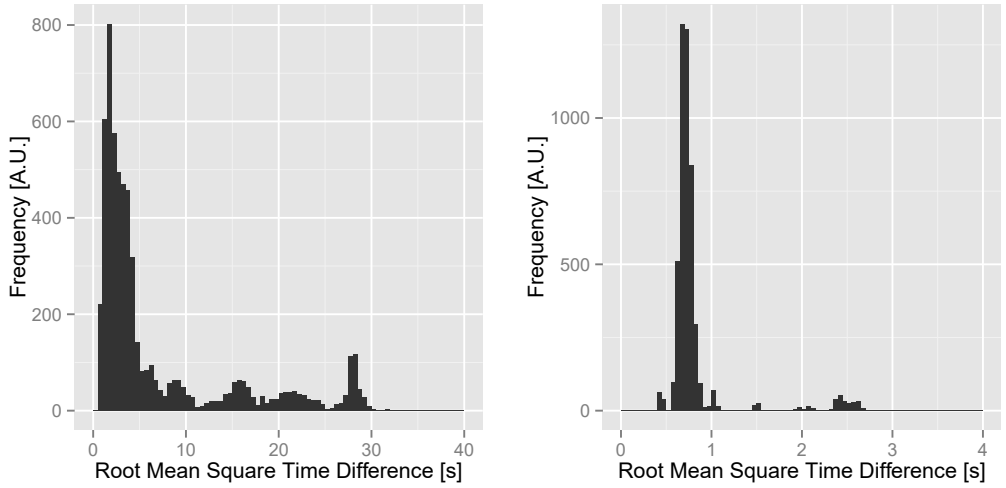

(a) 2012 Data (b) 2013 Data

Figure 37: Root Mean Square Deviation σ between simulated and recorded beam delivery sequences. The RMSD was calculated for the 2012 (left) and 2013 data set (right) separately.

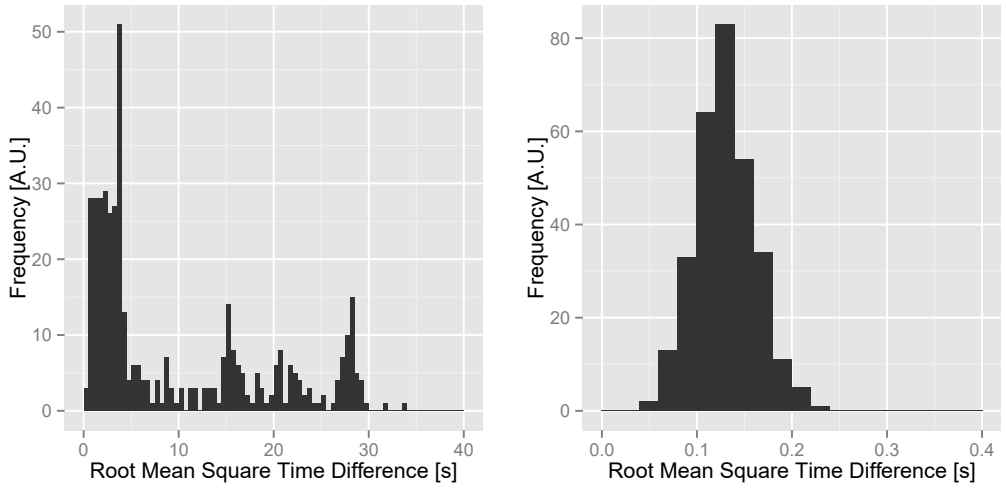

(a) 2012 Data (b) 2013 Data

Figure 38: Root Mean Square Deviation σ_{Auto} calculated from the recorded irradiation sequences only. Based on this "autocorrelation" data, reference values for the optimal simulation can be estimated. With the introduction of the intensity feedback system in 2013, the beam intensities are more stable which leads to a higher reproducibility of the irradiation.

INTERPRETATION OF 2012 DATA: Using the 2012 data set, the median RMSD σ was calculated to be 3.40 seconds, with the distribution reaching up to 30 seconds (Fig. 37 (a)). Using the recorded data only, the median value of the auto-correlated RMSD σ_{Auto}, was calculated to be 4.49 seconds. This is very close to the values obtained with the simulated data, and the distribution is similar to the simulated distribution (Fig. 38 (a)).

The similar values of σ and σ_{Auto} are an indication that the simulation is accurate in modeling the accelerator and the calculated beam delivery sequences are valid. On the other hand, the resulting beam delivery sequences have a large variance. To put the values into perspective, a typical breathing cycle has a duration of approximately four seconds. With a σ of 3.40 seconds, the motion phase in which a raster point is irradiated can not be accurately predicted.

Hence, for the 2012 data set, created prior to the introduction of the intensity feedback system, the simulation is accurate, but the resulting beam delivery sequences will have a large variance. This effect is dominated by large deviations of the beam intensity. The extreme RMSD values are most likely due to interruptions of the irradiation due to interlocks.

INTERPRETATION OF 2013 DATA: When using the 2013 data set, the median RMSD σ is reduced to 0.72 seconds, with a maximum deviation of 2.8 seconds (Fig. 37 (b)). The median auto-correlated RMSD σ_{Auto} is further reduced to 0.13 seconds with no values higher than 0.25 seconds (Fig. 38 (b)).

Assuming the same breathing cycle of four seconds, 0.72 seconds is equal to 18% of the cycle duration. Therefore, a prediction of the correct motion phase should be possible using the simulation. This will be further investigated in the dosimetric analyses.

While the predictive power of the simulation is improved using the 2013 data set, there is a significant difference between the recorded and the simulated beam delivery sequences. With a mean σ_{Auto} of 0.13 seconds, the differences between two recorded beam delivery sequences is smaller than the difference between a simulation and an irradiation.

SUMMARY: The first two analyses show a good agreement between the simulated and recorded beam delivery sequences. For the 2012 data set, the variance between individual beam delivery sequences is large, mainly due to the fluctuating beam intensity. This is reflected well by the simulation software but the quality of a dose prediction is likely reduced.

With the introduction of intensity feedback control (DIC), the beam intensities are more stable, which is reflected in the 2013 data set. Now, the variation between two beam delivery sequences is reduced and the irradiation becomes more reproducible. This increases the potential to predict dose distributions and reveals subtle differences between the simulation and the recorded data.

4.3.1.5 *Dosimetric Analyses*

Analyzing the beam delivery sequences by themselves showed an overall good performance of the simulation software, albeit with small deviations from the recorded data sets. The impact of those deviations on the dose distribution is hard to determine, as it depends on the patient, including the anatomy and breathing motion. To be able to interpret the differences between the simulated and recorded beam delivery sequences and to determine the simulation quality,

dose distributions were calculated from all beam delivery sequences using a standard phantom geometry and motion.

All dose distributions were calculated using TRiP-4D on the AIX computation cluster at GSI. The calculations assumed a homogeneous water phantom positioned in the isocenter, moving in a sinusoidal lateral motion of ± 7 mm at a motion period of $T = 4.0$ s. This resembles a typical abdominal motion, for example in the liver.

For the dose calculation, the motion was split into 21 motion phases, with phase $\phi = 0°$ defined as the water phantom centered ($x = 0.0$ mm), $\phi = 90°$ corresponds to maximum deflection in one direction ($x = 7.0$ mm). Dose distributions calculated from recorded BDS (*"Reconstructed Dose Distributions"*) were calculated using a starting phase $\phi = 0°$, that is, the first raster point is irradiated with the phantom at $x = 0.0$ mm. Dose distributions calculated from simulated BDS (*"Simulated Dose Distributions"*) were calculated using 5° phase shifts ($\phi = 0°, 5°, 10°, \ldots$).

All dose distributions were calculated using TRiP-4D's all-points divergent-beam (apdb) algorithm based on HIT beam data. This algorithm includes specific properties of the HIT facility and makes the dose distribution comparable to calculations of the HIT TPS and dose measurements.

Based on these calculations, several hundred different dose distributions have been created, which can not be compared manually. In the following sections, they are analyzed using statistical methods.

4.3.1.6 *Analysis III: χ^2 Analysis*

This analysis uses a modified χ^2 test to determine if a given dose distribution is similar to an ensemble of dose distributions. In this case, the simulated dose distributions are compared to the ensemble of reconstructed dose distributions.

The χ^2 values are calculated independently for each voxel $\vec{x}$ of the dose distribution. Before the χ^2 values can be calculated, the reconstructed dose distributions of the `VX-Vorbestrahlung` treatment plan (31 for the 2012 data, 26 for the 2013 data) are used to calculate two statistical properties: The mean dose of the ensemble in each voxel ($\mu_D(\vec{x})$) and the standard dose deviation of the ensemble in each voxel ($\sigma_D(\vec{x})$):

$$\mu_D(\vec{x}) = \frac{1}{n} \sum_{\text{Ensemble},i}^{n} D_i(\vec{x}) \tag{34}$$

$$\sigma_D(\vec{x}) = \sqrt{\frac{1}{n} \sum_{\text{Ensemble},i}^{n} (D_i(\vec{x}) - \mu_D(\vec{x}))^2} \tag{35}$$

Using this, the χ^2 value is calculated in each voxel $\vec{x}$:

$$\chi^2(\vec{x}) = \frac{(D(\vec{x}) - \mu_D(\vec{x}))^2}{\sigma_D^2(\vec{x})}, \tag{36}$$

where $D(\vec{x})$ is the dose distribution to be tested.

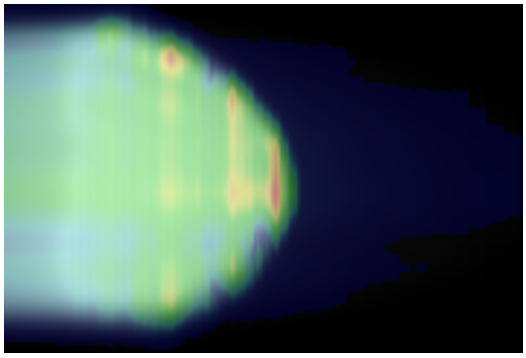

Figure 39: Example visualization of the mean dose $\mu_D(\vec{x})$ (gray scale) and standard deviation $\sigma_D(\vec{x})$ (color) for one slice of a patient treatment plan.

For the analysis, the mean χ^2 value is calculated for all voxels inside the high dose region volume of interest (VOI) by adding the individual χ^2 values and dividing by the number of voxels N:

$$\chi^2 = \frac{1}{N}\chi^2_{\text{total}} = \frac{1}{N}\sum_{\text{VOI}}\chi^2(\vec{x}). \tag{37}$$

Using the mean χ^2 has another benefit: For large numbers of degrees of freedom (n_{dof}), the mean χ^2 value of a normal distribution approaches n_{dof}. In this analysis, the dose values in the voxels are assumed to be independent, therefore the degrees of freedom are approximately equal to the number of voxels, $n_{\text{dof}} \approx N$. The VOI contains $N = 43920$ voxels, which is assumed to be sufficiently large. Hence, if all assumptions are correct and the dose values are in fact gaussian distributed, the mean χ^2 should be in the order of 1.

To analyze the performance of the simulation, χ^2 values of all simulated and reconstructed dose distributions are calculated. The dose distributions which are calculated from the recorded BDS are assumed to be the reference and are used to calculate $\mu_D(\vec{x})$ and $\sigma_D(\vec{x})$. The resulting mean χ^2 values of the reconstructed and simulated dose distributions are then compared to each other.

INTERPRETATION OF THE 2012 DATA SET: For the analysis of the 2012 data set, $\mu_D(\vec{x})$ and $\sigma_D(\vec{x})$ were calculated using 31 reconstructed dose distributions with a starting phase of $\phi = 0°$. Further, 10 simulated beam delivery sequences were used to calculate the simulated dose distributions. Out of the simulated dose distributions, 12 starting phases ($\phi = 0°$ to $330°$ in $30°$ increments) were evaluated.

Inside the VOI, the mean dose μ_D is (0.939 ± 0.110) Gy (with a planned dose of 1.00 Gy), the standard deviation σ_D is (0.243 ± 0.047) Gy.

In Fig. 40, the calculated mean χ^2 values are presented for the reconstructed dose distributions (left) and for the simulated dose distributions (right), separated into the different starting phases. For the reconstructed dose distributions, the median χ^2 value is 0.92, close to the expected value of 1 for a gaussian distribution. For the simulated dose distributions, the median χ^2 value depends weakly on the starting phase, between $\chi^2 = 1.46$ for $\phi = 30°$ and $\chi^2 = 1.16$ for $\phi = 270°$.

As in the previous analyses, the simulated dose distributions show no significant difference from the reconstructed dose distributions, hence, the simulation software calculates valid beam delivery sequences. Additionally, the starting

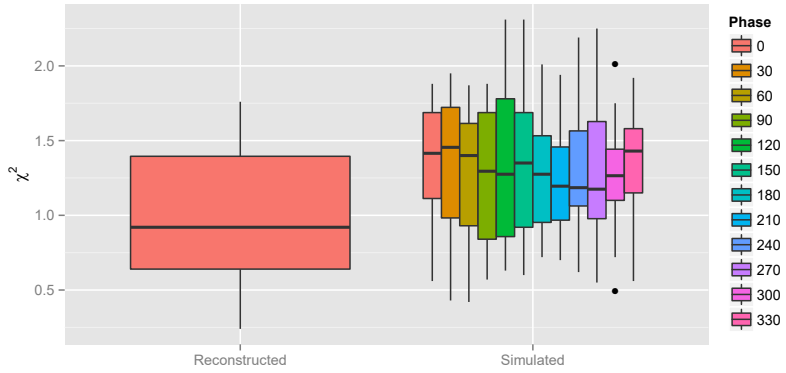

Figure 40: Resulting χ^2 values for the 2012 data set: The χ^2 values of the reconstructed dose distributions (left) are the reference for the simulated dose distributions (right). The graph shows a high agreement between reconstructed and simulated data and low dependence on the starting phase.

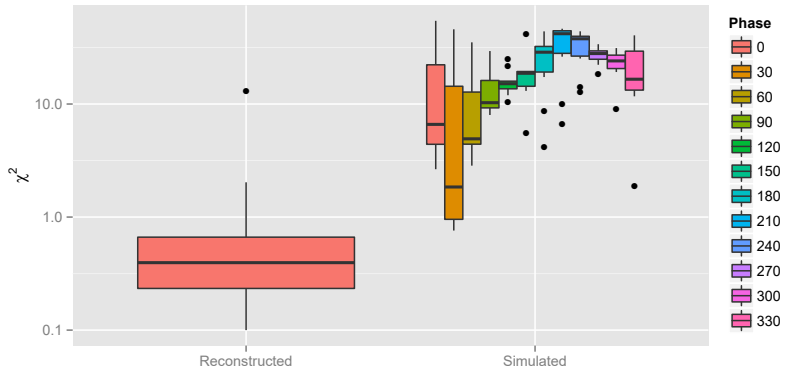

Figure 41: Resulting χ^2 values for the 2013 data set: In comparison to the 2012 data, the χ^2 values of the simulated dose distributions are elevated and highly dependent on the starting phase ϕ.

phase used in the calculation of the simulated dose distributions has no significant impact on the χ^2 values. This confirms the result of the previous analysis.

INTERPRETATION OF THE 2013 DATA SET: For the analysis of the 2013 data set, $\mu_D(\vec{x})$ and $\sigma_D(\vec{x})$ were calculated using 26 reconstructed dose distributions and a starting phase of $\phi = 0°$. As before, 10 simulated beam delivery sequences were used to calculate simulated dose distributions.

Within the VOI, the mean dose μ_D is (0.962 ± 0.286) Gy, the standard deviation σ_D is (0.095 ± 0.043) Gy. In comparison with the 2012 data set, μ_D exhibits a higher variation, while σ_D is reduced. This can be interpreted as a more pronounced interplay pattern which is repeated reliably in each repeated irradiation instead of canceling out.

In Fig. 41, the calculated χ^2 values are shown for the reconstructed and simulated dose distributions, note the logarithmic scale on the y axis. For the reconstructed dose distributions, the median χ^2 value is 0.40, which is below the expected value for a gaussian distribution. For the simulated dose distributions, the χ^2 values vary significantly with the starting phase, with values up to 40 for a starting phase $\phi = 210°$ and as low as 1 for a starting phase of $\phi = 30°$.

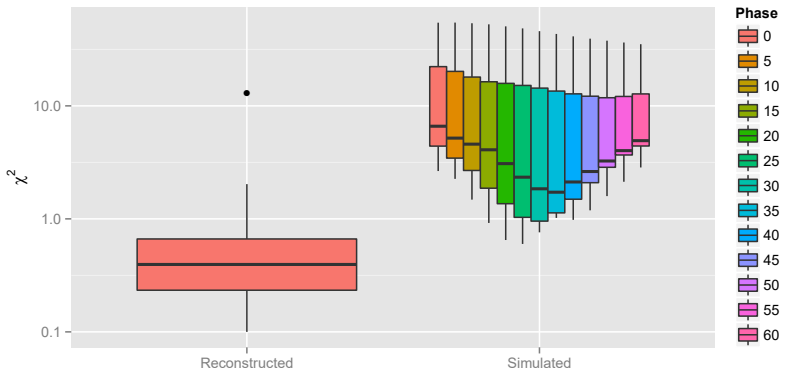

Figure 42: Detailed result of the χ^2 values for the 2013 data set: This plot shows the results for starting phases between $\phi = 0°$ and $\phi = 60°$. For $\phi = 35°$, the median χ^2 reaches a minimum.

To find the optimal starting phase, the resulting χ^2 values are shown in detail for starting phases $\phi = 0°$ to $\phi = 60°$ in Fig. 42. The best agreement is found in the simulated dose distribution with $\phi = 35°$, at a median χ^2 value of 1.82.

This confirms the results of the second analysis: The calculation of a BDS is more accurate than the duration of a breathing cycle, therefore, the dose distribution is sensitive to the starting phase of the dose calculation.

ESTIMATION OF THE DOSE DEVIATION: Using χ^2 in this analysis is a powerful tool to compare dose distributions, unfortunately, the values are hard to interpret by themselves. By rearranging equation 36, the uncertainty of the dose calculation can be estimated from the χ^2 values:

$$(D(\vec{x}) - \mu_D(\vec{x}))^2 = \chi^2(\vec{x}) \cdot \sigma_D^2(\vec{x}) \quad (38)$$

$$|D(\vec{x}) - \mu_D(\vec{x})| = \sqrt{\chi^2(\vec{x})} \cdot \sigma_D(\vec{x}) \quad (39)$$

Hence, by multiplying the square root of the χ^2 value and the standard deviation, an estimate of the mean dose uncertainty can be calculated. For the 2012 data, the median χ^2 value is around 1.3 across all starting phases, the mean standard deviation is 0.243 Gy. Hence, the mean uncertainty is about 0.28 Gy. For the 2013 data, the median χ^2 value of the 35° starting phase is 1.82, the mean standard deviation is 0.095 Gy, therefore the mean uncertainty is about 0.13 Gy.

4.3.1.7 *Analysis IV: Volumes of Interest*

The final analysis is inspired by the dose verification system currently used at HIT. Each treatment plan is verified by irradiating the treatment plan into a water phantom. Inside the water phantom, the dose is measured in 24 positions using pinpoint ionization chambers. By comparing the measured doses with the calculated dose distribution, the validity of the treatment plan can be assessed. In Fig. 33 (p. 68) the measurement positions and calculated dose values are shown as calculated in the HIT TPS *syngo® RT Planning*.

For the analysis, dose values are calculated in the same positions for simulated and reconstructed dose distributions. The similarity of the data sets is evaluated by comparing the doses in a representative part of the dose distribution. In this analysis, the distal part of the dose distribution was selected.

The 24 ionization chambers are positioned in a fixed geometry relative to each other in a chamber fixture referred to as the *detector block*. Using the *extract+* software, created by Christian Karger (at DKFZ) and further improved by Daniel Richter (at GSI), the doses of all detector positions are evaluated based on a calculated dose distribution. The *extract+* software uses trilinear interpolation of the dose values around each ionization chamber to calculate the dose value at each chamber position. Additionally, a standard deviation of the dose values is calculated from the surrounding dose values.

This analysis uses the same calculated dose distributions as before. The calculated dose values are presented using box plots. In addition, the dose values are analyzed using the Kolmogorov-Smirnov test (KS test). The KS test calculates the probability with which two sets of random variables are samples of the same distribution. It is designed to be valid independently of the actual probability density function and can be used for data samples which are not gaussian distributed (Kolmogorov (1933); Smirnov (1948)).

For set of simulated and reconstructed dose samples, the Kolmogorov-Smirnov test calculates the probability p with which the two samples are from the same probability density function. For values $p \leqslant 0.05$ (5%), two samples can be considered significantly different. Note that for 24 independent measurement positions, at least one position is likely to be significantly different due to statistical deviation.

In addition, the difference between the reconstructed and simulated median dose values is calculated to quantify their difference. This value is calculated as

$$\Delta D = \text{median}\,(D_{\text{Reconstructed}}) - \text{median}\,(D_{\text{Simulated}}) \tag{40}$$

for each detector position.

INTERPRETATION OF THE 2012 DATA SET: Using the same dose calculations as in the previous analysis, dose values were calculated from the 2012 data set. As before, the starting phase ϕ was chosen to be $\phi = 0°$ for the reconstructed dose distribution and $\phi = 0°, 30°, \ldots, 330°$ for the simulated dose distributions. In Fig. 43, the results are shown.

In the top graph, the reconstructed and simulated dose values are shown as box plots for each pinpoint chamber position. The edges of the box plots mark the first and third quartiles, the black center line marks the median dose value. As shown in Fig. 33, lower position numbers are in the plateau region, higher position numbers are in the spread-out bragg peak region. Visually, the two samples match well, with both samples having a large spread and similar median doses.

The lower graph shows the p-values of the two-sample Kolmogorov-Smirnov test, which confirms the visual assessment: Out of 24 pinpoint chamber positions, only one (number 17) exhibits a p value below 5%. Based on this data, there is no reason to assume that the two dose distributions are significantly different.

Additionally, the difference of the median dose, calculated for each ionization chamber, is $\Delta D = (0.069 \pm 0.124)$ Gy, at a planned dose of 1.0 Gy.

INTERPRETATION OF THE 2013 DATA SET: The results for the 2013 data set are presented in Fig. 44. As before, the calculations used a starting phase of $\phi = 0°$ for the reconstructed dose distribution and $\phi = 0°, 30°, \ldots, 330°$ for the

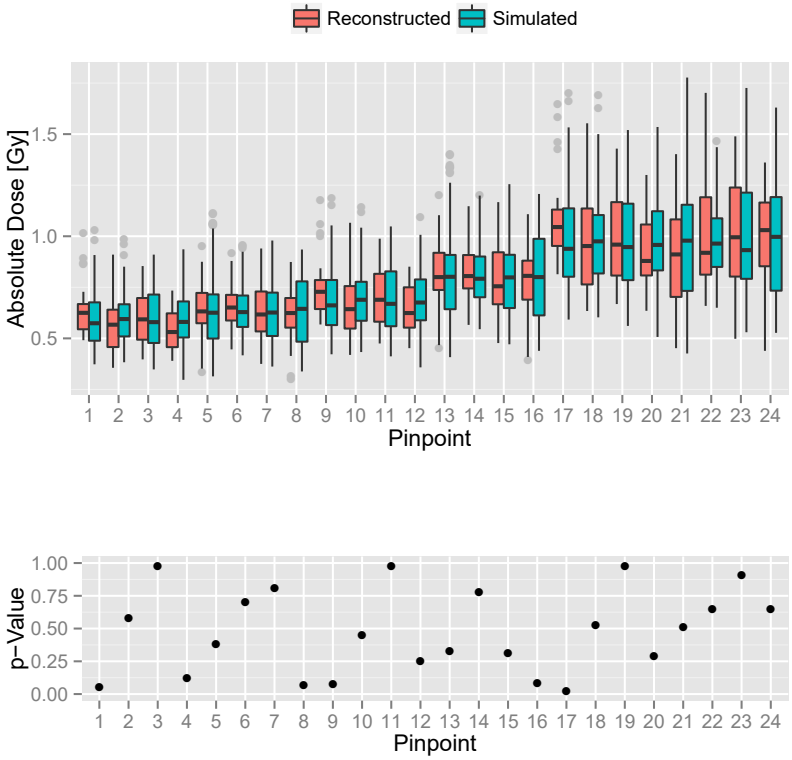

Figure 43: Dose values for the `VX-Verification` treatment plan, calculated in 24 measurement positions for the 2012 data set. Starting phase is $\phi = 0°$ for the reconstructed doses and $\phi = 0°, 30°, \ldots, 330°$ for the simulated doses. The simulated dose values (blue) match the reconstructed dose values (red) visually. In addition, the p values calculated for each measurement position are above 5% except in position 17. Deviation of the median doses $\Delta D = (0.069 \pm 0.124)$ Gy.

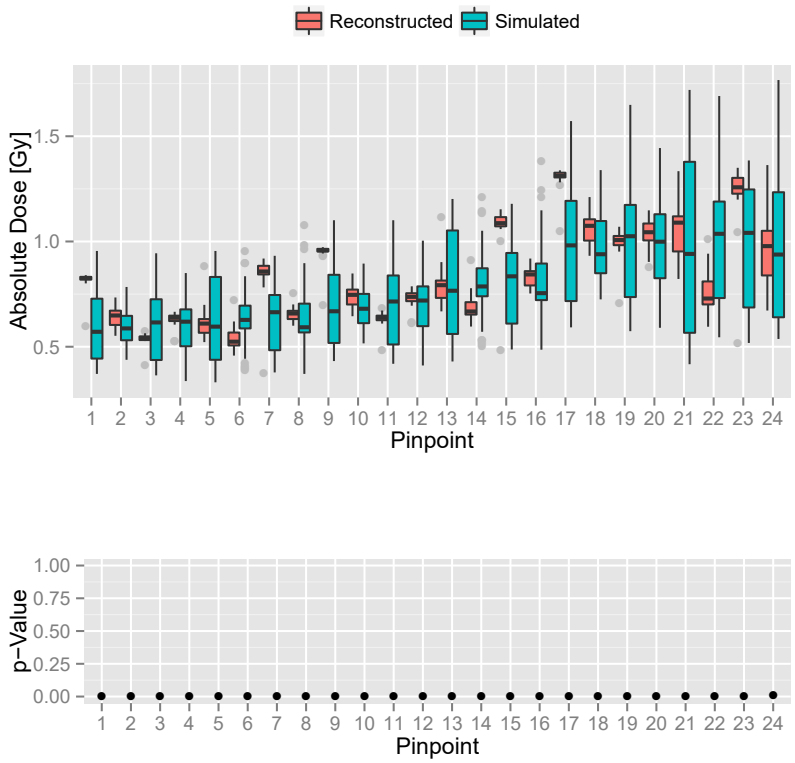

Figure 44: Dose values for the 2013 data set, using a sum of start phases $\phi = 0°, 30°, \ldots, 330°$ for the simulated dose distributions. Due to the different starting phases, the simulated dose distribution exhibit larger variation than the reconstructed dose distributions. This is also reflected in the low p values. Deviation of the median doses $\Delta D = (0.065 \pm 0.147)$ Gy.

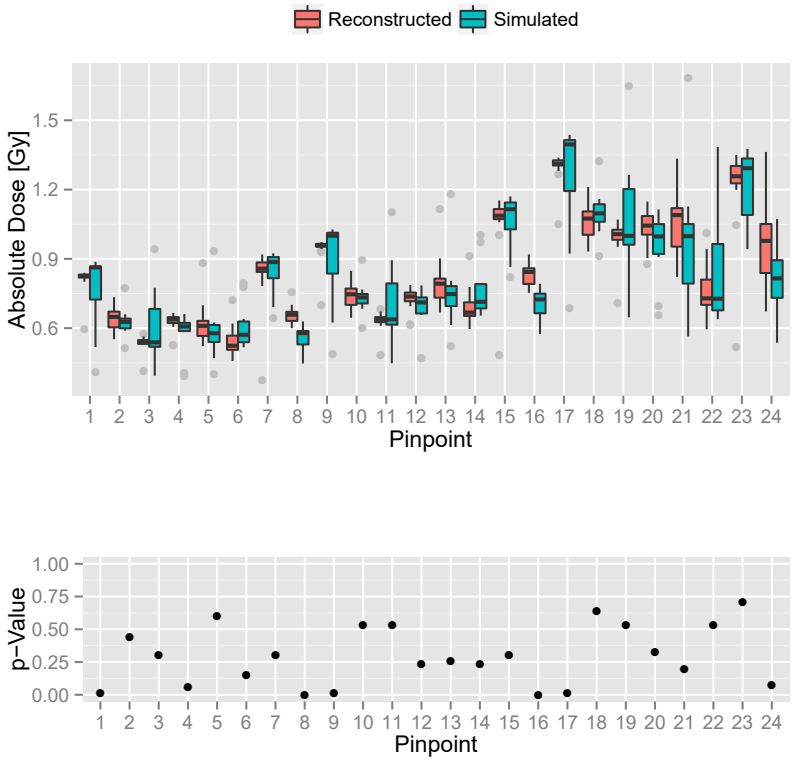

Figure 45: Dose values for the 2013 data set, using start phase $\phi = 30°$ for the simulated dose distributions. The difference between the simulated and reconstructed dose distributions is decreased, which is also reflected in the increased p values. Deviation of the median doses $\Delta D = (0.013 \pm 0.058)$ Gy.

simulated dose distributions. The differences can already be seen in the box plots, where the reconstructed dose values exhibit much smaller variance and substantially different median values in comparison to the simulated dose values. This is also reflected in the KS test, which yields a significant p value for each pinpoint position, and in the median dose deviation $\Delta D = (0.065 \pm 0.147)$ Gy.

This result reflects the results of the χ^2 analysis, which showed a strong dependence on the starting phase, with a minimum deviation for a simulation starting phase of $\phi = 35°$. Hence, the analysis was repeated using only single starting phases for the calculation of the simulated dose distributions.

Fig. 45 shows the result for starting phase $\phi = 30°$. The variance of the simulated dose values is reduced visibly and the median dose values of the simulation and reconstruction are now closer to each other. The p values are higher, although five measurement positions are significantly different (1, 8, 9, 16, 17). The calculated median dose deviation is $\Delta D = (0.013 \pm 0.058)$ Gy. Considering the planned dose of 1.0 Gy, this translates to a combined uncertainty of 5.9%.

The analysis was repeated using starting phases of $\phi = 0°$ and $\phi = 60°$, see Fig. 72 and 74 on pp. 135f in the appendix. With $\Delta D = (0.020 \pm 0.165)$ Gy (for $\phi = 0°$) and $\Delta D = (0.005 \pm 0.140)$ Gy (for $\phi = 60°$), a starting phase of $\phi = 30°$ was confirmed as optimal starting phase, similar to the χ^2 analysis.

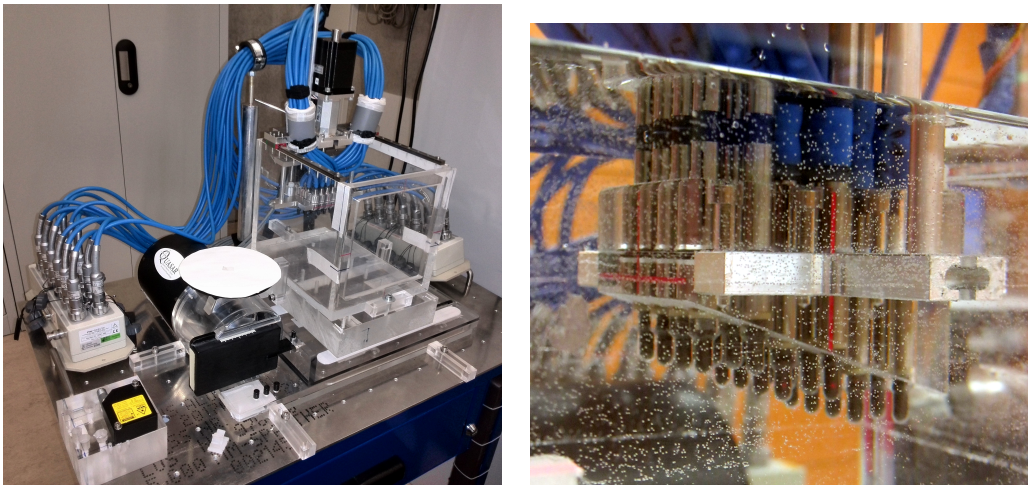

(a) (b)

Figure 46: Experimental setup: (a) The small water phantom, with the entrance window facing forwards, is attached to the *QUASAR(TM) Respiratory Motion Platform.* The whole water phantom is moved laterally by the stepper motor in the center. A LASER distance tracker (lower left) is used for position read out. (b) 24 *PTW PinPoint* ionization chambers are are used for dose measurement.

4.3.1.8 *Summary of Analyses*

In the previous four analyses of simulated beam delivery sequences, the efficacy of the simulation software could be established. While small deviations between the simulated and recorded irradiation records have been identified, the predictive power of the simulation has been shown for both the 2012 and 2013 data set.

For the 2012 data set, the agreement between simulated and recorded records was found to be very high, which can be partly attributed to the large variation between individual irradiation. Due to the large deviations, subtle differences between simulation and recorded data are less significant.

For the 2013 data set, the variation between the irradiation records is reduced, which reveals small differences between simulation and recorded data. Fortunately, the difference in absolute dose calculation was shown to be small, with uncertainties of 5.9% for the test plan used in the analysis.

In the following section, the analysis is continued using an experimental setup. The measurements were carried out in August of 2013, after the installation of the DIC extraction control system.

4.3.2 *Experimental Verification*

To complete the analysis of the simulation software and to investigate the applicability of the simulation method for experimental setups and in vivo dose calculation, an experimental verification was performed. In this experiment, the dose distributions of the *VX-Verification* treatment plan and a patient treatment plan were measured in treatment conditions in a moving water phantom using ionization chambers. The measured dose distributions were compared to simulated dose distributions calculated using the simulation software and TRiP-4D.

The experiment was performed in one of HIT's patient treatment rooms (H2) in regular patient treatment conditions. Fig. 46 (a) shows the experimental setup:

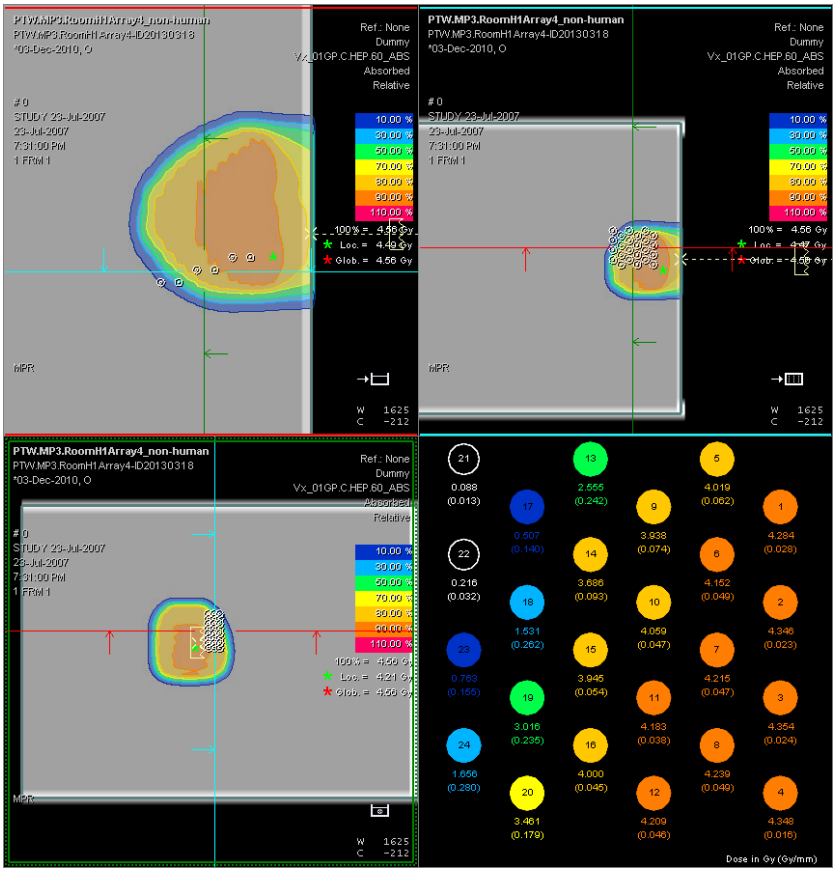

Figure 47: Patient treatment plan as displayed in the HIT TPS *syngo® RT Planning*. The dose calculations are performed in a water phantom geometry, the positions of the ionization chambers are indicated by white circled dots. In the lower right, the dose values and gradients are reported. This treatment plan was used in a stereotactic liver irradiation.

On top of a *ModusQA QUASAR(TM) Respiratory Motion Platform*, a small water phantom is attached. The motion platform can be moved laterally using a stepper motor and is controlled by a laptop computer. For all measurements, the motion of the phantom was chosen to match the previous calculations: Sinusoidal motion in the x direction with an amplitude of 14 mm peak-to-peak (±7 mm) and a motion period of 4 seconds.

The water phantom was developed and built at HIT (Chaudhri et al. (2012)) and contains the same detector block which is used in the regular verifications, Fig. 46 (b). The detector block contains 24 PTW TM31009 and TM31015 0.030 cm^3 pinpoint ionization chambers and can be moved freely inside the water phantom to match a planned position for which the doses were calculated in the TPS.

The dose was measured using a *PTW MULTIDOS* multi-channel dosemeter setup, which reads the dose from all 24 ionization chambers simultaneously. To calculate the dose, the chamber-specific calibration factor ($N_{D,w}$) and the correction factors for air density (k_ρ) and beam quality (k_Q) were applied.

Two treatment plans were used in the experiment: The previously analyzed *VX-Vorbestrahlung* treatment plan (with a maximum dose of 1.01 Gy in water and an irradiation time of one minute) was used for pre-irradiation of the ionization chambers and also for the experimental verification. Additionally, the experiments were carried out using a patient treatment plan for a liver irradia-

tion (with a maximum dose of 4.56 Gy in water and an irradiation time of nine minutes). The patient treatment plan is presented in Fig. 47.

The motion of the water phantom was recorded using a LASER distance tracker connected to the *ANZAI AZ-733V* gating system. This signal was not used for gating, but the *ANZAI AZ-733V* system was used for recording the actual motion and determination of the starting phase ϕ.

Before irradiation, the water phantom and the detector block was positioned using the treatment table (for positioning the water phantom in front of the beam nozzle) and the stepper motor of the detector block (to control the depth in water). The entrance window of the water phantom was positioned in the isocenter; the detector block was positioned to match the dose calculations in *syngo® RT Planning* and TRiP.

Prior to the measurements, the ionization chambers were pre-irradiated using the *VX-Vorbestrahlung* treatment plan. Irradiating with a total of 3 Gy is used to "warm up" the dosimetry equipment and increases the reliability of the measurements. After that, a zero balance was performed to mitigate any drift of the measurement values.

The measurements were performed in four sessions: First, the *VX-Vorbestrahlung* treatment plan was irradiated into the stationary water phantom once. Then, the sinusoidal motion of the water phantom was started and the *VX-Vorbestrahlung* treatment plan was irradiated into the moving water phantom for five times. Then, the position of the water phantom and detector block was readjusted for the patient treatment plan. This treatment plan was also irradiated into the stationary phantom once and into the moving phantom for an additional seven times. During all measurements, the doses in the pinpoint ICs, the motion trajectory measured using the *ANZAI AZ-733V* system and the accelerator records were recorded.

Results of the dose measurements are compared to 4D dose distributions calculated using TRiP-4D and *extract+*, similar to Analysis IV. To rule out setup errors and systematic errors in the dose calculation, measurements using the static phantom are compared to static dose calculations in *syngo® RT Planning* and TRiP.

4.3.2.1 *Results of the Static Measurements*

For both treatment plans, static dose distributions were calculated using the commercial TPS *syngo® RT Planning* and TRiP. For *syngo® RT Planning*, the dose values and gradients were taken directly from the verification preparation workspace, visible in the lower right of Fig. 33 and 47. For the doses calculated using TRiP, the dose values and uncertainties were calculated using the *extract+* program already used earlier.

In order to validate the dose calculation and the positioning of the water phantom during the experiment, the measured dose values are compared to the calculated doses at the positions of each *PinPoint* ionization chamber. Fig. 48 and Fig. 49 show the result of this comparison for the *VX-Vorbestrahlung* and the patient treatment plan, respectively. In the graph, the measured dose is presented in red, the calculation in the HIT TPS is presented in green and the dose calculation using TRiP in blue. The uncertainties for the *syngo® RT Planning* calculations were calculated from the provided dose gradient and a general uncertainty of 2 mm in setup.

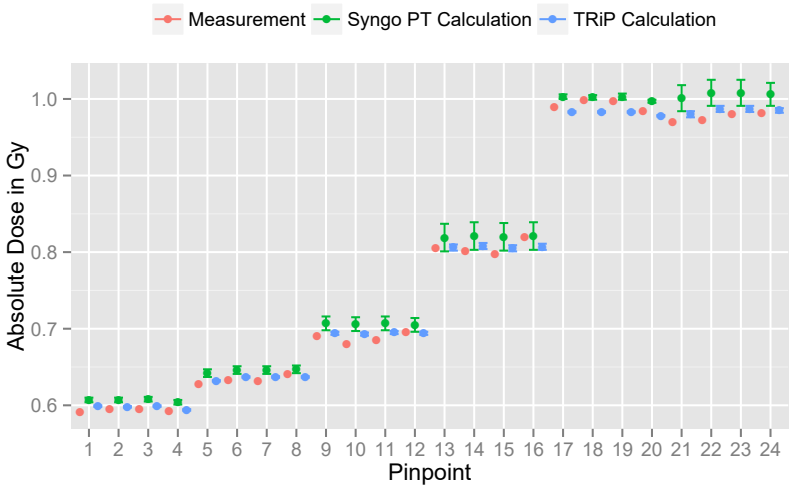

Figure 48: Static dose measurement results for the *VX-Vorbestrahlung* treatment plan: The measured doses are $(-1.6 \pm 0.8)\%$ lower than the *syngo® RT Planning* dose calculations, within the $\pm 3\%$ tolerance. The difference between the doses calculated with TRiP and *syngo® RT Planning* are acceptable, the TRiP results are even closer to the measurement.

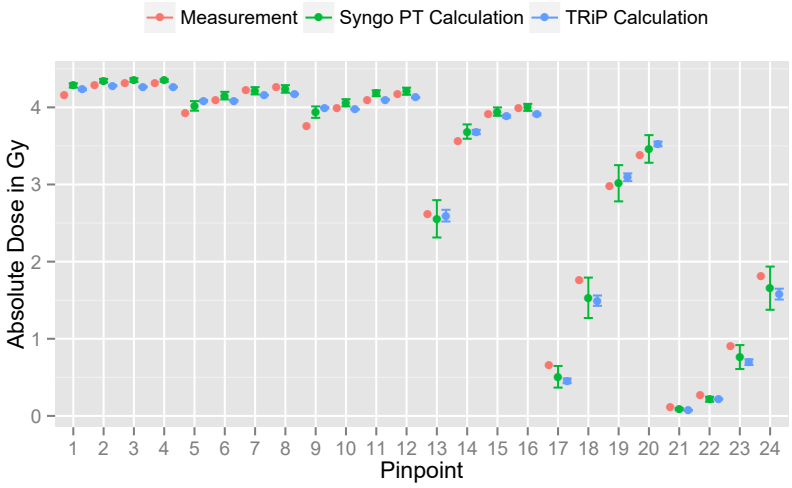

Figure 49: Static dose measurement results for the patient treatment plan: The measured doses are $(-0.2 \pm 2.2)\%$ lower than the *syngo® RT Planning* dose calculations, within the $\pm 3\%$ tolerance. The difference between the doses calculated with TRiP and *syngo® RT Planning* are acceptable.

For both treatment plans, the measured and calculated doses are close to each other, in the case of the *VX-Vorbestrahlung* treatment plan, the measured doses deviate by $(-1.6 \pm 0.8)\%$ (relative to D_{max}) from the HIT TPS calculations. For the patient plan, the measured doses deviate by $(-0.2 \pm 2.2)\%$. At HIT, the measured doses are required to deviate less than 3% from the calculation to be accepted in dose verification, which is the case for this measurement.

The small difference between the dose calculated by TRiP and *syngo® RT Planning* was found to be acceptable. Especially in the *VX-Vorbestrahlung* treatment plan, the TRiP dose calculation seems to match the measurements even better than the *syngo® RT Planning* dose calculation. Based on the results, the experimental setup and the dose calculations can now be assumed to be accurate.

4.3.2.2 *Results of the Motion Measurements*

The 4D dose distributions were calculated using the same calculation parameters as for the dosimetric analyses. For each treatment plan, 10 simulated beam delivery sequences were calculated using the simulation software and the 2013 model base data set. The dose distributions were again calculated using TRiP-4D.

Each calculation assumed a uniform water phantom moving laterally by $x = \pm 7$ mm in a sinusoidal motion, with a cycle length of 4 seconds. A starting phase of $\phi = 0°$ corresponds to the water phantom being centered ($x = 0$ mm) when the first raster point is irradiated. Simulated dose distributions were calculated with starting phases of $\phi = 0°, 30°, \ldots, 330°$. For each combination of starting phase and beam delivery sequence, the resulting dose distribution was sampled using the *extract+* software.

Similar to the previous analysis, the result of the dose calculation is shown as a box plot; the measured dose values are superimposed as red circles. As before, the calculated and measured dose values are analyzed using the Kolmogorov-Smirnov (KS) test. For p values below 5%, two samples can be assumed to be significantly different.

Finally, the difference between the measured and the simulated dose distribution is calculated. Due to the low number of samples in the experiment, instead of using the median (as in Analysis IV), the mean value of all measured doses $D_{Measured}$ is used instead:

$$\Delta_{Mean} D = \text{mean}\,(D_{Measured}) - \text{median}\,(D_{Simulated})\,. \tag{41}$$

Both treatment plans were irradiated multiple times into the moving water phantom and the doses measured. The *VX-Vorbestrahlung* treatment plan was irradiated five times, each time without an interlock. The patient treatment plan was irradiated seven times, four times encountering an interlock resulting in a treatment pause lasting several seconds, three times without interlock. Due to technical limitations, all irradiations were started with a random starting phase ϕ, which was recorded using the *ANZAI AZ-733V* system.

The measured dose values are now analyzed in two different ways: First, all measurements are grouped together and compared to dose calculations using all starting angles ϕ. Then, only the irradiations which were irradiated without interlocks and which had a common starting phase ϕ are considered. These are compared to the dose calculation with the same starting phase.

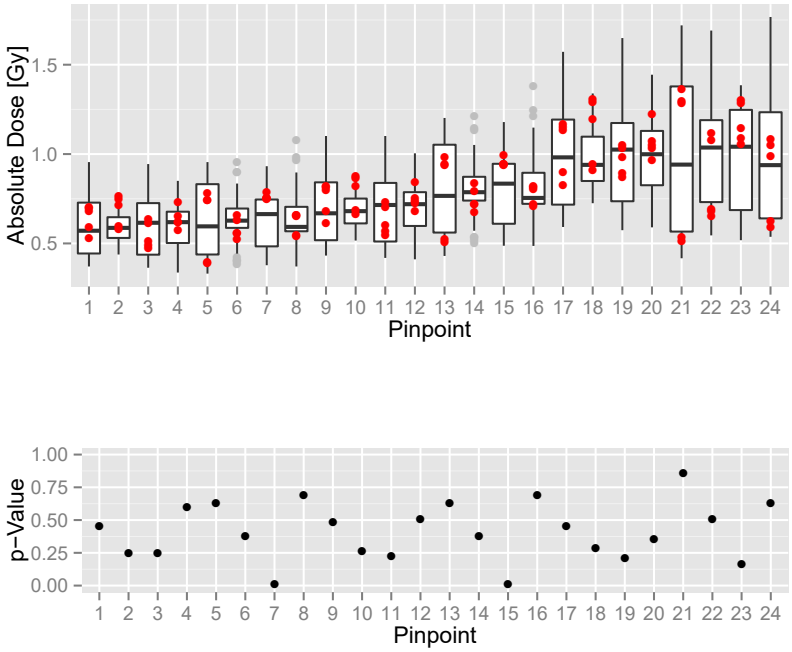

Figure 50: Experimental verification of the *VX-Vorbestrahlung*, using all starting phases ϕ. Top: The simulated doses are shown as box plots, the measured doses by the red circles. Bottom: The calculated p values of the Kolmogorov-Smirnov test. Both show high conformity of the two dose distributions. The deviation between measured and simulated doses is $\Delta_{\text{mean}}D = (0.057 \pm 0.138)$ Gy or $(5.6 \pm 13.7)\%$

ANALYSIS OF ALL IRRADIATIONS: In the first analysis, all measured dose distributions are considered, including the irradiations encountering interlocks. In this data set, the starting phase can be considered to be random, and the resulting doses are compared to dose calculations using all starting phases $\phi = 0°, 30°, \ldots, 330°$.

Fig. 50 shows the results for the *VX-Vorbestrahlung* treatment plan, with the simulated and measured doses indicated using the box plots and the red circles. Below, the p values calculated using the Kolmogorov-Smirnov (KS) test are presented.

From visual inspection, the simulated dose values fit the measured doses well. This is also reflected by the p values which are below 5% for chambers 7 and 15 only. Again, with 24 measuring positions, at least one can be expected to be significantly different due to statistical fluctuation. The dose deviation was calculated to be $\Delta_{\text{Mean}}D = (0.057 \pm 0.138)$ Gy or $(5.6 \pm 13.7)\%$.

Fig. 51 shows the results for the patient treatment plan. The simulated dose values fit the measurement results excellently in both the high-dose region (positions 1 to 16) and still very good in the distal region (17 to 24). This is also reflected by the p values, which are only significantly different reduced for the distal measurements with lower point doses. Note that the difference between measurement and calculation is already present in the static case, hence the low p values can most likely be attributed to the positioning in the steep dose gradient. The dose deviation was calculated to be $\Delta_{\text{mean}}D = (0.066 \pm 0.264)$ Gy or $(1.4 \pm 5.8)\%$).

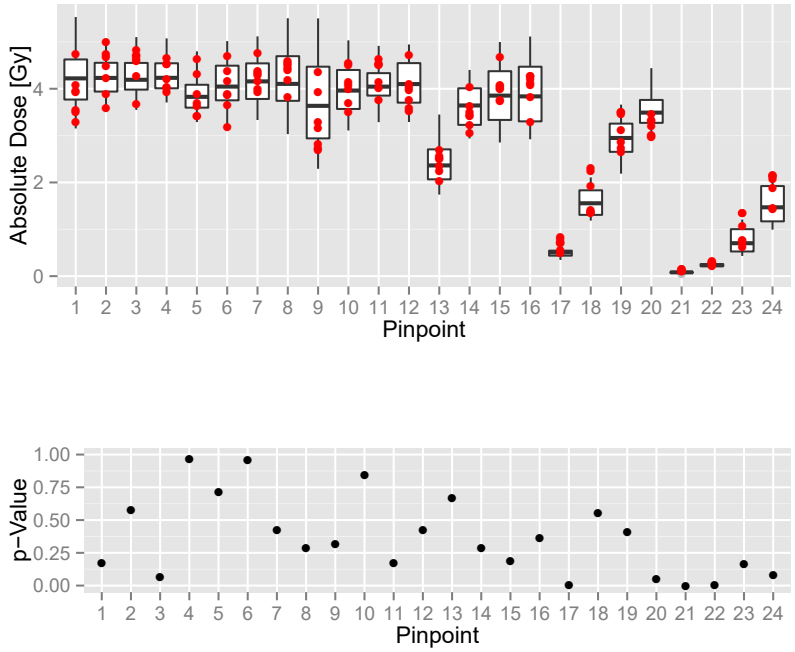

Figure 51: Experimental verification of the patient treatment plan, using all starting phases ϕ. Top: The simulated doses are shown as box plots, the measured doses by the red circles. Bottom: The calculated p values of the Kolmogorov-Smirnov test. Both show high conformity of the two dose distributions, especiall in the high dose region (1 to 16). The deviation between measured and simulated doses is $\Delta_{\text{mean}}D = (0.066 \pm 0.264)$ Gy or $(1.4 \pm 5.8)\%$)

ANALYSIS OF SPECIFIC STARTING PHASES: For the previous analysis, all measured doses were included regardless of interlocks and with arbitrary starting phases ϕ. To reduce the influence of these factors on the analysis, all irradiations which were disturbed by an interlock are now excluded. Further, all irradiations with a similar starting phase were found and grouped together. In the measured data set, three matching irradiations were found for each treatment plan: For the *VX-Vorbestrahlung* treatment plan, a starting phase of $\phi \approx 60°$ was recorded for measurements 2, 3 and 4; for the patient treatment plan, $\phi \approx 180°$ for measurements 2, 3 and 4. In this analysis, the measured doses are compared to the dose calculations with the respective starting phases ($\phi = 60°$ and $\phi = 180°$).

Fig. 52 and Fig. 53 show the result of this analysis for the *VX-Vorbestrahlung* and patient treatment plan. In comparison with the previous calculations, the calculated and measured dose values of both treatment plans show a smaller variance. This is especially visible in the shorter *VX-Vorbestrahlung* treatment plan, but also in the longer patient treatment plan[1].

For the *VX-Vorbestrahlung* treatment plan, the agreement between the measured and calculated dose is improved. This is confirmed by the increased p values calculated by the KS test and by the reduced dose difference $\Delta_{\text{Mean}}D = (0.000 \pm 0.076)$ Gy or $(0.0 \pm 7.5)\%$. Hence, the simulation has a high predictive power with the right starting phase, while being very sensitive to a shift in the starting phase or disturbances due to interlocks.

1 See section A.2.2.2 on page 137 in the appendix.

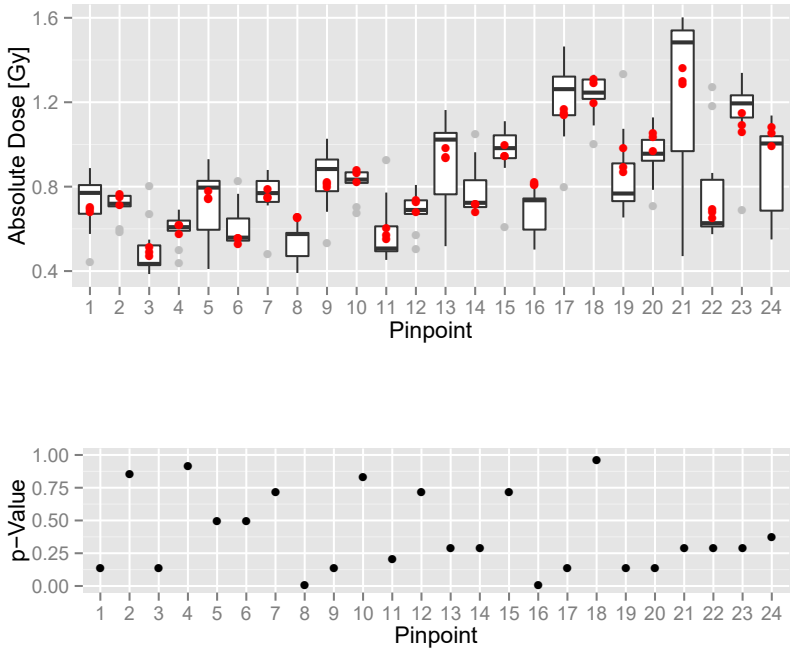

Figure 52: Resulting doses for the *VX-Vorbestrahlung* treatment plan for all measurements with a starting phase of $\phi \approx 60°$ and no interlocks (red dots). The simulated doses (box plot) were calculated with a starting phase of $\phi = 60°$. Below are the p values calculated using the Kolmogorov-Smirnov test.
$\Delta_{\text{Mean}}D = (0.000 \pm 0.076)$ Gy or $(0.0 \pm 7.5)\%$

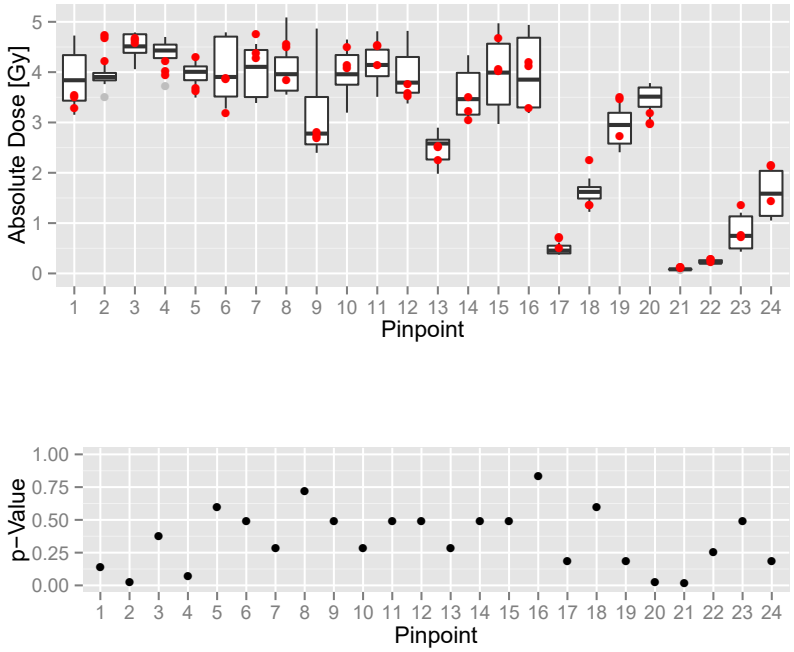

Figure 53: Resulting doses for the patient treatment plan for all measurements with a starting phase of $\phi \approx 180°$ and no interlocks (red dots). The simulated doses (box plot) were calculated with a starting phase of $\phi = 180°$.
$\Delta_{\text{Mean}}D = (0.045 \pm 0.331)$ Gy or $(1.0 \pm 7.3)\%$

For the patient treatment plan, the difference to the previous analysis is smaller. As before, three measurement positions have p values less than 5%, and the dose difference $\Delta_{\text{Mean}}D = (0.045 \pm 0.331)$ Gy or $(1.0 \pm 7.3)\%$ is comparable to the previous outcome[2].

One explanation is the longer irradiation time of the patient treatment plan of approximately nine minutes. During the longer irradiation time, small deviations will accumulate, this reduces the phase coherence due to the random nature of the beam pauses and irradiation times. This reduces the accuracy with which the correct phase for the distal raster points is estimated. These raster points usually are irradiated with the highest particle numbers and have the highest contributions to the overall dose.

4.3.3 *Summary: Simulation Analysis and Experimental Verification*

The quality of the simulated beam delivery sequences (BDS) were analyzed both using irradiation records extracted from the treatment control system (TCS) and using an experimental setup with a defined motion pattern. Both resulted in a satisfactory agreement between simulation and measurement.

For the retrospective analysis using irradiation records, a test treatment plan (*VX-Vorbestrahlung*) was used. This treatment plan was irradiated regularly before each treatment plan verification to pre-irradiate the ionization chambers, an ideal candidate for a retrospective study.

To create the data sets, irradiation records of the *VX-Vorbestrahlung* treatment plan from two time periods in 2012 and 2013 were extracted from the TCS, yielding 31 records in the 2012 and 26 records in the 2013 data set. Simulated beam delivery sequences were calculated with base data from the same periods, excluding the beam records used for analysis.

Four different analysis methods were used to compare the records to simulated BDS: Analysis I and II used spectra of irradiation times and root-mean-square calculation of the deviation of each raster point irradiation time to compare the BDS based on timing of each irradiated raster point alone. For Analysis III and IV, 4D dose calculations were performed based on the BDS and statistical analysis was performed on the dose distribution to find deviations.

Analysis I, which investigated the spectrum of raster point irradiation timing, found a good agreement between the simulated and recorded beam delivery sequences for both the 2012 and 2013 data set. Being more sensitive to subtle differences, the other analyses found qualitative and quantitative differences between both data sets.

2012 DATA SET Prior to the introduction of the dynamic intensity control (DIC), fluctuations of the ECR ion-beam sources caused beam intensity fluctuations leading to high variability between irradiations of the same plan. This variability was found in the irradiation records and is correctly reflected by the simulation but was found to reduce the predictive power of the simulation.

All analyses found a good agreement between the simulated beam delivery sequences and the irradiation records. At the same time, the uncertainty of the irradiation time of each raster point was so large that even for this relatively short

2 See section A.2.2.3 on page 140 in the appendix.

treatment plan (70 to 100 seconds), dose contributions to each motion phase can not be reliably predicted.

Analysis II found a median root-mean-square σ of 3.40 seconds. This is similar to the result obtained when irradiation records are compared to each other: $\sigma = 4.49$ seconds. With breathing cycle times of approximately four seconds, the uncertainty is in the same order of magnitude, limiting the predictive power in the 2012 data set.

Analysis III confirms the results, with χ^2 values of 0.92 for reconstructed dose distributions and 1.16 to 1.46 for simulated dose distributions. A good agreement is found between simulated and reconstructed dose distributions, but the agreement is independent on the motion starting phase. This indifference to the starting phase is indicative of high irradiation variability.

Analysis IV also confirms the previous results, with a high agreement between the simulated and reconstructed dose distribution (median dose difference $\Delta D = (6.9 \pm 12.4)\%$ for a comparison with mixed motion starting phases). Also here, the result is not dependent on the motion starting phase.

2013 DATA SET Early in 2013, the dynamic intensity control (DIC) system was introduced, which reduces beam intensity fluctuations and decreases variability between irradiations. This is reflected in the 2013 data set, leading to more reproducible irradiation sequences and more accurate predictions.

Analysis II found a median root-mean-square σ of 0.72 seconds, almost a factor five lower than with the 2012 data set. Due to the reduced irradiation variability, the quality of the simulation is improved with less than a second uncertainty, and offers an increased predictive power. When comparing the recorded BDS to each other, the median σ is even lower, at 0.13 seconds, which hints that the simulation could be further improved.

Analysis III confirms the results, with χ^2 values of 1.82 at a motion starting phase of $\phi = 35°$. In this analysis, a high dependency on the motion starting phase was found, confirming the reduced variability of the irradiation. Similar to Analysis II, the comparison of the irradiation records with each other show even lower χ^2 values of 0.40, confirming that the simulation could potentially be improved further.

Analysis IV also confirms the previous results, showing a high agreement between the simulated and reconstructed dose distributions. For motion starting phase $\phi = 30°$, the median dose difference $\Delta D = (1.3 \pm 5.8)\%$. Also here, a phase dependence is seen, a comparison with mixed motion starting phases ($\phi = 0°$, $30°, \ldots, 330°$) does not reproduce the dose values with $\Delta D = (6.5 \pm 14.7)\%$.

In the 2013 data set, both recorded and simulated irradiation sequences show less variability leading to more accurate predictions. The increased reproducibility is reflected by a dependency on the motion starting phase. The increased reproducibility also uncovers subtle differences between the simulated and recorded beam delivery sequences. Even with the already high predictive power, improvement of the simulation could be possible. Between the simulated and recorded BDS, an unexplained offset of $\phi = 35°$ was found. This vanished in the experimental verification, hence it is most likely an offset to be found in the TCS.

EXPERIMENTAL VERIFICATION Finally, the results of the simulated dose calculations were verified by a dose measurement using 24 ionization chambers

in a moving water phantom. Motions were chosen to mimic typical breathing amplitudes and frequencies encountered in treatments of abdominal tumors. Two treatment plans were selected, the *VX-Vorbestrahlung* treatment plan already used in the previous analyses, and one SBRT treatment plan used for the treatment of hepatocellular carcinoma. All measurements were performed in 2013 after the introduction of the dynamic intensity control (DIC), hence phase sensitivity was expected.

The resulting dose measurements were found to be in good agreement with the simulated dose calculations. In addition, a set of measurements with similar motion starting phases ϕ and no interlocks were selected for each treatment plan and compared to dose calculations with multiple simulated motion starting phases. This analysis found an optimal agreement for simulations with the same starting phase and less optimal agreement for differing starting phases, confirming the phase dependency. For the *VX-Vorbestrahlung* treatment plan, the mean dose difference $\Delta_{\text{Mean}}D$ was found to be (0.000 ± 0.076) Gy, equivalent to $(0.0 \pm 7.5)\%$. For the patient treatment plan, $\Delta_{\text{Mean}}D = (0.045 \pm 0.331)$ Gy, equivalent to $(1.0 \pm 7.3)\%$.

While the motion starting phase dependency could be found in both treatment plans, it was higher in the shorter (70 to 100 seconds) *VX-Vorbestrahlung* treatment plan and reduced in the longer (nine minutes) patient treatment plan.

4.4 SUMMARY

In this chapter, a new simulation software was presented which predicts the timing of an irradiation based on the treatment plan. The software uses model base data sets which were created in an extended analysis of the HICAT accelerator parameters.

The simulation uses a stochastic approach to model the observed variation in beam intensity and pause timing. For the beam intensity, an "intensity of the day" approach was used, which selects a fixed beam intensity in each repetition of the simulation. To calculate the pause timing, a combination of deterministic energy-dependent and stochastic parameters were used.

Due to modifications in the beam extraction system, the characteristic of the HICAT accelerator changed significantly in early 2013. To incorporate this change, two model base data sets were created for the simulation to reliably model the accelerator for 2012 and 2013 (see DIC, Schömers (2013); Schömers et al. (2013)).

In an extensive retrospective analysis of irradiation records, simulated accelerator response was compared to actual irradiation records of a test plan. This test plan was repeatedly irradiated during 2012 and 2013 and provided a good reference data set outside of the training data set. The result of these analyses suggest a good agreement between the simulation and the irradiation records.

The analysis of the 2012 data set found a large day-to-day beam intensity variation. This translates to large variations in the beam delivery sequence and large day-to-day differences in the resulting dose distributions. This is reproduced well by the simulation software. It also leads to a reduced dependence on the starting phase of the organ motion.

In the analysis of the 2013 data set, the variation in beam intensity was found to be much smaller. The beam delivery sequences have a higher reproducibility, which improves the predictive power of the simulation. This also translates into a stronger dependence on the starting phase of the organ motion, especially

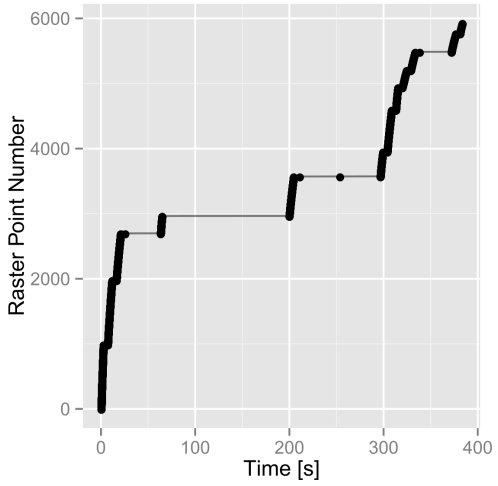

Figure 54: Example of an irradiation with several interlocks: During the irradiation of the *VX-Vorbestrahlung* treatment plan, at least five interlocks occured, visible as long horizontal lines between circles representing the irradiation of a raster point. This leads to unpredictable changes of the motion phase and complicates the calculation of dose distributions.

when calculating treatment plans with a shorter irradiation time. This is modeled well by the simulation, although subtle differences between simulated and reconstructed data are apparent.

Finally, dose measurements were performed using a moving phantom. In this experiment, a test plan and a patient treatment plan were measured in conditions comparable to typical patient motion. For the patient treatment plan, a dose deviation of $(1.0 \pm 7.3)\,\%$ was observed between the measurement and the dose prediction. This demonstrated the predictive power of the simulation as well as the dependence on the starting phase.

The simulation software has been used for further research in the research group (Batista (2016); Batista et al. (2018)).

4.5 DISCUSSION

While the simulation software already gives a high agreement between simulated and recorded data, subtle differences are apparent, especially in the analysis of the 2013 data set. The inclusion of several effects into the simulation could lead to improved simulation results: Implementation of the correct extraction behavior, inclusion of a spill pause and mitigation of the effects of interlocks.

In the current simulation, the extracted beam rises to full intensity immediately, when, in reality, it takes some milliseconds. By implementing a realistic *spill shape*, some of the deviation between simulation and measurements could be removed (Grözinger et al. (2006); Peters et al. (2008)). Further, the accelerator includes a *spill pause*, a voluntary beam hold, when the distance between two irradiated raster points exceeds a threshold. This 300 ms pause is currently not considered in the simulation.

Finally, the influence of interlocks has not been studied or implemented in this analysis. Due to their properties, they are hard to consider, as they are very infrequent and introduce a long pause of ≈ 40 seconds. This adds a random phase shift. Fig. 54 shows an example of an irradiation with at least five inter-

locks. Fortunately, the ongoing improvement of the HIT systems also reduces the number of interlocks.

Currently, calculating beam delivery sequences for gated treatment is not yet implemented. This could be added by taking the patient's breathing curve into account and would enable the simulation of gated irradiations using TRiP-4D.

The ongoing changes to the accelerator operation pose a challenge to the simulation software: Due to the implementation of new features of the acceleration process (for example, second-generation DIC, dynamic field control), the software can get out of date fast. Additionally, to calculate the model base data, a lot of manual data processing is necessary.

One solution could be an easy to use implementation of the simulation software. The model base data, which is currently calculated from several different measurements and data processing, could in future be automatically created using a specialized treatment plan. This treatment plan could be used to probe wide ranges of possible beam parameter combinations, which are automatically translated into base data. Further, this could be integrated into the normal QA process and also used for other automated measurements (intensity, beam position and width, homogeneity, ...).

With TRiP being a modular platform for dose calculation in ion beam therapy, it can be used for other facilities as well. Therefore, it could be beneficial to expand the simulation to encompass other proton or carbon facilities. Finally, the χ^2 and other statistical analyses could in future be used to characterize interplay in the clinical context.

5

4D TREATMENT PLANNING STUDY FOR ESOPHAGEAL CANCER

In this chapter, a treatment planning study for the treatment of esophageal carcinoma is presented. With the introduction of the heavy-ion gantry at HIT, new treatment options are available for tumors of the thorax and abdominal region. This study investigates the robustness of different planning geometries using a simplified 4D dose calculation and recommends optimal treatment planning options for each study patient.

5.1 INTRODUCTION

Similar to hepato-cellular carcinoma, esophageal cancer is a relatively rare disease. Only 1.5% of cancer incidences in Germany is attributed to esophageal cancer. Unfortunately, five-year survival rates are low at 21%, attributing to 2.4% of cancer deaths in 2014 (Robert Koch-Institut (Hrsg.) und die Gesellschaft der epidemiologischen Krebsregister in Deutschland e.V. (Hrsg.) (2017)).

In the treatment of esophageal cancer, radiotherapy is usually combined with surgery and chemotherapy (Sjoquist et al. (2011); Kranzfelder et al. (2011)). To improve the efficacy of the treatment, dose escalation studies (Minsky et al. (2002)) and new chemotherapy agents (Crosby et al. (2013)) have been introduced, albeit with little improvement of the treatment outcome. On the other hand, high dose conformity and local dose escalation (Carrington et al. (2016); Roeder et al. (2014)) have been shown to have a positive effect on the treatment outcome. In addition, the introduction of carbon ion radiotherapy has already been shown to have beneficial effects in the treatment of other cancers (Kamada et al. (2015); Jensen et al. (2015)). Hence, treating patients suffering from esophageal cancer using carbon ion radiotherapy may be beneficial as well.

In October of 2012, the heavy ion gantry at HIT has been introduced into the clinical routine (Galonska et al. (2013)). Since then, new beam angles are available in addition to the fixed horizontal beam lines, facilitating the treatment of esophageal cancer and other tumor sites closer to the center of thorax and abdomen.

In this chapter, a preliminary treatment planning study for the treatment of esophageal cancer is presented. Several questions are investigated within the study: Which are the best gantry angles for the therapy? Which of them are least affected by organ motion due to breathing? For the calculation of the dose, a simplified 4D dose calculation algorithm has been used. Hence, the sensitivity of this dose calculation to organ motion is a further topic of this study.

For the treatment planning study, CT data of four bronchial carcinoma patients has been used. Each data set contains a treatment planning CT and a 4D-CT consisting of seven motion phases. For each data set, a boost target volume for esophageal cancer was created by a physician, as well as contours for the lungs, heart muscle and spinal cord.

Treatment plans were created based on thirteen different treatment planning geometries and optimized using the treatment planning CT. The resulting treat-

ment plan was re-calculated quasi-statically on each of the motion phases and the resulting dose distributions were evaluated for target volume coverage and dose to organs at risk.

For each patient, it was possible to find at least one acceptable treatment plan geometry. In addition, the sensitivity of the calculation method to organ motion could be tested. For example, it is possible to estimate the size of a required ITV margin, further, a gating window was calculated which increases PTV coverage and reduces dose to organs at risk.

5.2 MATERIALS AND METHODS

In this section, the patient data sets and the details of the treatment planning are discussed. Further, the methods of evaluating the dose distributions are presented.

5.2.1 *Patient Datasets*

5.2.1.1 *CT Images*

For the study, treatment planning CTs and co-registered 4D-CTs of four bronchial carcinoma patients were used as a basis of a treatment planning study. Because the study was done retrospectively on selected patient data sets, breathing motion was not recorded during imaging or treatment and was not available for analysis. For each patient, one free-breathing treatment planning CT as well as a time-resolved 4D-CT was available. Both CTs were created in the same imaging session and using the same position and immobilization equipment. The CT scanner used was a *SIEMENS SOMATOM Sensation Open*.

In the case of patients 1 and 2, the slice distance of the planning CT was 5 mm, in the case of patients 3 and 4, the slice distance was 3 mm. In all cases, the slice distance of the co-registered 4D-CT was 3 mm. For each time-resolved CT, three images were reconstructed for the inhale phase ($In_{25\%}$, $In_{50\%}$, $In_{75\%}$) and four for the exhale phase ($Ex_{100\%}$, $Ex_{70\%}$, $Ex_{40\%}$, $Ex_{0\%}$). In this terminology, "$In_{25\%}$" refers to a patient inhaling, who has reached 25% of the maximum motion amplitude. "$Ex_{70\%}$" refers to the patient exhaling, with 70% of the maximum motion amplitude still left. Hence, in motion phase "$Ex_{40\%}$", the patient has exhaled further than at "$Ex_{70\%}$".

The validity of the co-registration of the planning CT and the 4D-CT was checked visually by opening the CTs in a DICOM viewer and verification of the relative position of the bony anatomy. It was found to be accurate within the error of a slice distance.

Further, the presence of contrast agent was checked in each CT image. Contrast agent has a large impact on range uncertainties and reduces the accuracy of the dose calculation. It was not found in any CT image.

COMPATIBILITY OF HOUNSFIELD UNITS Treatment planning CTs and 4D-CTs are using different reconstruction algorithms. Most noteworthy, the reconstruction kernels used are different, which leads to different Hounsfield Unit values for the same structures. Because the treatment planning system relies on a fixed relationship between electron density (represented by the Hounsfield Units in the CT) and the Water-Equivalent Path Length (WEPL) in a piece of

material, differences in the reconstructed electron density may lead to dose calculation errors.

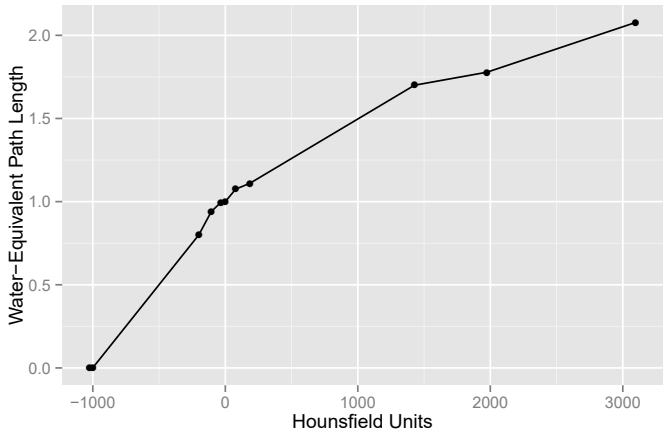

Figure 55: Representation of the Hounsfield Look-Up Table (*Body-HLUT*) used in this study.

In treatment planning, this issue is addressed by agreeing on a fixed set of imaging parameters and regularly measuring the electron density using standardized samples with known WEPL. This relationship is represented in the Hounsfield Lookup Table (HLUT). Unfortunately, this data is not available for the CT images used in this study.

Instead, the standard Body HLUT is used, shown in Fig. 55, which introduces a systematic error in particle range calculations. This systematic error does not exist if the Hounsfield Units of the planning CT and the 4D-CT are similar to each other, canceling out. Hence, the difference in Hounsfield units was evaluated for each patient data set.

For each CT, the Hounsfield Units (HU) of all CT voxels were entered into a histogram, as shown in Fig. 56 for the treatment planning CT and the 4D-CT of patient 1. In this histogram, several peaks are prominent, each representing a type of tissue: Air (at -1000 HU), lung tissue (at -900 HU) and soft tissues (at -150 to $+100$ HU).

The position of the peak center is similar, although the increased noise level of the 4D-CTs leads to a broadening of the peak widths. The largest peak center deviation of all patients is a shift of approximately 10 HU of the peak at -100 HU (Fatty Tissue). The fatty tissue in the 4D-CT appears to be more dense than in the treatment planning CT. Similar shifts were also found in the other patient datasets, the positions of other peaks were unaffected.

To estimate the impact of this shift, the change in Water-Equivalent Path Length can be calculated: At this position, the Hounsfield Lookup Table has a slope of 0.08/100 [WEPL/HU], a shift of 10 HU is therefore equivalent to a shift of 0.008 in WEPL. At -100 HU, the WEPL is 0.95, the relative error is therefore $0.008/0.95 = 0.8\%$. In 5 cm of fatty tissue, this introduces a range error of less than a millimeter. This uncertainty is considered small relative to the motion effects and was not corrected for this analysis.

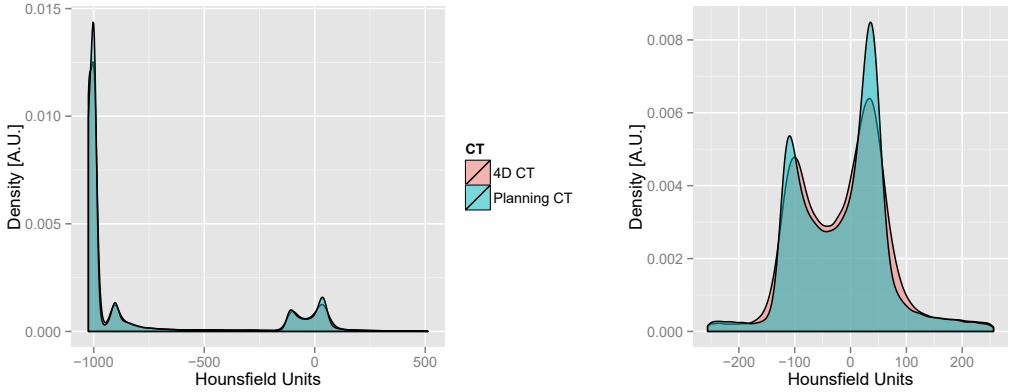

(a) Total Range (b) Soft Tissue

Figure 56: Comparison of Hounsfield Units (HU) of the Planning and 4D CTs for Patient 1. Each peak represents a certain type of tissue, with air (at −1000 HU), lung tissue (at −900 HU), fatty tissue (at −100 HU), and muscle tissue (at +40 HU). While most tissues are relatively unaffected, fatty tissue (at −100 HU) is shifted by ≈ 10 HU.

5.2.1.2 *Patient Contours*

Each patient data set was contoured by a physician, who delineated the patient's organs at risk (both lungs, the spinal cord and heart) on the treatment planning CT. Because none of the patients were originally patients suffering from esophageal cancer, a treatment volume was assumed for each patient and the corresponding PTV created by the physician.

The locations of the target volumes are shown in Fig. 57. For patients 1 and 2, the target volume is medium sized and approximately in the center of the esophagus. For patient 3, a smaller target volume located more in the cranial direction was chosen. Patient 4 has a large target volume, approximately twice the size of the one in patients 1 and 2, extending closer to the stomach.

CONTOUR PROPAGATION To evaluate the quality of the treatment plan, the contour sets created on the treatment planning CT were transferred to the 4D-CTs. To reduce the necessary work and to increase the reproducibility of the contour transfer, the *4D re-contouring* module of *OnQ rts V*2.0 by *OSL Oncology Systems Limited* was utilized. This software uses non-rigid registration to propagate patient volumes between non-rigid registered CT images.

The resulting contours were then reviewed by a physician, who removed any artifacts introduced by the automatic contour propagation and checked the validity of all contours.

ITV MARGIN APPROXIMATION Later in the study, an additional question was introduced: Is the calculation method sensitive enough to define an ITV margin? For this reason, the definition of CTV contours would have been necessary and the calculation of several dose optimizations for each PTV derived from the CTVs and ITVs. This was not done in this study, instead, a CTV was derived from the PTV on the 4D-CT images by subtracting a uniform margin of 2, 4, 6, 8 and 10 mm. These volumes were used to estimate the size of an ITV margin

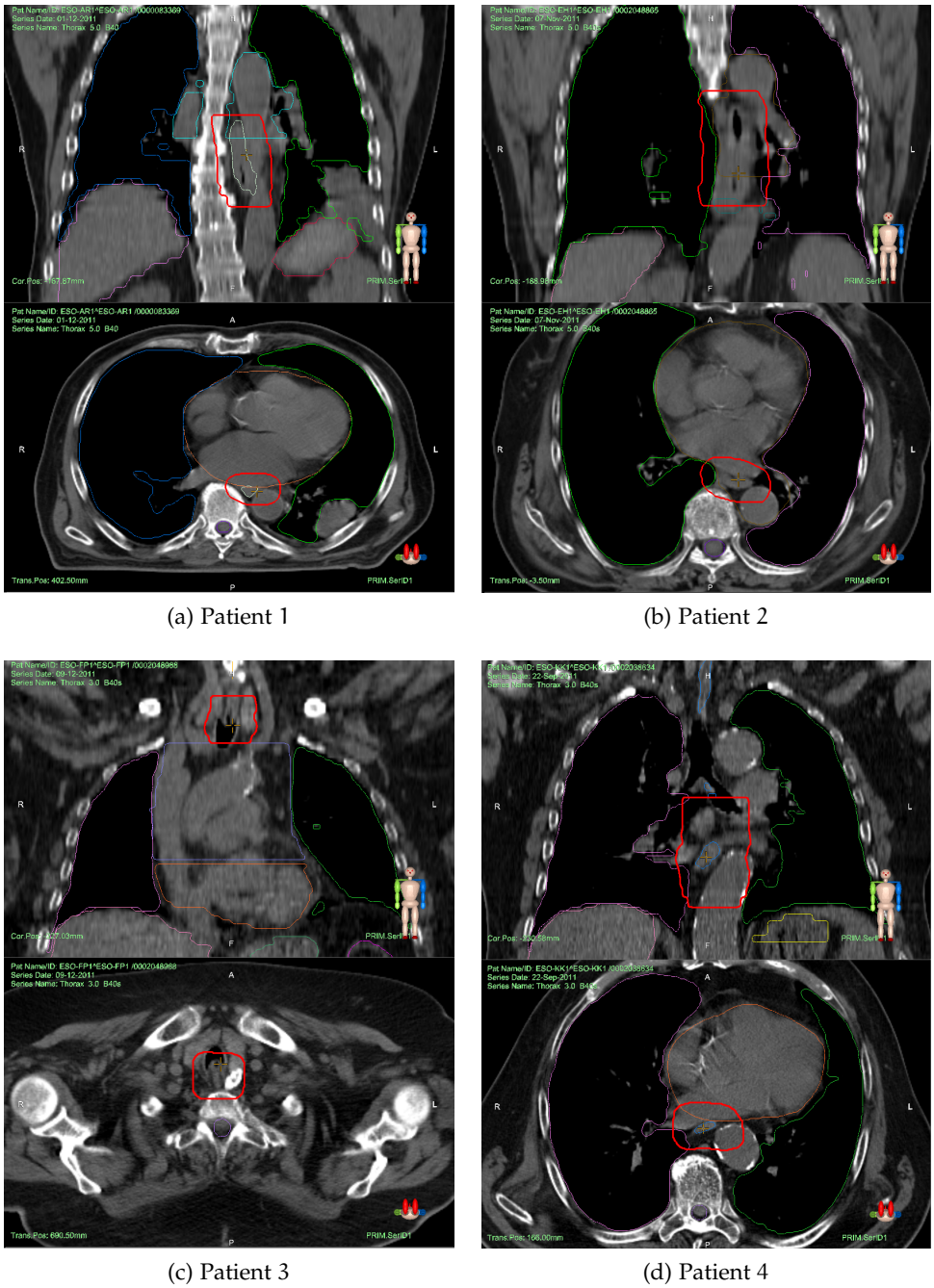

(a) Patient 1

(b) Patient 2

(c) Patient 3

(d) Patient 4

Figure 57: Planning CTs and assumed target volume locations (PTV in red) of all four patients.

necessary to attenuate the motion effects. Of course, this can only be viewed as a preliminary study.

5.2.2 *Treatment Planning*

The treatment planning study was performed based on 13 different planning templates with different treatment field geometries. Treatment plan optimization and quasi-static dose calculation was performed using the TRiP software; the resulting dose distributions were evaluated using dose-volume parameters.

5.2.2.1 *Geometries*

Taking into account the current and projected capabilities of the Heavy Ion Gantry used at the Heidelberg Ion Therapy center, four single-beam treatment plan variations and nine dual-beam treatment plan variations have been selected. It was assumed that the four principal gantry angles (0°, 90°, 180°, 270°) would be available initially. Only later, more gantry angles would be available.

All planning geometries are shown in Table 3 and Fig. 58 and 59, starting with simple single-beam geometries and following up with more complex two-field geometries with gantry angles more appropriate for the treatment of esophageal carcinoma.

Plan Geometry	Gantry Angle (Field 1)	Gantry Angle (Field 2)
Geometry 1	0°	
Geometry 2	180°	
Geometry 3	90°	
Geometry 4	270°	
Geometry 5	90°	270°
Geometry 6	135°	225°
Geometry 7	0°	180°
Geometry 8	25°	335°
Geometry 9	155°	205°
Geometry 10	175°	135°
Geometry 11	185°	225°
Geometry 12	90°	180°
Geometry 13	270°	180°

Table 3: Planning Template Geometries: Geometries 1 to 4 are using one single treatment field from one of the principal gantry angles. For geometries 5 to 13, two treatment fields are used from different gantry angles.

5.2.2.2 *Treatment Plan Optimization*

Dose calculations were performed in two steps. First, a treatment plan was optimized based on the treatment planning CT and each of the Template Planning Geometries. The resulting doses were then calculated, first on the treatment

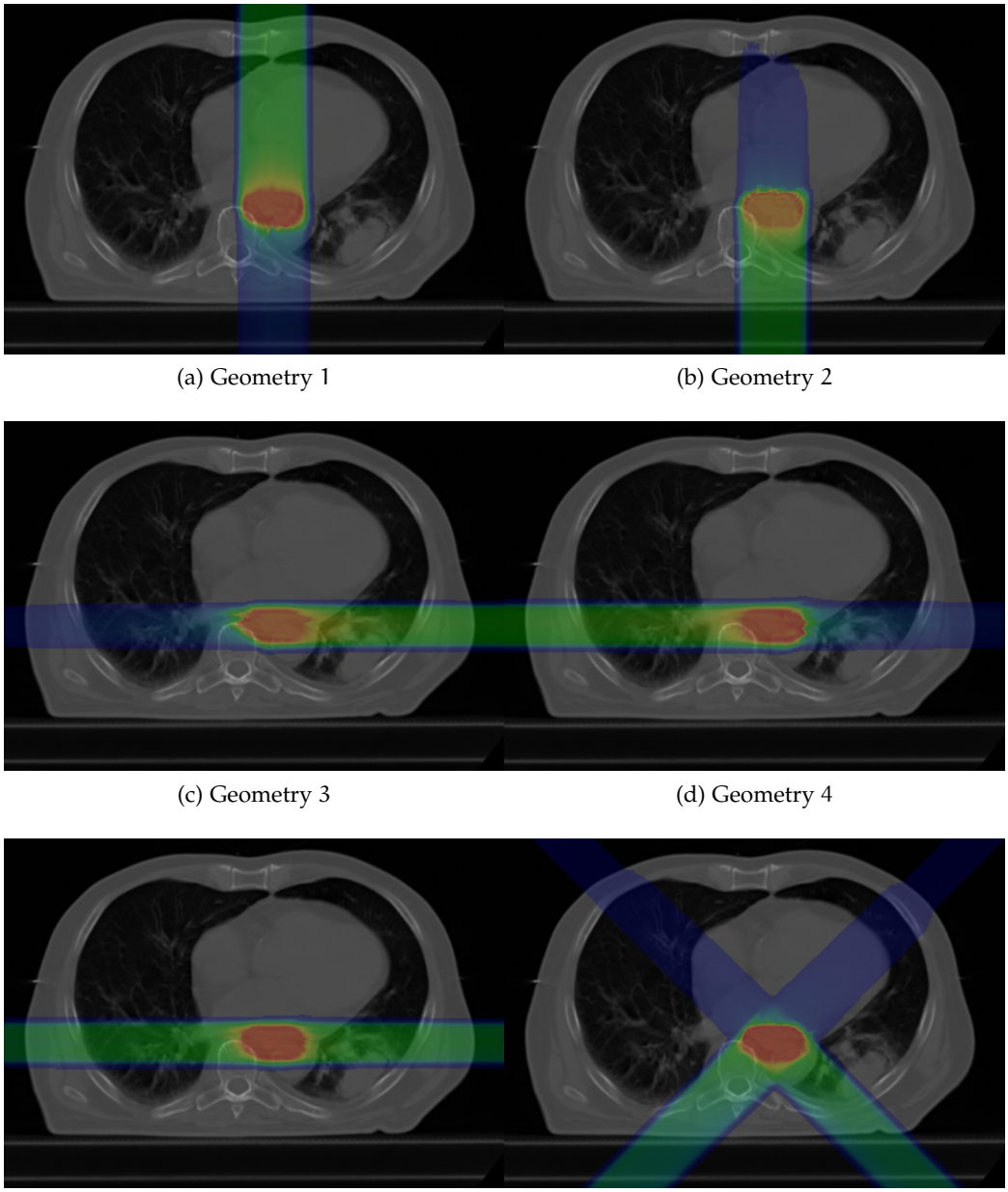

(a) Geometry 1 (b) Geometry 2

(c) Geometry 3 (d) Geometry 4

(e) Geometry 5 (f) Geometry 6

Figure 58: One- and two-field configurations used in this study. The angles were chosen to match the initially available and projected capabilities of the HIT heavy-ion gantry. At first, only the main angles (0, 90, 180 and 270° would be available, later, the full upper hemisphere would be added. Finally, all angles would be available for treatment. Thus, some simpler geometries and some more specific for the irradiation of the esophagus were selected.

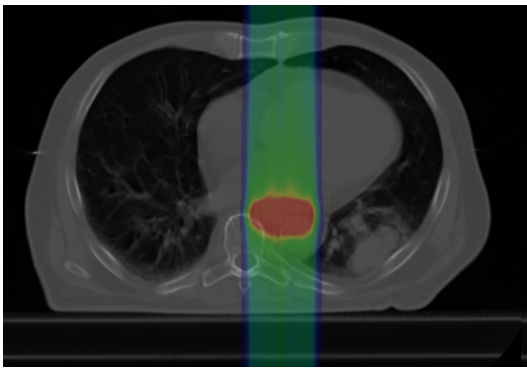

(a) Geometry 7

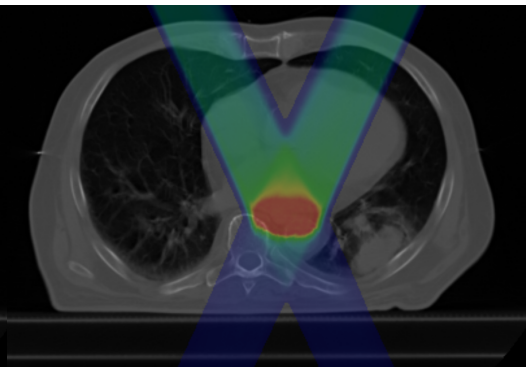

(b) Geometry 8

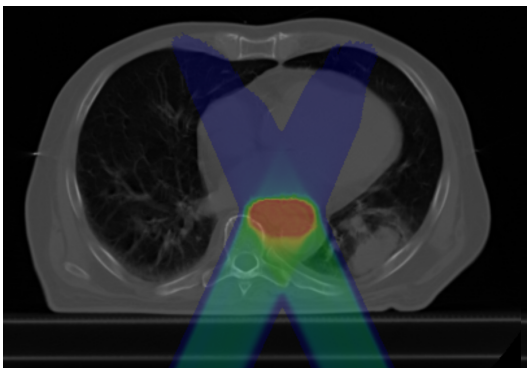

(c) Geometry 9

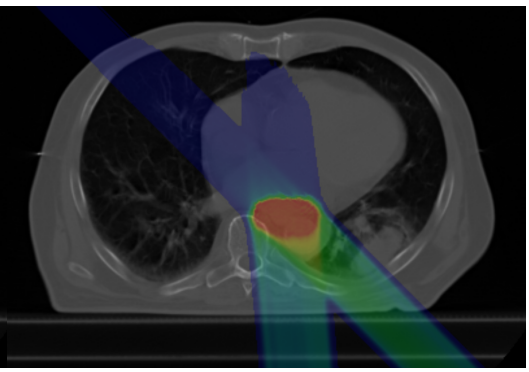

(d) Geometry 10

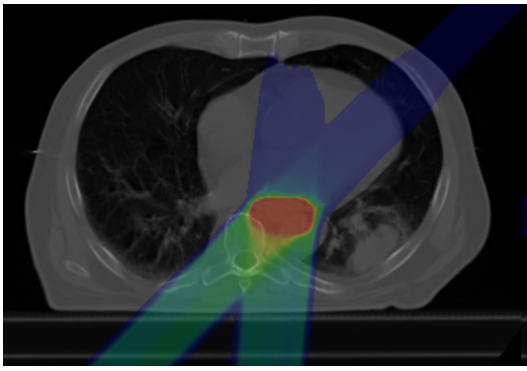

(e) Geometry 11

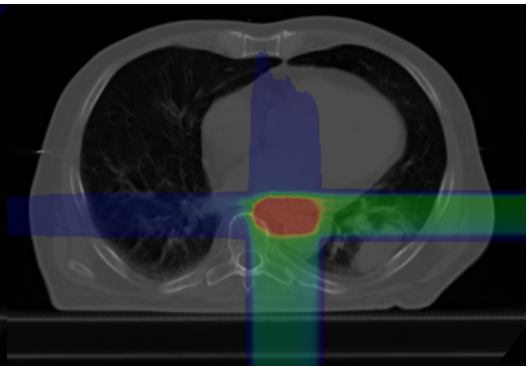

(f) Geometry 12

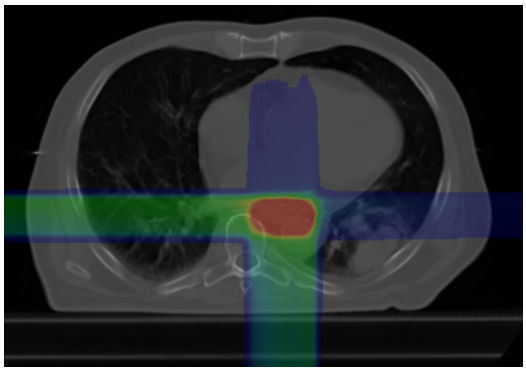

(g) Geometry 13

Figure 59: The remaining two-field configurations used in the study.

planning CT as a reference, but also on each of the motion phases of the 4D-CT. In this calculation, the treatment plan was not split up between the 4D-CT motion phase, but calculated on one motion phase only. This is referred to as "quasi-static" dose calculation.

All treatment plans use an actively raster scanned carbon ion pencil beam with parameters similar to the Heidelberg Ion Gantry. In coherence with the clinical protocol used in most carbon ion irradiations at HIT, the prescribed fraction dose was selected as 3 Gy (RBE). Hence, treatment is hypo-fractionated, with 15 fractions leading to a total dose of 45 Gy (RBE), 18 fractions to a total of 54 Gy (RBE).

All dose calculations were performed using the non-4D capable version of TRiP, developed at GSI. Because it uses text files as input for all commands, it has an inherent scripting support, hence it was possible to optimize thirteen different treatment plans for each of the four patients and calculate the doses on each of the seven motion phases.

Treatment planning was performed with TRiP's *optimize* command, using the recommended default calculation options[1]. No explicit constraints were used for sparing of organs at risk, and the treatment plan was normalized to the median dose inside the target volume. In this study, this set of options yielded a good coverage of the PTV with a reasonable sparing of normal tissue and organs at risk.

For patient 4, the calculation volume was especially large and the plan optimization could not be calculated using the 32 bit version of TRiP. Because the 64 bit version could not reproduce already calculated results of smaller volumes, it was decided to optimize the treatment plan on the regular 32 bit version of TRiP, but using a coarser dose calculation grid. The sub-sampling was only used in the memory-intensive optimization step, the later dose calculation was performed using the normal CT grid for each patient.

5.2.2.3 *Dose Calculation*

The dose distributions resulting from each optimized treatment plan were then calculated for the treatment planning CT as well as each of the 4D-CT motion phases. Each calculation results in an individual dose distribution, with the dose distribution calculated on the treatment planning CT regarded as the reference dose distribution. The dose distributions calculated on the motion phases reflect the deviations introduced by the organ motion.

Dose calculation was also performed using the non-4D version of TRiP. As in the optimization, the *dose* command was used with the *allpoints* dose calculation algorithm and *lowdose* biological effect calculation model. Hence, the algorithms used in the optimization and dose calculation are comparable to each other.

In the previous chapters, to calculate a 4D dose distribution, the particle fluence was accurately distributed between all motion phases to take into account all motion effects. This information is not available in this study, hence, accounting for the exact motion had to be neglected. Instead, the whole treatment plan was calculated on each of the motion phases. This approach, a "quasi-static" irradiation, is comparable to a breath-hold irradiation or a very fast application of the irradiation fields. This approach neglects the interplay pattern which would

1 *allpoints* dose calculation algorithm, *lowdose* biological effect calculation model, *fletcher-reeves* dose optimization algorithm, optimization cut-off of $\epsilon = 10^{-3}$ and dose cut-off of $\epsilon_g = 10^{-4}$.

normally result from breathing motion, but still accounts for range differences and motion of the target volume and organs at risk.

5.2.3 *Dose Evaluation*

With four patients, thirteen planning geometries and eight CTs used for dose calculation, over 400 different dose distributions have to be examined and compared to each other. Instead of inspecting every dose distribution individually, the quality of each treatment plan is evaluated using statistical dose parameters.

All dose distributions were analyzed for PTV coverage, over- and underdosage, dose homogeneity and dose in the organs at risk. Three different types of indices are used in this analysis: Dose Volume Histogram (DVH) parameters of the target volume and the organs at risk, a homogeneity index for the dose inside the PTV and a conformity index for the PTV. The organs at risk considered in this analysis are the heart, the spinal cord and the lungs.

DOSE VOLUME HISTOGRAM PARAMETERS In radiotherapy, the Dose Volume Histogram (DVH) is a universally used tool to characterize the quality of a treatment plan (Drzymala et al. (1991)). The cumulative DVH describes the volume $V(D)$ which receives at least the dose D and can be calculated either for the whole patient or target volumes and organs at risk.

Information about over- and underdosage and homogeneity of the dose in the target volume is evaluated by calculating the fraction of the volume receiving 95% or 107% of the prescribed dose ($V_{95\%}$, $V_{107\%}$).

Other indices can be derived from the DVH and have been proven significant in determining the quality of a treatment plan. In this study, the minimum and maximum dose in the volume (D_{Min}, D_{Max}) as well as the mean and the median dose in the volume (D_{Mean}, D_{Median}) have been calculated. Using these indices, deviation from the planned dose can be evaluated as well as high dose regions in organs at risk.

HOMOGENEITY INDEX In addition to the $V_{95\%}$ and $V_{107\%}$ indices, the Homogeneity Index (HI) is used to determine the homogeneity of the dose distribution inside the PTV. It is calculated from the dose difference between the highest and the lowest dose inside the PTV. Small high- and low-dose regions are excluded and instead of using D_{Max} and D_{Min}, $D_{5\%}$ and $D_{95\%}$ are used (Richter (2012)):

$$HI = \frac{D_{5\%} - D_{95\%}}{D_P} \tag{42}$$

To calculate $D_{5\%}$ and $D_{95\%}$, the dose percentiles with the 5% highest and lowest dose are removed. $D_{5\%}$ is the maximum dose remaining, $D_{95\%}$ is the minimum dose remaining. The dose prescribed to the PTV (D_P) is used to normalize the dose values.

In a homogeneous dose distribution, the difference between the highest and lowest dose in the PTV is smaller, therefore the resulting HI is smaller.

CONFORMITY INDEX In addition to the previous indices, the conformity index (CI) is a measure of the the conformality of the treatment plan. In the

implementation used in this study, it compares the dose deposited inside the PTV to the dose deposited inside the whole body (Steidl (2011)). It is defined as

$$\text{CI (PTV)} = \frac{\int_{\text{PTV}} D(\vec{x})\, d\vec{x}}{\int D(\vec{x})\, d\vec{x}} \tag{43}$$

The integral in the numerator ($\int_{\text{PTV}}$) evaluates only the dose inside the PTV; the integral in the denominator covers the whole patient.

An ideal plan has a high CI (closer to 100%), and all dose is deposited inside the target volume. When a higher fraction of the dose is deposited in the normal tissue, this value decreases.

ORGANS AT RISK For each of the evaluated organs at risk, a different dose index was used. Because there is no absolute dose prescribed to the treatment plans, no definitive dose limits can be established. Instead, the most suitable predictors for adverse effects was employed for each organ at risk.

For the lungs, the relevant clinical end point is symptomatic pneumonitis. Being a parallel organ, the dose response is gradual and depending on both the dose level and affected volume (Marks et al. (2010a)). Studies have identified the highest predictive power when using volume indices, hence, the $V_{20\%}$ was used to describe the dose to each lung (Marks et al. (2010b)).

For the spinal cord, the relevant clinical end point is myelopathy. The spinal cord is a serial organ and therefore susceptible to damage from small volumes of high doses. Here, the maximum dose D_{Max} has a high predictive power.

For the heart, pericarditis is the relevant clinical end point. Here, the mean dose D_{Mean} to the heart muscle has the highest predictive power.

5.3 RESULTS

In this section, two sets of results are presented. First, the optimal planning geometries are presented for each patient. Then, the viability of the dose calculation and analysis for use in an organ motion case is presented.

5.3.1 *Optimal Treatment Planning Geometries*

For each of the patients, optimal treatment planning geometries are presented. In an optimal treatment plan, the dose coverage of the PTV is high and homogeneous; at the same time, the dose to the organs at risk must be reasonably small. Because of the limited capabilities of the heavy ion gantry at the introduction, two optimal treatment planning geometries are determined: One single-field geometry for the initially usable gantry angles and one two-field geometry using gantry angles which should become available later.

First, the results of the dose optimization based on the treatment planning CTs are presented. After that, the dose calculation on the motion 4D-CT is evaluated.

5.3.1.1 *Planning CT Results*

As a reference for the quality of the treatment plan, the results of the dose optimization and calculation based on the treatment planning CT are evaluated first. The evaluation encompasses the coverage of the PTV including over- and

underdosage, as well as the dose to organs at risk (lungs, spinal cord and heart muscle). Only the most important indices are shown in Fig. 60, detailed results are found in the appendix in section B.1 on page 143.

PTV COVERAGE Coverage of the PTV was assessed using $V_{95\%}$(PTV), the Conformity Index (CI) and Homogeneity Index (HI) of the PTV. Independent of the patient, the coverage was better in treatment plans using two irradiation fields. $V_{95\%}$(PTV) is $> 94\%$ for all one-field geometries, $> 98\%$ for all two-field geometries. All treatment plans show high conformality (CI(PTV) values > 0.82 for all one-field geometries and > 0.90 for all two-field geometries) and high homogeneity (HI(PTV) $< 9.5\%$ for all one-field geometries, $< 6\%$ for all two-field geometries).

Every treatment plan exhibited good PTV coverage, high dose conformity and good homogeneity. Treatment plans using two fields had a small advantage over plans using only one field.

PTV HOT SPOTS Overdose regions ("hot spots") inside the PTV were assessed using $V_{107\%}$(PTV) and D_{Max}(PTV). The size of the volume subject to overdose was similar in all patients, with $V_{107\%}$(PTV) $< 1.2\%$ for all one-field plans and $< 0.3\%$ for all two-field plans. In all patients and planning geometries, D_{Max}(PTV) $< 120\%$ D_P except for patient 4 (geometry 2 (122%) and geometry 11 (133%)).

In general, only small volumes received a moderate amount of overdose. Again, two-field treatment plans performed slightly better, with smaller overdose regions. The dose maximum was similar in all geometries, and no pronounced difference between one- and two-field geometries were found.

PTV COLD SPOTS Underdose regions ("cold spots") inside the PTV were assessed using $V_{95\%}$(PTV) and D_{Min}(PTV). The size of the volume subject to underdosage was dependent on the number of fields and the patient. For one-field treatment plans, D_{Min}(PTV) was as low as 40%, irrespective of the patient. For two-field treatment plans, it depends on the patient: For patient 1, D_{Min}(PTV) $> 85\%$, patient $2 > 70\%$, patient 3: $> 80\%$. For patient 4, D_{Min}(PTV) $> 70\%$, except for geometry 9 with D_{Min}(PTV) $= 52\%$.

In general, one-field geometries showed more pronounced underdose regions than two-field geometries. Additionally, patient 4, with a larger PTV and a higher fraction of lung tissue inside the PTV, the treatment plan exhibited more cold spots.

DOSE NORMALIZATION Large regions with over- or underdosage, or regions of extremely high or low doses inside the PTV, as well as errors in the normalization of the dose can lead to a deviation in either median or mean dose of the PTV. In all patients and all plan geometries, D_{Median}(PTV) and D_{Mean}(PTV) were 98 - 100%. No severe dose deviations were found in any plan and each treatment plan was well normalized.

ORGANS AT RISK For the organs at risk, $V_{20\%}$ of the individual lungs, as well as D_{Max}(Spinal Cord) and D_{Mean}(Heart) were evaluated. For patients 1, 2 and 4, V_{20}(Left Lung) $< 22\%$, V_{20}(Right Lung) $< 20\%$. For patient 3, this was even smaller, with V_{20}(Lung) $< 5\%$ for both sides. For all patients, D_{Max}(Spinal Cord) was between 0 and 78% planned dose (D_P). For an assumed planned

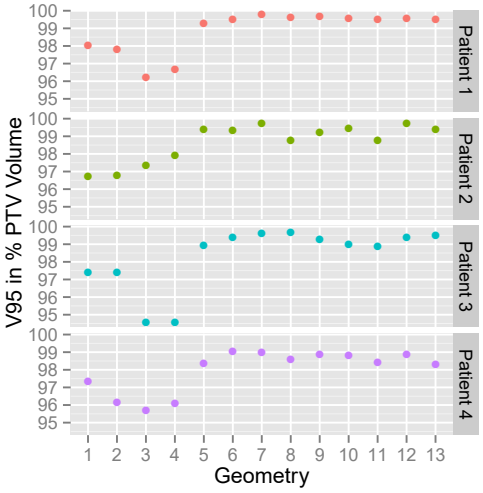

(a) $V_{95\%}$

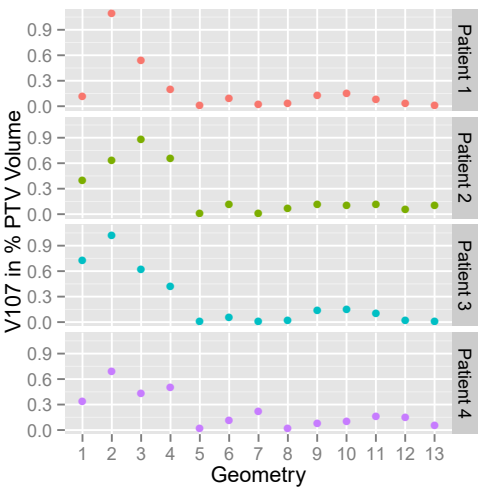

(b) $V_{107\%}$

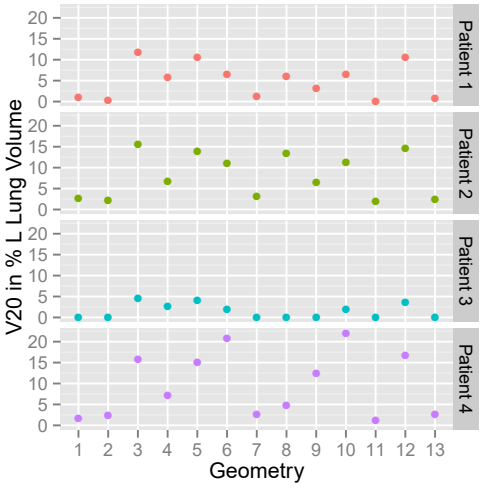

(c) Left Lung $V_{20\%}$

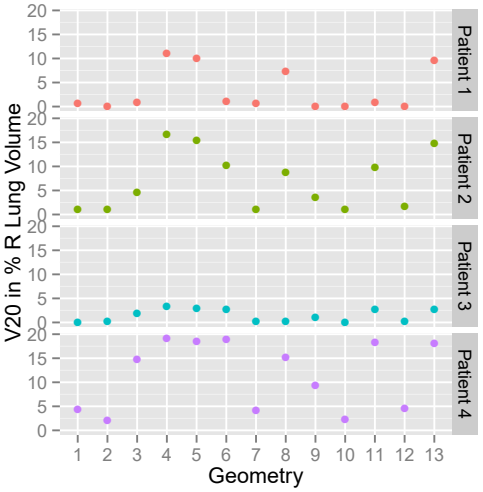

(d) Right Lung $V_{20\%}$

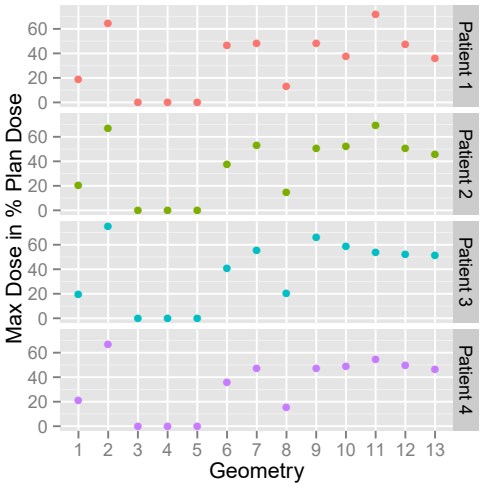

(e) Spinal Cord D_{Max}

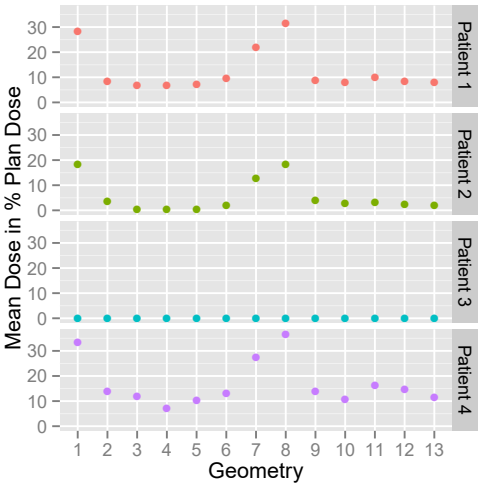

(f) Heart D_{Mean}

Figure 60: Treatment Planning Results: Selected parameters of the resulting dose distributions, calculated on the treatment planning CTs. All treatment plans are viable treatment options; generally speaking, the two-field geometries (5 to 13) result in better treatment plans compared to one-field geometries (1 to 4).

dose of 60 Gy (RBE), the tolerable dose to the spinal cord corresponds to 83%, so all treatment plans are safe for treatment. The heart muscle and PTV are overlapping in patients 1, 2 and 4, this region was not explicitly spared. For these patients, D_{Mean}(Heart) ranged from 0 to 37%, depending on patient and geometry. For patient 3, D_{Mean}(Heart) $< 1\%$. For the assumed planned dose of 60 Gy (RBE), the tolerable dose corresponds to 43%, which was achieved in all treatment plans.

SUMMARY With regard to the static planning CT, every generated treatment plan is of high quality in terms of target coverage and achieves a high level of organ at risk sparing. Some underdose regions are expected, mainly because of the lung tissue included inside of the PTV, but all of the treatment plans can potentially be used for treatment. In the static case, treatment plans with two irradiation fields were performing better than treatment plans with only one field.

5.3.1.2 *4D-CT Quasistatic Calculation Results*

In this section, the results of the quasistatic dose calculations are presented. Again, only the most important dose indices are shown in Fig. 61, the detailed results can be found in the appendix in section B.1 on page 143. For each dose index and planning geometry, the range of the index values of all motion phases are presented in a box plot.

PTV COVERAGE For all patients and planning geometries, V_{95}(PTV) is reduced in contrast to the planning CT, in some cases down to 50%. The difference between single and dual field geometries has vanished. Instead, individual beam geometries perform better than others, geometries 1, 2, 9, 10 and 11 are universally good in each patient. There is a large difference between individual patients: For patient 1, V_{95}(PTV) is 60-90%, patient 2: 50-90%, patient 3: 80-98% and patient 4: 60-95%.

Similarly, the Conformity Index (CI) is reduced. As for the V_{95}, geometries 1, 2, 9, 10 and 11 are still above 65% in all patients. For patient 1, CI is 35-80%, patient 2: 40-80%, patient 3: 65-85% and patient 4: 50-85%.

The dose distribution is more inhomogeneous, which is reflected in the Homogeneity Index (HI). It is largely dependent on the patient. For patient 1, HI is 25-50%, patient 2: 15-80%, patient 3: 5-25%, patient 4: 5-25% (except for geometry 3 with up to 70%).

PTV HOT SPOTS Differences in water-equivalent path lengths can also lead increased dose in overlapping treatment fields. Treatment plans with only one treatment field are less susceptible to overdoses.

In comparison to the planning CTs, V_{107}(PTV) is increased, although still below 5% in most planning geometries. Geometry 5, 12 and 13 are exhibit high-dose regions in up to 18% of the target volume.

For patient 1, V_{107}(PTV) is 1 - 7%, (except for geometry 5: 18%), patient 2: 1 - 5%, (geometry 5: 10%), patient 3: 1 - 5%, (geometry 5: 15%), patient 4: 1 - 5%.

The maximum dose (D_{Max}) has a median value between 110% and 125% planned dose D_P for most geometries. Only for patient 4 and geometry 11, a max dose D_{Max} of 140% D_P is reached.

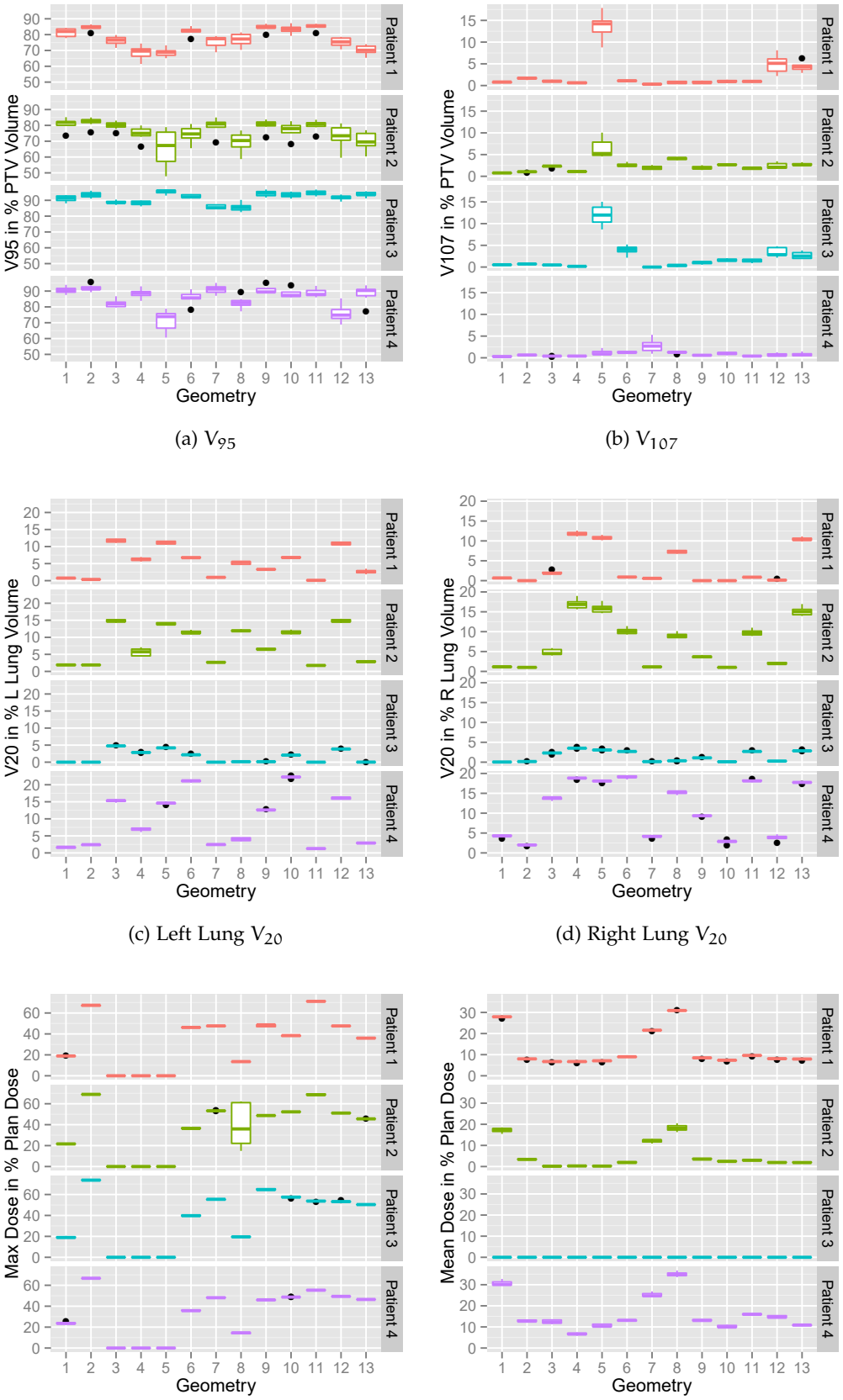

(a) V_{95}

(b) V_{107}

(c) Left Lung V_{20}

(d) Right Lung V_{20}

(e) Spine Maximum Dose

(f) Heart Mean Dose

Figure 61: Quasistatic Calculation Results: Selected parameters of the resulting dose distributions, calculated on the 4D-CTs. All treatment plans have a reduced target volume coverage, depending on the patient and treatment geometry. The difference between one- and two-field geometries is reduced. Doses to organs at risk do not vary for most patients and geometries.

Regarding V_{107}(PTV) and D_{Max}, planning geometries with only one irradiation field only show small deviations from the planning CT results. Treatment plans with two fields show an increase of D_{Max} due to overlapping fields.

PTV COLD SPOTS In comparison with the treatment planning CT calculations, the minimum dose (D_{Min}(PTV)) is decreased: For patient 1: 0-30% planned dose D_P, patient 2: 0-40% D_P, patient 3: 20-80% D_P, patient 4: 10 - 60% D_P.

Of course, cold spots are a direct result of the organ motion inside of the PTV. This is expected and the reason for the introduction of the ITV and PTV margins. A cold spot inside the PTV can be tolerated as long as the CTV is still properly irradiated.

DOSE NORMALIZATION Larger volumes of over- or underdosage or extreme deviations from the planned dose affect the median and mean dose applied to the PTV. In this study, the median dose D_{Median} is 96 - 102% planned dose for all patients, the mean dose D_{Mean} 90 - 102% planned dose.

D_{Mean} is reduced by up to 10% for patients 1 and 2, and by up to 3% for patients 3 and 4. This result can be explained by larger low dose regions inside the lung tissue.

ORGANS AT RISK All organs at risk have a very similar radiation exposure in comparison to the planning CT; the organ motion has almost no influence. Hence, the results for lung, heart and spinal cord dose from the static calculation are still valid.

There is only one exception in the case of patient 2, geometry 8. Here, a shift in the position of the heart muscle reduces the water-equivalent path length for one irradiation field, as seen in Fig. 67 on page 120. Here, the dose to the spinal cord (D_{Max}(Spinal Cord)) is dependent on the motion phase. This phenomenon will be discussed later in context of the sensitivity of the algorithm.

SUMMARY As expected, all plan quality indices are degraded, which is due to the free-breathing treatment planning CT not exactly matching any particular motion phase. Depending on the slice position of the free-breathing CT, the image data is acquired in different motion phases.

The distinction in plan quality between one-field and two-field geometries is reduced, instead, individual geometries (1, 2, 9, 10, 11) provide a good coverage of the PTV, with $V_{95} > 80\%$.

Doses to the organs at risk are similar to the treatment planning CT calculations, with the exception of one treatment geometry in patient 2, where a small change in the water-equivalent path length increases the dose to the spinal cord in some motion phases.

5.3.1.3 *Optimal Treatment Geometries*

Using the results of the quasi-static calculations, optimal treatment plans can now be recommended. First, a general treatment planning strategy viable for all patients is discussed. Then, the optimal treatment plans for each individual patient are presented.

OPTIMAL TREATMENT PLANS FOR ALL PATIENTS Based on the V_{95}(PTV) and Conformity Index, the planning geometries 1, 2, 9, 10 and 11 all performed

reliably in each patient with a good coverage of the PTV. All treatment plans exhibit a high plan quality, with V_{107}(PTV) below 2.5% and D_{Min}(PTV) comparable to other treatment plans.

The difference between the treatment plans is found in the resulting dose to organs at risk. Geometries 1 and 2 are single irradiation fields from anterior and posterior, respectively, with almost no dose to the lungs (V_{20}(Lung) below 5%). Instead, dose is deposited in the heart muscle (D_{Mean}(Heart) up to 35% in Geometry 1) or in the spinal cord (D_{Max}(Spinal Cord) up to 75% in Geometry 2). These geometries could give an advantage in patients with respiratory preconditions.

Geometries 9, 10 and 11 are all from posterior and using two treatment fields, which reduces the dose to the heart muscle ($D_{Mean} < 16\%$) and the spinal cord, depending on the geometry. However, the dose to the lungs is increased, either to both lungs (Geometry 9, V_{20}(Lung) $< 13\%$) or mainly to one side (Geometry 10, V_{20}(Left Lung) $< 23\%$; Geometry 11, V_{20}(Right Lung) $< 18\%$). Geometry 9 features the best compromise between both lungs and dose to the spinal cord (D_{Max}(Spinal Cord) $< 65\%$).

All treatment plans result in a good target volume coverage in each patient and tolerable doses to the organs at risk. Individual patient predispositions can be accounted for by choosing a treatment plan which spares the corresponding organ.

INDIVIDUAL OPTIMAL TREATMENT PLANS While the treatment planning geometries 1, 2, 9, 10 and 11 are universally good treatment options in all patients alike, it is desirable to know which treatment plan is optimal for each individual patient and their respective target volume position and size. To find this optimal treatment plan, the treatment plans with the best coverage of the PTV, indicated by a high V_{95} and Conformity Index, were selected. Out of this selection, the treatment plan which best spared the organs at risk was chosen as optimal treatment plan. For each patient, a one-field and a two-field treatment plan was selected.

OPTIMAL TREATMENT PLAN FOR PATIENT 1 For patient 1, geometries 1, 2, 6, 9, 10 and 11 yield plans with good coverage (V_{95}(PTV) $> 80\%$, CI $> 70\%$). None of the treatment plans show signs of severe overdosage ($V_{107} > 4\%$ only in geometries 5, 12 and 13).

Out of the one-field geometries, the selection between Geometry 1 and 2 is a trade-off between higher dose to the heart muscle or the spinal cord. Geometry 1 yields 29% D_{Mean}(Heart), 20% D_{Max}(Spinal Cord); Geometry 2 yields 9% D_{Mean}(Heart), 68% D_{Max}(Spinal Cord). In both cases, V_{20}(Lung) $< 1\%$. To reduce the risk of damage to the spinal cord, Geometry 1 is preferred.

Out of the selected two-field geometries, all plans yield a similar dose to the lungs and heart muscle (V_{20}(Lung) $< 7\%$, D_{Mean}(Heart) $< 10\%$. The largest difference is found in the dose to the spinal cord, with 39% D_{Max}(Spinal Cord) as the minimum value in Geometry 10. Therefore, this geometry is preferred.

The optimal treatment plans for patient 1 are Geometries 1 and 10, as shown in Fig. 62. This treatment plan might even be optimized by weighting the fields differently or a combination of 1 and 10 to spare the spinal cord even further.

OPTIMAL TREATMENT PLAN FOR PATIENT 2 For patient 2, geometries 1, 2, 7, 9 and 11 yield plans with good coverage (V_{95}(PTV) $> 80\%$, CI $> 70\%$). None

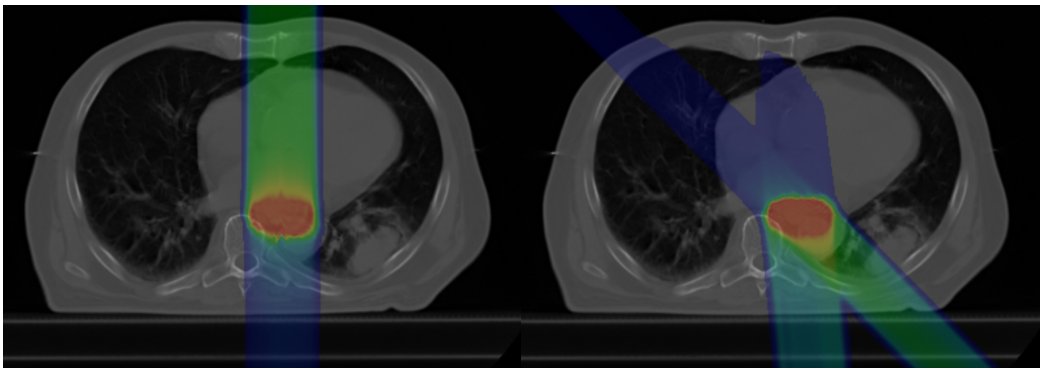

(a) Geometry 1 (b) Geometry 10

Figure 62: Optimal Treatment Plans for Patient 1: Both Geometry 1 and 10 reduce the dose to the spinal cord while yielding a high PTV coverage. A combination of geometry 1 and 10 could further improve the resulting dose distribution.

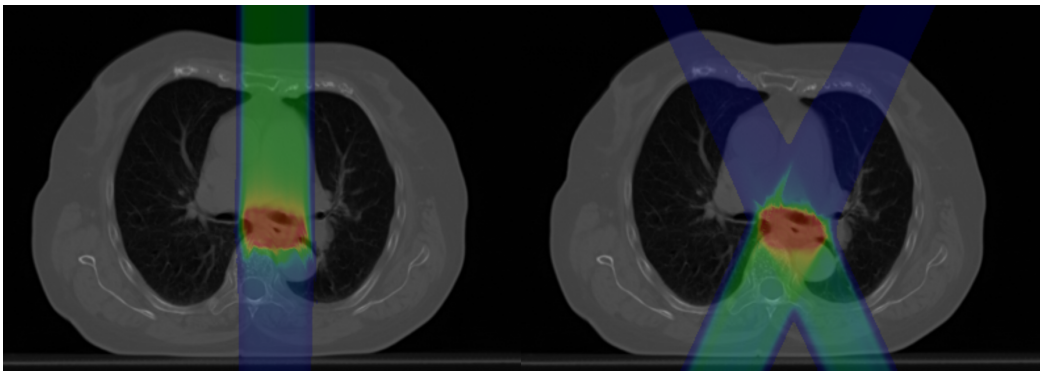

(a) Geometry 1 (b) Geometry 9

Figure 63: Optimal Treatment Plans for Patient 2: Geometries 1 and 9 yield the highest PTV coverage and lowest dose to the spinal cord. The results are similar to Patient 1.

of the treatment plans show signs of severe overdosage ($V_{107} > 4\%$ only in geometries 5 and 8).

As with the previous patient, the selection between geometries 1 and 2 is a trade-off between higher dose to the heart muscle or the spinal cord. Geometry 1 yields 18% D_{Mean}(Heart), 22% D_{Max}(Spinal Cord); Geometry 2 yields 4% D_{Mean}(Heart), 69% D_{Max}(Spinal Cord). In both cases, V_{20}(Lung) $< 2\%$. To reduce the risk of damage to the spinal cord, Geometry 1 is preferred.

Out of the selected two-field geometries, all plans yield a similar dose to the lungs and heart muscle (V_{20}(Lung) $< 12\%$, D_{Mean}(Heart) $< 12\%$. The largest difference is found in the dose to the spinal cord, with 49% D_{Max}(Spinal Cord) as the minimum value in geometry 9. Therefore, this geometry is preferred.

The optimal treatment plans for patient 2 are geometries 1 and 9, as shown in Fig. 63. This patient is very similar to patient 1 in terms of PTV size and localization and has similar treatment planning results.

OPTIMAL TREATMENT PLAN FOR PATIENT 3 Patient 3 is different from the first two patients, with a smaller, more cranial and less mobile PTV, which results in a better coverage in the quasi-static dose calculations. In this patient,

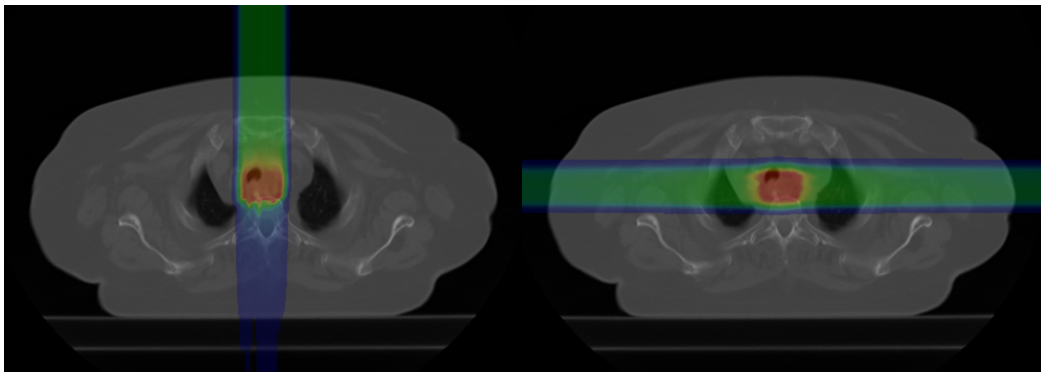

(a) Geometry 1 (b) Geometry 5

Figure 64: Optimal Treatment Plans for Patient 3: The cranial position of the PTV reduces the dose to the lungs and the heart muscle. Geometries 1 and 5 yield the highest PTV coverage with the smallest dose to the spinal cord.

geometries 1, 2, 5, 6, 9, 10, 11, 12 and 13 result in plans with very good coverage (V_{95}(PTV) $>$ 90%, CI $>$ 70%). Some of the treatment plans show signs of overdosage ($V_{107} > 4\%$ in geometries 5 and 6).

Because of the cranial position of the PTV, the dose to the heart muscle can be neglected for all treatment plans, D_{Mean}(Heart) $<$ 1%. Similarly, the dose to the lungs is reduced. Therefore, the selection between Geometry 1 and 2 is simple, in both cases, V_{20}(Lung) $<$ 1%. Geometry 1 yields 20% D_{Max}(Spinal Cord), geometry 2 72% D_{Max}(Spinal Cord), hence, geometry 1 is preferred.

Choosing the optimal two-field geometry is less straightforward. Out of the selected two-field geometries, all plans yield a similar dose to the lungs (V_{20}(Lung) $<$ 4%. Again, the largest difference is found in the dose to the spinal cord, with D_{Max}(Spinal Cord) $<$ 1% as the minimum value in geometry 5. Unfortunately, this is also the treatment plan with the highest overdose volume (V_{107}(PTV) $=$ 13%). On the other hand, this approach reduces the dose to the spinal cord to almost zero.

The optimal treatment plans for patient 3 are Geometries 1 and 5, as shown in Fig. 64. While Geometry 5 allows an irradiation with almost no dose to the spinal cord, setup uncertainties and motion might lead to overdose regions inside the PTV. Here, the single-field treatment plan might be more robust, especially as the intra-fractional motion is smaller and the general coverage of the PTV is already high with just one treatment field. Indeed, the irradiation through the shoulder section might not be practical in every patient.

OPTIMAL TREATMENT PLAN FOR PATIENT 4 Patient 4 is also different from the other patients, with a caudal PTV twice as large as compared to patients 1 and 2. This can lead to a larger dose to the lung tissue. In this patient, geometries 1, 2, 7, 9, 10, 11 and 13 yield plans with very good coverage (V_{95}(PTV) $>$ 90%, CI $>$ 75%). None of the treatment plans show signs of severe overdosage ($V_{107} <$ 4%).

As with patients 1 and 2, the selection between Geometry 1 and 2 is a trade-off between higher dose to the heart muscle or the spinal cord. Geometry 1 yields 31% D_{Mean}(Heart), 24% D_{Max}(Spinal Cord); Geometry 2 yields 13% D_{Mean}(Heart), 68% D_{Max}(Spinal Cord). In both cases, V_{20}(Lung) $<$ 4%. To reduce the risk of damage to the spinal cord, Geometry 1 is preferred.

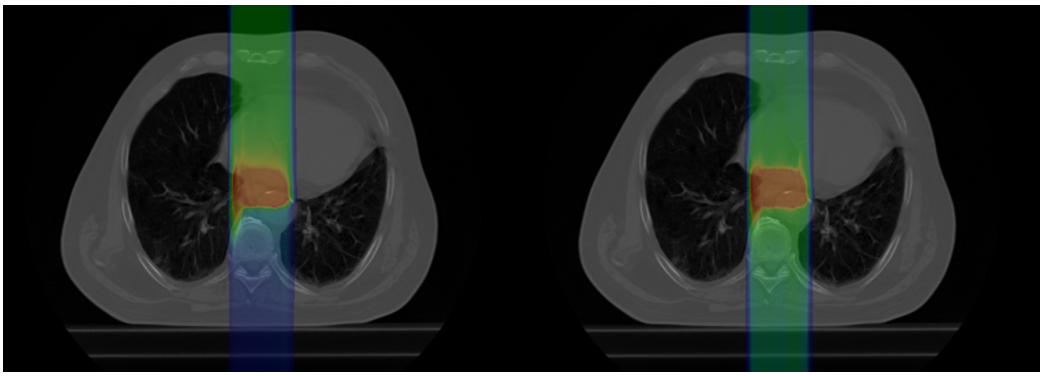

(a) Geometry 1 (b) Geometry 7

Figure 65: Optimal Treatment Plans for Patient 4: Geometries 1 and 7 yield a high PTV coverage. The selection of treatment fields from anterior and posterior reduces the dose to the lungs significantly, as this larger target volume is situated between the lungs.

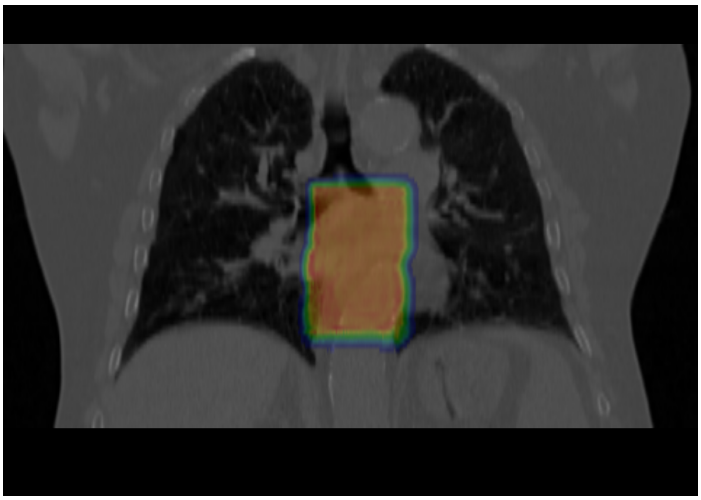

Figure 66: Coronal View of the Target Volume of Patient 4 and the dose distribution resulting from geometry 1 (one field from 0° gantry angle): Due to the size and position of the PTV, lateral treatment fields increase the dose to the lung significantly. Hence, treatment fields from anterior and posterior are preferred.

Out of the selected two-field geometries, all plans yield a similar dose to the spinal cord (D_{Max}(Spinal Cord) $< 56\%$). A large difference can be found between the planning geometries 9, 10, 11 and 13 (higher lung dose, V_{20}(Lung) $< 23\%$, lower heart dose, D_{Mean}(Heart) $< 16\%$) and Geometry 7 (lower lung dose, V_{20}(Lung) $< 4\%$, higher heart dose, D_{Mean}(Heart) $= 26\%$). Using Geometry 7, a small increase in heart dose yields a better sparing of lung tissue.

The optimal treatment plans for patient 4 are therefore geometries 1 and 7, as shown in Fig. 65. The longer PTV (illustrated in Fig. 66) leads to an increased dose to the lungs which can be mitigated by irradiating from the front and the back of the patient, sparing the lung tissue.

5.3.2 *Sensitivity of the Dose Calculation to Organ Motion*

In contrast to the previous section, which concentrated on the optimal treatment solution, this section concentrates on the sensitivity of the calculation method.

Three examples are presented: Variation of the calculated dose to organs at risk due to organ motion, definition of a CTV margin from quasi-static dose calculation and definition of gating window sizes from 4D dose calculation results.

5.3.2.1 *Variation in Spinal Cord Dose*

For most organs at risk, the calculated dose indices did not vary in between the dose calculations based on the treatment planning CT and the 4D-CTs. This was not the case for patient 2, geometry 8. In this case, D_{Max}(Spinal Cord) calculated on the treatment planning CT is 17% D_P. In the quasi-static calculation, D_{Max}(Spinal Cord) covers a range of 17% to 63% D_P.

In Fig. 67, this phenomenon is explained: Because of the motion of the heart muscle in the different motion phases, the water-equivalent path length changes in between the treatment planning CT and individual motion phases of the 4D-CT. Because of that, some parts of the treatment fields have a higher range than necessary and the dose is deposited in the spinal cord. This effect is not foreseeable from the treatment planning CT alone and can be used to increase robustness of treatment plans.

5.3.2.2 *CTV Coverage and Margins*

According to ICRU reports 50, 62 and 83 (Landberg et al. (1993, 1999); Grégoire et al. (2010)), a PTV should be created by adding a margin to the CTV, accounting for uncertainties in patient setup and motion. It is designed in such a way, that the respective CTV is always covered by the prescribed dose. In the previous analysis, only the coverage of the PTV is assessed, not the coverage of the CTV.

To estimate the required internal margin from the dose calculations, it is necessary to start from a CTV and add margins of different sizes to the PTV, optimize a treatment plan and evaluate the dose inside the CTV. Due to the preliminary scope of this study, this was not done. Instead, a CTV is calculated from the PTV by uniformly shrinking the PTV. The resulting dose inside this CTV is then evaluated.

The CTVs are created in steps of 2 mm (CTV 1 is PTV minus 2 mm, CTV 2 is PTV minus 4 mm). Using the dose distributions calculated earlier, $V_{95\%}$(CTV) is calculated for each of the CTV contours.

For this analysis, only the optimal treatment plans, as defined in the previous section, are analyzed. Once the median V_{95}(CTV) exceeds 95%, the coverage is assumed to be a sufficient. In Fig. 68, the results of the evaluation are presented.

For patient 1, the optimal plan geometries were 1 and 10. For this patient, a margin of 6 mm is required to reach sufficient coverage(V_{95}(CTV 3) $>$ 95%). Similarly, for patient 2 (plan geometries 1 and 9), a margin of 6 mm is required.

For patient 3, the initial coverage of the PTV is already higher. For this patient (plan geometries 1 and 5), only a margin of 2 mm is required (V_{95}(CTV 1) $>$ 95%). For patient 4 (plan geometries 1 and 7), a margin of 4 mm is sufficient (V_{95}(CTV 2) $>$ 95%).

An isotropic margin of 6 mm is therefore sufficient for the optimal plan geometries of all patients. An increased margin of 8 mm results in a V_{95}(CTV) $>$ 95% for all recommended geometries (1, 2, 9, 10 and 11) in all patients.

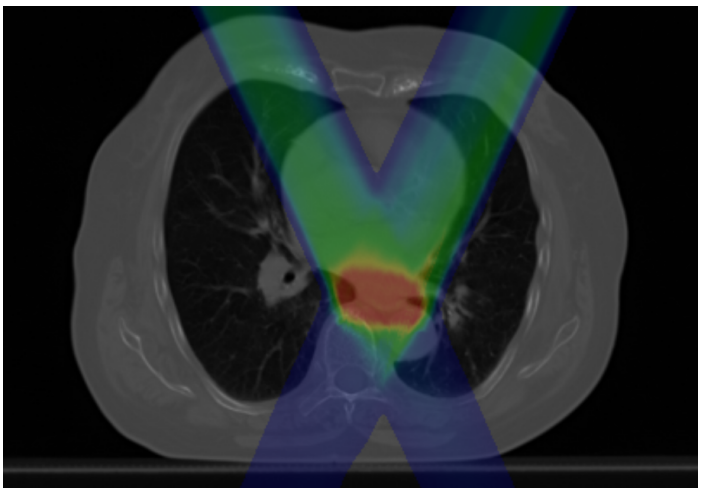

(a) Static Planning CT

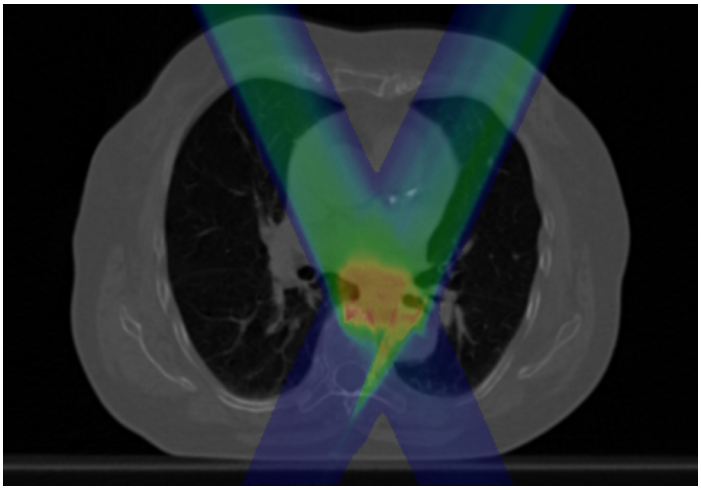

(b) 4D-CT $In_{75\%}$

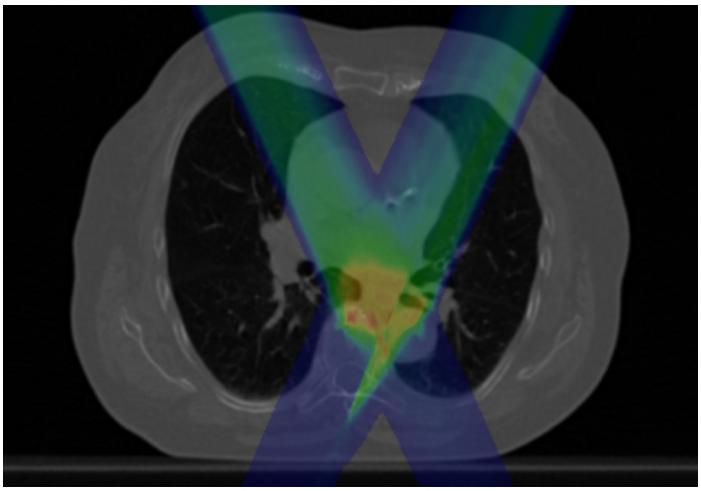

(c) 4D-CT $Ex_{0\%}$

Figure 67: Sensitivity of the Algorithm to Organ Motion: Overshoot into the spinal cord, observed in patient 2, plan geometry 8: The dose to the spinal cord is small in the planning CT (a). Due to movement of the heart muscle, visible in the 4D-CT (b), (c), parts of the treatment field overshoot into the spinal cord, leading to higher doses. Depending on the motion phase, the maximum dose changes.

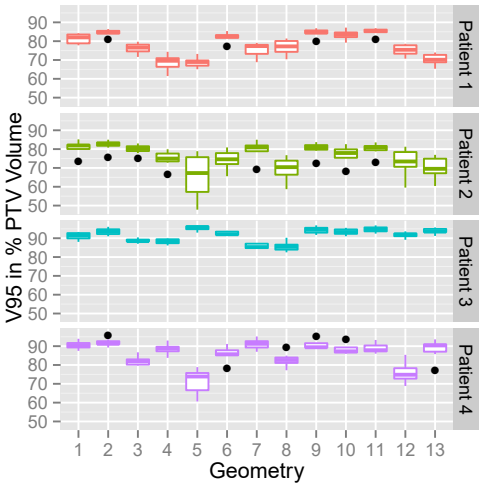

(a) PTV

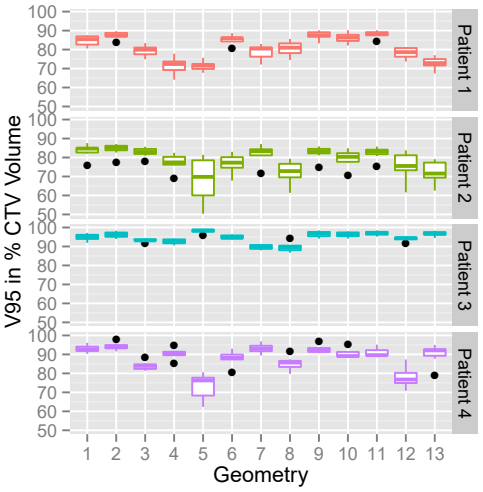

(b) CTV 1 (PTV - 2 mm)

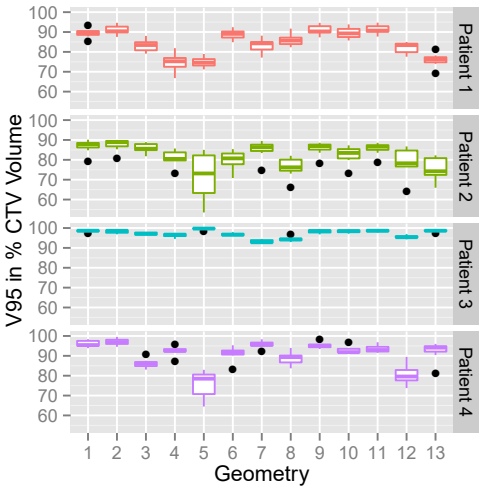

(c) CTV 2 (PTV - 4 mm)

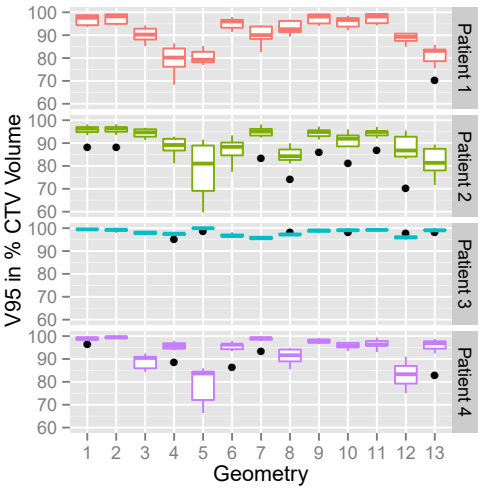

(d) CTV 3 (PTV - 6 mm)

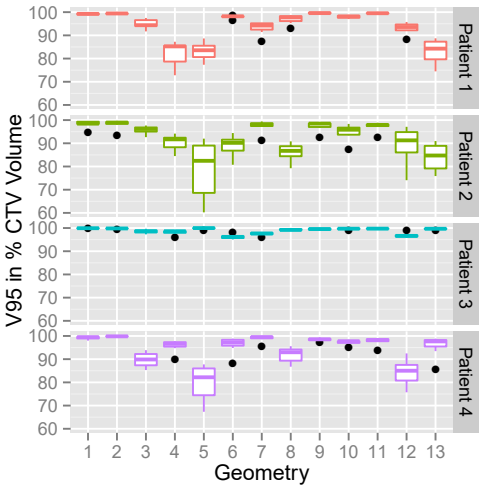

(e) CTV 4 (PTV - 8 mm)

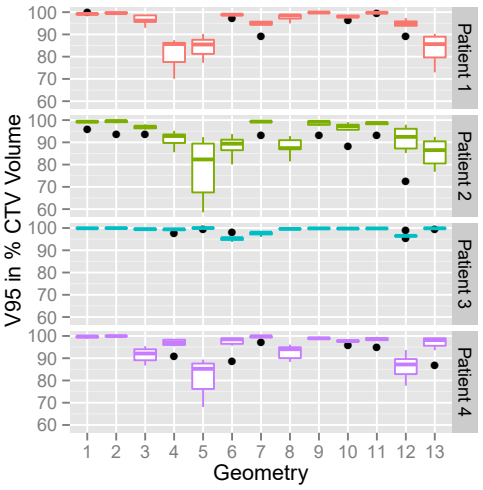

(f) CTV 5 (PTV - 10 mm)

Figure 68: CTV Coverage and Margins: An artificial CTV is created from the PTV which is used to estimate the necessary internal margin. For patients 1 and 2, a margin of 6 mm is necessary to reach the same $V_{95\%}$ as in the treatment planning calculation. For patient 2, a margin of 2 mm is sufficient, for patient 4, a margin of 4 mm is necessary.

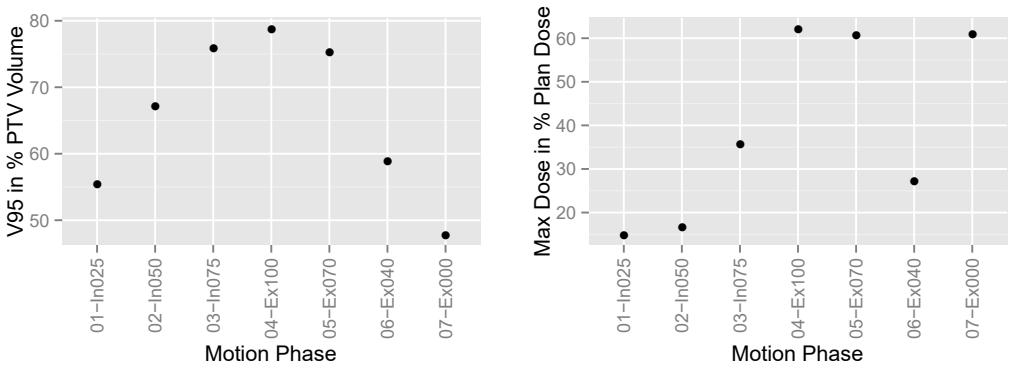

(a) $V_{95\%}$(PTV) for Patient 2, Geometry 5 (b) D_{Max}(Spinal Cord) for Patient 2, Geometry 8

Figure 69: Gating Window Definition: Results of the quasi-static dose calculations as a function of the 4D-CT motion phase. This information can be used to define the size of a gating window.

5.3.2.3 *Gating Window Definition*

Finally, a preliminary investigation into the definition of gating window sizes was started. While the quasistatic calculation is not able to predict interplay effects as a result of organ motion, it can give a hint at which motion phases result in a reduced PTV coverage or increased dose to an organ at risk. This information can be used to base a decision for or against gating, and to define a gating window size.

To find an optimal gating window, one treatment plan is selected for an individual patient. Then, a desired dose parameter which describes the treatment plan quality or dose to an organ at risk ($V_{95\%}$(PTV) or D_{Max}(Spinal Cord)) is calculated as a function of the motion phase. If there is a large variation of this parameter as a function of motion phase, gating can be beneficial for the patient and the gating window should be chosen to encompass the motion phases with high PTV coverage or low organ at risk dose.

Two examples based on the results of patient 2 are illustrated in Fig. 69. In Fig. 69a, the $V_{95\%}$(PTV) values for planning geometry 5 exhibit a dependence on the motion phase, the values oscillate between 45% to 80%. A gating window between $In_{75\%}$ and $Ex_{70\%}$ could increase the $V_{95\%}$(PTV) to between 75% to 80%.

In Fig. 69b, D_{Max}(Spinal Cord) is presented for planning geometry 8. Without gating, the maximum dose in the spinal cord could reach up to 63% prescribed dose D_P. With a gating window between $In_{25\%}$ and $In_{50\%}$, the max dose could be reduced to 17% D_P.

Using gating, critical motion phases can be avoided and optimal gating windows can improve sparing of organs at risk and cover of the target volume. The quasistatic dose calculation can be used as a basis to define the gating windows.

5.4 SUMMARY

In October 2012, the HIT Heavy Ion Gantry was introduced, offering new treatment planning options. This treatment planning study explored the feasibility of using the gantry for the treatment of esophageal cancer patients. Using the data sets of four patients with different target volumes, the robustness of 13 different

planning geometries were tested. The tested plan geometries reflect the initial and projected capabilities of the gantry.

For each patient, a free-breathing treatment planning CT and a co-registered 4D-CT with seven motion phases was available. Using the treatment planning CTs, treatment plans were optimized, with all treatment plans passing acceptance criteria as a suitable patient treatment plan.

The resulting dose distributions of each treatment plan were then calculated on each individual motion phase of the 4D-CT. In contrast to a proper 4D dose calculation, the beam was not split up and divided over the motion phase, instead, the whole treatment plan was calculated on one phase. This quasi-static approach made the calculation possible despite the lack of breathing curves and removes a lot of complexity from the calculations. On the other hand, this removes the interplay effects from the calculated dose distributions.

For each patient and treatment plan combination, the quasi-static calculations showed an expected decrease in target volume coverage. In most cases, doses to the organs at risk were unaffected, with the exception of one treatment plan where the dose to the spinal cord was highly sensitive to organ motion.

In total, five treatment planning geometries were found which universally resulted in a high target volume coverage and low doses to organs at risk for each patient. Additionally, two optimal treatment plans were found for each patient: One optimal treatment plan using just one treatment field, reflecting the initial capabilities of the heavy ion gantry, and one optimal treatment plan using two treatment fields, reflecting the projected capabilities of the heavy ion gantry.

While treatment plans with two irradiation fields showed better target volume coverage in the treatment planning calculation using the static treatment planning CT, they were not found to perform better than the single-field treatment plans when organ motion was considered.

In addition to investigating the optimal treatment plans, the feasibility of using the quasi-static dose calculation to account for the effects of organ motion was tested. The preliminary study concluded that this method is sensitive to organ motion and was useful in detecting changes in target volume coverage and doses to organs at risk. It was shown to be sensitive enough to estimate the size of ITV margins and gating window, increasing the target coverage and reducing the dose to organs at risk.

5.5 DISCUSSION

While this treatment planning study resulted in several recommendations with regard to esophageal irradiations using the HIT Heavy Ion Gantry, it should be treated as a preliminary study due to the omission of several motion effects. In the previous chapters, the particle fluence was accurately distributed between all motion phases to include interplay effects. This calculation is sensitive to the breathing pattern, starting phase and accelerator performance, all of which was not included. In addition, only one treatment planning CT and a co-registered 4D-CT was used in the study, both of which were created on the same day. Hence, inter-fractional motion and setup inaccuracies were not part of this study.

Including these motion effects could alter the optimal treatment planning strategy. Especially the difference in dose distributions between this quasi-static calculation and a full 4D dose calculation should be examined in a follow-up study.

It should include a patient data set with more CTs to estimate the inter-fractional variability as well as measured or estimated breathing patterns.

Aside from these shortcomings, the quasi-static approach still accounts for range differences and the motion of the target volume and has been shown to be sensitive to motion effects.

Future studies should include refined treatment planning geometries. With the HIT Heavy Ion Gantry now in operation, all available gantry angles can now be included into the study. Additionally, treatment plans with three or more irradiation fields could be included.

Regarding the treatment planning process, the organs at risk were not specifically spared in this study. While all treatment plans feature a suitable sparing of organs at risk, this dose could be further reduced in favor of re-irradiation possibilities. The robustness of such treatment plans could be the focus of further studies.

6 DISCUSSION

In 2009, the Heidelberg Ion-Beam Therapy Center (HIT) started treatment of the first patients, most of them suffering from head and neck cancer. Treatment of the first hepatocellular carcinoma (HCC) patients with stereotactic body radiotherapy (SBRT) in 2011 and the introduction of the heavy ion gantry in 2012 presents new challenges and offers new treatment options.

Treatment of moving organs requires the employment of adequate motion mitigation techniques and evaluation of the irradiation, for which a new work flow was introduced. In this thesis, the additions to the work flow for the SBRT of HCC were presented, including the treatment of the first beam-gated patient at HIT and the calculation of 4D dose distributions, contributing to a safe and reliable treatment.

Calculation of 4D dose distributions not only require a precise understanding of organ motion, but also of the dynamics of the irradiation process. To provide this, an analysis and simulation of the HIT accelerator timing structure was presented and verified using patient treatment records and experimental data. This offers an improved 4D dose calculation and is currently used to simulate the HIT accelerator.

Finally, the introduction of the heavy ion gantry provides new degrees of freedom for treatment planning, which was investigated in a treatment planning study for esophageal carcinoma. This study demonstrated the efficacy of the heavy ion gantry for the treatment of esophageal cancer and demonstrated the sensitivity of a quasi-static dose calculation to organ motion.

INTRODUCTION OF A NEW WORK FLOW FOR LIVER IRRADIATIONS

While the introduction of SBRT for the treatment of HCC was a success (Habermehl et al. (2013); Richter et al. (2014)) and the irradiation of moving organs is now performed routinely at HIT, the work involved in the preparation, data acquisition and evaluation necessary for each patient is substantial. It is in theory possible to calculate simulated dose distributions directly after treatment planning and to reconstruct dose distributions after each treatment fraction. In reality, dose calculations were finished when the patient was already treated. This is due to a very time-consuming data acquisition and evaluation process, in which the breathing curves, the irradiation logs, the CTs, vector fields and contours must be exported, calculated and converted into the proper input files needed for TRiP-4D. In addition, at the time of writing, the standard implementation of TRiP-4D was only available on the computer cluster at GSI, which required a transfer of the data to Darmstadt for calculation and return to Heidelberg for evaluation. Accelerating this process would substantially increase the relevance of these calculations, enabling treatment planners and physicians to adapt the treatment.

Some steps of the data preparation and conversion have been automated using python scripts and dynamic TRiP executables. While this certainly simplified the work during this thesis, it was not user-friendly enough to be used by clinical

personnel. To meet this requirement, an integration into a more user-friendly framework (*MeVisLab* by *MeVis Medical Solutions AG*, Bremen, Germany) was initiated, but not completed.

Currently, relevant treatment data is acquired from several different sources, like the treatment control system (TCS) and the *ANZAI AZ-733V* gating interface, which have to be synchronized manually. This data acquisition during the patient treatment could be further improved by a close integration of the *EtherCAT* system. The *EtherCAT* system is a part of the accelerator control system (ACS) already in place at HIT and provides all relevant accelerator data simultaneously and in real time, including the *ANZAI AZ-733V* breathing motion signal, and could become the exclusive source for data acquisition.

With integrated automation, further features could be implemented, like automatic dose calculation on the daily CT used for image guidance. Current fast dose calculation developments, like the *FRoG* framework (Mein et al. (2018)), might enable fast re-planning in the future.

Using the *ANZAI AZ-733V* system to monitor the organ motion only gives limited information, as it operates only with a load cell in one position on the chest wall. Changes in the correlation between this surrogate signal and the internal motion is not detectable with this set-up, and should be augmented with regular imaging of internal markers (Seppenwoolde et al. (2011)) or ultrasound imaging (O'Shea et al. (2016)).

Gating was successfully introduced as a motion mitigation technique in this work flow. One of the main characteristics of this mitigation technique is the long duration of the treatment, especially when patient compliance is low. To increase the speed of the treatment, other motion mitigation techniques, like rescanning and tumor tracking should be investigated and implemented. Further, implementation of deep-inspiration breath hold techniques instead of free breathing has been shown to reduce residual motion and irradiation times in treatment of hepatocellular carcinoma (Boda-Heggemann et al. (2016)).

Treatment planning with the HIT treatment planning system (TPS) *syngo® RT Planning* is currently limited to 3D dose calculation. Other TPS are capable of 4D dose calculation and can be used to create more robust treatment plans, including rescanning. It would be desirable to be able to import more robust treatment plans into the HIT TPS.

ANALYSIS AND MODELING OF THE HIT ACCELERATOR CYCLE

In this thesis, an improved version of the accelerator simulation was presented, which takes the specific properties and variability of the HICAT accelerator into account. The quality of the prediction was demonstrated in various analyses of beam data and validated experimentally. However, deviations between the simulation and the measurements have been identified.

With the implementation of the intensity feedback system (Schömers et al. (2011); Schömers (2013)), the variability of the irradiation decreased, revealing subtle deviations between the simulation an the actual behavior of the accelerator. The reasons for this discrepancy may be in the data acquisition and processing, or it may be from accelerator properties which were not implemented yet. This includes effects like spill pauses (short interruptions of the beam extraction in treatment plans with disjunctive fluence patterns), interlocks (longer interruptions introduced by errors encountered during treatment) and deviations in the

spill structure from the ideal (finite rise time and deviation from the nominal intensity). Also, the reduction of beam intensity at low beam energies has not been implemented, although all measurements have been carried out at higher energies, evading this effect in this study.

Along with the desire to implement current properties of the HICAT accelerator, new features should become available in the simulation as they are implemented in the actual accelerator. This encompasses plan-specific intensity control (Schömers et al. (2013)), which adjusts the beam intensity for each raster point, and re-acceleration, which will enable the accelerator to change the beam energy using the remaining particles in the synchrotron. Introduction of different accelerators or accelerator modes could be used to study the influence of accelerator properties on treatment plan robustness. Introduction of proton, helium and oxygen ion beams should be simple to implement and offer the flexibility to conduct comparative treatment planning studies. Gating is not yet implemented in the current implementation, because it requires the knowledge of the treatment plan, breathing motion curve and gating window, but could be added to future implementations.

The base data set used in the simulation is compiled from multiple sources of the accelerator control system and treatment control system. Gathering all the information is a time-consuming task and must be repeated each time a feature of the accelerator is changed, or else the simulation will become outdated. A solution to this challenge could be the implementation of specially devised treatment plans which automatically irradiate a wide range of the accelerator parameter space. The resulting irradiation records could be evaluated automatically, extracting the parameters necessary for the simulation. This approach may even improve the quality of the simulation by removing some of the complexity.

Experimental verification of the simulation software was performed in a moving water phantom, which is already a very sensitive test of the dose calculation quality. However, measurements anthropomorphic phantoms can be used to reveal the clinical impact of organ motion and verify the dose calculation accuracy. Anthropomorphic abdominal phantoms have already been used to validate the accuracy of image registration, including dosimetric measurements (Liao et al. (2017)). Similar pelvis phantoms are developed at DKFZ, including MRI and PET contrast enhancements for improved imaging (Johnen et al. (2018, 2019)).

4D TREATMENT PLANNING STUDY FOR ESOPHAGEAL CANCER

This treatment planning study found optimal treatment plans for carbon-ion boosts of esophageal cancer. However, due to the difference between the free-breathing treatment planning CT and the motion phases of the 4D-CT, the PTV coverage calculated for the 4D-CTs was reduced in most patients. The analysis showed that additional margins could be used to increase the target coverage, however, this approach also increases the dose to the organs at risk. Hence, further motion mitigation methods should be introduced, including deep-inspiration breath hold, rescanning techniques and beam gating.

Due to the limited data set, effects of inter-fractional motion could not be taken into account. Effects of anatomical variability and tumor response, for example volume reduction, will change radiological path lengths and PTV coverage. Daily image guided radiotherapy (IGRT) and adaptive planning strategies are advised for the treatment of esophageal carcinoma (Han et al. (2012)).

In the study, optimal treatment plans for each patient were selected from thirteen fixed geometry templates. Treatment plans could be further improved by fine-tuning the treatment geometries to better fit the patient anatomy and by introducing treatment geometries with more treatment fields. Further, prioritizing the optimization for increased coverage of the target volume or better sparing of organs at risk could increase the treatment plan quality.

Closely related, the role of the organs at risk is not entirely understood. Pulmonary toxicity is a major problem and the dose must be as low as reasonably achievable (Lee et al. (2003)). Further, even low-dose volumes of sufficient sizes are an important risk factor (Wang et al. (2006)). On the other hand, increased sparing of the lungs comes at the cost of higher heart dose, as seen in this study and by Zhang et al. (2008). This increases the risk for reduced myocardial perfusion (Gayed et al. (2006)) and reduced heart volume (Haj Mohammad et al. (2015)). Currently, the significance of cardiac toxicity is not yet fully understood in esophageal cancer therapy, mainly due to the limited prognosis of esophageal cancer patients (Beukema et al. (2015)). For the final treatment decision, these options must be weighed, however, compared to conventional therapy, carbon-ion irradiation will likely reduce the dose to the heart and lungs, reducing the adverse effects.

Due to the lack of motion information, intra-fractional motion could not be properly included in the dose calculation, leading to the quasi-static dose calculation approach seen in this study. This way, the interplay effect between the scanning motion of the ion beam and the organ motion is not properly taken into account (Phillips et al. (1992); Bert et al. (2008)). To quantify the impact of the interplay effect on the proposed treatment plans, the study could be extended to patients with more available data, such as breathing curves and additional CTs over the course of the treatment. Using a proper 4D dose calculation and 4D-CTs from different treatment days, the robustness of treatment plans with respect to intra- and inter-fractional motion could be quantified.

Diaphragm motion and the gas-filling of the stomach have already been shown to impact target volume coverage (Zhang et al. (2008)) and need to be taken into account. As a mitigation measure, asymmetrical margins have been proposed (Zhao et al. (2007)). The calculations performed in this analysis offer a way to determine the impact of organ motion on the target coverage and estimate necessary margin and gating window sizes. By improving the calculation speed, it could become a tool to help during the treatment planning process, estimate the robustness of a patient plan and quickly select the optimal treatment.

7 CONCLUSION

In this thesis, a new work flow and data acquisition strategy were presented for the treatment of hepatocellular carcinoma (HCC) using stereotactic body radiotherapy (SBRT) at the Heidelberg Ion-Beam Therapy Center (HIT). Initially, thirteen patients were treated, including the first patient treatment using respiratory beam gating. Based on the data sets acquired from each patient, simulated and reconstructed 4D dose distributions can now be calculated. The implemented work flow is used for treatment of HCC and other SBRT treatments at HIT.

To improve the accelerator timing prediction, the properties of the HIT synchrotron cycle were investigated, revealing energy-dependent and stochastic aspects as well as day-to-day beam intensity fluctuations. A simulation was implemented based on a realistic energy-dependent model of the synchrotron cycle, the stochastic daily intensity fluctuations were implemented as a randomly selected beam intensity. The accuracy of the resulting irradiation sequences was verified using treatment records. Experimental verification of a patient treatment plan was performed in a moving water phantom, where a total dose deviation of $(1.0 \pm 7.3)\%$ was determined. The simulation software has been used for research done by other colleagues of the work group.

To assess the potential of the HIT heavy-ion gantry, introduced into the clinical routine in late 2012, a treatment planning study was presented. In the study, optimal plan geometries for a carbon ion boost for the treatment of esophageal carcinoma were determined for four patient cases and a selection of thirteen different planning geometries. Using a quasi-static dose calculation approach, the effects of intra-fractional organ motion were taken into account. The resulting dose distributions can potentially be used to define volume margins and gating window sizes.

A

ANALYSIS AND MODELING OF THE HIT ACCELERATOR CYCLE

A.1 EXAMPLE OF A SIMULATED LMDOUT FILE

Simulated beam delivery sequence for the `VX-Vorbestrahlung` treatment plan:

```
!comment This file was created by makeLmdout
!modality CVS
!fileversion 1.0
!date 20130919
!patient_name patient
!comment Offset, timeunit and items are specific for CVS files
!offset 0
!timeunit 1
!items T NP BS ES EOP E F I
0 0 0 0 0 0 0 0
25000  0 1 0 0 0 0 0
26690  1 1 0 0 0 0 0
28311  2 1 0 0 0 0 0
29885  3 1 0 0 0 0 0
31455  4 1 0 0 0 0 0
33033  5 1 0 0 0 0 0
34603  6 1 0 0 0 0 0
36163  7 1 0 0 0 0 0
37728  8 1 0 0 0 0 0
39298  9 1 0 0 0 0 0
40865  10 1 0 0 0 0 0

[...]

77515468  5925 11 10 5 0 0 0
77528759  5926 11 10 5 0 0 0
77542825  5927 11 10 5 0 0 0
77559500  5928 11 10 5 0 0 0
77559501  5928 11 10 6 0 0 0
77559502  5928 11 11 6 0 0 0
```

T: Time in microseconds, NP: NextPoint (raster point index), BS: BeginSlice (start of a beam extraction), ES: EndSlice (end of a beam extraction), EOP: EndOfPlane (change of energy)

A.2 ADDITIONAL RESULTS

A.2.1 *Results of the Broadcast Pause Correction*

In the initial implementation of the simulation software, a discrepancy between the simulated and reconstructed beam delivery sequences became apparent. The length of the pause between two consecutive irradiations was under-estimated by approximately 400 milliseconds. For easier readability, this was not discussed in detail in the main body of the thesis and all results presented already use the corrected pause length (see section 4.3.1.3, page 74). For comparison and to see the validity of the corrections, here are the results of the first, un-corrected simulation calculations.

Fig. 70 shows the results of Analysis I using the initial version of the simulation software, showing a discrepancy between the simulated pause times T_{Pause} and the observed pause times[1]. In this first analysis, the median duration of all pauses larger than 2 seconds in the 2012 data set is 4.48 s ("Measurement"), while the simulation has a median value of 4.01 s. Likewise, in the 2013 data set, the median pause duration is 4.43 s, while the simulation yields a median value of 4.02 s.

This difference between the simulated and measured pause lengths led to the investigation presented in section 4.2.2.3, page 52. This investigation found that the additional pause can be attributed mainly to the broadcast delay introduced by the accelerator control system (ACS) in the beginning and the end of each synchrotron cycle. In addition to the broadcast delay, which is contributes approximately 350 milliseconds of pause time, the time needed to start the beam extraction adds another 50 milliseconds.

The simulation software was corrected by adding an additional 400 ms pause to each acceleration cycle. To test the validity of this additional pause, Analysis II was performed with both versions of the simulation software. In Fig. 71, both analyses are presented next to each other, with the uncorrected simulation on the left and the corrected simulation on the right. Further, Table 4 contains the median root mean square time difference.

Data Set	Uncorrected	Corrected
2012	3.73 s	3.40 s
2013	1.34 s	0.72 s

Table 4: Median Root Mean Square Deviation in seconds for the uncorrected and corrected version of the simulation software.

In summary, the additional pause reduces the deviation between the simulated and the recorded beam delivery sequences, improving the accuracy of the simulation. The investigation and results of the analysis legitimize the implementation of the broadcast pause correction in the simulation software.

1 Compare to Fig. 36, page 73.

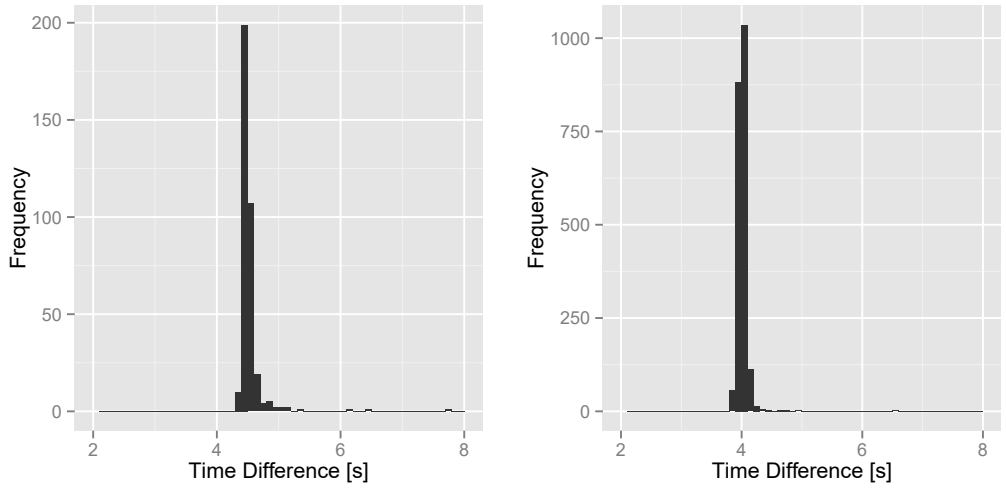

(a) Measurement, 2012

(b) Simulation, 2012

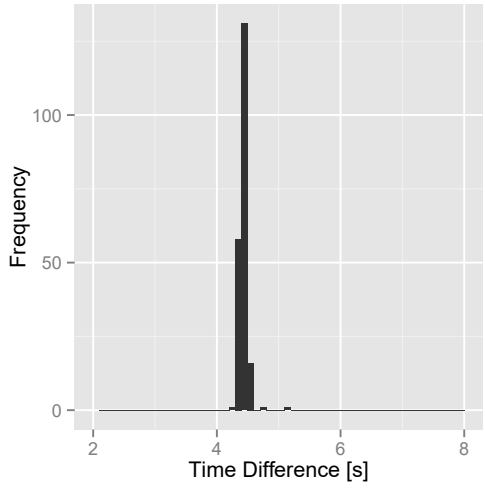

(c) Measurement, 2013

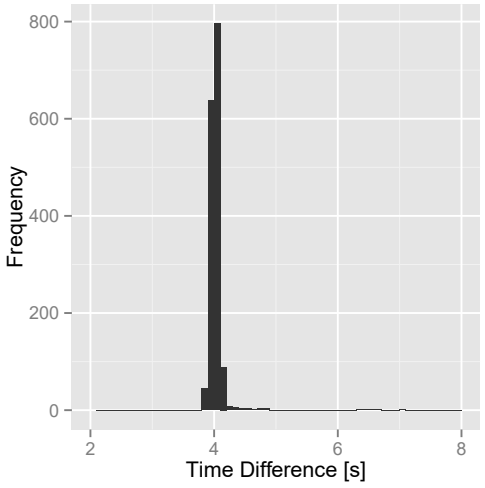

(d) Simulation, 2013

Figure 70: Results of Analysis I (Timing Spectra Analysis) of the first simulations of the `VX-Vorbestrahlung` treatment plan. In this analysis, a discrepancy of 400 ms was found between the measured (left) and simulated (right) beam delivery sequences. This led to the investigation of the accelerator pause times and inclusion of the broadcast delay time into the simulation.

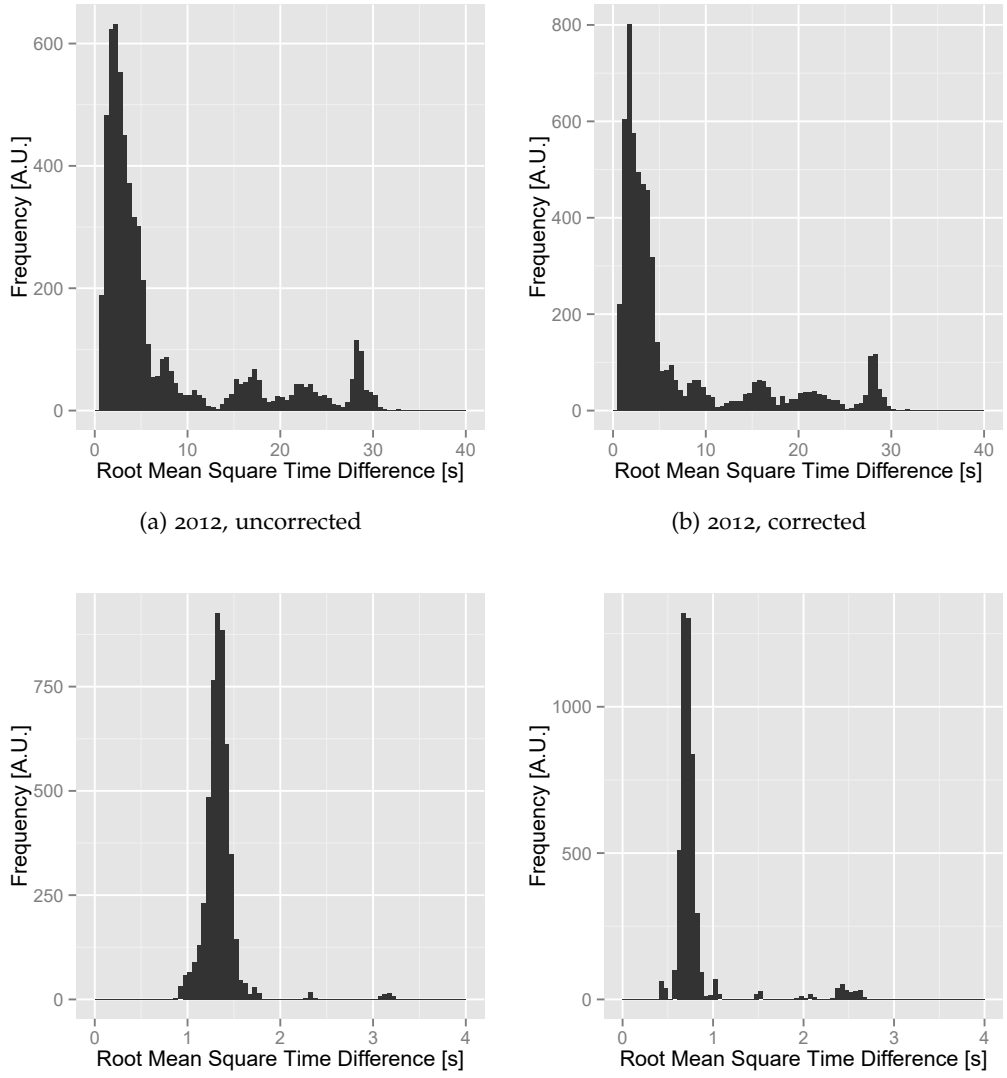

(a) 2012, uncorrected

(b) 2012, corrected

(c) 2013, uncorrected

(d) 2013, corrected

Figure 71: Results of Analysis II (Root Mean Square Deviation) using the uncorrected (left) and corrected (right) simulation software. Smaller values correspond to a better agreement between simulation and measured beam delivery sequences. By including the broadcast delay into the simulation, the results are improved. This is also reflected by the median Root-Mean-Square values presented in Table 4.

A.2.2 *Sensitivity of the Measured Doses to Phase Deviation*

A.2.2.1 *Phase Shift Between Simulated and Reconstructed Dose Distributions*

In the analysis comparing the simulated dose distributions to the dose distribution reconstructed from irradiation records, a difference was found between the 2012 and 2013 data set, which is mainly attributed to the introduction of the Dynamic Intensity Control (DIC) in early 2013. Before, the beam intensity varied immensely from day to day, leading to low repeatability of the irradiation. Because of the large variation in the timing of the irradiation, the resulting dose distribution is very independent of the starting phase of the motion, which was also found in Fig. 43 on page 82. With the introduction of the DIC, beam intensities are more stable and irradiations show higher repeatability. Dose distributions are now dependent on the starting phase of the motion.

In the analysis, only the comparison with all phases (Fig. 44 on page 83) and the $\phi = 30°$ starting phase (Fig. 45, page 84) were shown, proving the motion starting phase dependence of the 2013 data set and showing a phase shift of 30°.

Here, additional results for Analysis IV for the 2013 data set are presented, showing that a motion starting phase of $\phi = 30°$ is the best fit for the simulated dose distributions. In Figs. 72, 73 and 74, the simulated dose distributions (shown as box plots) were calculated with starting phases $\phi = 0°$, 30° and 60°, respectively. The dose distributions reconstructed from beam records (shown as blue circles) were calculated with a motion starting phase of $\phi = 0°$.

Both in the upper plots of the dose values and the Kolmogorov-Smirnov test below, the highest agreement between the simulation and reconstruction is achieved with a simulated motion starting phase of $\phi = 30°$. Reasons for this phase deviation may be found in the irradiation records, as the phase shift vanishes in the experimental verification.

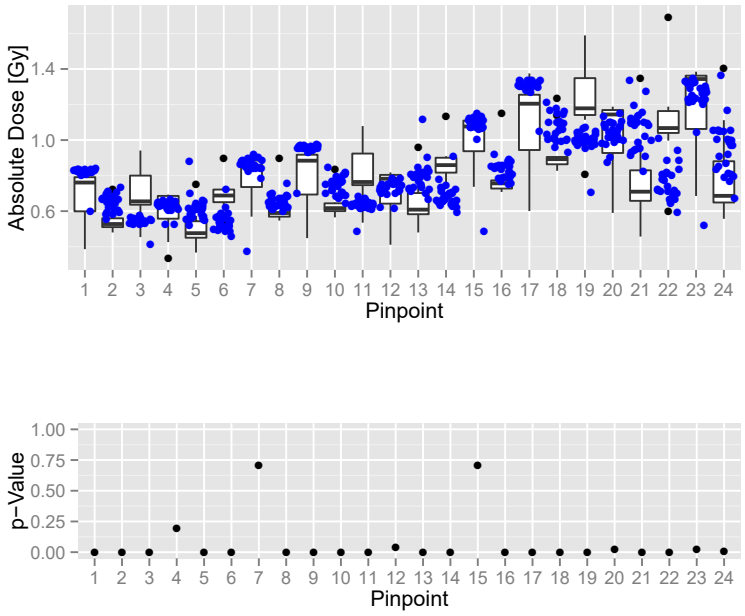

Figure 72: Reconstructed dose values for the 2013 data set, using start phase $\phi = 0°$ for the simulated dose distributions. Above: Simulated data (box plots), reconstructed data (blue circles); below: Kolmogorov-Smirnov p values.

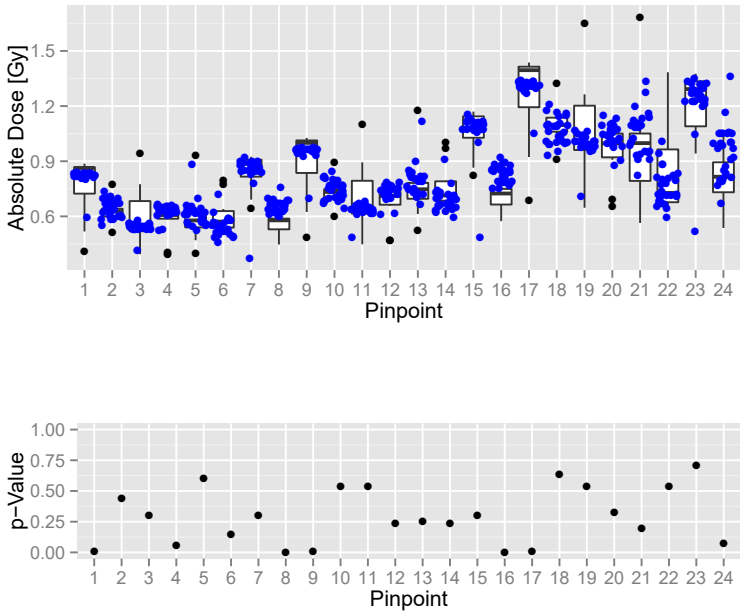

Figure 73: Reconstructed dose values for the 2013 data set, using start phase $\phi = 30°$ for the simulated dose distributions. Above: Simulated data (box plots), reconstructed data (blue circles); below: Kolmogorov-Smirnov p values.

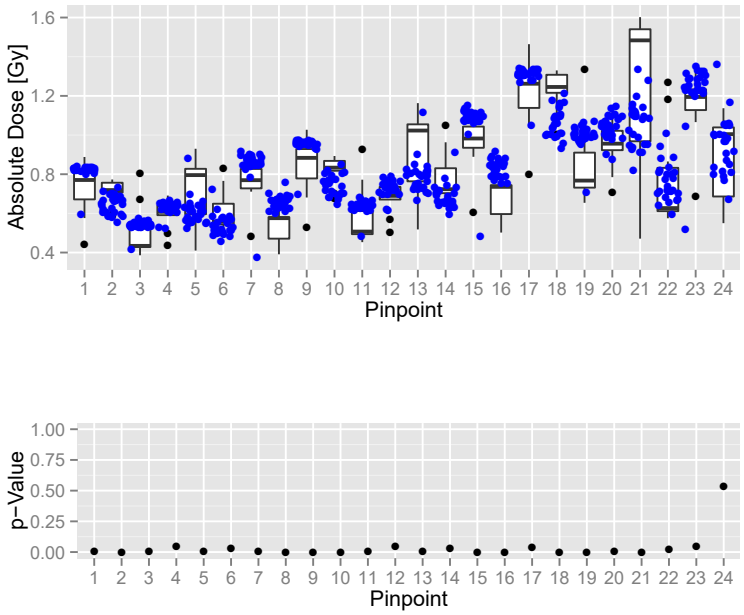

Figure 74: Reconstructed dose values for the 2013 data set, using start phase $\phi = 60°$ for the simulated dose distributions. Above: Simulated data (box plots), reconstructed data (blue circles); below: Kolmogorov-Smirnov p values.

A.2.2.2 *Experiment: Phase Dependence of the VX-Vorbestrahlung Treatment Plan*

The experimental verification of the simulation software was performed in 2013, after the introduction of the Dynamic Intensity Control (DIC). Based on the analysis of the irradiation records, a dependence on the starting motion phase ϕ is expected in this experiment.

Using the *VX-Vorbestrahlung* treatment plan, three un-interrupted irradiations were recorded with a motion starting phase of $\phi \approx 60°$. The results of these measurements were compared to simulated dose distributions with starting phases from $\phi = 0°$ to 330°.

In the analysis, only the result for motion starting phase $\phi = 60°$ was presented (Fig. 52 on page 92). Here, additional results are shown for phases $\phi = 30°$, 60° and 90° in Figs. 75, 76 and 77. Additionally, a dose calculation using 12 starting phases ($\phi = 0°$, 30°, ..., 330°) is presented in Fig 78. In the figures, the measured doses are represented as red circles, while the simulated dose values are represented as box plots. The specified p values are calculated using the Kolmogorov-Smirnov (KS) test.

Out of the data sets, the data set with the simulated motion starting phase $\phi = 60°$ shows the highest agreement, also indicated by the highest p values. In addition, the comparison with the sum of multiple starting phases in Fig 78 has a lower agreement.

For the relatively short *VX-Vorbestrahlung* treatment plan, which has an irradiation time of 70 to 100 seconds, the motion starting phase is a crucial property. In the experimental verification, the phase shift observed in the analysis of irradiation records has vanished.

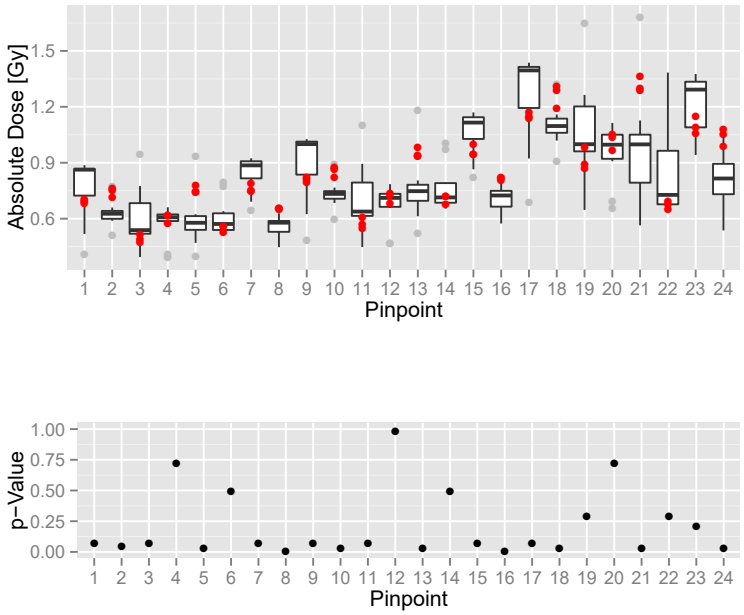

Figure 75: Measured dose values for the *VX-Vorbestrahlung* treatment plan, using all dose distributions with motion starting phase $\phi \approx 60°$. Simulated dose distributions were calculated using motion starting phase $\phi = 30°$. Above: Simulated doses (box plots), measured doses (red circles); below: Kolmogorov-Smirnov p values.

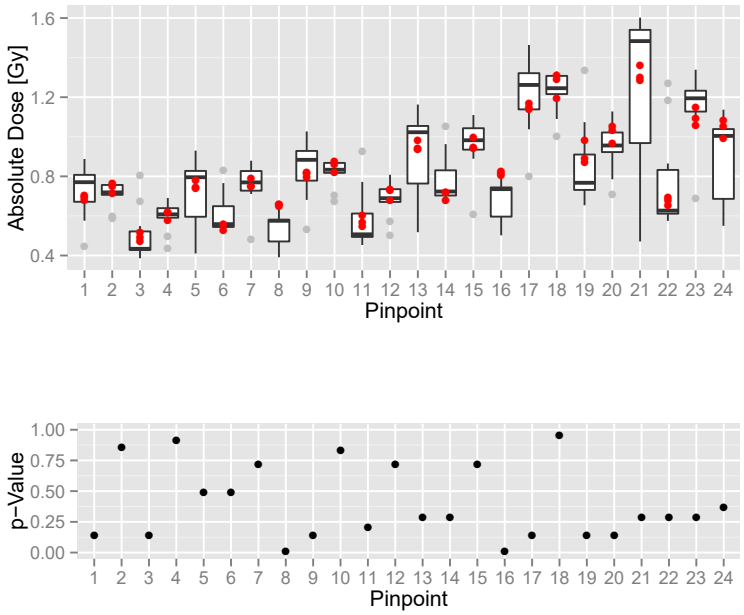

Figure 76: Measured dose values for the *VX-Vorbestrahlung* treatment plan, using all dose distributions with motion starting phase $\phi \approx 60°$. Simulated dose distributions were calculated using motion starting phase $\phi = 60°$. Above: Simulated doses (box plots), measured doses (red circles); below: Kolmogorov-Smirnov p values.

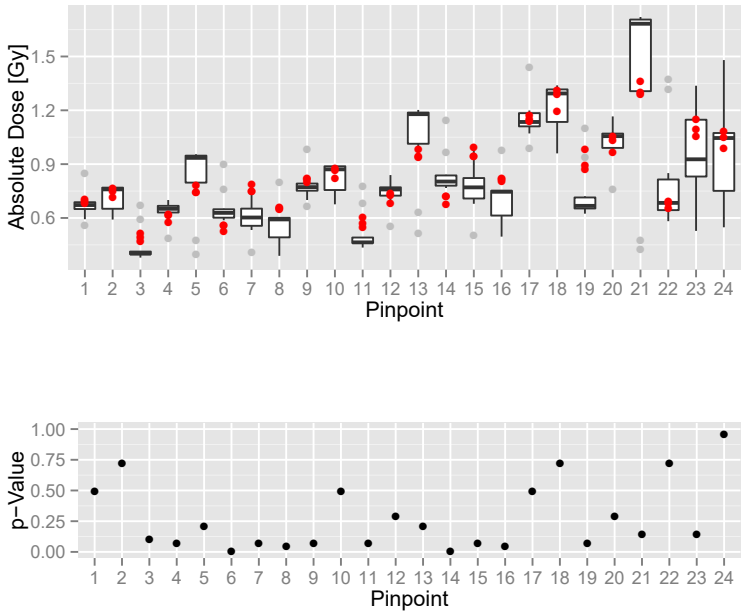

Figure 77: Measured dose values for the *VX-Vorbestrahlung* treatment plan, using all dose distributions with motion starting phase $\phi \approx 60°$. Simulated dose distributions were calculated using motion starting phase $\phi = 90°$. Above: Simulated doses (box plots), measured doses (red circles); below: Kolmogorov-Smirnov p values.

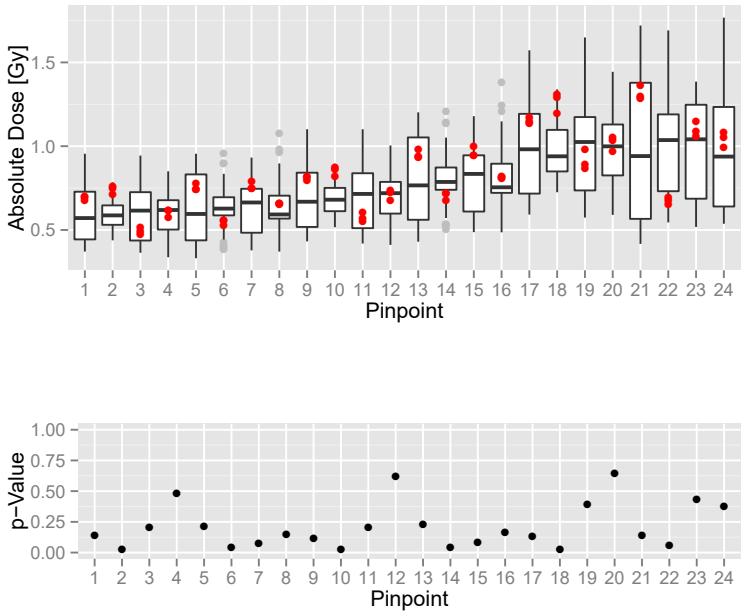

Figure 78: Measured dose values for the *VX-Vorbestrahlung* treatment plan, using all dose distributions with motion starting phase $\phi \approx 60°$. Simulated dose distributions were calculated using multiple motion starting phases $\phi = 0°, 30°, \ldots, 330°$. Above: Simulated doses (box plots), measured doses (red circles); below: Kolmogorov-Smirnov p values.

A.2.2.3 *Experiment: Phase Dependence of the Patient Treatment Plan*

In addition to the relatively short *VX-Vorbestrahlung* treatment plan with an irradiation time of 70 to 100 seconds, a patient treatment plan used for the treatment of hepatocellular carcinoma was irradiated for the experimental verification. This treatment plan has a higher dose per fraction and takes approximately nine minutes to irradiate.

Three un-interrupted irradiations with a motion starting phase $\phi \approx 180°$ were measured and compared to simulated dose distributions. In the analysis, only the comparison with a simulated dose distribution with starting phase $\phi = 180°$ was presented (Fig. 53, page 92). To illustrate the reduced dependence on the motion starting phase experienced with longer treatment plans, this result is compared to a calculation using multiple motion phases.

In Fig. 79, the results of the comparison with only the $\phi = 180°$ motion starting phase are repeated. The dose calculation has an accuracy of $\Delta_{\text{Mean}}D = (0.045 \pm 0.331)$ Gy or (1.0 ± 7.3)%.

In comparison, Fig. 80 shows the results of a dose calculation with multiple motion starting phases $\phi = 0°, 30°, \ldots, 330°$. Here, the dose calculation accuracy is $\Delta_{\text{Mean}}D = (0.024 \pm 0.409)$ Gy or (0.5 ± 9.0)%. This result shows a larger deviation of the dose values, but is still acceptable.

With longer treatment plans, small deviations of individual raster point irradiation times will add up. Because significant parts of the patient dose is irradiated at the end of the treatment, this deviation translates to larger phase deviations, reducing the dependence on the starting phase.

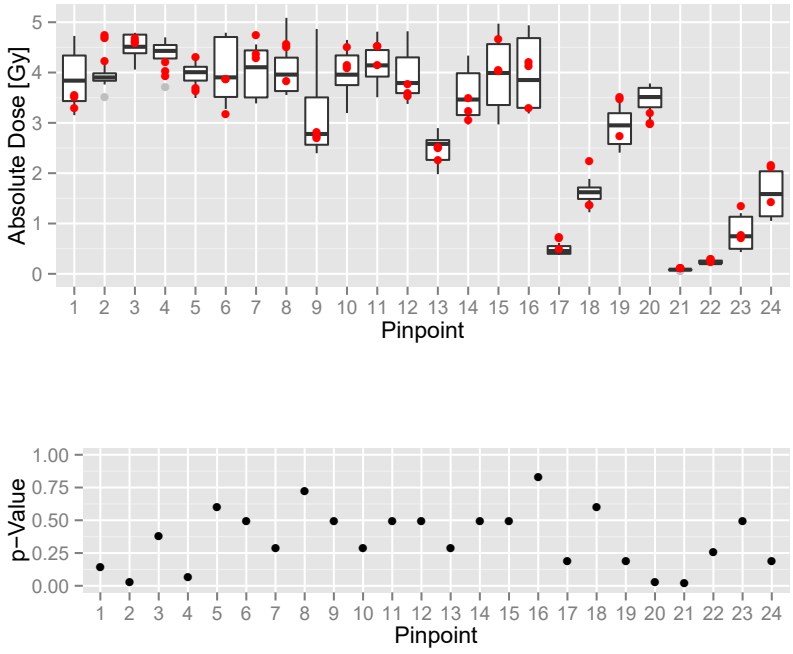

Figure 79: Resulting doses for the patient treatment plan for all measurements with a starting phase of $\phi \approx 180°$ and no interlocks (red dots). The simulated doses (box plot) were calculated with a starting phase of $\phi = 180°$. Dose calculation accuracy $\Delta_{\text{Mean}}D = (0.045 \pm 0.331)$ Gy or (1.0 ± 7.3)%.

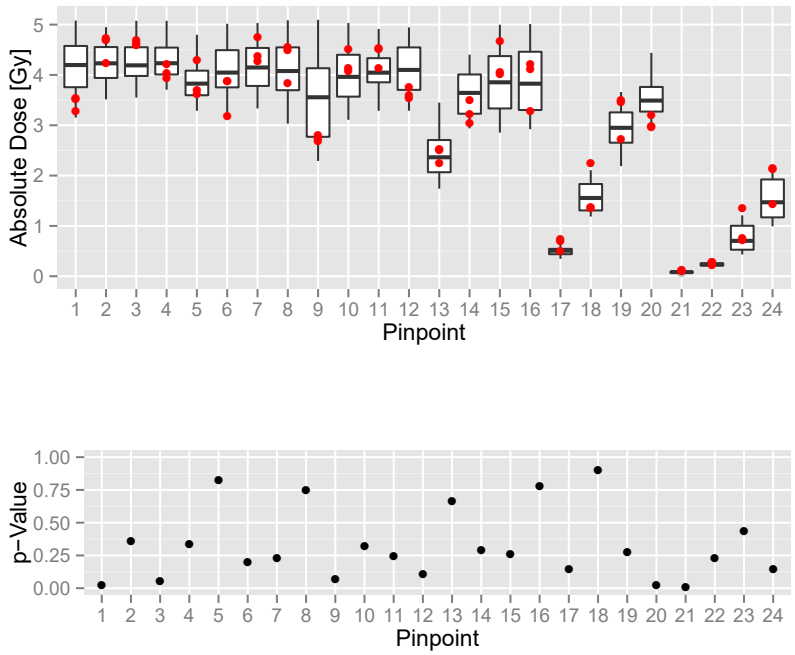

Figure 80: Resulting doses for the patient treatment plan for all measurements with a starting phase of $\phi \approx 180°$ and no interlocks (red dots). The simulated doses (box plot) were calculated with a multiple starting phases of $\phi = 0°, 30°, \ldots, 330°$. Dose calculation accuracy $\Delta_{\text{Mean}}D = (0.024 \pm 0.409)$ Gy or $(0.5 \pm 9.0)\%$.

B

4D TREATMENT PLANNING STUDY FOR ESOPHAGEAL CANCER

B.1 DETAILED RESULTS

To improve readability, only the most relevant graphs were included in chapter 5 (page 99. Additional data is presented on the following pages.

In the graphs presented in Fig. 81 to 84, the resulting dose index for the treatment planning CT is presented on the left, the respective results for the quasistatic dose calculation are presented on the right. Fig. 81 presents the indices associated with PTV coverage ($V_{95\%}$, Conformity Index, Homogeneity Index). Figs. 82 and 83 present the indices associated with PTV over- and underdosage ($V_{107\%}$, D_{Max}, D_{Min}, D_{Median}, D_{Mean}) and the mean dose to the heart muscle. Fig. 84 presents the indices associated with the lung and spinal cord dose ($V_{20\%}$ Lung, D_{Max} Spinal Cord).

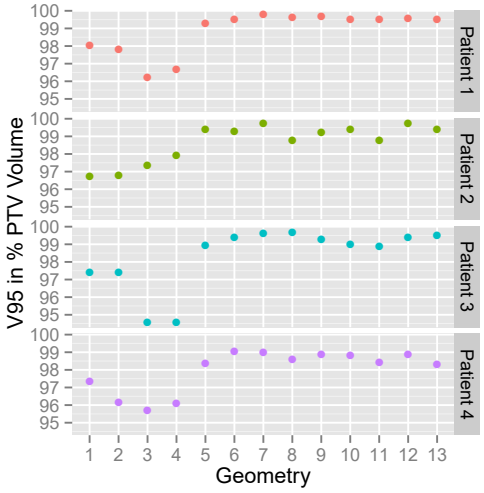

(a) V_{95}

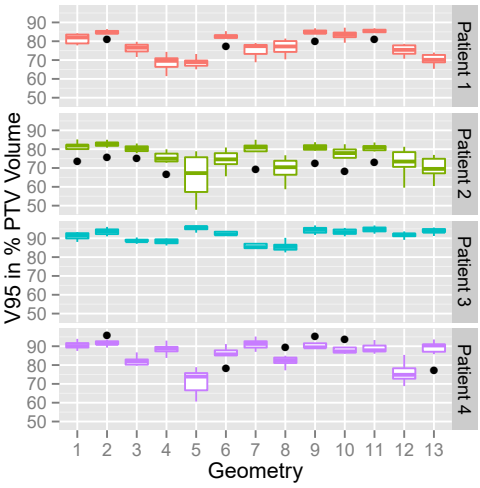

(b) V_{95}

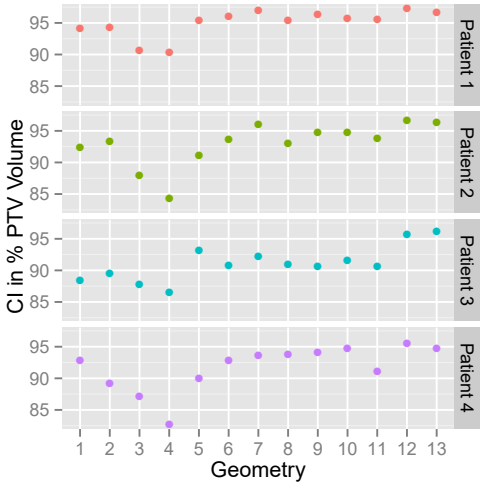

(c) Conformity Index

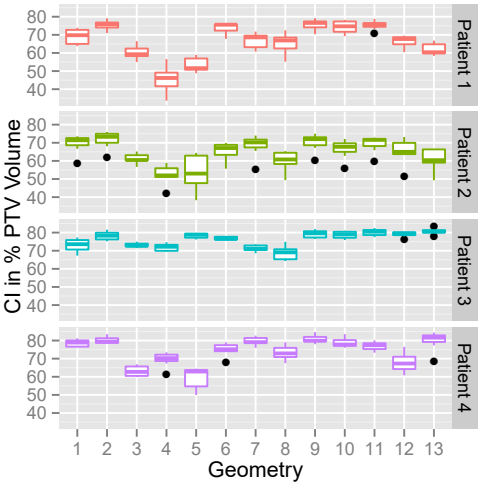

(d) Conformity Index

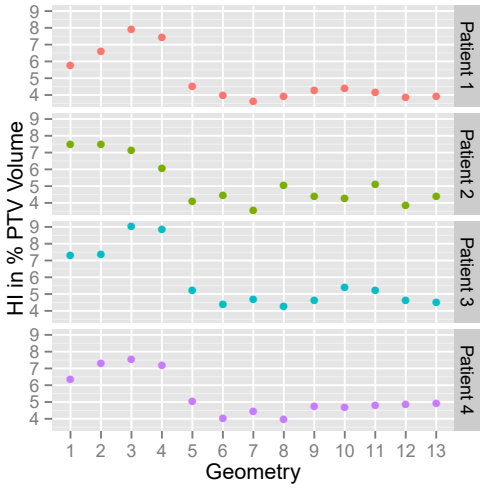

(e) Homogeneity Index

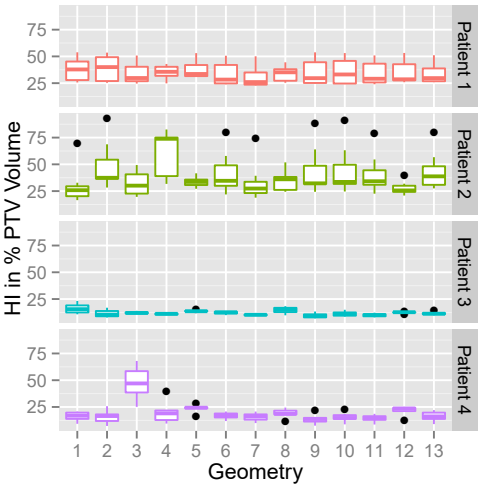

(f) Homogeneity Index

Figure 81: PTV Coverage ($V_{95\%}$, Conformity Index, Homogeneity Index)

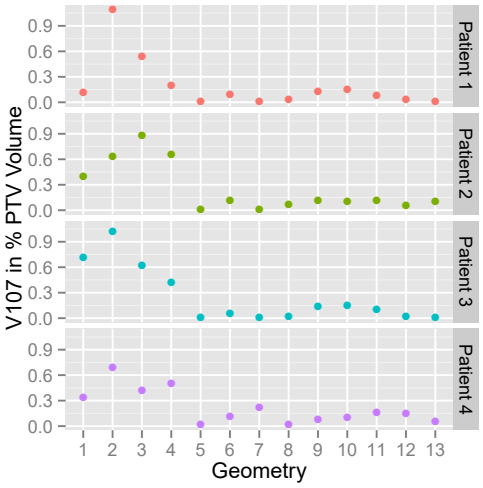

(a) V_{107}

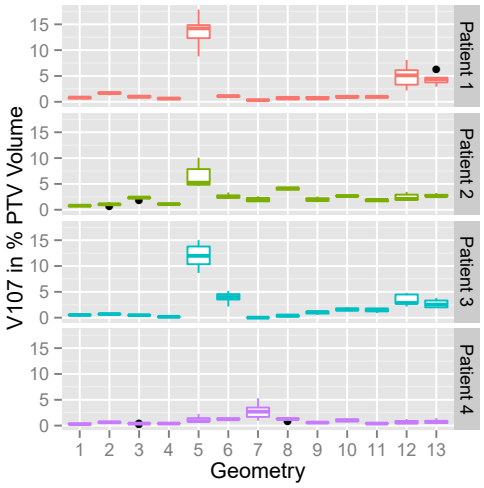

(b) V_{107}

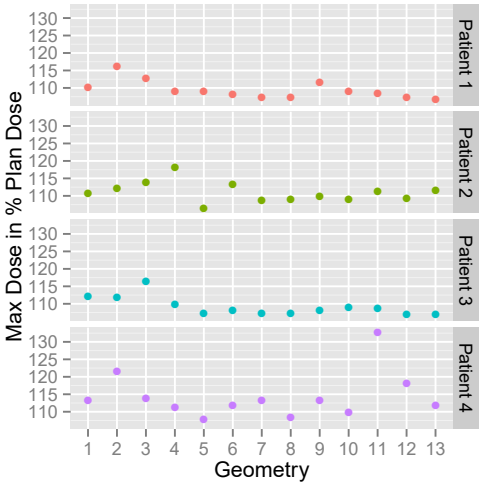

(c) Maximum Dose

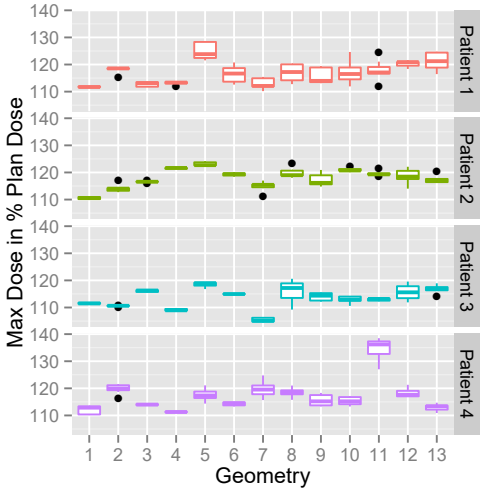

(d) Maximum Dose

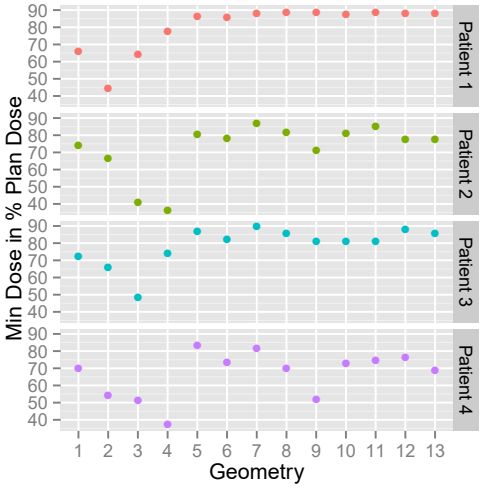

(e) Minimum Dose

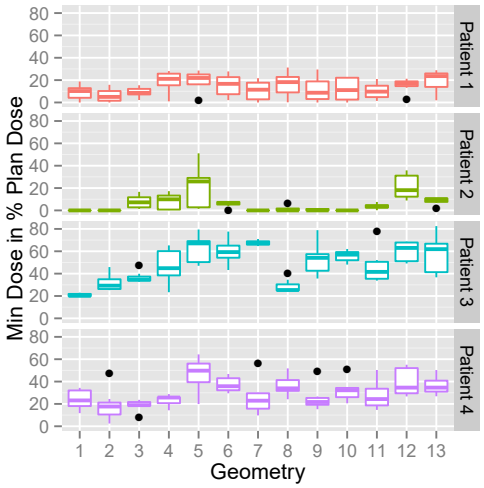

(f) Minimum Dose

Figure 82: PTV Over- and Underdosage ($V_{107\%}$, D_{Max}, D_{Min})

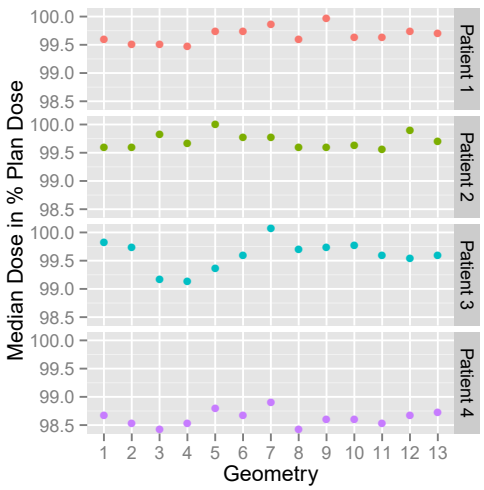

(a) Median Dose

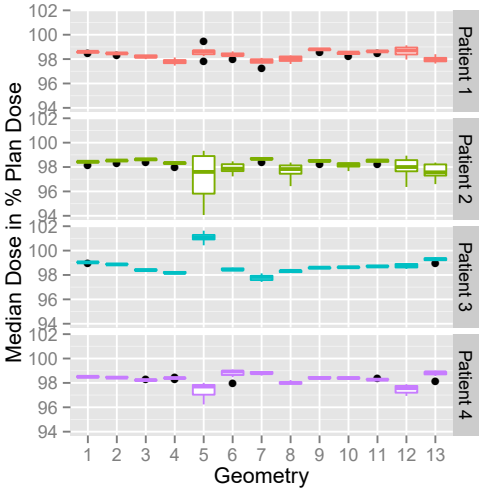

(b) Median Dose

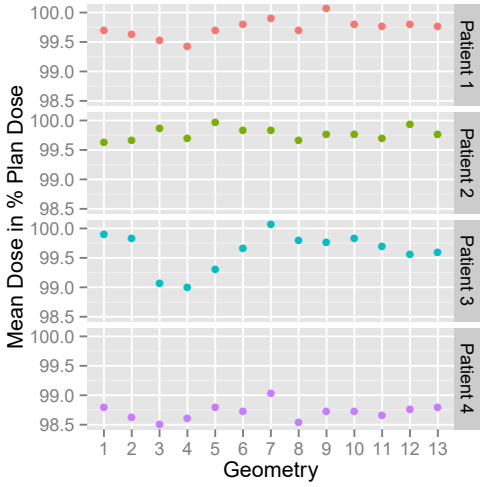

(c) Mean Dose

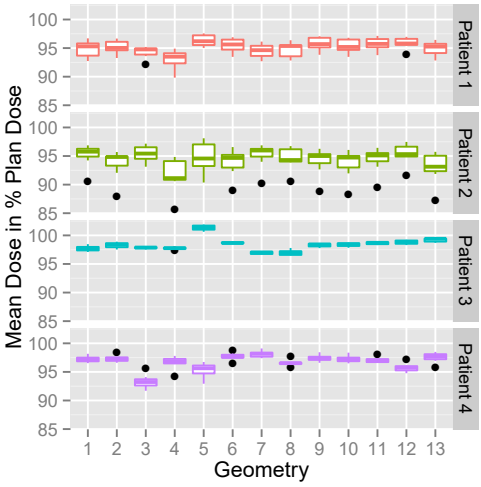

(d) Mean Dose

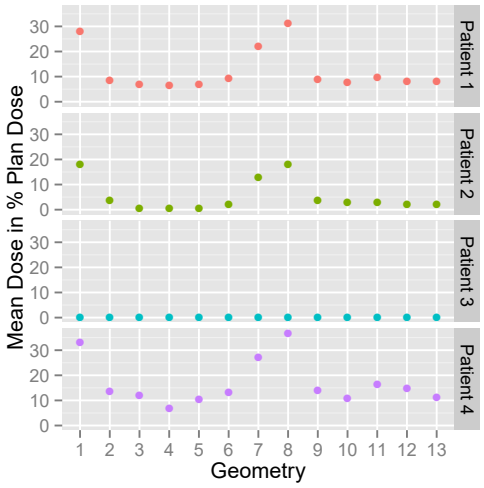

(e) Heart Mean Dose

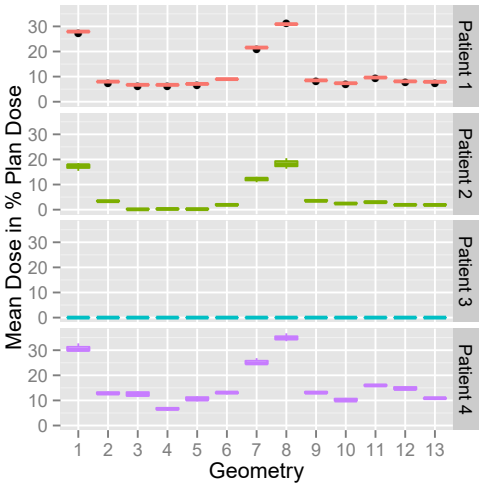

(f) Heart Mean Dose

Figure 83: PTV Over- and Underdosage (Median Dose, Mean Dose), D_{Mean} to the Heart Muscle

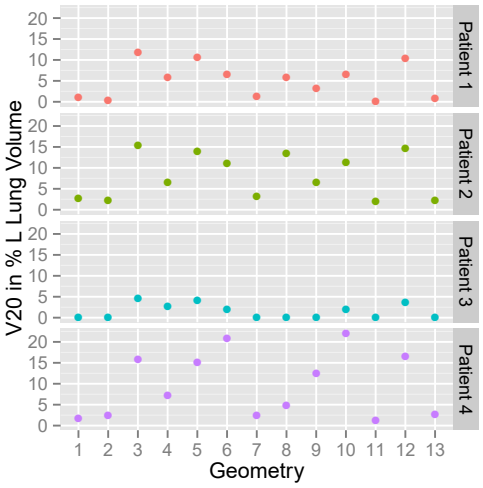

(a) Left Lung V_{20}

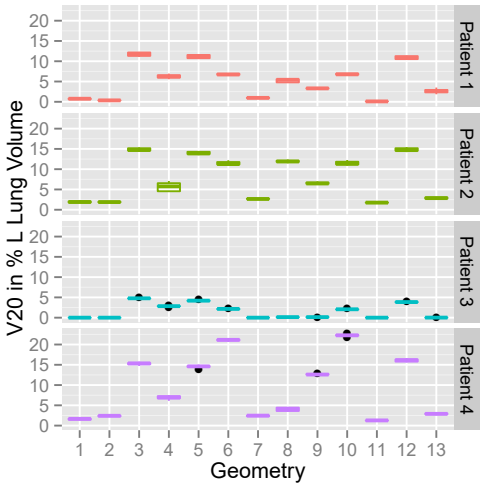

(b) Left Lung V_{20}

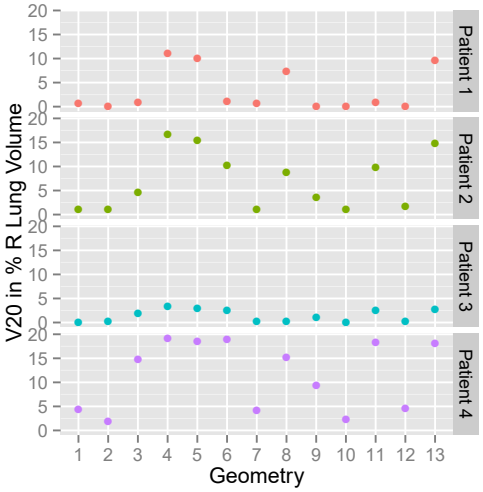

(c) Right Lung V_{20}

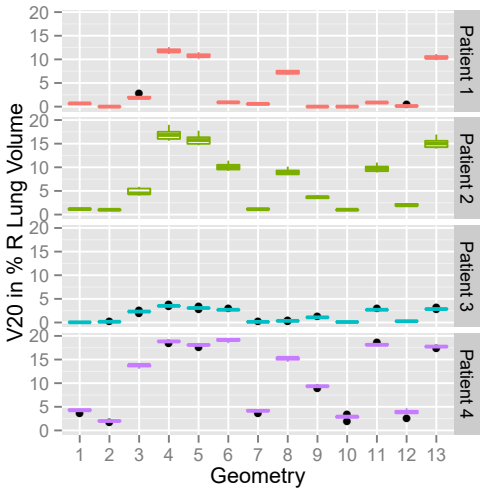

(d) Right Lung V_{20}

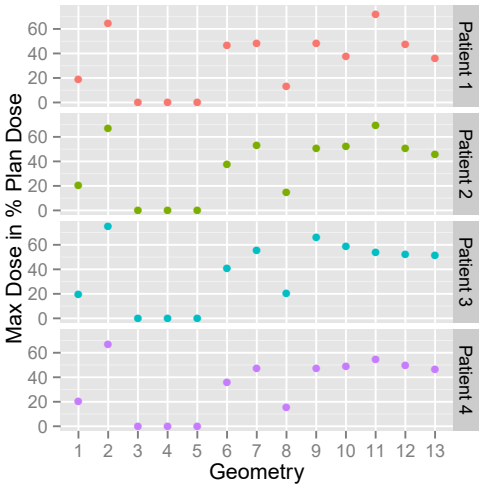

(e) Spine Maximum Dose

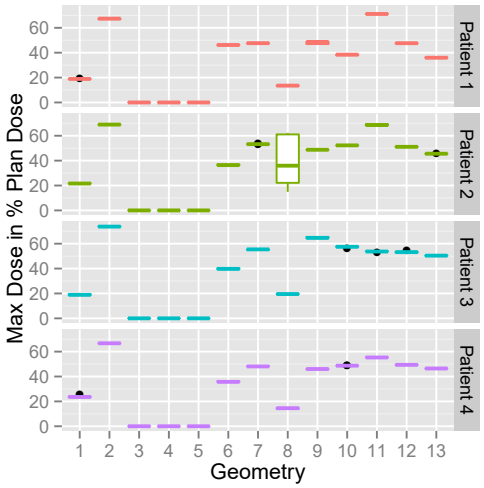

(f) Spine Maximum Dose

Figure 84: Organs at Risk ($V_{20\%}$ Lung, D_{Max} Spinal Dose

BIBLIOGRAPHY

S. P. Ahlen. Theoretical and Experimental Aspects of the Energy Loss of Relativistic Heavily Ionizing Particles. *Reviews of Modern Physics*, 52:121–173, 1980.

U. Amaldi and G. Kraft. European Developments in Radiotherapy with Beams of Large Radiobiological Effectiveness. *Journal of Radiation Research*, 48(Suppl.): A27–A41, 2007.

U. Amaldi, P. Berra, K. Crandall, D. Toet, M. Weiss, R. Zennaro, E. Rosso, B. Szeless, M. Vretenar, C. Cicardi, C. De Martinis, D. Giove, D. Davino, M. R. Masullo, and V. Vaccaro. LIBO - A Linac-Booster for Protontherapy: Construction and Tests of a Prototype. *Nuclear Instruments and Methods in Physics Research Section A*, 521:512–529, 2004.

V. Batista. *Treatment Plan Robustness in Pancreatic Patients Treated with Scanned Ion-Beam Therapy: Inter- and Intra-Fractional Aspects*. PhD thesis, Medizinische Fakultät der Ruprecht-Karls-Universität Heidelberg, 2016.

V. Batista, D. Richter, N. Chaudhri, P. Naumann, K. Herfarth, and O. Jäkel. Significance of Intra-Fractional Motion for Pancreatic Patients Treated with Charged Particles. *Radiation Oncology*, 13:120, 2018.

J. Bauer, D. Unholtz, C. Kurz, and K. Parodi. An Experimental Approach to Improve the Monte Carlo Modelling of Offline PET/CT-Imaging of Positron Emitters Induced by Scanned Proton Beams. *Physics in Medicine & Biology*, 58 (15):5193–213, 2013a.

J. Bauer, D. Unholtz, F. Sommerer, C. Kurz, T. Haberer, K. Herfarth, T. Welzel, S. Combs, J. Debus, and K. Parodi. Implementation and Initial Clinical Experience of Offline PET/CT-Based Verification of Scanned Carbon Ion Treatment. *Radiotherapy & Oncology*, 107(2):218–226, 2013b.

M. Belli, F. Cera, R. Cherubini, M. Dalla Vecchia, A. M. Haque, F. Ianzini, G. Moschini, O. Sapora, G. Simone, M. A. Tabocchini, and P. Tiveron. RBE-LET Relationships for Cell Inactivation and Mutation Induced by Low Energy Protons in V79 cells: Further Results at the LNL Facility. *International Journal of Radiation Biology*, 74(4):501–509, 1998.

C. Bert and M. Durante. Motion in Radiotherapy: Particle Therapy. *Physics in Medicine and Biology*, 56(16):R113–R144, 2011.

C. Bert and E. Rietzel. 4D Treatment Planning for Scanned Ion Beams. *Radiation Oncology*, 2:24, Jan. 2007.

C. Bert, S. O. Grözinger, and E. Rietzel. Quantification of Interplay Effects of Scanned Particle Beams and Moving Targets. *Physics in Medicine and Biology*, 53(9):2253–2265, 2008.

C. Bert, A. Gemmel, N. Saito, and E. Rietzel. Gated Irradiation with Scanned Particle Beams. *International Journal of Radiation Oncology, Biology, Physics*, 73 (4):1270–1275, 2009.

H. Bethe. Zur Theorie des Durchgangs schneller Korpuskularstrahlen durch Materie. *Annalen der Physik*, 5(5):325 – 400, 1930.

J. C. Beukema, P. van Luijk, J. Widder, J. A. Langendijk, and C. T. Muijs. Is Cardiac Toxicity a Relevant Issue in the Radiation Treatment of Esophageal Cancer? *Radiotherapy and Oncology*, 114(1):85–90, 2015.

F. Bloch. Bremsvermögen von Atomen mit mehreren Elektronen. *Zeitschrift für Physik*, 81(5-6):363 – 376, 1933a.

F. Bloch. Zur Bremsung rasch bewegter Teilchen beim Durchgang durch Materie. *Annalen der Physik*, 5(16):285 – 320, 1933b.

H. Blomgren, I. Lax, I. Näslund, and R. Svanström. Stereotactic High Dose Fraction Radiation Therapy of Extracranial Tumors Using an Accelerator. Clinical Experience of the First Thirty-One Patients. *Acta Oncologica, Stockholm, Sweden*, 34(6):861–870, 1995.

J. Boda-Heggemann, A. C. Knopf, A. Simeonova-Chergou, H. Wertz, F. Stieler, A. Jahnke, L. Jahnke, J. Fleckenstein, L. Vogel, A. Arns, M. Blessing, F. Wenz, and F. Lohr. Deep Inspiration Breath Hold-Based Radiation Therapy: A Clinical Review. *International Journal of Radiation Oncology, Biology, Physics*, 94(3): 478–492, 2016.

N. Bohr. Scattering and Stopping of Fission Fragments. *Physical Review*, 58(7): 654 – 655, 1940.

R. C. Bär, H. Eickhoff, and T. Haberer. Status and Controls Requirements of the Planned Heavy Ion Tumor Therapy Accelerator Facility HICAT. *8th International Conference on Accelerator and Large Experimental Physics Control Systems, San Jose, California*, pages 134–136, 2001.

R. C. Bär, D. Ondreka, A. Redelbach, S. Scheloske, M. Galonska, E. Feldmeier, and C. Schömers, editors. *Steuerdatenversorgung für den Heidelberger Therapiebeschleuniger HICAT*. GSI Helmholtzzentrum für Schwerionenforschung GmbH, Darmstadt, Germany, September 2012. Version 2.8.

W. H. Bragg and R. Kleeman. XXXIX. On the α Particles of Radium, and their Loss of Range in passing through various Atoms and Molecules. *The London, Edinburgh, and Dublin Philosophical Magazine and Journal of Science*, 10(57):318–340, 1905.

R. Brun and F. Rademakers. ROOT – An Object Oriented Data Analysis Framework. *Nuclear Instruments and Methods in Physics Research A*, 389:81–86, 1997.

R. Carrington, E. Spezi, S. Gwynne, P. Dutton, C. Hurt, J. Staffurth, and T. Crosby. The Influence of Dose Distribution on Treatment Outcome in the SCOPE 1 Oesophageal Cancer Trial. *Radiation Oncology*, 11:19, 2016.

N. Chaudhri, D. Richter, M. Härtig, S. Ecker, B. Ackermann, J. Naumann, T. Haberer, C. Bert, D. Habermehl, K. K. Herfarth, M. Ellerbrock, and O. Jäkel. SU–E–T–334: Clinical Implementation of Gating and Dose Verification with Scanned Ion Beams at HIT. *Medical Physics*, 39:3780, 2012.

S. E. Combs, K. K. Herfarth, D. Habermehl, and J. Debus. Strahlentherapie von Lebermetastasen. *Der Chirurg: Zeitschrift für alle Gebiete der operativen Medizin*, 81(6):526 – 532, 2010.

S. E. Combs, D. Habermehl, T. Ganten, J. Schmidt, L. Edler, I. Burkholder, O. Jäkel, T. Haberer, and J. Debus. Phase I Study Evaluating the Treatment of Patients with Hepatocellular Carcinoma (HCC) with Carbon Ion Radiotherapy: The PROMETHEUS-01 Trial. *BMC Cancer*, 11:67, 2011.

T. Crosby, C. N. Hurt, S. Falk, S. Gollins, S. Mukherjee, J. Staffurth, R. Ray, N. Bashir, J. A. Bridgewater, J. I. Geh, D. Cunningham, J. Balzeby, R. Roy, T. Maughant, and G. Griffiths. Chemoradiotherapy with or without Cetuximab in Patients with Oesophageal Cancer (SCOPE1): A Multicentre, phase 2/3 Randomised Trial. *Lancet Oncology*, 14:627–637, 2013.

J. Debus, K. D. Gross, and M. Pavlovic, editors. *Proposal for a Dedicated Ion Beam Facility for Cancer Therapy*. GSI, Darmstadt, Germany, 1998.

S. Deuffic, T. Poynard, L. Buffat, and A. J. Valleron. Trends in Primary Liver Cancer. *The Lancet*, 351(9097):214–215, 1998.

A. Dolinskii, H. Eickhoff, and B. Franczak. The Synchrotron of the Dedicated Ion Beam Facility for Cancer Therapy, Proposed for the Clinic in Heidelberg. *Proceedings of EPAC 2000, Vienna, Austria*, pages 2509–2511, 2000.

R. Drzymala, R. Mohan, L. Brewster, J. Chu, M. Goitein, W. Harms, and M. Urie. Dose-Volume Histograms. *International Journal of Radiation Oncology, Biology, Physics*, 21:71–78, 1991.

H. Eickhoff, D. Böhne, T. Haberer, B. Schlitt, P. Spiller, J. Debus, and A. Dolinskii. The Proposed Dedicated Ion Beam Facility for Cancer Therapy at the Clinic in Heidelberg. *Proceedings of EPAC 2000, Vienna, Austria*, pages 2512–2514, 2000.

H. Eickhoff, T. Haberer, B. Schlitt, and U. Weinrich. HICAT – The German Hospital-Based Light Ion Cancer Therapy Project. *Proceedings of EPAC 2003, Lucerne, Switzerland*, pages 290–294, 2004.

H. B. El-Serag and A. C. Mason. Rising Incidence of Hepatocellular Carcinoma in the United States. *The New England Journal of Medicine*, 340(10):745–750, 1999.

U. Fano. Penetration of Protons, Alpha Particles, and Mesons. *Annual Review of Nuclear Science*, 13(1):1–66, 1963.

R. Fuchs, U. Weinrich, and P. Emde. The Heavy Ion Gantry of the HICAT Facility. *Proceedings of EPAC 2004, Lucerne, Switzerland*, pages 2550–2552, 2004.

R. Fuchs, U. Weinrich, and E. Sust. Assembly of the Carbon Beam Gantry at the Heidelberg Ion Therapy (HIT) Accelerator. *Proceedings of EPAC 2008, Genoa, Italy*, pages 1839–1841, 2008.

Y. Furusawa, K. Fukutsu, M. Aoki, H. Itsukaichi, K. Equchi-Kasai, H. Ohara, F. Yatagai, T. Kanai, and K. Ando. Inactivation of Aerobic and Hypoxic Cells from Three Different Cell Lines by Accelerated (3)He-, (12)C- and (20)Ne-ion beams. *Radiation Research*, 154(5):485–496, 2000.

M. Galonska, S. Scheloske, S. Brons, R. Cee, K. Höppner, J. Mosthaf, A. Peters, and T. Haberer. The HIT Gantry: From Commissioning to Operation. *Proceedings of IPAC 2013, Shanghai, China*, pages 3636–3638, 2013.

I. W. Gayed, H. H. Liu, S. W. Yusuf, R. Komaki, X. Wei, X. Wang, J. Y. Chang, J. Swafford, L. Broemeling, and Z. Liao. The Prevalence of Myocardial Ischemia After Concurrent Chemoradiation Therapy as Detected by Gated Myocardial Perfusion Imaging in Patients with Esophageal Cancer. *Journal of Nuclear Medicine*, 47(11):1756–1762, 2006.

A. Gemmel, E. Rietzel, G. Kraft, M. Durante, and C. Bert. Calculation and Experimental Verification of the RBE-Weighted Dose for Scanned Ion Beams in the Presence of Target Motion. *Physics in Medicine and Biology*, 56(23):7337–7351, 2011.

C. Gianoli, M. Riboldi, G. Fontana, C. Kurz, K. Parodi, and G. Baroni. Sinogram Warping Strategy for Pre-Reconstruction 4D PET Optimization. *Medical & Biological Engineering & Computing*, 54(2-3):535–546, 2015.

B. Gottschalk, A. M. Koehler, R. J. Schneider, J. M. Sisterson, and M. S. Wagner. Multiple Coulomb Scattering of 160 MeV Protons. *Nuclear Instruments and Methods in Physics Research Section B: Beam Interactions with Materials and Atoms*, 74(4):467–490, 1993.

V. Grégoire, T. R. Mackie, W. De Neve, M. Gospodarowicz, J. A. Purdy, M. van Herk, and A. Niemierko. ICRU Report 83: Prescribing, Recording and Reporting Photon-Beam Intensity-Modulated Radiation Therapy (IMRT). *Journal of the International Commission on Radiation Units and Measurements*, 10(1), 04 2010.

S. O. Grözinger, E. Rietzel, Q. Li, C. Bert, T. Haberer, and G. Kraft. Simulations to Design an Online Motion Compensation System for Scanned Particle Beams. *Physics in Medicine and Biology*, 51(14):3517–3531, 2006.

S. O. Grözinger, C. Bert, T. Haberer, G. Kraft, and E. Rietzel. Motion Compensation with a Scanned Ion Beam: A Technical Feasibility Study. *Radiaion Oncology*, 3(34):1–7, 2008.

T. Haberer, W. Becher, D. Schardt, and G. Kraft. Magnetic Scanning System for Heavy Ion Therapy. *Nuclear Instruments and Methods in Physics Research, Section A*, 330:296–305, 1993.

T. Haberer, J. Debus, H. Eickhoff, O. Jäkel, D. Schulz-Ertner, and U. Weber. The Heidelberg Ion Therapy Center. *Radiotherapy and Oncology*, 73(Supplement 2): 186–190, 2004.

D. Habermehl, J. Debus, T. Ganten, M.-K. Ganten, J. Bauer, I. C. Brecht, S. Brons, T. Haberer, M. Härtig, O. Jäkel, K. Parodi, T. Welzel, and S. E. Combs. Hypofractionated Carbon Ion Therapy Delivered with Scanned Ion Beams for Patients with Hepatocellular Carcinoma – Feasibility and Clinical Response. *Radiation Oncology (London, England)*, 8(1):59, 2013.

N. Haj Mohammad, M. Kamphuis, M. C. C. M. Hulshof, L. J. Lutkenhaus, S. S. Gisbertz, J. J. G. H. M. Bergman, H. A. C. M. R. de Bruin-Bon, E. D. Geijsen, A. Bel, S. M. Boekholdt, and H. W. M. van Laarhoven. Reduction

of Heart Volume During Neoadjuvant Chemoradiation in Patients with Resectable Esophageal Cancer. *Radiotherapy and Oncology*, 114(1):91–95, 2015.

E. J. Hall. *Radiobiology for the Radiologist*. Lippincott Williams & Wilkins, 5th edition, 2000.

C. Han, D. C. Schiffner, T. E. Schultheiss, Y. J. Chen, A. Liu, and J. Y. C. Wong. Residual Setup Errors and Dose Variations with Less-Than-Daily Image Guided Patient Setup in External Beam Radiotherapy for Esophageal Cancer. *Radiotherapy and Oncology*, 102(2):309–314, 2012.

P. Heeg, H. Eickhoff, and T. Haberer. Die Konzeption der Heidelberger Ionentherapieanlage HICAT. *Zeitschrift für Medizinische Physik*, 14(1):17–24, 2004.

R. M. Henkelman and K. Mah. How Important is Breathing in Radiation Therapy of the Thorax? *International Journal of Radiation Oncology, Biology, Physics*, 8(11): 2005–2010, 1982.

K. K. Herfarth, J. Debus, F. Lohr, M. L. Bahner, P. Fritz, A. Höss, W. Schlegel, and M. F. Wannenmacher. Extracranial Stereotactic Radiation Therapy: Set-Up Accuracy of Patients Treated for Liver Metastases. *International Journal of Radiation Oncology, Biology, Physics*, 46(2):329–335, 2000.

M. F. Häfner, F. Sterzing, D. Krug, S. A. Körber, O. Jäkel, J. Debus, and M. M. Härtig. Intrafractional Dose Variation and Beam Configuration in Carbon Ion Radiotherapy for Esophageal Cancer. *Radiation Oncology*, 11:150, 2016.

T. Hoffmann, D. Ondreka, A. Peters, A. Reiter, and M. Schwickert. Beam Quality Measurements at the Synchrotron and HEBT of the Heidelberg Ion Therapy Center. *Proceedings of BIW 2008, Tahoe City, California*, pages 210–212, 2008.

A. D. Jensen, A. V. Nikoghosyan, M. Poulakis, A. Höss, T. Haberer, O. Jäkel, M. W. Münter, D. Schulz-Ertner, P. E. Huber, and J. Debus. Combined Intensity-Modulated Radiotherapy Plus Raster-Scanned Carbon Ion Boost for Advanced Adenoid Cystic Carcinoma of the Head and Neck Results in Superior Locoregional Control and Overall Survival. *Cancer*, 121(17):3001–3009, 2015.

O. Jäkel, C. Jacob, D. Schardt, C. P. Karger, and G. H. Hartmann. Relation Between Carbon Ion Ranges and X-Ray CT Numbers. *Medical Physics*, 28(4): 701–703, 2001a.

O. Jäkel, M. Krämer, C. P. Karger, and J. Debus. Treatment Planning for Heavy Ion Radiotherapy: Clinical Implementation and Application. *Physics in Medicine and Biology*, 46(4):1101–1116, 2001b.

W. Johnen, N. Niebuhr, A. Runz, and G. Echner. EP-1737: The ADAM-Pelvis Phantom: From DICOM data to a Patient-Like Model. *Radiotherapy and Oncology*, 127(Supplement 1):S930, 2018.

W. Johnen, A. Runz, N. Homolka, N. Niebuhr, P. Mann, B. Beuthien-Baumann, C. Gillmann, A. Pfaffenberger, A. Elter, A. L. Hoffmann, E. Troost, S. A. Körber, and G. Echner. EP-1710 Update ADAM-Pelvis Phantom: New Possibilities to Simulate Treatment Scenarios in Radiotherapy. *Radiotherapy and Oncology*, 133 (Supplement 1):S920–S921, 2019.

T. Kamada, H. Tsujii, E. A. Blakely, J. Debus, W. De Neve, M. Durante, O. Jäkel, R. Mayer, R. Orecchia, R. Pötter, S. Vatnitsky, and W. T. Chu. Carbon Ion Radiotherapy in Japan: An Assessment of 20 Years of Clinical Experience. *Lancet Oncology*, 16:e93–100, 2015.

P. Keall, S. Vedam, R. George, C. Bartee, J. Siebers, F. Lerma, E. Weiss, and T. Chung. The Clinical Implementation of Respiratory-Gated Intensity-Modulated Radiotherapy. *Medical Dosimetry*, 31(2):152–162, 2006.

A. Kolmogorov. Sulla Determinazione Empirica di una Legge di Distribuzione. *Giornale dell'Istituto Italiano degli Attuari*, 4:83–91, 1933.

S. S. Korreman. Motion in Radiotherapy: Photon Therapy. *Physics in Medicine and Biology*, 57(23):R161–R191, Nov. 2012.

G. Kraft. Tumor Therapy with Heavy Charged Particles. *Progress in Particle and Nuclear Physics*, 45:473–544, 2000.

M. Kranzfelder, T. Schuster, H. Geinitz, H. Friess, and P. Büchler. Meta-Analysis of Neoadjuvant Treatment Modalities and Definitive Non-Surgical Therapy For Oesophageal Squamous Cell Cancer. *British Journal of Surgery*, 98:768–783, 2011.

M. Krämer and M. Scholz. Treatment Planning for Heavy-Ion Radiotherapy: Calculation and Optimization of Biologically Effective Dose. *Physics in Medicine and Biology*, 45(11):3319–3330, 2000.

M. Krämer, O. Jäkel, T. Haberer, G. Kraft, and W. U. Treatment Planning for Heavy-Ion Radiotherapy: Physical Beam Model and Dose Optimization. *Physics in Medicine and Biology*, 45(11):3299–3317, 2000.

C. Kurz, J. Bauer, M. Conti, L. Guérin, L. Eriksson, and K. Parodi. Investigating the Limits of PET/CT Imaging at Very Low True Count Rates and High Random Fractions in Ion-Beam Therapy Monitoring. *Medical Physics*, 42(7):3979, 2015.

T. Landberg, J. Chavaudra, J. Dobbs, G. Hanks, K.-A. Johansson, T. Möller, and J. Purdy. ICRU Report 50: Prescribing, Recording and Reporting Photon Beam Therapy. *Journal of the International Commission on Radiation Units and Measurements*, 09 1993.

T. Landberg, J. Chavaudra, J. Dobbs, J. P. Gerard, G. Hanks, J. C. Horiot, K. A. Johansson, T. Möller, J. Purdy, N. Suntharalingam, and H. Svensson. ICRU Report 62: Prescribing, Recording and Reporting Photon Beam Therapy (Supplement to ICRU Report 50). *Journal of the International Commission on Radiation Units and Measurements*, 11 1999.

K. M. Langen and D. T. L. Jones. Organ Motion and its Management. *International Journal of Radiation Oncology, Biology, Physics*, 50(1):265–278, 2001.

T. S. Lawrence, R. K. Ten Haken, M. L. Kessler, J. M. Robertson, J. T. Lyman, M. L. Lavigne, M. B. Brown, D. J. DuRoss, J. C. Andrews, W. D. Ensminger, and A. S. Lichter. The Use of 3-D Dose Volume Analysis to Predict Radiation Hepatitis. *International Journal of Radiation Oncology, Biology, Physics*, 23(4):781–788, 1992.

H. K. Lee, A. A. Vaporciyan, J. D. Cox, S. L. Tucker, J. B. Putnam Jr., J. A. Ajani, Z. Liao, S. G. Swisher, J. A. Roth, W. R. Smythe, G. L. Walsh, R. Mohan, H. H. Liu, D. Mooring, and R. Komaki. Postoperative Pulmonary Complications after Preoperative Chemoradiation for Esophageal Carcinoma: Correlation with Pulmonary Dose-Volume Histogram Parameters. *International Journal of Radiation Oncology, Biology, Physics*, 57(5):1317–1322, 2003.

Z. Liang, H. Liu, J. Xue, B. Hu, B. Zhu, Q. Li, S. Zhang, and G. Wu. Evaluation of the Intra- and Interfractional Tumor Motion and Variability by Fiducial-Based Real-Time Tracking in Liver Stereotactic Body Radiation Therapy. *Journal of Applied Clinical Medical Physics*, 19(3):94–100, 2018.

Y. Liao, L. Wang, X. Xu, H. Chen, J. Chen, G. Zhang, H. Lei, R. Wang, S. Zhang, X. Gu, X. Zhen, and L. Zhou. An Anthropomorphic Abdominal Phantom for Deformable Image Registration Accuracy Validation in Adaptive Radiation Therapy. *Medical Physics*, 44(6):2369–2378, 2017.

J. M. Llovet, A. Burroughs, and J. Bruix. Hepatocellular Carcinoma. *The Lancet*, 362(9399):1907–1917, 2003.

M. Maier, W. Barth, W. Bayer, L. Dahl, L. Groening, C. Kleffner, B. Schlitt, K. Tinschert, H. Vormann, S. Yaramyshev, U. Ratzinger, and A. Schempp. Commissioning of the LINAC for the Heidelberg Heavy Ion Cancer Therapy Centre (HIT). *Proceedings of PAC 2007, Albuquerque, New Mexico, USA*, pages 2734–2736, 2007.

L. B. Marks, S. M. Bentzen, J. O. Deasy, F.-M. Kong, J. D. Bradley, I. S. Vogelius, I. El Naqa, J. L. Hubbs, J. V. Lebesque, R. D. Timmerman, M. K. Martel, and A. Jackson. Radiation Dose Volume Effects in the Lung. *International Journal of Radiation Oncology, Biology, Physics*, 76(3 Supplement):S70–S76, 2010a.

L. B. Marks, E. D. Yorke, A. Jackson, R. K. Ten Haken, L. S. Constine, A. Eisbruch, S. M. Bentzen, J. Nam, and J. O. Deasy. Use of Normal Tissue Complication Probability Models in the Clinic. *International Journal of Radiation Oncology, Biology, Physics*, 76(3 Supplement):S10–S19, 2010b.

V. Mazzaferro, E. Regalia, R. Doci, S. Andreola, A. Pulvirenti, F. Bozzetti, F. Montalto, M. Ammatuna, A. Morabito, and L. Gennari. Liver Transplantation for the Treatment of Small Hepatocellular Carcinomas in Patients with Cirrhosis. *The New England Journal of Medicine*, 334(11):693–699, 1996.

V. Mazzaferro, J. M. Llovet, R. Miceli, S. Bhoori, M. Schiavo, L. Mariani, T. Camerini, S. Roayaie, M. E. Schwartz, G. L. Grazi, R. Adam, P. Neuhaus, M. Salizzoni, J. Bruix, A. Forner, L. De Carlis, U. Cillo, A. K. Burroughs, R. Troisi, M. Rossi, G. E. Gerunda, J. Lerut, J. Belghiti, I. Boin, J. Gugenheim, F. Rochling, B. Van Hoek, and P. Majno. Predicting Survival After Liver Transplantation in Patients with Hepatocellular Carcinoma Beyond the Milan Criteria: a Retrospective, Exploratory Analysis. *The Lancet Oncology*, 10:35–43, 2009.

S. Mein, K. Choi, B. Kopp, T. Tessonnier, J. Bauer, A. Ferrari, T. Haberer, J. Debus, A. Abdollahi, and A. Mairani. Fast Robust Dose Calculation on GPU for High-Precision ^{1}H, ^{4}He, ^{12}C and ^{16}O Ion Therapy: The FRoG Platform. *Scientific Reports*, 8:14829, 2018.

B. D. Minsky, T. F. Pajak, R. J. Ginsberg, T. M. Pisansky, J. Martenson, R. Komaki, G. Okawara, S. A. Rosenthal, and D. P. Kelsen. INT 0123 (Radiation Therapy Oncology Group 94-05) Phase III Trial of Combined-Modality Therapy for Esophageal Cancer: High-Dose Versus Standard-Dose Radiation Therapy. *Journal of Clinical Oncology*, 20(5):1167–1174, 2002.

G. Molière. Theorie der Streuung schneller geladener Teilchen II: Mehrfach- und Vielfachstreuung. *Zeitschrift für Naturforschung A*, 3a(2):78–97, 1948.

S. Mori, S. Zenklusen, and A.-C. Knopf. Current Status and Future Prospects of Multi-Dimensional Image-Guided Particle Therapy. *Radiological Physics and Technology*, 6(2):249–272, 2013.

J. M. Mosthaf, A. Peters, S. Hanke, S. Scheloske, S. Vollmer, and T. Fleck. Overview of the Communication Structure of the HIT Accelerator Control System. *Proceedings of PCaPAC 2008, Ljubljana, Slovenia*, pages 168–170, 2008.

D. Ondreka and U. Weinrich. The Heidelberg Ion Therapy (HIT) Accelerator Coming Into Operation. *Proceedings of EPAC 2008, Genoa, Italy*, pages 979–981, 2008.

T. O'Shea, J. Bamber, D. Fontanarosa, S. van der Meer, F. Verhaegen, and E. Harris. Review of Ultrasound Image Guidance in External Beam Radiotherapy Part II: Intra-Fraction Motion Management and Novel Applications. *Physics in Medicine & Biology*, 61:R90–R137, 2016.

H. Paganetti, A. Nimierko, M. Ancukiewicz, L. E. Gerweck, M. Goitein, J. S. Loeffler, and H. D. Suit. Relative Biological Effectiveness (RBE) Values for Proton Beam Therapy. *International Journal of Radiation Oncology, Biology, Physics*, 53 (2):407–421, 2002.

H. C. Park, J. Seong, K. H. Han, C. Y. Chon, Y. M. Moon, and C. O. Suh. Dose-Response Relationship in Local Radiotherapy for Hepatocellular Carcinoma. *International Journal of Radiation Oncology, Biology, Physics*, 54(1):150–155, 2002.

D. M. Parkin, F. Bray, J. Ferlay, and P. Pisani. Estimating the World Cancer Burden: GLOBOCAN 2000. *International Journal of Cancer*, 94(2):153–156, 2001.

K. Parodi. *On the Feasibility of Dose Quantification with In-Beam PET Data in Radiotherapy with* 12*C and Proton Beams*. PhD thesis, Technische Universität Dresden, Fakultät Mathematik und Naturwissenschaften, 2004.

K. Parodi, H. Paganetti, A. H. Shih, S. Michaud, J. S. Loeffler, T. F. Delaney, N. J. Liebsch, J. E. Munzenrider, A. J. Fischman, A. Knopf, and T. Bortfeld. Patient Study of In Vivo Verification of Beam Delivery and Range, Using Positron Emission Tomography and Computed Tomography Imaging After Proton Therapy. *International Journal of Radiation Oncology, Biology, Physics*, 68 (3):920–934, 2007.

K. Parodi, T. Bortfeld, W. Enghardt, F. Fiedler, A. Knopf, H. Paganetti, J. Pawelke, G. Shakirin, and A. H. Shih. PET Imaging for Treatment Verification of Ion Therapy: Implementation and Experience at GSI Darmstadt and MGH Boston. *Nuclear Instruments and Methods in Physics Research Section A: Accelerators, Spectrometers, Detectors and Associated Equipment*, 591(1):282–286, 2008.

A. Peters, R. Cee, T. Haberer, T. Hoffmann, A. Reiter, M. Schwickert, and T. Winkelmann. Spill Structure Measurements at the Heidelberg Ion Therapy Centre. *Proceedings of EPAC 2008, Genoa, Italy*, pages 1824–1826, 2008.

F. Petrelli, T. Comito, S. Barni, G. Pancera, M. Scorsetti, and A. Ghidini. Stereotactic Body Radiotherapy for Colorectal Cancer Liver Metastases: A Systematic Review. *Radiotherapy and Oncology*, 129:427–434, 2018.

M. H. Phillips, E. Pedroni, H. Blattmann, T. Boehringer, A. Coray, and S. Scheib. Effects of Respiratory Motion on Dose Uniformity with a Charged Particle Scanning Method. *Physics in Medicine and Biology*, 37(1):223–234, 1992.

PTCOG and M. Jermann. Particle Therapy Patient Statistics per End of 2015. `https://www.ptcog.ch/index.php/patient-statistics`, 2016. Accessed: 2018-10-15.

PTCOG and M. Jermann. Particle Therapy Patient Statistics per End of 2016. `https://www.ptcog.ch/index.php/patient-statistics`, 2017. Accessed: 2018-10-15.

T. T. Puck and P. I. Marcus. Action of X-Rays on Mammalian Cells. *The Journal of Experimental Medicine*, 103(5):653–666, 1956.

D. Richter. *Treatment Planning for Tumors with Residual Motion in Scanned Ion Beam Therapy*. PhD thesis, Physikalische Fakultät, Technische Universität Darmstadt, Germany, 2012.

D. Richter, P. Steidl, N. Saito, M. Härtig, O. Jäkel, M. Durante, and C. Bert. Simulation of Uncompensated and Gated Treatments of a Liver Cancer Patient with Scanned Carbon Ions. *GSI Scientific Report 2011*, page 548, 2011.

D. Richter, N. Saito, N. Chaudhri, M. Härtig, S. E. Combs, D. Habermehl, K. Herfarth, O. Jäkel, M. Durante, and C. Bert. 4D Treatment Dose Reconstruction for Scanned Ion Beam Therapy. *International Journal of Radiation Oncology, Biology, Physics*, 87(2 Supplement):S183, 2013a.

D. Richter, A. Schwarzkopf, J. Trautmann, M. Krämer, M. Durante, O. Jäkel, and C. Bert. Upgrade and Benchmarking of a 4D Treatment Planning System for Scanned Ion Beam Therapy. *Medical Physics*, 40(5):051722, May 2013b.

D. Richter, N. Saito, N. Chaudhri, M. Härtig, M. Ellerbrock, O. Jäkel, S. E. Combs, D. Habermehl, K. Herfarth, M. Durante, and C. Bert. Four-Dimensional Patient Dose Reconstruction for Scanned Ion Beam Therapy of Moving Liver Tumors. *International Journal of Radiation Oncology Biology Physics*, 89(1):175–181, 2014.

E. Rietzel and C. Bert. Respiratory Motion Management in Particle Therapy. *Medical Physics*, 37(2):449–460, 2010.

E. Rietzel, G. T. Y. Chen, N. C. Choi, and C. G. Willet. Four-Dimensional Image-Bsaed Treatment Planning: Target Volume Segmentation and Dose Calculation in the Presence of Respiratory Motion. *International Journal of Radiation Oncology, Biology, Physics*, 61(5):1535–1550, 2005.

Robert Koch-Institut (Hrsg.) und die Gesellschaft der epidemiologischen Krebsregister in Deutschland e.V. (Hrsg.). *Krebs in Deutschland für 2013/2014, 11. Ausgabe*. Robert Koch-Institut, Berlin, Germany, 2017.

J. M. Robertson, T. S. Lawrence, L. M. Dworzanin, J. C. Andrews, S. Walker, M. L. Kessler, D. J. DuRoss, and W. D. Ensminger. Treatment of Primary Hepatobiliary Cancers with Conformal Radiation Therapy and Regional Chemotherapy. *Journal of Clinical Oncology: Official Journal of the American Society of Clinical Oncology*, 11(7):1286–1293, 1993.

J. M. Robertson, T. S. Lawrence, J. C. Andrews, S. Walker, M. L. Kessler, and W. D. Ensminger. Long-Term Results of Hepatic Artery Fluorodeoxyuridine and Conformal Radiation Therapy for Primary Hepatobiliary Cancers. *International Journal of Radiation Oncology, Biology, Physics*, 37(2):325–330, 1997.

F. Roeder, N. H. Nicolay, T. Nguyen, L. Saleh-Ebrahimi, V. Askoxylakis, T. Bostel, F. Zwicker, J. Debus, C. Timke, and P. E. Huber. Intensity Modulated Radiotherapy (IMRT) with Concurrent Chemotherapy as Definitive Treatment of Locally Advanced Esophageal Cancer. *Radiation Oncology*, 9:191, 2014.

A. W. Ruciński. *Organ Motion Management for Optimisation of Fractionated Ion Therapy of Prostate Cancer at HIT*. PhD thesis, Medizinische Fakultät der Ruprecht-Karls-Universität Heidelberg, 2013.

D. Schardt and T. Elsässer. Heavy-ion tumor therapy: Physical and radiobiological benefits. *Reviews of Modern Physics*, 82(1):383–425, Feb. 2010.

B. Schlitt, K. Dermati, G. Hutter, F. Klos, C. Muehle, W. Vinzenz, C. Will, O. Zurkan, A. Bechtold, Y. R. Lu, U. Ratzinger, and A. Schempp. Status of the 7 MeV/u, 217 MHz Injector LINAC for the Heidelberg Cancer Therapy Facility. *Proceedings of LINAC 2004, Lübeck, Germany*, pages 51–53, 2004.

C. Schömers. *Entwicklung einer dynamischen Intensitätsregelung für das Heidelberger Ionenstrahl-Therapiesynchrotron*. PhD thesis, Goethe-Universität, Frankfurt am Main, Germany, 2013.

C. Schömers, E. Feldmeier, T. Haberer, J. Naumann, R. E. Panse, and A. Peters. Implementation of an Intensity Feedback-loop for an Ion-Therapy Synchrotron. *Proceedings of IPAC 2011, San Sebastian, Spain*, pages 2851–2853, 2011.

C. Schömers, E. Feldmeier, T. Haberer, J. Naumann, R. E. Panse, and A. Peters. Patient-Specific Intensity-Modulation of a Slowly Extracted Beam at the HIT-Synchrotron. *Proceedings of IPAC 2013, Shanghai, China*, pages 2944–2946, 2013.

M. Scholz and G. Kraft. Track Structure and the Calculation of Biological Effects of Heavy Charged Particles. *Advances in Space Research: The Official Journal of the Committee on Space Research (COSPAR)*, 18(1-2):5–14, 1996.

S. M. Seltzer, J. M. Fernández-Varea, P. Andreo, P. M. Bergstrom Jr, D. T. Burns, I. Krajcar Bronic, C. K. Ross, and F. Salvat. ICRU Report 90: Key Data for Ionizing-Radiation Dosimetry: Measurement Standards and Applications. *Journal of the International Commission on Radiation Units and Measurements*, 14 (1), 2014.

Y. Seppenwoolde, W. Wunderink, S. R. Wunderink-van Ween, P. Storchi, A. Méndez Romero, and B. J. M. Heijmen. Treatment Precision of Image-Guide Liver SBRT Using Implanted Fiducial Markers Depends on Marker-Tumour Distance. *Physics in Medicine and Biology*, 56:5445–5468, 2011.

R. Serber. Nuclear Reactions at High Energies. *Physical Review*, 72(11):1114–1115, 1947.

G. C. Sharp and Plastimatch Development Team. Plastimatch 1.7.3. `http://plastimatch.org/`, 2011. Accessed: 2018-10-29.

K. M. Sjoquist, B. H. Burmeister, B. M. Smithers, J. R. Zalcberg, R. J. Simes, A. Barbour, and V. Gebski. Survival after Neoadjuvant Chemotherapy or Chemoradiotherapy for Resectable Oesophageal Carcinoma: An Updated Meta-Analysis. *Lancet Oncology*, 12:681–692, 2011.

N. Smirnov. Table for Estimating the Goodness of Fit of Empirical Distributions. *The Annals of Mathematical Statistics*, 19(2):279–281, 1948.

Statistisches Bundesamt (Destatis). *Todesursachen in Deutschland 2015*. Fachserie 12 Reihe 4. Statistisches Bundesamt, Wiesbaden, Germany, 2017.

P. Steidl. *Gating for Scanned Ion Beam Therapy*. PhD thesis, Physikalische Fakultät, Technische Universität Darmstadt, Germany, 2011.

H. Suit, T. DeLaney, S. Goldberg, H. Paganetti, B. Clasie, L. Gerweck, A. Niemierko, E. Hall, J. Flanz, J. Hallman, and A. Trofimov. Proton vs Carbon Ion Beams in the Definitive Radiation Treatment of Cancer Patients. *Radiotherapy and Oncology*, 95(1):3–22, 2010.

M. Suzuki, Y. Kase, T. Kanai, and K. Ando. Correlation Between Cell Killing and Residual Chromatin Breaks Measured by PCC in Six Human Cell Lines Irradiated with Different Radiation Types. *International Journal of Radiation Biology*, 76(9):1189–1196, 2000.

R. Timmerman, L. Papiez, and M. Suntharalingam. Extracranial Stereotactic Radiation Delivery: Expansion of Technology Beyond the Brain. *Technology in Cancer Research and Treatment*, 2(2):153–160, 2003.

K. Tinschert, R. Iannucci, and R. Lang. Electron Cyclotron Resonance Ion Sources in Use for Heavy Ion Cancer Therapy. *Review of Scientific Instruments*, 79 (02C505):1–3, 2008.

M. Tomizawa, M. Yoshizawa, K. Chida, J. Yoshizawa, Y. Arakaki, R. Nagai, A. Mizobuchi, A. Noda, K. Noda, M. Kanazawa, A. Ando, H. Muto, and T. Hattori. Slow Beam Extraction at TARN II. *Nuclear Instruments and Methods in Physics Research Section A: Accelerators, Spectrometers, Detectors and Associated Equipment*, 326(3):399–406, 1993.

P. Vavilov. Ionization Losses of High-Energy Heavy Particles. *Journal of Experimental and Theoretical Physics*, 5(4):749 – 751, 1957.

M. von Siebenthal, G. Székely, U. Gamper, P. Boesiger, A. Lomax, and P. Cattin. 4D MR Imaging of Respiratory Organ Motion and its Variability. *Physics in Medicine and Biology*, 52:1547–1564, 2007a.

M. von Siebenthal, G. Székely, A. Lomax, and P. Cattin. Inter-Subject Modelling of Liver Deformation During Radiation Therapy. *International Conference on Medical Image Computing and Computer-Assisted Intervention (MICCAI), Lecture Notes in Computer Science (LNCS)*, 4791:659–666, 2007b.

S. L. Wang, Z. Liao, A. A. Vaporciyan, S. L. Tucker, H. Liu, X. Wei, S. Swisher, J. A. Ajani, J. D. Cox, and R. Komaki. Investigation of Clinical and Dosimetric Factors Associated with Postoperative Pulmonary Complications in Esophageal Cancer Patients Treated with Concurrent Chemoradiotherapy Followed by Surgery. *International Journal of Radiation Oncology, Biology, Physics*, 64(3):692–699, 2006.

W. K. Weyrather, S. Ritter, M. Scholz, and G. Kraft. RBE for Carbon Track-Segment Irradiation in Cell Lines of Differing Repair Capacity. *International Journal of Radiation Biology*, 75(11):1357–1364, 1999.

R. R. Wilson. Radiological Use of Fast Protons. *Radiology*, 47(5):487 – 491, 1946.

T. Winkelmann, R. Cee, T. Haberer, B. Naas, A. Peters, J. Schreiner, and E. Ritter. Status Report at the Heidelberg Ion-Beam Therapy (HIT) Ion Sources and the Testbench. *Proceedings of ECRIS 2014, Nizhny Novgorod, Russia*, pages 49–51, 2014.

J. Wulf, U. Hädinger, U. Oppitz, B. Olshausen, and M. Flentje. Stereotactic Radiotherapy of Extracranial Targets: CT-Simulation and Accuracy of Treatment in the Stereotactic Body Frame. *Radiotherapy and Oncology: Journal of the European Society for Therapeutic Radiology and Oncology*, 57(2):225–36, 2000.

Z. Q. Xie. State of the Art of ECR Ion Sources. *Proceedings of the 1997 Particle Accelerator Conference, Vancouver, B.C., Canada*, 3:2662–2666, 1998.

X. Zhang, K. L. Zhao, T. M. Guerrero, S. E. McGuire, B. Yaremko, R. Komaki, J. D. Cox, Z. Hui, Y. Li, W. D. Newhauser, R. Mohan, and Z. Liao. Four-Dimensional Computed Tomography-Based Treatment Planning for Intensity-Modulated Radiation Therapy and Proton Therapy for Distal Esophageal Cancer. *International Journal of Radiation Oncology, Biology, Physics*, 72(1):278–287, 2008.

K. L. Zhao, Z. Liao, M. K. Bucci, R. Komaki, J. D. Cox, Z. H. Yu, L. Zhang, R. Mohan, and L. Dong. Evaluation of Respiratory-Induced Target Motion for Esophageal Tumors at the Gastroesophageal Junction. *Radiotherapy and Oncology*, 84(3):283–289, 2007.

Notre nature est dans le mouvement;
le repos entier est la mort.

— Blaise Pascal

DANKSAGUNG

An den vielen schönen Momenten, an die ich mich im Zusammenhang mit dieser Arbeit erinnere, waren viele liebe Menschen beteiligt, denen ich jetzt meinen Dank ausdrücken möchte.

Mein erster Dank geht an meinen Betreuer Prof. Dr. Oliver Jäkel, ohne den diese Arbeit einfach nicht entstanden wäre und der mich nicht nur finanziert und fachlich beraten hat, sondern organisatorische Steine aus dem Weg räumte und mir durch seine charismatische und offene Art auf Retreats, Wanderungen und sommerlichen Barbecues die Zeit in Heidelberg zu einer großen Freude hat werden lassen. Vielen Dank, dass du dir immer die Zeit genommen hast, die es gebraucht hat!

Außerdem möchte ich meiner Doktormutter Prof. Dr. Katia Parodi für ihre Unterstützung danken. Auch wenn die Entfernung Heidelberg-München nicht so unmittelbar war wie "über den Korridor schlendern", konnte ich jederzeit mit Unterstützung von ihr oder aus ihrer Arbeitsgruppe rechnen. Gerade bei den Leberbestrahlungen war diese Zusammenarbeit Gold wert!

Ich möchte meinem Gutachter Prof. Dr. João Seco für die schnelle und unkomplizierte Übernahme der Begutachtung der Dissertation, sowie meinen Prüfern Prof. Dr. Klaus Blaum und Prof. Dr. Jörg Jäckel für die bereitwillige Übernahme der Prüfer-Aufgaben in der Disputation danken.

Meine größte Dankbarkeit möchte ich "meinem" Post-Doc Dr. Daniel Richter ausdrücken – TRiP-Lexikon, C-Guru, Mit-Experimentator, GSI-Koordinator, Motivationstrainer, Thema-Feinschleifer, Navigator, Schlechtes Gewissen, Kletterer, Fotograf – ohne deine Unterstützung hätte ich keinen Fuß auf die Erde gebracht, keine bewegte Dosisverteilung gerechnet, hätte mich deutlich mehr verirrt. Kurz: Diese Arbeit würde heute nicht hier liegen. Danke für deine Expertise und Motivation!

Ein großer Dank geht außerdem an die vielen lieben Bürokollegen: Nicht nur für die wichtigen "fruitful discussions" über alle wichtigen Themen, sondern auch für gemeinsamen Kaffee, Tee, Kakao, Miso-Suppe, Bier, Wein, alten Sekt zur DIC-Inbetriebnahme und alle "extracurricular activities"! Großer Dank geht an meine Freunde Dres. Clarissa Gillmann, Christian Schömers und Antoni Ruciński, die sich knapp vier Jahre kaum meinem Einfluss entziehen konnten und in einer Art Stockholmsyndrom sogar freuten, Zeit mit mir zu verbringen. Aber auch allen anderen Bürokollegen – Ilaria, Marion, Mona, Wenjing, Lorena, Vânia, Julian, Alex – vielen Dank für die gemeinsame Zeit!

Gedankt sei auch der HIT-Medizinphysik, die mich während meiner Praxiszeit unter die Fittiche genommen hat, mir die Grundlagen der Strahlentherapie, der Qualitätssicherung, die Geduld mit Siemens-Systemen und die Feinheiten der $k_{p,0}$-Bestimmung gelehrt hat. Vielen Dank für Gans-Essen und "Jugend forscht"!

Ein ganz lieber Dank auch an das Beschleuniger-Team! Ohne euch hätte die ganze Promotion nicht halb so viel Spaß gemacht. Spezieller Dank geht an die Dres. Feldmeier, Galonska und Höppner, die den Schleier um die obskure Maschine "Synchrotron" so weit lüften konnten, dass ich darüber eine Arbeit schreiben konnte.

Mein großer Dank an die PET-Gruppe von Prof. Dr. Katia Parodi, die mit mir die Leberbestrahlungen immer wieder vor- und nachbereitet haben. Obwohl nach "meiner" Behandlung die Atemkurve der Patienten meistens so flach war, dass sie praktisch nicht mehr erkennbar war, wurde ich trotzdem immer mit einem Lächeln empfangen. Vielen Dank für den zuverlässigen Flurfunk!

Vielen Dank an die DKFZ-Arbeitsgruppe für Hilfestellung und Diskussionen, Freitagsseminar und immer wieder interessante Einblicke in die grundlegendere Forschung.

Vielen Dank an die GSI-Arbeitsgruppe für Unterstützung, Diskussion, Rechenzeit auf dem AIX-Cluster und die vielen anderen Ressourcen, die ich nutzen durfte. Die Langendorff-Experimente waren einfach faszinierend!

Großer Dank geht an das medizinische Team der Kopfklinik, den MTRAs und Ärzten, die mich immer wieder bei medizinischen Fragen beraten haben, mir Bilder und Konturen zur Verfügung gestellt haben und mir beim Umgang mit Patienten geholfen haben. Vielen Dank für die Motivation, aus den ganzen Erkenntnissen Paper zu schreiben!

Vielen Dank an das Sekretariat des Physikalischen Instituts und der HGSFP. Insbesondere in der stressigen Zeit vor der Disputation war die Unterstützung, insbesondere durch Frau Miller, einfach Gold wert.

Und ganz am Schluss, vielen Dank allen, die einfach so ein Stückchen mitgegangen sind und noch ein wenig weiter mit mir mitkommen, meine Familie und Freunde, die mir all diese Erfahrungen erst ermöglicht haben. Die eben nicht direkt auf meine Arbeit eingewirkt haben, sondern einfach gern Musik machten, interessante Geschichte erzählten, einer Geschichte von mir zuhörten oder bei denen ich Gast sein durfte. Danke für die Zeit in Heidelberg!

Diese Arbeit wurde gefördert durch die Deutsche Forschungsgemeinschaft im Rahmen der Klinischen Forschungsgruppe KFO 214 *Schwerionentherapie*.